

---

---

# Lattice Quantum ChromoDynamics with approximately chiral fermions

---

---



Dissertation  
zur Erlangung des Doktorgrades  
der Naturwissenschaften (Dr. rer. nat.)  
der naturwissenschaftlichen Fakultät II - Physik  
der Universität Regensburg

vorgelegt von  
**Dieter Hierl**

aus Hemau

Mai 2008



Die Arbeit wurde von Prof. Dr. Andreas Schäfer angeleitet.  
Das Promotionsgesuch wurde am 22. April 2008 eingereicht.  
Das Promotionskolloquium fand am 27. Juni 2008 statt.

Prüfungsausschuss:

Vorsitzender:	Prof. Dr. W. Wegscheider
1. Gutachter:	Prof. Dr. A. Schäfer
2. Gutachter:	Prof. Dr. T. Wettig
weiterer Prüfer:	Prof. Dr. J. Fabian

FÜR MEINE ELTERN



# Contents

<b>1</b>	<b>Introduction</b>	<b>1</b>
1.1	Background . . . . .	1
1.2	Outline of this work . . . . .	2
1.3	Publications . . . . .	3
<b>I</b>	<b>Quantum Chromodynamics</b>	<b>5</b>
<b>2</b>	<b>The QCD action and its symmetries</b>	<b>10</b>
2.1	The QCD action . . . . .	10
2.2	The path integral method . . . . .	11
2.3	Local and global symmetries . . . . .	12
2.4	Topology . . . . .	15
2.5	Anomalies . . . . .	16
<b>3</b>	<b>Perturbation theories</b>	<b>18</b>
3.1	Introduction to QCD perturbation theory . . . . .	18
3.2	Introduction to chiral perturbation theory . . . . .	19
3.3	Finite volume effects . . . . .	22
<b>4</b>	<b>Random Matrix Theory</b>	<b>26</b>
4.1	Introduction to RMT . . . . .	26
4.2	Chiral RMT . . . . .	27
<b>II</b>	<b>Lattice Quantum Chromodynamics</b>	<b>29</b>
<b>5</b>	<b>Discretizations</b>	<b>33</b>
5.1	The lattice . . . . .	33
5.2	The gauge action . . . . .	34
5.3	The Dirac operator . . . . .	38

<b>6</b>	<b>Chiral fermions</b>	<b>41</b>
6.1	Chiral symmetry on the lattice . . . . .	41
6.2	Consequences of the Ginsparg-Wilson equation . . . . .	45
6.3	The chirally improved Dirac operator . . . . .	48
6.4	The parametrized fixed-point Dirac operator . . . . .	49
<b>7</b>	<b>Ensemble creation</b>	<b>51</b>
7.1	Monte Carlo integration . . . . .	51
7.2	Running a simulation . . . . .	54
7.3	Improvements . . . . .	56
<b>8</b>	<b>Analysis</b>	<b>58</b>
8.1	Propagators . . . . .	58
8.2	Correlators . . . . .	61
8.3	Improvements I . . . . .	67
8.4	Improvements II - Low-mode averaging for meson correlators . . . . .	69
8.5	Improvements III - Correlators using covariant operators . . . . .	74
<b>9</b>	<b>Data Modeling</b>	<b>79</b>
9.1	Setting the scale . . . . .	79
9.2	Two-point correlation functions in Hilbert space . . . . .	79
9.3	LECs from "unphysical" regimes . . . . .	84
9.4	Extrapolations . . . . .	87
9.5	Interpreting the data and its errors . . . . .	89
<b>III</b>	<b>LQCD with chirally improved fermions</b>	<b>93</b>
<b>10</b>	<b>The baryon spectrum in the quenched approximation</b>	<b>95</b>
10.1	Computing the baryon masses . . . . .	96
10.2	Effective masses, eigenvectors and fit ranges . . . . .	96
10.3	Nucleon . . . . .	98
10.4	Sigma and Xi . . . . .	100
10.5	Lambda . . . . .	102
10.6	Delta and Omega . . . . .	102
10.7	Chiral extrapolations for the fine lattice . . . . .	104
10.8	Predictions . . . . .	105

<b>11 The pentaquark</b>	<b>107</b>
11.1 Quark models . . . . .	107
11.2 The Quantum Numbers of the Pentaquark . . . . .	110
11.3 Details of our lattice calculation . . . . .	112
11.4 Analysis . . . . .	114
11.5 Results . . . . .	114
11.6 What is still missing? . . . . .	116
<b>IV LQCD with 2+1 flavors using the fixed-point action</b>	<b>119</b>
<b>12 Algorithm for dynamical fermions</b>	<b>121</b>
12.1 Update . . . . .	121
12.2 Reduction . . . . .	122
12.3 Subtraction . . . . .	124
12.4 Relative gauge fixing . . . . .	125
12.5 Determinant breakup . . . . .	125
12.6 Nested Accept/Reject steps . . . . .	128
12.7 Matrix-vector multiplications . . . . .	128
<b>13 Low Energy Constants</b>	<b>136</b>
13.1 The delta regime . . . . .	136
13.2 The epsilon regime . . . . .	139
13.3 Comparing results in the epsilon-regime with RMT predictions . . . . .	142
13.4 Comparing results in the epsilon-regime with ChPT predictions . . . . .	146
<b>V Conclusion</b>	<b>151</b>
<b>Summary</b>	<b>152</b>
<b>Outlook</b>	<b>155</b>
<b>Acknowledgements</b>	<b>156</b>
<b>Appendix</b>	<b>157</b>
<b>A Definitions</b>	<b>158</b>
A.1 Gamma matrices . . . . .	158
A.2 Gell-Mann matrices . . . . .	159
A.3 Grassmann Numbers . . . . .	160
A.4 Discrete symmetries . . . . .	161

<b>B Path integral formalism on the lattice</b>	<b>163</b>
B.1 The generating functional for fermions . . . . .	163
B.2 Expectation values of fermionic operators . . . . .	164
<b>C Chiral transformations (extended)</b>	<b>165</b>
C.1 Left- and right handed projectors . . . . .	165
C.2 Global covariant densities and conserved currents . . . . .	166
C.3 Local covariant densities and conserved currents . . . . .	166
C.4 Neglecting contact terms in the densities . . . . .	168
C.5 The AWI mass in 2+1 flavors . . . . .	169
<b>D Chiral transformations with non-constant operator R</b>	<b>170</b>
D.1 The general chiral transformations on the lattice . . . . .	170
D.2 Neglecting the contact terms in the densities . . . . .	171
D.3 Covariant conserved currents with non-constant operator R . . . . .	172
<b>E Group Theory</b>	<b>173</b>
E.1 Young tableaux . . . . .	173
E.2 SU(2) symmetry group . . . . .	174
E.3 SU(3) symmetry group . . . . .	175
E.4 SU(6) symmetry group . . . . .	177
<b>F Quark models</b>	<b>180</b>
F.1 The spin-0 and spin-1 meson nonets . . . . .	180
F.2 The baryon octet and decuplet . . . . .	181
F.3 Diquarks and triquarks . . . . .	182
<b>G Parameters for CI fermions</b>	<b>183</b>
G.1 Parameters of the simulation . . . . .	183
G.2 Dirac structure and quark sources . . . . .	183
<b>H Parameters for FP fermions</b>	<b>185</b>
H.1 Parameters in the algorithm . . . . .	185
H.2 Parameters of the simulations . . . . .	187
<b>Bibliography</b>	<b>189</b>

# Chapter 1

## Introduction

### 1.1 Background

The so-called standard model of elementary particle physics provides actually the description of all phenomena in particle physics. Only gravitation, which is acting very weakly on elementary particles, is not included in it. Research activities in the last 30 years have verified the standard model with a very high degree of accuracy. It serves the description of both, the particle contents and the particle dynamics, i.e., the forces between the matter particles. Those forces were represented by the exchange of particles, the gauge bosons.

According to the standard model matter consists of 12 matter particles (6 quarks and 6 leptons) and 3 forces (electromagnetic, weak and strong force), which were described by 12 gauge bosons (photon, 8 gluons and 3 electroweak bosons). In addition to that, it is believed that the so-called Higgs particles explain the creation of particle masses. It has not been found yet, but there is a strong hope of the whole particle physics community to find it at the LHC starting 2008. The 12 matter particles are grouped into 3 families or generations. The particles of higher generations are heavy copies of the particles in the first generation and are not stable. They decay into particles of the first generation, so that nearly all matter surrounding us consists of first generation particles.

The language of the standard model is quantum field theory (QFT). All predictions are mathematically derived from the Lagrange density  $\mathcal{L}$ . Due to the fact that the Lagrange density contains more than 27 free parameters (at least 3 coupling constants, 12 particle masses, 6 mixing angles for quarks and leptons, 2 angles for the description of CP violation<sup>1</sup> and the Higgs particle mass), which have to be tuned to get physical results, there is no doubt that there has to be a more fundamental theory in physics.

A very successful part of the standard model is the quantum field theory of the strong force, the quantum chromodynamics abbreviated as QCD. There the basic parameters are the quark and gluon fields. Like every quantum field theory in the standard model it is a local gauge theory. The gauge fields are the 8 gluons which assure the local gauge invariance and create the interaction among the matter fields, the quarks. From experiments one finds that the color forces are realized by the  $SU(3)_C$  group.

In contrast to the abelian QED, where the mediator particle, the photon, is not charged, in QCD the mediator particles, the gluons, are also carrying color charge, which makes the color force always attractive. For QED and QCD the strength of the interaction is scale dependent. While for QED the coupling becomes smaller when the energy scale decreases it is vice versa for QCD, i.e., the coupling is small at high energy transfers and becomes larger when the energy decreases. The latter behavior is known as asymptotic freedom. The energy to separate two quarks, which are bound within a hadron, increases when the distance between the two quarks becomes larger and larger. At a certain point the energy to separate the two quarks is high enough to create a new quark/anti-quark pair out of the vacuum. Therefore, quarks have never been observed as isolated particles up to now. This fact is known as confinement.

---

<sup>1</sup>Cabibbo-Kobayashi-Maskawa-Matrix (CKM-Matrix)

In perturbation theory one performs an expansion in the coupling constant, which is expected to be smaller than  $\mathcal{O}(1)$ . Hence, for QCD perturbation theory can be applied for the high energy regime, where the coupling  $\alpha_s$  is small. Investigating the low energy regime of QCD perturbation theory does no longer hold and one has to use non-perturbative methods or different expansion parameters which are smaller than  $\mathcal{O}(1)$  again. There exists a effective perturbation theory, chiral perturbation theory abbreviated as  $\chi$ PT or ChPT, where an expansion is done in the pion mass, the pion decay constant and hadron momenta. But this is, of course, only an effective theory which has to be tuned via so-called low energy constants (LECs). However, if we can determine those LECs to a high precision we can also calculate physical quantities in the low-energy regime of QCD using perturbation theory methods.

A huge amount of evidence has been found, that QCD is the right theory of the strong interaction. However, a complete understanding of non-perturbative QCD effects based on the fundamental equations exclusively is still missing. This gap of knowledge limits the extraction of the free parameters in the standard model from experiments. Calculations in Lattice QCD (LQCD) applying Monte Carlo simulations can help to fill that gap, because lattice field theory provides a systematic way to solve QCD from first principles.

The physics in the low-energy regime is strongly influenced by the chiral symmetry and its breaking. For a long time it was a fundamental problem to introduce chirality in lattice simulations. Naive lattice discretizations always violate explicitly the chiral symmetry of the massless Dirac operator. One way to circumvent this problem is to use solutions of the Ginsparg-Wilson relation. The spectral properties of Ginsparg-Wilson Dirac operators have made it possible to study the structure of the QCD vacuum, in which the reasons of the chiral symmetry breaking are hidden, very efficiently.

Another problem in Lattice QCD is the huge amount of computer time needed to generate independent configurations. So, in the beginning usually the fermion determinant was set to a constant. This approximation is equal to omitting the internal quark loops and simplifies the technical procedure tremendously. For many observables the effects of these internal loops are indeed negligible and one has to add only a relatively small systematical error to the results. With the progress in computer technology, however, full QCD simulations (also called dynamical quark simulations) have become the standard and we are now even in the start-up phase for so-called dynamical chiral QCD calculations.

## 1.2 Outline of this work

This work is made up of five parts. In part I, we concentrate on QCD in the continuum. There we lay the foundations for the present work. In Chapter 2, we first introduce the QCD action and discuss several symmetries and their breaking. Two important ways one can go to solve QCD, perturbative QCD (pQCD) and chiral Perturbation theory ( $\chi$ PT), are discussed in Chapter 3. We also need predictions from the Random Matrix Theory (RMT), especially from Chiral Random Matrix Theory (ChRMT). A short introduction into those topics can be found in Chapter 4.

Solving QCD in the low energy regime from first principles means to apply non-perturbative methods like lattice quantum chromodynamics (LQCD). In part II, we explain the used tools of LQCD and guide the reader from the start to the end of a LQCD simulation. First we introduce in Chapter 5 the discretizations which allow to put a continuous field theory on a discrete space-time lattice. Because of its central importance in this work we discuss the used fermion actions in greater detail in Chapter 6. From here on one has to evaluate an integral with nearly infinite degrees of freedom. This will be reduced to a Monte Carlo calculation and to the task to create configurations which are good representatives for the physical vacuum. In Chapter 7, we explain this calculation. From these configurations one can extract the physics of interest by evaluating expectation values of operators, which have to have the correct symmetries. This is the analysis part of a lattice calculation and we are dealing with that in Chapter 8. Once we have the data produced, it has to be brought in a shape such that it can be compared with other results. Furthermore, one has to estimate the statistical and systematical uncertainties and usually to extrapolate these results to physical regions afterwards. In Chapter 9, we will pick up these issues.

In Part III, we show examples which can be calculated by LQCD methods. We will start in a chronological way with the chirally improved Dirac operator (CI Dirac operator). Here we made use of the quenched approximation

which allows us to have very large statistics. For the first project in Chapter 10, we worked on the quenched baryon spectrum which already gives a very good agreement with the physical values<sup>2</sup>. We also followed the hype about the pentaquark which was believed to have been found a few years ago by many independent experiments as well as earlier lattice calculations. We did not obtain any indication of its existence and in fact, meanwhile the experimental evidence has basically disappeared. This is discussed in Chapter 11.

Part IV contains our most recent work. In Chapter 12, we present an algorithm for dynamical fixed-point fermions. Because of our gauge update we cannot use the standard method, the Hybrid Monte Carlo (HMC) or one of its variants. This is the reason why we have to introduce nested Accept/Reject (A/R) steps and some improvements to get better acceptance rates. In addition to that we also report on some benchmarks of the applied algorithm, in particular of the most time consuming matrix-vector multiplication. In Chapter 13, we use the dynamical configurations to determine Low Energy Constants (LECs) of chiral perturbation theory. Therefore, we need very small quark masses and a volume which is so small that even a pion does not fit into it. This case is known as the  $\epsilon$ -regime which can be compared to ChRMT predictions. Elongating the time direction we are switching from the  $\epsilon$ -regime to the so-called  $\delta$ -regime which is a pretty untouched field in LQCD which in principle offers a different method to extract LECs.

We conclude this work in Part V with a summary, an outlook and the acknowledgements.

In the appendix (pp. 157) one can find calculations and definitions which do not fit into the context of the main parts. We summarize in Appendix A the definitions of the  $\gamma$ - and Gell-Mann matrices, repeat the rules for calculus with Grassmann numbers and the properties of discrete symmetry transformations which are important for hadron spectroscopy on the lattice. In Appendix B we recapitulate the path integral formalism on the lattice. Appendix C contains all the calculations suppressed in the main part for putting chiral symmetry on the lattice which were used in this work. Here we also introduce covariant densities, conserved currents and show the relevant terms for the AWI mass with  $N_f = 2 + 1$  flavors. The subsequent Appendix D is structured quite similar to Appendix C, but here we use the more general Ginsparg-Wilson equation to introduce chiral symmetry on our lattice. In Appendix E we introduce the group theory needed to obtain two-, three- or even five quark states. We start with Young tableaux and using them to classify the different symmetry classes. We also discuss and analyze some quark models in Appendix F. The Appendices G and H summarize the parameters of the CI fermions (Part III) and the FP fermions (Part IV), respectively.

## 1.3 Publications

In [1], [2] and [3] we used several baryon operators on the lattice to combine them in a correlation matrix. This matrix can be used to extract not only the ground states of baryons, but also some excited states. We give a summary of the content of these three papers in Chapter 10.

We also investigated whether one can find the pentaquark in our simulations. In [4] and [5] we used different operators which had not been tested by other groups yet to find the pentaquark on the lattice. In Chapter 11 we give some published and non-published results of these investigations.

The most recent work was done in collaboration with Prof. Dr. P. Hasenfratz and Dr. F. Niedermayer from University of Bern. In [6], [7] and [8] we published the results that were found in the  $\delta$ - and  $\epsilon$ -regime, respectively.

---

<sup>2</sup>But there are also some serious exceptions to this statement.

### 1.3.1 List of Publications

1. [1] **“Masses of excited baryons from chirally improved quenched lattice QCD”**  
T. Burch *et al.*  
Nucl. Phys. A **755**, 481 (2005)  
[arXiv:nucl-th/0501025] SPIRES entry
2. [2] **“Baryon spectroscopy with spatially improved quark sources”**  
T. Burch, C. Hagen, D. Hierl, A. Schäfer, C. Gattringer, L. Y. Glozman and C. B. Lang  
PoS **LAT2005**, 075 (2006)  
[arXiv:hep-lat/0509051] SPIRES entry
3. [9] **“Excited meson spectroscopy with chirally improved fermions”**  
T. Burch, C. Hagen, D. Hierl, A. Schäfer, C. Gattringer, L. Y. Glozman and C. B. Lang  
PoS **LAT2005**, 097 (2006)  
[arXiv:hep-lat/0509086] SPIRES entry
4. [4] **“The exotic baryon  $\Theta(1540)^+$  on the lattice”**  
D. Hierl, C. Hagen and A. Schäfer  
PoS **LAT2005**, 026 (2006)  
[arXiv:hep-lat/0509109] SPIRES entry
5. [3] **“Excited hadrons on the lattice: Baryons”**  
T. Burch, C. Gattringer, L. Y. Glozman, C. Hagen, D. Hierl, C. B. Lang and A. Schäfer  
Phys. Rev. D **74**, 014504 (2006)  
[arXiv:hep-lat/0604019] SPIRES entry
6. [5] **“Search for the  $\Theta(1540)^+$  in lattice QCD”**  
C. Hagen, D. Hierl and A. Schäfer  
Eur. Phys. J. A **29**, 221 (2006)  
[arXiv:hep-lat/0606006] SPIRES entry
7. [6] **“First results in QCD with 2+1 light flavors using the fixed-point action”**  
A. Hasenfratz, P. Hasenfratz, F. Niedermayer, D. Hierl and A. Schäfer  
PoS **LAT2006**, 178 (2006)  
[arXiv:hep-lat/0610096] SPIRES entry
8. [7] **“2+1 Flavor QCD simulated in the  $\epsilon$ -regime in different topological sectors”**  
P. Hasenfratz, D. Hierl, V. Maillart, F. Niedermayer, A. Schäfer, C. Weiermann and M. Weingart  
arXiv:0707.0071 [hep-lat] SPIRES entry
9. [8] **“2+1 flavor QCD with the fixed-point action in the  $\epsilon$ -regime”**  
P. Hasenfratz, D. Hierl, V. Maillart, F. Niedermayer, A. Schäfer, C. Weiermann and M. Weingart  
PoS **LATTICE2007** 077  
arXiv:0710.0551 [hep-lat] SPIRES entry
10. [10] **“QCD on the Cell Broadband Engine”**  
F. Belletti *et al.*  
PoS **LATTICE2007**, 039 (2007)  
arXiv:0710.2442 [hep-lat] SPIRES entry

## Part I

# Quantum Chromodynamics

Quantum Chromodynamics is the quantum field theory of the strong force. It describes the interactions of the quarks and gluons found in hadrons. The quarks are the fundamental ingredients of the hadrons, and the gluons are responsible for the interaction among the quarks. Here the underlying  $SU(3)_C$  gauge group is non-Abelian. One consequence is that the theory is asymptotically free for small distances and strong for large distances causing confinement in QCD. At large distances or low energies we can also find chiral symmetry breaking which leads to a characteristic gap in the hadron spectrum. Determining the phase diagram of QCD could presumably answer the question whether chiral symmetry breaking is able to explain confinement or shed light on the relations between those two exceptional features of QCD.

## Asymptotic freedom

Asymptotic freedom means that in high-energy reactions quarks and gluons interact very weakly. That QCD incorporates this behavior was first discovered in the early 1970s by David Politzer and Frank Wilczek and by David Gross. For this work they were awarded the 2004 Nobel Prize in Physics<sup>3</sup>.

They have calculated the  $\beta$ -function for a non-Abelian  $SU(N)$  and found that it is negative at least for small numbers of flavors  $N_f$ . For  $SU(3)_C$  gauge group it is in leading order:

$$\beta(g) = -\frac{g^3}{(4\pi)^2} \left[ 11 - \frac{2}{3}N_f \right]. \quad (1.1)$$

From the  $\beta$ -function one gets the running coupling  $\bar{g}(p)$ :

$$\bar{g}^2(p) = \frac{g^2}{1 + \frac{g^2}{(4\pi)^2} \left[ 11 - \frac{2}{3}N_f \right] \ln(p/\Lambda_{\text{QCD}})}, \quad (1.2)$$

where  $\Lambda_{\text{QCD}}$  is called the QCD scale.

For large energies the renormalized coupling  $\bar{g}(p)$  becomes small and the theory is called asymptotically free. Therefore it is possible to use perturbative expansions in orders of the coupling constant. However, for low energies this is not possible. Here quarks and gluons interact so strongly, that a perturbative expansion in the coupling constant does no longer make sense.

Asymptotic freedom also legitimates the use of the parton quark model. This model was very successful and using it one could even calculate radiation corrections in experiments which agree very well for hard processes. In the parton model one proposes that nucleons consist of free, massless partons at high energies, whose momenta sum up to the momentum of the nucleon.

## Confinement

In contrast to asymptotic freedom confinement is a non-perturbative feature. Perturbation theory implies that color charged particles propagate like free particles in leading order or interact very weakly in next-to-leading order. However, quarks do not propagate like free particles for large distances.

Color confinement (often just called confinement) is the phenomenon stating that color charged particles cannot be isolated. Quarks are confined with other quarks by the strong interaction so that the net color is neutral. There are three color charges and their corresponding anti-color charges. A particle can only be color neutral if it consists of one color charge and the corresponding anti-color charge (called meson) or if it consists of three different (anti-)color charges (called baryon)<sup>4</sup>. One consequence of confinement is that the strong interaction takes only effect in short range distances, otherwise one would expect to find color charges outside hadrons.

As two quarks get separated, the gluon field forms a narrow flux tube of color charge. Thus the force experienced by the quark remains constant regardless of its distance from the other quark. Since energy goes as force times

<sup>3</sup>The original papers one finds in [11, 12, 13, 14]

<sup>4</sup>Mesons are bosonic hadrons, while baryons are fermionic ones. In Chapter 11 we also call a pentaquark a baryon, because it has three different colored valence quarks.

distance, the total energy increases linearly with distance. When two quarks become separated, it is at some point energetically more favorable for a new quark/anti-quark pair to be created out of the vacuum than to allow the quarks to separate further. An video animation of the so-called string breaking has been published in Ref. [15].

However, up to now there is only an intuitive understanding of the confining mechanism and a fundamental knowledge is still missing.

## Chiral symmetry breaking

In the case of massless quarks the QCD action is symmetric under  $SU(N_f)$  flavor symmetry and one can introduce left- and right-handed projectors to find an additional symmetry, the chirality, which is  $SU(N_f)_L \times SU(N_f)_R$ .

If we introduce masses for the quarks, we find that at least for the two smallest quark masses,  $m_u$  and  $m_d$ , the  $SU(2)$  chiral symmetry is still approximatively intact. Furthermore the strange quark mass  $m_s$  is still small compared to the hadronic scale which makes it plausible, that also the  $SU(3)$  chiral symmetry should be preserved relatively well in nature.

The expectation value of the vacuum ground state  $\langle \bar{\psi}\psi \rangle$ , the chiral condensate, possesses less symmetries than the action itself, because the chiral symmetry is broken spontaneously:

$$SU(N_f)_L \times SU(N_f)_R \rightarrow SU(N_f)_V . \quad (1.3)$$

The Goldstone theorem states that for every broken generator of a global, continuous symmetry group there exists a so-called Goldstone boson. Thus, in the case of chiral symmetry breaking one gets  $N_f^2 - 1$  massless Goldstone bosons. In nature the quarks possess masses which breaks the chiral symmetry also explicitly. Due to that explicit breaking of chiral symmetry, the  $N_f^2 - 1$  Goldstone bosons can no longer be massless. However, this explains their relative small masses compared to other hadronic particles and makes chiral symmetry breaking very important for the understanding of mass generation in the low energy regime of QCD.

## Phase diagram of QCD

The phase diagram of QCD is not well known, neither experimentally nor theoretically. In some regions it is only applicable to matter in a compact star, where the only relevant thermodynamic quantities are quark chemical potential  $\mu$  and temperature  $T$ . Fig. 1.1 shows a proposed phase diagram for QCD [16].

Ordinary atomic matter, as we know it, is really a mixed phase, droplets of nuclear matter (nuclei) surrounded by vacuum, which exists at the low-temperature phase boundary between vacuum and nuclear matter. If we increase the quark density (i.e., increase  $\mu$ ) keeping the temperature low, we move into a phase of more and more compressed nuclear matter. Following this path corresponds to burrowing more and more deeply into a neutron star. Eventually, at an unknown critical value of  $\mu$ , there is a transition to a diquark-superconducting (2SC) quark matter phase, where quarks can build non-color-neutral diquarks. At ultra-high densities we even expect to find a color-flavor-locked (CFL) phase of color-superconducting quark matter. The difference between the 2SC and the CFL phases is the different types of diquarks which are created:

$$\langle qq \rangle_{2SC} = \epsilon^{\alpha\beta 3} \epsilon_{ab} \langle \psi_a^\alpha(k, \uparrow) \psi_b^\beta(-k, \downarrow) \rangle \neq 0 . \quad (1.4)$$

$$\langle qq \rangle_{CFL} = \sum_i \epsilon^{\alpha\beta i} \epsilon_{abi} \langle \psi_a^\alpha(k, \uparrow) \psi_b^\beta(-k, \downarrow) \rangle \neq 0 , \quad (1.5)$$

where  $\alpha, \beta = 1, 2, 3$  are color and  $a, b = 1, 2$  are flavor indices. There are also speculations that in the 2SC phase chiral symmetry is restored (i.e.,  $\langle \bar{\psi}\psi \rangle = 0$ ), while in the CFL phase it is broken again (i.e.,  $\langle \bar{\psi}\psi \rangle \neq 0$ ).

Let us start at the bottom left corner of the phase diagram in Fig. 1.1, in the vacuum where  $\mu = T = 0$ . If we heat up the system without introducing any preference for quarks over anti-quarks, i.e.,  $\mu = 0$ , the quarks are

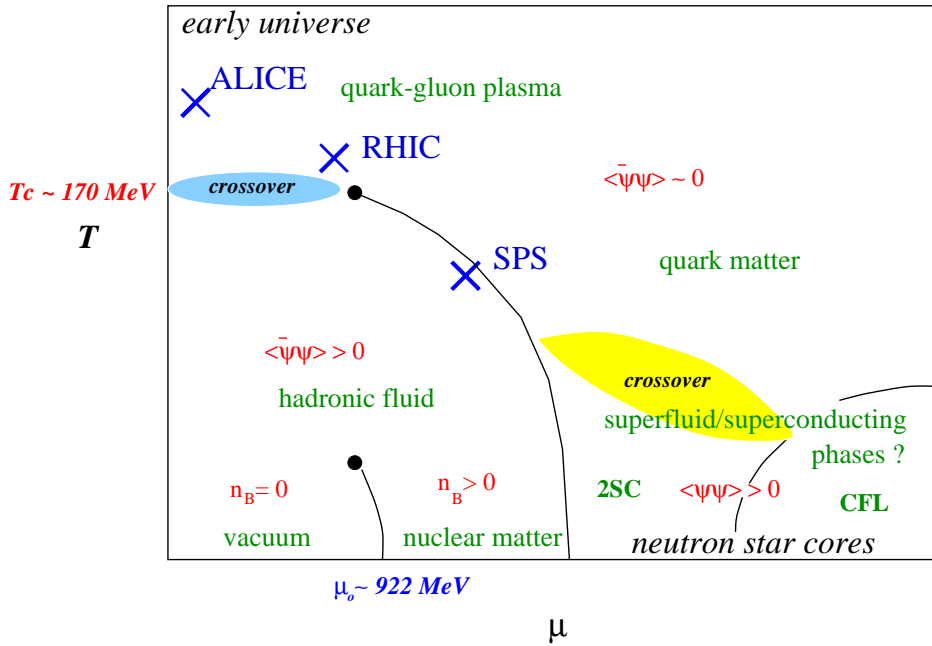


Figure 1.1: Proposed phase diagram for QCD. SPS, RHIC and ALICE are the names of relativistic heavy-ion collision experiments. 2SC and CFL refer to the diquark condensates in Eqs. (1.4) and (1.5), respectively. This figure was taken from [16]. The names of the various phases are shown in green, and the environment in which they might be found in black. Phase coexistence lines are shown as solid lines, critical points as filled circles, and crossovers by shaded regions.

still confined and we create a gas of hadrons (mostly pions). Then, around  $T = 170 \text{ MeV}$  there is a crossover to the quark gluon plasma (QGP): thermal fluctuations break up the pions, and we find a gas of quarks, anti-quarks, and gluons, as well as lighter particles such as photons, electrons, positrons, etc. Following this path corresponds to traveling far back in time, to the state of the universe shortly after the Big Bang.

The line that rises up from the nuclear/2SC matter transition and then bends back towards the  $T$  axis is the conjectured boundary between confined and unconfined phases. Until recently it was also believed to be a boundary between phases where chiral symmetry is broken (low temperature and density) and phases where it is unbroken (high temperature and density). It is now known that the CFL phase exhibits chiral symmetry breaking, and other quark matter phases like the 2SC phase may also break chiral symmetry, so it is not clear whether this is really a chiral transition line. The line ends at the "chiral critical point" which is a special temperature and density at which striking physical phenomena are expected.

If the phase transition between deconfining and confining phase coincides with the phase transition between the chiral symmetry breaking phase and the phase where chiral symmetry is restored, there is a high possibility that both phenomena are the same or have the same origin.

On the lattice the confining phase is usually measured by the behavior of the Wilson loop, which is simply the path in space-time traced out by a quark/anti-quark pair created at one point and annihilated at another point. In a non-confining theory like QED, such a loop is proportional to its perimeter. However, in a confining theory like the QCD at low temperature and densities, the action of the loop is instead proportional to its area. Since the area will be proportional to the separation of the quark/anti-quark pair, free quarks are suppressed. Mesons are allowed in such a picture, since a loop containing another loop in the opposite direction will only have a small area between the two loops.

## Outline

In this part we start to introduce the QCD action and its symmetries. Symmetries are a basic concept in modern physics which we clarify in Chapter 2. Here we introduce QCD action (Section 2.1), the concept of path integrals (Section 2.2), local and global symmetries of the QCD action (Section 2.3) and define topology on the lattice (Section 2.4). We conclude this chapter with some remarks on anomalies as an important ingredient of the theory (Section 2.5).

To understand why one simulates QCD on a lattice it is also important to know why it cannot be done differently. In Chapter 3 one finds perturbative methods which work very successfully for QED for instance. Unfortunately, these methods can no longer be applied when investigating the low-energy regime of QCD. However, in this regime we find all the hadrons of which we consist and which surround us. In Section 3.1 we collect some of the concepts which are also important for Lattice QCD. In Section 3.2 we put together some effective theories of the low-energy regime which have also influenced LQCD. Chiral perturbation theory, for instance, is used to extrapolate lattice results obtained at unphysical masses to the physical values. We cope with finite volume effects in Section 3.3.

In Chapter 4 we introduce random matrix theory (RMT), which deals with random matrices satisfying the same symmetries as, e.g., the Dirac operator. A special case of RMT is the chiral RMT in Section 4.2, where we are even able to make predictions for LQCD in the  $\epsilon$ -regime.

## Chapter 2

# The QCD action and its symmetries

The action has been firstly applied in classical mechanics and with its help one is able to introduce the variational principle. The variational principle states that every physical system behaves in such a way that the action of this system becomes stationary. This important principle could also be generalized to quantum field theory. The QCD action is the result of this principle and with it the whole system is described, i.e., one can derive the equations of motion of the system. Therefore one has to put into the action all the symmetries of the system.

In order to develop Lattice QCD one needs a formalism which is suitable for computation. This formalism is the Feynman's path integral formalism in Euclidean space-time. Using this formalism one is able to apply methods of statistical mechanics to a quantum field theory. We also apply the path integral method to identify hidden symmetries in a quantized field theory. In this context we have to consider the Jacobian of the path integral measure under a symmetry transformation.

In general symmetries can be divided in local and global symmetries. Each local symmetry is the basis of a gauge theory and requires the introduction of its own gauge bosons. Whereas local symmetries act independently at each point in space-time, global symmetries are symmetries whose operations must be simultaneously applied to all points of space-time. One can find also some global discrete symmetries in physics which are listed in Appendix A.4.

QCD is a gauge theory of the  $SU(3)$  gauge group obtained by taking the color charge to define a local symmetry. Since the strong interaction does not discriminate between different flavors of quarks, QCD has approximate flavor symmetry, which is broken by the differing masses of the quarks explicitly. There are additional global symmetries whose definitions require the notion of chirality, discrimination between left and right-handed.

Finally we introduce topology and conclude this Chapter with a brief discussion of anomalies in QCD which are the source of issues where a full understanding of the theory is missing.

### 2.1 The QCD action

The QCD is defined by its action  $S_{\text{QCD}}$  which is the space-time integral over the QCD Lagrangian  $\mathcal{L}$ :

$$S_{\text{QCD}} = \int d^4x \mathcal{L} = S_{\text{ferm}} + S_{\text{gauge}} , \quad (2.1)$$

where  $S_{\text{ferm}}$  is called the fermion action and  $S_{\text{gauge}}$  is called the gauge action.

### 2.1.1 Fermion action

The fermion action describes the interaction of the quarks in a gluonic background field. We denote the quark fields with  $\psi^f$ , where  $f$  is the flavor index of the quark. For Euclidian QCD it is<sup>1</sup>:

$$S_{\text{ferm}}[\psi, \bar{\psi}, A] = \sum_f \int d^4x \bar{\psi}^f(x) [\gamma_\mu D_\mu(x) + m^f] \psi^f(x), \quad (2.2)$$

where  $m^f$  is the mass of the quark with flavor  $f$  and diagonal in flavor space.  $D_\mu(x)$  is the covariant derivative at the space-time  $x$  in direction  $\mu$ . The covariant derivative in QCD is defined by:

$$D_\mu(x) = \partial_\mu - \sum_a ig A_\mu^a(x) t^a = \partial_\mu + A_\mu(x). \quad (2.3)$$

where  $g$  is the strong coupling constant and  $t^a = \frac{1}{2}\lambda^a$  are the generators of the  $su(3)$  algebra and  $\lambda^a$  are the Gell-Mann matrices which can be found in Appendix A.2. The gluon fields of the strong interaction are denoted as  $A_\mu^a$ .

One can show that  $S_{\text{ferm}}$  is invariant under a local  $SU(3)$  gauge transformation  $\Lambda(x) \in SU(3)$  which acts in the following way on the particle fields:

$$A'_\mu(x) = \Lambda(x) A_\mu(x) \Lambda^{-1}(x) + \Lambda(x) (\partial_\mu \Lambda^{-1}(x)) \quad (2.4)$$

$$= \Lambda(x) D_\mu(x) \Lambda^{-1}(x),$$

$$\psi'(x) = \Lambda(x) \psi(x), \quad (2.5)$$

$$\bar{\psi}'(x) = \bar{\psi}(x) \Lambda^{-1}(x). \quad (2.6)$$

### 2.1.2 Gauge action

The gauge action describes the interaction between the gluons and their propagation:

$$\begin{aligned} S_{\text{gauge}} &= -\frac{1}{2g^2} \int d^4x \text{tr} [F_{\mu\nu}(x) F_{\mu\nu}(x)], \quad (2.7) \\ &= \frac{1}{4} \int d^4x F_{\mu\nu}^a(x) F_{\mu\nu}^a(x). \end{aligned}$$

The definition of the field strength tensor  $F_{\mu\nu}^a(x)$  is:

$$\begin{aligned} F_{\mu\nu}(x) &= [D_\mu(x), D_\nu(x)] \quad (2.8) \\ &= \partial_\mu A_\nu(x) - \partial_\nu A_\mu(x) + [A_\mu(x), A_\nu(x)] \\ &= -ig (\partial_\mu A_\nu^a(x) - \partial_\nu A_\mu^a(x) + g f^{abc} A_\mu^b(x) A_\nu^c(x)) t^a \\ &= -ig F_{\mu\nu}^a(x) t^a. \end{aligned}$$

The gauge invariance under a local  $SU(3)$  gauge transformation  $\Lambda(x)$  of  $S_{\text{gauge}}$  can be written as:

$$F'_{\mu\nu} = \Lambda(x) F_{\mu\nu}(x) \Lambda(x)^{-1} \quad (2.9)$$

## 2.2 The path integral method

The Euclidean path integral formalism for the calculation of vacuum expectation values  $\langle 0 | \mathcal{O}[\psi, \bar{\psi}, A] | 0 \rangle$  is:

$$\langle 0 | \mathcal{O}[\psi, \bar{\psi}, A] | 0 \rangle = \frac{\int [d\psi] [d\bar{\psi}] [dA] \mathcal{O}[\psi, \bar{\psi}, A] e^{-S_{\text{QCD}}[\psi, \bar{\psi}, A]}}{\int [d\psi] [d\bar{\psi}] [dA] e^{-S_{\text{QCD}}[\psi, \bar{\psi}, A]}}. \quad (2.10)$$

<sup>1</sup>Here and in the following we always suppress the color and Dirac indices of the fields.

Both the operator  $\mathcal{O}[\psi, \bar{\psi}, A]$  and the Euclidean QCD action  $S_{\text{QCD}}$  are functionals of the quark and gluon fields. To get an expectation value one has to integrate over the following measures:

$$\begin{aligned} [d\psi] &\equiv \prod_f \prod_{x,\alpha,c} d\psi_{\alpha,c}^f(x), \\ [d\bar{\psi}] &\equiv \prod_f \prod_{x,\alpha,c} d\bar{\psi}_{\alpha,c}^f(x), \\ [dA] &\equiv \prod_{x,a,\mu} dA_{\mu}^a(x). \end{aligned} \quad (2.11)$$

The denominator in (2.10) normalizes the unity operator to one, i.e.,  $\langle \mathbf{1} \rangle = 1$ .

### 2.2.1 The generating functional

In order to implement a quantum description of currents and current matrix elements, one studies the generating functional  $Z[\bar{\eta}, \eta, j]$  of the theory:

$$Z[\bar{\eta}, \eta, j] = \int [d\psi] [d\bar{\psi}] [dA] e^{-S_{\text{QCD}}[\psi, \bar{\psi}, A] - \bar{\eta}\psi - \bar{\psi}\eta - j_{\mu}^a A_{\mu}^a}, \quad (2.12)$$

where  $\bar{\eta}, \eta$  are Grassmann variables and  $j_{\mu}(x) = j_{\mu}^a(x)t^a$  are currents in  $SU(3)$  color space.  $\bar{\eta}(x), \eta(x), j(x)$  are so-called source fields at  $x$  and can be arbitrary. They allow us to probe the theory by studying its response to the sources. All matrix elements needed to describe physical processes in the theory can be obtained from  $\ln Z[\bar{\eta}, \eta, j]$  by functional derivations, e.g.,  $\mathcal{O}[\psi, \bar{\psi}, A]$  is the time-ordered product of  $A_{\mu}^0(x)\bar{\psi}(y)\psi(z)$ :

$$\langle 0|\mathcal{O}[\psi, \bar{\psi}, A]|0\rangle = \langle 0|T(A_{\mu}^0(x)\bar{\psi}(y)\psi(z))|0\rangle \quad (2.13)$$

$$= \frac{\delta^3 \ln Z[\bar{\eta}, \eta, j]}{\delta j_{\mu}^0 \delta \eta(x) \delta \bar{\eta}(y)} \Big|_{\substack{\eta=0 \\ \bar{\eta}=0 \\ j=0}}. \quad (2.14)$$

This way of calculating the vacuum expectation values produces naturally the normalization function in the denominator of (2.10). Following this method one can also integrate out the fermion fields from the path integral in (2.10). This is explicitly shown in Appendix B.1.

## 2.3 Local and global symmetries

Global transformations are a special case of local transformations. Thus the postulation of a local symmetry should have a stronger impact on a theory than the postulation of only a global symmetry. Only local symmetries exclude the unphysical possibilities of interactions among the particles. A theory of free particles can be globally, but not locally symmetric, i.e., local symmetry enforces interactions. In Section 2.1 we have already seen how the local  $SU(3)_C$  color symmetry acts on the fields. In the next Section we take a closer look on that issue again.

### 2.3.1 Color symmetry

Quarks and gluons are carrying a color charge which is an additional internal quantum number. Although quarks are fermions there can be up to 3 quarks in the same state as long as they differ in their color quantum number<sup>2</sup>. The three colors of a quark  $|b\rangle$ ,  $|g\rangle$  and  $|r\rangle$  create the color space of the quark. There are two requirements to a theory of the strong interaction<sup>3</sup>:

<sup>2</sup>The most direct experimental evidence that quarks have exact 3 colors comes from the measurements of the total cross sections for the annihilation of electron-positron pairs in colliding beam experiments.

<sup>3</sup>cf. Appendix E

generation	charge +2/3 e		MeV	charge -1/3 e		MeV
1	u	up	1 to 3	d	down	3 to 7
2	c	charm	1250 ± 90	s	strange	95 ± 25
3	t	top	172500 ± 2700	b	bottom	4200 ± 70

Table 2.1: The current masses of the quarks as one can find them in [17].

- The strong interaction is supposed to be locally symmetric under  $SU(3)_C$ .
- Only singlets of the  $SU(3)_C$  are allowed in the theory.

As we have already used in the previous Section 2.1, the transformations of the symmetry group can be written in terms of products of the following<sup>4</sup>:

$$\psi(x) \rightarrow \psi'(x) = e^{i\alpha^a(x)t^a} \psi(x) \quad (2.15)$$

$$= (1 + i\alpha^a(x)t^a)\psi(x) \quad (2.16)$$

$$= \Lambda(x)\psi(x), \quad (2.17)$$

where  $\alpha^a(x)$  are infinitesimal small, real angles. It is easy to show that the action (2.1) is invariant under this transformation<sup>5</sup>:

$$S_{\text{QCD}} \rightarrow S'_{\text{QCD}}[\psi', \bar{\psi}', A'_\mu] = S_{\text{QCD}}[\psi, \bar{\psi}, A_\mu]. \quad (2.18)$$

### 2.3.2 Flavor vector symmetry

All observed meson or baryon resonances can be classified by quantum numbers. One quantum number which is only carried by quarks is the flavor quantum number. There are 6 different quarks, which are grouped into 3 generations or families and differ in their masses from each other.

In Table 2.1 the masses of the lightest three quarks (up, down and strange) are small compared to the hadronic mass scale of 1 GeV which is still smaller than the masses of hadrons containing charm-, bottom- or top-quarks. If we are only interested in the low-energy regime of QCD, we can approximate the full Lagrangian  $\mathcal{L}$  by its light flavor version, i.e., consider only the up, down and strange type quarks.

For  $N_f$  degenerate quark masses the action (2.1) is invariant under the global vector transformations<sup>6</sup>:

$$\psi_f \rightarrow \psi'_f = e^{i\alpha^a t_{ff}^a} \psi_f, \quad \bar{\psi}_f \rightarrow \bar{\psi}'_f = \bar{\psi}_f e^{-i\alpha^a t_{ff}^a}, \quad (2.19)$$

$$\psi_f \rightarrow \psi'_f = e^{i\alpha^0 \mathbb{1}_{ff}} \psi_f, \quad \bar{\psi}_f \rightarrow \bar{\psi}'_f = \bar{\psi}_f e^{-i\alpha^0 \mathbb{1}_{ff}}, \quad (2.20)$$

where the coefficients  $\alpha^a$  are real, space-time independent angles. In this context (2.19) is also known as the isospin symmetry, generalized to  $N_f$  flavors.

For arbitrary masses the  $U(1)_V$  in (2.20) still holds for (2.1) and one can easily show that its conserved quantity is the baryon number  $\mathcal{B}$ . One of the consequences of this is that there is no proton decay into leptons within the standard model.

### 2.3.3 Chiral symmetry

A second kind of global symmetry of the Lagrangian, called chiral symmetry, is valid for massless quarks if the quark fields transform like:

$$\psi_f \rightarrow \psi'_f = e^{i\gamma_5 \beta^a t_{ff}^a} \psi_f, \quad \bar{\psi}_f \rightarrow \bar{\psi}'_f = \bar{\psi}_f e^{i\gamma_5 \beta^a t_{ff}^a}, \quad (2.21)$$

<sup>4</sup>cf. Eq. (2.5)

<sup>5</sup>see Eqs. (2.1), (2.4), (2.5), (2.6) and (2.9)

<sup>6</sup>It is called vector transformation because the corresponding Noether currents are vector currents.

$$\psi_f \rightarrow \psi'_f = e^{i\gamma_5 \beta^0 \mathbf{1}_{ff'}} \psi_{f'} , \quad \bar{\psi}_f \rightarrow \bar{\psi}'_f = \bar{\psi}_{f'} e^{i\gamma_5 \beta^0 \mathbf{1}_{f'f}} , \quad (2.22)$$

where the coefficients  $\beta^a$  are again real, space-time independent angles.

Usually one introduces the following left- and right-handed projectors:

$$P_{\pm} = \frac{1}{2}(\mathbf{1} \pm \gamma_5) = P_{L,R} \quad \text{with} \quad P_{\pm}^2 = P_{\pm} , \quad P_+ P_- = P_- P_+ = 0 , \quad P_+ + P_- = 1 , \quad (2.23)$$

and defines:

$$\psi_{L,R} = P_{L,R} \psi \quad \text{with} \quad \gamma_5 \psi_{L,R} = \pm \psi_{L,R} . \quad (2.24)$$

In the massless case we find a decoupling of left- and right-handed components:

$$\mathcal{L}^{m=0} = \mathcal{L}_L + \mathcal{L}_R = \bar{\psi}_L D \psi_L + \bar{\psi}_R D \psi_R . \quad (2.25)$$

Thus we find that left- and right-handed components do not mix with each other. A mass term, however, mixes the components:

$$\bar{\psi}^f M^{ff'} \psi^{f'} = \bar{\psi}_R^f M^{ff'} \psi_L^{f'} + \bar{\psi}_L^f M^{ff'} \psi_R^{f'} . \quad (2.26)$$

One can summarize the essence of chiral symmetry in the single equation

$$D\gamma_5 + \gamma_5 D = 0 , \quad (2.27)$$

which expresses the fact that the massless Dirac operator anti-commutes with  $\gamma_5$ .

Since the chiral symmetry of the Lagrangian holds only for massless quarks, the limit of vanishing quark masses is called the chiral limit. In the chiral limit the action has the symmetry

$$U(N_f)_L \times U(N_f)_R = U(N_f)_V \times U(N_f)_A , \quad (2.28)$$

which is the same as

$$SU(N_f)_V \times U(1)_V \times SU(N_f)_A \times U(1)_A . \quad (2.29)$$

If one considers the fully quantized theory one finds that the fermion determinant is not invariant under (2.22) and the corresponding  $U(1)_A$  is broken explicitly by the non-invariant fermion integration measure in the path integral formalism. So the remaining symmetry for the massless theory is:

$$SU(N_f)_V \times U(1)_V \times SU(N_f)_A . \quad (2.30)$$

### 2.3.4 Spontaneous breaking of chiral symmetry

The spontaneous breaking of symmetries is a concept which is well known in physics. While the action of the system is invariant under a global transformation, the ground state is not. An order parameter for chiral symmetry breaking is the chiral condensate  $\langle \bar{\psi} \psi \rangle$ . The chiral condensate transforms like a mass term and is not invariant under chiral rotations [18]:

$$\langle \bar{\psi} \psi \rangle \neq 0 . \quad (2.31)$$

Another important aspect of a spontaneously broken continuous symmetry is the appearance of Goldstone bosons. Goldstone bosons are massless bosonic excitations. In the case of QCD the chiral condensate is not invariant under a  $SU(N_f)_A$  transformation and therefore in the  $N_f = 2$  case the 3 pions are interpreted as the Goldstone bosons of chiral symmetry breaking<sup>7</sup>. For massless quarks a spontaneous breaking mechanism of QCD would explain massless pions. Their relatively small masses can be understood as resulting from the explicit symmetry breaking due to the small quark masses  $m_u, m_d \neq 0$ .

<sup>7</sup>There have to be three Goldstone bosons for  $N_f = 2$ , because the spontaneously broken  $SU(2)_A$  has three generators. For  $N_f = 3$  we have 8 generators and the corresponding Goldstone bosons are identified with the pseudoscalar meson octet  $(\pi^{\pm}, \pi^0, K^{\pm}, K^0, \bar{K}^0, \eta)$ .

## 2.4 Topology

### 2.4.1 The fermionic measure

If one applies the  $U(1)_A$  transformation in (2.22) to the QCD action  $S_{\text{QCD}}$ , it remains invariant  $S' \equiv S$ , if the classical conservation law for the axial current is satisfied:

$$\partial_\mu j_\mu^5 = 2imP, \quad (2.32)$$

where  $j_\mu^5 = \bar{\psi}\gamma_\mu\gamma_5\psi$  is the axialvector current and  $P = \bar{\psi}\gamma_5\psi$  is the pseudoscalar current.

In a quantized field theory we have to take into account the measures in the path integral. The generating functional for the Green functions in Euclidean space reads<sup>8</sup>:

$$\int [d\psi] [d\bar{\psi}] \exp \left[ \sum_f \int d^4x \bar{\psi}^f(x) (\gamma_\mu D_\mu(x) + m^f) \psi^f(x) \right] = \prod_f \det (\gamma_\mu D_\mu(x) + m^f). \quad (2.33)$$

The path integral measure transforms chirally as<sup>9</sup>

$$[d\psi'] [d\bar{\psi}'] = [d\psi] [d\bar{\psi}] \mathcal{J}[\beta, A_\mu], \quad (2.34)$$

where the transformation Jacobian

$$\mathcal{J}[\beta, A_\mu] = \exp \left[ - \int d^4x \beta(x) \mathcal{A}[A_\mu](x) \right], \quad (2.35)$$

contains precisely the singlet anomaly (2.36) discussed in Section 2.5.2:

$$\mathcal{A}[A_\mu(x)] = 2i \sum_n \varphi_n^\dagger(x) \gamma_5 \varphi_n(x) = \frac{-i}{16\pi^2} \epsilon^{\mu\nu\alpha\beta} \text{tr} F_{\mu\nu} F_{\alpha\beta}, \quad (2.36)$$

where  $\{\varphi_n(x)\}$  is a complete set of orthogonal eigenfunctions of the Dirac operator and is defined in Section 2.4.2. The calculations to get (2.36) are rather lengthy and will not be included here. The interested reader is referred to [19].

At the end of the day we have to modify the classical conservation law for the axial current in (2.32) into

$$\partial_\mu j_\mu^{a5}(x) = 2imP^a(x) + \delta^{0a} \mathcal{A}[A_\mu(x)], \quad (2.37)$$

where one can see that even in the massless theory the axialvector current for flavor-singlets is not conserved anymore.

### 2.4.2 Atiyah-Singer index theorem

Let us consider the eigenvalue equation for the Dirac operator  $D(x) = \gamma_\mu D_\mu(x)$  in Euclidean space:

$$D \varphi_n(x) = \lambda_n \varphi_n(x), \quad (2.38)$$

with  $\{\varphi_n(x)\}$  being a complete set of orthogonal system of eigenfunctions. Then due to (2.27)  $\gamma_5 \varphi_n$  satisfies the equation with negative eigenvalues  $-\lambda_n$ :

$$D \gamma_5 \varphi_n(x) = -\lambda_n \gamma_5 \varphi_n(x). \quad (2.39)$$

The eigenfunctions  $\varphi_n$  and  $\gamma_5 \varphi_n$  are orthogonal for  $\lambda_n \neq 0$ :

$$\int d^4x \varphi_n^\dagger(x) \gamma_5 \varphi_n(x) = 0. \quad (2.40)$$

<sup>8</sup>cf. Appendix B.1

<sup>9</sup>For a better readability from now on we only use a single flavor.

A proof of (2.40) can be found in textbooks<sup>10</sup>. However, the eigenfunctions are not orthogonal for zero-eigenvalue  $\lambda_n = 0$ . According to (2.38) and (2.39)  $\varphi_n^0$  and  $\gamma_5 \varphi_n^0$  are eigenfunctions of the same eigenvalue  $\lambda_n = 0$ . We introduce positive and negative eigenfunctions

$$\varphi_{n^+}^0 = P_+ \varphi_n^0, \quad \varphi_{n^-}^0 = P_- \varphi_n^0, \quad (2.41)$$

where  $P_{\pm} = \frac{1}{2}(\mathbb{1} \pm \gamma_5)$ . We define:

$$D \varphi_{n^{\pm}}^0 = \frac{1}{2} D (\mathbb{1} \pm \gamma_5) \varphi_n^0 = D_{\pm} \varphi_n^0 = 0. \quad (2.42)$$

Using the orthogonality condition (2.40) we find:

$$\begin{aligned} \int d^4x \sum_n \varphi_n^{\dagger}(x) \gamma_5 \varphi_n(x) &= \int d^4x \sum_n \varphi_n^{0\dagger}(x) \gamma_5 \varphi_n^0(x); \\ &= \int d^4x \sum_n \varphi_{n^+}^{0\dagger}(x) \gamma_5 \varphi_{n^+}^0(x) - \int d^4x \sum_n \varphi_{n^-}^{0\dagger}(x) \gamma_5 \varphi_{n^-}^0(x), \\ &= n^+ - n^- = \text{index } D_+, \end{aligned} \quad (2.43)$$

where  $n_{\pm}$  denote the number of positive and negative chirality zero-modes.

At the end of the day we get for the massless theory:

$$\begin{aligned} \int d^4x \partial_{\mu} j_{\mu}^5(x) &= \int d^4x \mathcal{A}[A_{\mu}(x)], \\ &= 2i \int d^4x \sum_n \varphi_n^{\dagger}(x) \gamma_5 \varphi_n(x), \\ &= 2i \cdot \text{index } D_+ \equiv 2iQ, \end{aligned} \quad (2.44)$$

where  $Q$  is the topological charge and we define the topological charge density as:

$$q(x) = \sum_n \varphi_n^{\dagger}(x) \gamma_5 \varphi_n(x) = -\frac{1}{32\pi^2} \epsilon^{\mu\nu\alpha\beta} \text{tr } F_{\mu\nu} F_{\alpha\beta}. \quad (2.45)$$

## 2.5 Anomalies

In quantum physics an anomaly is the failure of a symmetry of the action to be a symmetry of any regularization of the full quantum theory. Technically, an anomalous symmetry in a quantum theory is a symmetry of the action, but not of the measure.

### 2.5.1 Scale invariance anomaly

Looking at QCD in the chiral limit, the theory has no mass scale and so there is a conformal symmetry  $x \rightarrow x' = \lambda x$  for arbitrary  $\lambda$ . The associated quark and gluon scale transformations would be:

$$\psi(x) \rightarrow \lambda^{3/2} \psi(\lambda x) \quad A_{\mu}^a(x) \rightarrow \lambda A_{\mu}^a(\lambda x). \quad (2.46)$$

While the Lagrangian itself is not invariant the action is easily seen to be unchanged. The Noether current associated with the change of scale is

$$J_{\text{scale}}^{\mu} = x_{\nu} \theta^{\mu\nu}, \quad (2.47)$$

where  $\theta^{\mu\nu}$  is the energy-momentum tensor [20]. Since the energy-momentum tensor is conserved,  $\partial_{\mu} \theta^{\mu\nu} = 0$ , the conservation of scale current is equivalent to the vanishing trace of  $\theta^{\mu\nu}$ :

$$\partial_{\mu} J_{\text{scale}}^{\mu} = \theta_{\mu}^{\mu} = 0. \quad (2.48)$$

---

<sup>10</sup>cf. Ref. [19]

For any hadron  $H$ , the matrix element of the energy-momentum tensor at zero momentum transfer is:

$$\langle H(\vec{k}) | \theta^{\mu\nu} | H(\vec{k}) \rangle = 2k^\mu k^\nu . \quad (2.49)$$

A vanishing trace would imply zero mass:

$$\langle H(\vec{k}) | \theta_\mu{}^\mu | H(\vec{k}) \rangle = 2M_H^2 = 0 . \quad (2.50)$$

We would not expect, e.g., the proton mass to vanish if the quark masses were set equal to zero, yet the scale invariance argument implies it must.

However, due to an anomaly the measure is not invariant under conformal symmetry and this introduces a scale, which is the scale  $\Lambda_{\text{QCD}}$ . This scale breaks the conformal symmetry and determines the sizes and masses of hadrons. The scale invariance anomaly is responsible for most of the mass of ordinary matter. A more detailed discussion one finds in [20].

### 2.5.2 $U(1)_A$ anomaly

The QCD Lagrangian in the chiral limit contains a further axial  $U(1)_A$  symmetry, besides the chiral  $SU(N_f)_L \times SU(N_f)_R$  symmetry and the vector  $U(1)_V$  symmetry. The axial symmetry is, however, neither observed in the hadron spectrum nor realized as a Goldstone boson. The resolution of this problem is found in the existence of the  $U(1)_A$  anomaly and of gauge field configurations with non-vanishing topological charge, called instantons. Then the  $U(1)_A$  symmetry is spontaneously broken without generating a Goldstone boson [21, 22].

The chirally transformed path integral measure, discussed in Section 2.4.1, contains precisely the singlet anomaly in (2.36). Due to the fact that the action is invariant under  $U(1)_A$  symmetry, but the measure is not, this is called an anomaly again. It is also called singlet anomaly, because it does not vanish for flavor singlet terms only.

### 2.5.3 Strong CP problem

It is often listed among the positive features of QCD that it conserves baryon number, flavor and CP. If QCD would be the only ingredient in our theory, we could remove the strong CP problem by imposing an additional discrete CP symmetry on the QCD Lagrangian. In reality, this will not work for the full Standard model since the electroweak sector always violates CP. In principle one can add to the QCD action (2.1) the following term:

$$\begin{aligned} S_{\text{gen}} &= S_{\text{QCD}} + S_\theta , \\ &= S_{\text{QCD}} - \frac{\theta}{32\pi^2} \int d^4x \epsilon^{\mu\nu\alpha\beta} \text{tr} F_{\mu\nu} F_{\alpha\beta} . \end{aligned} \quad (2.51)$$

This additional term is also related to the  $U(1)_A$  anomaly and the topological charge  $Q$  via:

$$- \frac{\theta}{32\pi^2} \int d^4x \epsilon^{\mu\nu\alpha\beta} \text{tr} F_{\mu\nu} F_{\alpha\beta} = \frac{i\theta}{2} \mathcal{A}[A] = \theta Q[A] . \quad (2.52)$$

As we see in Section 2.4.2 the topological charge is connected to the index of the Dirac operator  $D$  which is in turn connected to the number of zero modes of the Dirac operator. If we integrate out the fermion fields in the action (2.51) we get the fermion determinant, which is  $\det D$ . From this follows that if the Dirac operator  $D$  has a zero mode the fermion determinant vanishes and the partition function becomes zero. If the Dirac operator does not have a zero mode, the topological charge  $Q[A]$  is zero and  $S_\theta$  vanishes in the partition function, i.e.,  $S_\theta$  does not contribute to the partition function of the QCD. However, one can show that in correlation functions there can be contributions of  $S_\theta$  which have influence to nature. Due to the fact that  $\theta$  is very small, i.e.,  $|\theta| < 10^{-9}$  derived from the measurement of the electric dipole moment of the neutron, these effects are very hard to measure if they are there at all. The angle  $\theta$  is like the quark masses an input parameter of the Standard model. It has to be fixed via experiments and cannot be predicted from the theory at the moment. It is not clear why it has to be so small or even zero. This puzzle is the so-called strong CP problem of QCD.

<sup>10</sup>The measure is still invariant under  $SU(N_f)_A$ , which is spontaneously broken by the chiral condensate.

# Chapter 3

## Perturbation theories

### 3.1 Introduction to QCD perturbation theory

In contrast to quantum electrodynamics (QED) in QCD also the gauge bosons are charged and are able to interact among themselves directly. Because the coupling constant  $\alpha_{\text{strong}}$  of the QCD is not small for large distances or low energies, one cannot apply perturbation theory methods to solve QCD in this regime. But for small distances or large energies the strong force becomes weak and one can use perturbation theory techniques like in the QED. Nevertheless, due to the color charge of the quarks and gluons these techniques are more complicated than in QED. In this Section we discuss some important techniques which are also used either in Lattice QCD or are differently used putting them on a finite lattice.

#### 3.1.1 Gauge fixing

First consider the quantization of the pure gauge theory without fermions. In Euclidean space-time we obtain the functional integral

$$\int [dA] \exp \left[ \frac{1}{4} \int d^4x F_{\mu\nu}^a(x) F^{\mu\nu a}(x) \right]. \quad (3.1)$$

The Lagrangian is unchanged along the infinite number of directions in the space of field configurations corresponding to local gauge transformations. To compute the functional integral we must factor out the integrations along these directions, constraining the remaining integral to a much smaller space.

We will constrain the gauge directions by applying a gauge condition  $G(A) = 0$  at each point  $x$ . Following Faddeev and Popov, we can introduce this constraint by inserting into the functional integral the identity:

$$1 = \int [d\alpha] \delta(G(A^\alpha)) \left| \det \left( \frac{\delta G(A^\alpha)}{\delta \alpha} \right) \right|. \quad (3.2)$$

Here  $A^\alpha$  is a gauge field  $A$  transformed through a finite gauge transformation:

$$(A^\alpha)_\mu^a t^a = e^{i\alpha^a t^a} \left[ A_\mu^b t^b + \frac{i}{g} \partial_\mu \right] e^{-i\alpha^c t^c}. \quad (3.3)$$

We bring this into the infinitesimal form for small  $\alpha$ :

$$(A^\alpha)_\mu^a = A_\mu^a + \frac{1}{g} \partial_\mu \alpha^a + f^{abc} A_\mu^b \alpha^c + \mathcal{O}(\alpha^2) = A_\mu^a + \frac{1}{g} D_\mu \alpha^a + \mathcal{O}(\alpha^2). \quad (3.4)$$

Now we have to choose a gauge condition, e.g., the generalized Lorentz gauge condition:

$$G(A) = \partial^\mu A_\mu^a(x) - \omega^a(x), \quad (3.5)$$

with a Gaussian weight for  $\omega^a(x)$ . In contrast to QED, the determinant in (3.2) is not independent of  $A$ , and thus it does not vanish. Faddeev and Popov chose to represent this determinant as a functional integral over a new set of anti-commuting fields:

$$\det\left(\frac{\delta G(A^\alpha)}{\delta \alpha}\right) = \det\left(\frac{1}{g}\partial^\mu D_\mu\right) = \int [dc][d\bar{c}] \exp\left[i \int d^4x \bar{c}(-\partial^\mu D_\mu)c\right]. \quad (3.6)$$

$c, \bar{c}$  must be anti-commuting fields that are scalar under Lorentz transformations. Thus quantum excitations of these fields have the wrong relation between spin and statistics to be physical particles. Nevertheless one can work out Feynman rules for those particles which are called Faddeev-Popov ghosts.

Later we will see that gauge fixing on the lattice is not necessary in principle. Due to the fact that we are using Monte Carlo techniques we do not see gauge copies in our calculations and therefore we do not need to fix the gauge. Nevertheless if one is interested in ghost propagators for instance, also on the lattice gauge fixing can be applied.

In Section 12.4 we use a special gauge fixing to improve the acceptance rate of our algorithm by reducing the fluctuations in the determinant.

## 3.2 Introduction to chiral perturbation theory

In the low energy regime the chiral perturbation theory is another effective theory which is able to describe many effects. There the pion masses and their small momenta are the perturbation parameters. Therefore it cannot be a fundamental theory and so it has a natural cutoff for large energies. However, chiral perturbation theory depends in the basic equations on constants which can be found via experiments or computer simulations.

An effective low energy theory of QCD must be such that chiral symmetry and its spontaneous and explicit breaking are implemented. The degrees of freedom in QCD at low energies are composite hadrons, primarily the Goldstone bosons. First of all we need an effective Lagrangian  $\mathcal{L}_{\text{eff}}$  for  $N_f = 2$ . Later we will extend it to a  $N_f = 3$  theory.

As discussed in Section 2.3.3 we have the chiral transformations (2.21) which almost give rise to an invariance of the QCD Lagrangian  $\mathcal{L}_{\text{QCD}}$  for small quark masses  $m_u, m_d$ . We will use the exponential representation of the pseudoscalar Goldstone bosons. It is a unitary  $2 \times 2$  matrix field  $U(x) \in SU(2)$ :

$$U(x) = \exp\left(\frac{i\vec{\tau} \cdot \vec{\pi}}{F}\right). \quad (3.7)$$

Under chiral transformations the matrix  $U$  transforms as

$$U \rightarrow U' = RUL^\dagger, \quad R, L \in SU(2)_{\text{R,L}}. \quad (3.8)$$

In general the effective Lagrangian  $\mathcal{L}_{\text{eff}}$  is a functional of  $U(x)$  and its derivative  $\partial^\mu U(x)$ , and thus it follows:

$$\mathcal{L}_{\text{QCD}} \rightarrow \mathcal{L}_{\text{eff}} = \mathcal{L}_{\text{eff}}[U, \partial_\mu U]. \quad (3.9)$$

$\mathcal{L}_{\text{eff}}$  is expanded in terms of powers of these derivatives

$$\mathcal{L}_{\text{eff}} = \mathcal{L}_2 + \mathcal{L}_4 + \mathcal{L}_6 + \dots \quad (3.10)$$

where the index gives the number of derivatives  $\partial^\mu U(x)$ . The leading term looks like

$$\mathcal{L}_2 = \frac{F^2}{4} \text{tr} [\partial^\mu U^\dagger \partial_\mu U]. \quad (3.11)$$

After adding the leading symmetry breaking term proportional to a constant  $B$  such that  $\mathcal{L}_2$  is still even in the Goldstone boson fields, we obtain

$$\mathcal{L}_2 = \frac{F^2}{4} \text{tr} [\partial^\mu U^\dagger \partial_\mu U] + \frac{B}{2} F^2 \text{tr} [M(U^\dagger + U)]. \quad (3.12)$$

We expand Eq. (3.12) in the isotriplet pion fields  $\vec{\pi}(x)$  defined in Eq. (3.7) and get:

$$\mathcal{L}_2 = \frac{1}{2} \partial^\mu \vec{\pi} \cdot \partial_\mu \vec{\pi} - \frac{B}{2} (m_u + m_d) \vec{\pi}^2 + BF^2 (m_u + m_d) . \quad (3.13)$$

Due to the fact that the pions are bosons and thus should follow the Gordon-Klein equation we can identify the constant  $B$  with the pion mass:

$$m_\pi^2 = B(m_u + m_d) . \quad (3.14)$$

To be able to use the path integral formalism one has to introduce sources in the Lagrangian and we extend the theory from  $N_f = 2$  to  $N_f = 3$ . This leads us to the partition function  $Z$ :

$$Z[l_\mu, r_\mu, s, p] = \int [dU] e^{-\int d^4x \mathcal{L}_{\text{eff}}[U, \partial_\mu U, l_\mu, r_\mu, s, p]} , \quad (3.15)$$

where  $l_\mu, r_\mu, s, p$  are  $3 \times 3$  matrix source functions expressible as

$$l_\mu = l_\mu^0 + l_\mu^a \lambda^a , \quad r_\mu = r_\mu^0 + r_\mu^a \lambda^a , \quad s = s^0 + s^a \lambda^a , \quad p = p^0 + p^a \lambda^a \quad (3.16)$$

for the left- and right-handed, scalar and pseudoscalar source terms.  $U$  usually contains the Goldstone boson fields. These sources transform like:

$$\psi_L \rightarrow L(x) \psi_L , \quad \psi_R \rightarrow R(x) \psi_R , \quad (3.17)$$

$$l_\mu \rightarrow L(x) l_\mu L^\dagger(x) + i \partial_\mu L(x) L^\dagger(x) , \quad (3.18)$$

$$r_\mu \rightarrow R(x) r_\mu R^\dagger(x) + i \partial_\mu R(x) R^\dagger(x) , \quad (3.19)$$

$$(s + ip) \rightarrow L(x) (s + ip) R^\dagger(x) , \quad (3.20)$$

where  $L, R \in SU(3)$ . These transformations provides an invariance of the theory under chiral symmetry. The left- and right-handed source terms enter like a gauge field in the covariant derivative:

$$D_\mu U = \partial_\mu U + i l_\mu U - i U r_\mu . \quad (3.21)$$

The effective action is then expressed in terms of these quantities and at lowest order one gets:

$$\mathcal{L}_2 = \frac{F^2}{4} \text{tr} [D^\mu U^\dagger D_\mu U] + \frac{F^2}{4} \text{tr} [\chi U^\dagger + U \chi^\dagger] , \quad (3.22)$$

where

$$\chi = 2B(s + ip) , \quad (3.23)$$

and  $B$  is a constant. In the limit  $l_\mu = r_\mu = p = 0, s = M$ , this is the same effective Lagrangian as in Eq. (3.12). We could now extract matrix elements such as the scalar density matrix element for instance:

$$\langle \bar{u}u \rangle + \langle \bar{d}d \rangle = \left. \frac{\delta \ln Z}{\delta s^0} \right|_{l=r=p=0, s=M} = -2F^2 B . \quad (3.24)$$

### 3.2.1 The Gell-Mann-Oakes-Renner relation

The constant  $F$  appears in the matrix element  $\langle 0 | j_\mu^5 | \pi^+(p) \rangle = iF p_\mu$  of the axialvector current  $j_\mu^5 = \bar{\psi} \gamma_\mu \gamma_5 \psi$  and determines the charged pion decay rate  $f_\pi$ . If we also identify  $F$  with the pion decay constant  $f_\pi$  and combine Eqs. (3.14) and (3.24), we find the famous Gell-Mann-Oakes-Renner (GMOR) relation [23]:

$$m_\pi^2 f_\pi^2 = -\frac{1}{2} (m_u + m_d) (\langle \bar{u}u \rangle + \langle \bar{d}d \rangle) . \quad (3.25)$$

This relation expresses in first order chiral perturbation theory the quadratic dependence of the pion mass in terms of the quark masses:  $m_\pi^2 \propto m_q$ . This is a well settled relation which can be found even on small lattice simulations.

Coefficient	Value	Origin
$L_1^r$	$0.65 \pm 0.28$	$\pi\pi$ scattering
$L_2^r$	$1.89 \pm 0.26$	and
$L_3^r$	$-3.06 \pm 0.92$	$K_{\ell 4}$ decay
$L_5^r$	$2.3 \pm 0.2$	$F_K/F_\pi$
$2L_7^r + L_8^r$	$0.4 \pm 0.1$	meson masses
$L_9^r$	$7.1 \pm 0.3$	$\pi$ charge radius
$L_{10}^r$	$-5.6 \pm 0.3$	$\pi \rightarrow e\nu\gamma$
$L_7^r$	$-0.4 \pm ?$	$\eta$ - $\eta'$ mixing
$L_4^r$	$\sim 0$	vanishes in $N_c \rightarrow \infty$ limit
$L_6^r$	$\sim 0$	vanishes in $N_c \rightarrow \infty$ limit

Table 3.1: Gasser-Leutwyler counterterms, given in units of  $10^{-3}$  at renormalization point  $\mu = m_\eta$ , and the means by which they are determined. The table was taken from [20].

### 3.2.2 Low energy constants

In Eq.(3.12), we have already seen two low energy constants, namely  $F$  and  $B$ . In the next higher order for  $N_f = 3$  flavors there occur 10 further low energy constants:

$$\begin{aligned}
\mathcal{L}_4 &= \sum_{i=1}^{10} L_i \mathcal{O}_i, \\
&= L_1 [\text{tr}(D_\mu U D^\mu U^\dagger)]^2 + L_2 \text{tr}(D_\mu U D_\nu U^\dagger) \cdot \text{tr}(D^\mu U D^\nu U^\dagger) + L_3 \text{tr}(D_\mu U D^\mu U^\dagger D_\nu U D^\nu U^\dagger), \\
&+ L_4 \text{tr}(D_\mu U D^\mu U^\dagger) \text{tr}(\chi U^\dagger + U \chi^\dagger) + L_5 \text{tr}(D_\mu U D^\mu U^\dagger (\chi U^\dagger + U \chi^\dagger)) + L_6 [\text{tr}(\chi U^\dagger + U \chi^\dagger)]^2, \\
&+ L_7 [\text{tr}(\chi^\dagger U - U \chi^\dagger)]^2 + L_8 \text{tr}(\chi U^\dagger \chi U^\dagger + U \chi^\dagger U \chi^\dagger), \\
&+ iL_9 \text{tr}(L_{\mu\nu} D^\mu U D^\nu U^\dagger + R_{\mu\nu} D^\mu U^\dagger D^\nu U) + L_{10} \text{tr}(L_{\mu\nu} U R^{\mu\nu} U^\dagger),
\end{aligned} \tag{3.26}$$

where the covariant derivative is defined via (3.21), the constants  $L_i$ ,  $i = 1, \dots, 10$  are arbitrary (not determined from chiral symmetry alone) and  $L_{\mu\nu}$ ,  $R_{\mu\nu}$  are external field strength tensors

$$L_{\mu\nu} = \partial_\mu l_\nu - \partial_\nu l_\mu + i[l_\mu, l_\nu], \quad L_{\mu\nu} \rightarrow L(x) L_{\mu\nu} R^\dagger(x), \tag{3.27}$$

$$R_{\mu\nu} = \partial_\mu r_\nu - \partial_\nu r_\mu + i[r_\mu, r_\nu], \quad R_{\mu\nu} \rightarrow L(x) R_{\mu\nu} R^\dagger(x). \tag{3.28}$$

The bare parameters  $L_i$  which appear in this Lagrangian are not physical quantities. Instead the experimentally relevant renormalized values of these parameters are obtained by appending to these bare values the divergent one-loop contributions

$$L_i^r = L_i - \frac{\gamma_i}{32\pi^2} \left[ -\frac{2}{\epsilon} - \ln(4\pi) + \gamma - 1 \right]. \tag{3.29}$$

By comparing predictions with experiment, Gasser and Leutwyler were able to determine empirical numbers for each of these 10 parameters. Typical values are shown in Table 3.1.

If we can determine these low energy constants, we have a valid theory of the low energy regime of QCD. Lattice QCD is a first principle method which can derive those low energy constants without experiments and as we will see, e.g., in Section 9.4.3, LQCD makes strongly use of the chiral perturbation theory in the extrapolations to physical masses. For a more detailed discussion of chiral perturbation theory the interested reader is referred to [24] and [20].

### 3.3 Finite volume effects

Numerical simulations of QCD are necessarily done in a finite volume. Since real experiments are performed in volumes much larger than the hadronic scale ( $\mathcal{O}(1 \text{ fm})$ ), in comparing the numerical results with experiments the finite size distortion is a nuance. One should eliminate the finite size effects by different volumes and extrapolate to infinite volume.

There are, however, cases when finite size effects can be used directly to pin down physical effects. This is in the case of QCD at very high temperatures. Finite temperature in QFTs are realized by a finite, periodic extension along the time direction in Euclidean space-time. QCD in extreme environment can be simulated this way, the related finite size effects describe directly observable physics.

An other situation is when the finite size effects in the numerical simulations cannot be compared directly with real experiments, but rather with analytic theoretical results. This is the case in a finite box, where the finite size effect are dominated by the lightest particles, the pions. In this case ChPT gives analytic predictions on the finite size effects in terms of the low energy constants (LECs) of the effective theory. A comparison with the numerical results gives predictions on this low energy constants. The interested reader is referred to [25].

#### 3.3.1 ChPT in finite volume

It is useful to consider QCD with two degenerate flavors:  $N_f = 2$ ,  $m_u = m_d = m_{ud}$ . Chiral symmetry is spontaneously broken and the lightest excitations are the Goldstone bosons which are massless if  $m_{ud} = 0$ . The low energy physics is dominated by the pions. This art of QCD is equivalent to a  $O(4) \simeq SU(2) \times SU(2)$  ferromagnet. This connection will help to explain the physics in some cases below.

The expansion parameters in ChPT are

$$\frac{p}{4\pi F}, \quad \frac{m_\pi}{4\pi F} \quad (3.30)$$

where the theory can only be applied if both are small. In a finite volume the spatial momenta are discretized according to Eq. (5.2). Therefore one can have small non-zero momenta and apply ChPT only if the condition

$$L \gg \frac{1}{2F} \sim 1 \text{ fm} \quad (3.31)$$

is satisfied. Note that unlike  $FL$  the combination  $m_\pi L$  is not constrained. Both  $m_\pi L \ll 1$  and  $m_\pi L \gg 1$  are acceptable [26, 27, 28], but they imply different ways to organize the chiral series<sup>1</sup>,

$$m_\pi L \gg 1 \leftrightarrow p\text{-expansion} \quad (3.32)$$

$$m_\pi L \lesssim 1 \leftrightarrow \epsilon\text{-expansion} . \quad (3.33)$$

#### 3.3.2 $p$ -regime

The so-called  $p$ -expansion applies to large volumes where finite size effects are exponentially small ( $\mathcal{O}(e^{-m_\pi L})$ ), which is the standard situation. When the linear size  $L$  of the lattice is much larger than the Compton wavelength of the pions  $1/m_\pi$ , the system hardly feels the finite volume, and the typical momentum scale is thus  $p \sim m_\pi$ . As the size of the box or the quark mass becomes smaller, finite size effects start to become important, but provided  $m_\pi L \geq 1$ , ordinary perturbation theory is still applicable. In the boundary of this regime, when  $m_\pi L \sim 1$ , the expansion of the field  $U(x)$  in Eq. (3.7) around the classical solution and the expansion in powers of momenta of the Lagrangian itself become the same expansion in powers of  $(FL)^{-1}$ . This is the so-called  $p$ -expansion [27] in which

$$\frac{m_\pi}{\Lambda_{\text{QCD}}} \sim \frac{p}{\Lambda_{\text{QCD}}} \sim \frac{1}{FL} . \quad (3.34)$$

<sup>1</sup>The conditions  $m_\pi L \gg 1$  or  $m_\pi L \lesssim 1$  obtain a less formal meaning in the explicit results. Actually, the different regimes go smoothly over in each other.

If the chiral limit is approached further in such a way that the Compton wavelength of the pion is larger than the box size ( $L > 1/m_\pi$ ), the conventional  $p$ -expansion eventually breaks down due to propagation of pions with zero momenta. In this regime, the chiral effective theory in a finite box looks very much like in infinite volume, i.e., finite-volume effects are exponentially suppressed by factors  $\sim \exp(-m_\pi L)$ , while mass-effects are dominant.

### 3.3.3 $\epsilon$ -regime

In Lattice QCD it is possible, in principle, to determine the parameters of the effective chiral Lagrangian by performing numerical simulations in the  $\epsilon$ -regime [26, 27], i.e., at quark masses where the physical extent of the lattice is much smaller than the Compton wave length of the pion. The use of a formulation of the lattice theory that preserves chiral symmetry is attractive in this context, but the numerical implementation of any such approach requires special care in this kinematic situation due to the presence of some very low eigenvalues of the Dirac operator.

The  $\epsilon$ -regime is where  $m_{\text{PS}}L_\mu \ll 1$  for all  $\mu = 1, \dots, 4$ , i.e., the box size in all directions is much smaller than the inverse pion mass (defined in the infinite volume). Then it is:

$$\frac{m_\pi}{\Lambda_{\text{QCD}}} \sim \frac{p^2}{\Lambda_{\text{QCD}}^2} \sim \frac{1}{F^2 L^2} \sim \epsilon^2. \quad (3.35)$$

It follows that mass effects are suppressed, while volume effects are enhanced and become polynomial in  $L^{-2}$ . At a given order in the effective theory the  $\epsilon$ -regime contains less LECs compared to the  $p$ -regime. The NLO predictions are less contaminated by higher order effects, making the  $\epsilon$ -regime particularly advantageous and clean to compute the leading order couplings  $F$  and  $\Sigma$ . Furthermore, in the  $\epsilon$ -regime topology is relevant [29]. Observables can be defined at fixed values of the topological charge, and the dependence on this charge should also be well reproduced by the effective theory. Therefore topology is a new variable in this regime, in addition to the mass and the volume. However, in the infinite volume limit, the dependence on the topology is expected to vanish.

#### Quark condensate from finite-size scaling

The quark condensate is the order parameter of spontaneous chiral symmetry breaking and it is non-vanishing in the chiral limit. However, in the  $\epsilon$ -regime we are restricted to a finite box with a finite volume, where it is expected that spontaneous symmetry breaking does not occur. Therefore the chiral condensate in finite volume is proportional to the scaled mass  $\mu = m\Sigma V$  and is vanishing in the chiral limit [29]. It is:

$$\Sigma(\mu) \equiv \frac{\Sigma}{N_f} \frac{\partial}{\partial \mu} \ln Z \sim \Sigma \mu, \quad (3.36)$$

where  $Z$  is the partition function at leading order in the  $\epsilon$ -regime.

We hold the topology fixed and define

$$Z = \sum_{\nu=-\infty}^{\infty} e^{i\nu\theta} Z_\nu, \quad (3.37)$$

where  $\theta$  is discussed in Section 2.5.3. If we now have a look at the chiral condensate, one finds:

$$\Sigma_\nu(\mu) \equiv \frac{\Sigma}{N_f} \frac{\partial}{\partial \mu} \ln Z_\nu = \frac{\Sigma \nu}{\mu} + \chi_\nu, \quad (3.38)$$

$$\text{with } \chi_\nu = \frac{\Sigma}{2(N_f + \nu)} \mu + \dots, \quad (3.39)$$

where the infrared divergence proportional to  $\mu^{-1}$  is due to zero-mode contributions.

In Eqs. (3.36) and (3.38) we express the chiral condensate in the finite volume which vanishes in the chiral limit, in terms of the bare chiral condensate, which is an order parameter of chiral symmetry breaking and is

non-vanishing for  $\mu \rightarrow 0$ . But although chiral symmetry in finite volumes is not spontaneously broken, the chiral condensate is still affected with contributions which depends on the bare chiral condensate  $\Sigma$ . In [27] Gasser and Leutwyler show that it is even possible to correct the finite-volume chiral condensate for the finite size errors. We get in the  $\epsilon$ -regime:

$$\Sigma = \rho_1 \Sigma_\infty = \Sigma_\infty \left[ 1 + \frac{N_f^2 - 1}{N_f} \frac{\beta_1}{F^2 L^2} \right], \quad (3.40)$$

where  $\beta_1$  is a known universal shape coefficient [30, 31, 32].

### 3.3.4 $\delta$ -regime

In [33] Leutwyler introduces the  $\delta$ -regime when in the spatial directions the lattice is the same as in the  $\epsilon$ -regime, but the time extent of the box is much larger than the spatial extent:

$$L_4 \gg L_i, \quad i = 1, 2, 3 \quad \text{and only} \quad m_{\text{PS}} L_i \ll 1. \quad (3.41)$$

In this case a effective  $dim = 4$  spin system is described by the quantum mechanics of an  $O(4)$  rotator with the spectrum

$$E_l = \frac{l(l+2)}{2\Theta}, \quad (3.42)$$

where  $\Theta$  is the moment of inertia.

In general the  $\delta$ -regime is somewhat more difficult to handle theoretically than the  $\epsilon$ -regime, since for  $L_t \rightarrow \infty$  the direction of the  $\vec{S}$  spin field is decorrelated at sufficiently large relative distances in time. But the condition  $m_{\text{PS}} L_i \ll 1$  means that in space they are very strongly correlated, so there is in practice an average direction  $\vec{S}_0(t)$ , which has a large but finite correlation length in  $t$ .

### 3.3.5 Rotator spectra in $\delta$ - and $\epsilon$ -regimes

The pattern of the spontaneous breaking of the  $N_f = 2$  chiral symmetry is related to the same phenomenon in  $O(4)$  spin model<sup>2</sup>. There we also have spontaneous symmetry breaking, where  $O(4) \rightarrow O(3)$  is the same as  $SU(2)_L \times SU(2)_R \rightarrow SU(2)_V$  in QCD.

Consider now the transfer matrix  $U(t', t) = e^{-H(t'-t)}$  of both, the spin or the QCD system. If you take  $m_q = 0$ , which corresponds to zero magnetic field for the spin model, then there are different types of modes, classified by the conserved quantities<sup>3</sup>. In particular, one has the translation invariance (momentum) and  $O(4)$  invariance, i.e., rotation of all spins on a timeslice<sup>4</sup>. Now the  $p \neq 0$  states have an energy of  $\mathcal{O}(2\pi/L_s)$ . If two such states are put together to have zero total momentum, the new state gets an energy of at least  $4\pi/L_s$ .

The rotator excitations can also be read off the action. These are states with  $p = 0$ , i.e., translational invariant states, with some values of the magnetization  $M(t) = \sum_x s(x, t)$ , where  $s(x, t) = (\uparrow, \downarrow) = (1, -1)$ . Neglecting the  $x$ -dependence, i.e., summing over the spatial volume, one gets  $|M(t)| = L_s^3$  assuming all spins on a timeslice are parallel to each other and take this to renormalize the moment of inertia. Then one recovers the path integral of a rotator with the moment of inertia  $\Theta = F^2 L_s^3$ . Hence the spectrum of these states is the rotator spectrum, which for  $N = 4$  reads as Eq. (3.42).

Now we build the ratio

$$\frac{\Delta E_l}{\Delta E_{p=1}} \sim \frac{1}{4\pi F^2 L_s^2}. \quad (3.43)$$

So if  $F^2 L_s^2 \gg 1$  then the rotator spectrum lies significantly below the scattering states and dominates the correlation functions. This is quite true for  $L_t \gg L_s$  ( $\delta$ -regime!) since then the scattering states contribute as

<sup>2</sup>Heisenberg model in  $dim = 4$

<sup>3</sup>Conserved quantities are in this context those quantities which commute with the transfer matrix

<sup>4</sup>Note that this may not be confused with the real angular momentum which due to the lattice is not a symmetry for finite  $a$ .

---

$\exp(-4\pi L_t/L_s) \ll 1$ . But they are still dominating the correlation function at  $L_t = L_s$  ( $\epsilon$ -regime!), although the scattering states cannot be completely ignored. Moreover, unlike in the  $\delta$ -regime at large time distances, where the lowest rotator excitation dominates, for  $L_t \sim L_s$  a lot of rotator excitations are important. But the  $\epsilon$ -regime has another way to calculate the same thing, not using the rotator modes necessarily, but applying chiral perturbation theory directly.

# Chapter 4

## Random Matrix Theory

Random matrix theory (RMT) has been a unifying approach in physics and mathematics. It is also possible to apply RMT to QCD, e.g., the behavior of the lowest lying eigenvalues of the Dirac operator can be described by Chiral Random Matrix Theory (ChRMT).

### 4.1 Introduction to RMT

RMT has been very successful in describing certain properties of complicated physical systems with a large number of degrees of freedom. The idea of RMT is based on the concept of universality. If a complex physical system has universal properties and can be assigned to a given universality class, these properties can be studied in the simplest model of the latter. For the case of QCD, the simplest model is chiral RMT (ChRMT), which respects the same global symmetries as the QCD Dirac operator, but otherwise has Gaussian-distributed random matrix elements.

See Ref. [34] for a detailed and pedagogical review.

#### 4.1.1 The Banks-Casher relation

The eigenvalue equation for the Dirac operator in the continuum is given by

$$D\psi_n = i\lambda_n\psi_n, \quad \lambda_n \in \mathbb{R}. \quad (4.1)$$

Based on this equation the spectral density  $\rho(\lambda)$  of the Dirac operator is defined as

$$\rho(\lambda) = \left\langle \sum_n \delta(\lambda - \lambda_n) \right\rangle. \quad (4.2)$$

As shown by Banks and Casher in [35] the spectral density is related to the chiral condensate  $\Sigma$  as:

$$\Sigma = \langle \bar{\psi}\psi \rangle = \lim_{\epsilon \rightarrow 0} \lim_{m \rightarrow 0} \lim_{V \rightarrow \infty} \frac{\pi\rho(\epsilon)}{V}, \quad (4.3)$$

where the ordering of the limits cannot be commuted. A direct consequence of the Banks-Casher relation (4.3) is that the (mean level) spacing of the smallest eigenvalues is given by:

$$\Delta\lambda \approx \frac{1}{\rho(0)} \approx \frac{\pi}{V\Sigma}. \quad (4.4)$$

In order to investigate individual eigenvalue distributions, it is convenient to define the microscopic spectral density [36]:

$$\rho_S(\xi) = \lim_{V \rightarrow \infty} \frac{1}{V\Sigma} \rho\left(\frac{\xi}{V\Sigma}\right), \quad (4.5)$$

where  $\xi = \lambda\Sigma V$  is the scaled eigenvalue. This density describes the deep IR properties of the Dirac operator spectrum. The results obtained by computing this quantity using LO chiral perturbation theory and RMT coincide [37]. In RMT analytical predictions can even be given for individual distributions of the eigenvalues with an arbitrary number of dynamical quark flavors.

## 4.2 Chiral RMT

The domain where RMT is valid is given by chiral perturbation theory. Leutwyler and Gasser have shown in [27], that the QCD partition function considered in a finite volume  $V = L^4$ , is dominated by pions, if the following relation is fulfilled

$$\frac{1}{\Lambda_{\text{QCD}}} \ll L \ll \frac{1}{m_\pi}. \quad (4.6)$$

In this case, when the Compton wavelength of the pion is larger than the box size  $L$ , the pion field is almost a constant. In this approximation we are in the  $\epsilon$ -regime and chiral perturbation theory and RMT coincide [37].

In the  $\epsilon$ -regime the low-lying eigenvalue spectrum of the QCD Dirac operator matches that of ChRMT up to a scale factor. This can be shown by identifying the QCD partition function in the  $\epsilon$ -regime with the partition function of ChRMT [37]. The RMT partition function is given in [34, 36, 38, 39]:

$$Z_\nu^{\text{RMT}} = \int [dW] P(W) \prod_{f=1}^{N_f} \det \begin{pmatrix} m_f & iW \\ iW^\dagger & m_f \end{pmatrix}. \quad (4.7)$$

Here,  $W$  is a  $(n + \nu) \times n$  matrix with  $P(W)$ -distributed random entries,  $N \equiv 2n + \nu$  and the parameters  $m_f$  play the role of the quark masses. The simplest case is the Gaussian case, where  $P(W) = \exp[-\frac{N}{2} \text{tr}(W^\dagger W)]$  and hence we only regard the chiral Gaussian Unitary Ensemble (chGUE) with the Dyson index  $\beta = 2$ .

This model reproduces the following symmetries of the QCD partition function [34]:

1. The  $U_A(1)$  symmetry. All eigenvalues of the random matrix Dirac operator occur in pairs  $\pm i\lambda_n$  or are zero.
2. The topological structure of the QCD partition function. The Dirac matrix has exactly  $\nu$  zero eigenvalues. This identifies  $\nu$  as the topological sector of the model.
3. The flavor symmetry, which is  $SU(N_f) \times SU(N_f)$  and therefore the same as in QCD.
4. The spontaneously breaking of chiral symmetry by the chiral condensate given by

$$\Sigma = \lim_{N \rightarrow \infty} \pi\rho(0)/N, \quad (4.8)$$

where  $N$  is the dimensionless volume of space-time.

Using this model, analytic predictions for the eigenvalue spectra can be made [40]. In [41] Damgaard and Nishigaki work out the probability distributions of the smallest eigenvalues of the Dirac operator. Analytic expressions for individual distributions of the  $k$ -th smallest eigenvalues are given. These predictions can be compared to the distribution of the eigenvalues from lattice data. The chiral condensate  $\Sigma$  is the only unknown quantity in these predictions. The parameters in the RMT predictions are the scaled eigenvalues  $\xi = \lambda\Sigma V$  and RMT masses  $\mu_f = m_f\Sigma V$ . The value of  $\Sigma$  can then be fitted so that the predictions of RMT and the lattice data match for all given topological sectors  $\nu$ .



## Part II

# Lattice Quantum Chromodynamics

When we put QCD on a discrete 4-dimensional space-time lattice, we always speak about Lattice QCD which is based on lattice gauge theory. Lattice QCD is suited for computer simulations and for obtaining physical quantities from first principles, even in the low energy regime, where perturbative methods fail. To avoid strongly oscillating contributions in the path integration one has to Wick-rotate the Minkowski space-time to the Euclidean space-time. A typical computer simulation makes heavily use of Monte Carlo methods which were originally developed in statistical physics.

## Lattice gauge theory

The description of the long distance strong color force requires non-perturbative methods. The main motivation for the introduction of lattice gauge theory by Wilson [42] was to formulate QCD non-perturbatively, in order to explain confinement, and to allow for a numerical determination of the hadron spectrum and other low energy hadron properties. A successful calculation of low energy hadronic parameters in Lattice QCD can, in principle, also yield convincing evidence for QCD to be a valid description of strong interactions at all.

The lattice gauge theory is a quantum field theory, in which the regularization is done via the discretization of the space-time. Due to the introduction of a minimal distance  $a$  (called lattice spacing) between two lattice points the divergencies of the theory, which would occur at high momenta, are eliminated. The changeover to a quantum field theory in the continuum takes place in the extrapolation of the lattice spacing to zero  $a \rightarrow 0$ . The lattice gauge theory has become very important, because its regularization is non-perturbative and so, it is also possible to realize calculations in the low energy limit of QCD, where it is not possible to use perturbative methods in principle<sup>1</sup>.

## Euclidization

Quantum field theories can be described in terms of classical fields which enter in path integrals of the kind

$$Z = \int [d\phi] e^{iS_M[\phi]} . \quad (4.9)$$

The functional integral in (4.9) is over all field configurations  $\phi(x)$  which are weighted by the exponentiated imaginary Minkowski action  $iS_M$  of the configuration. The importance of the path integral formalism has increased tremendously since the installation of better and better computer systems allows to solve most complicated integrations very fast.

To avoid strongly oscillating contributions in the path integration, we perform an analytic continuation from Minkowski to Euclidean space-time, i.e., we change the metric from  $g_{\mu\nu}$  to  $\delta_{\mu\nu}$ , which is called Wick rotation:

$$x_0 \rightarrow -ix_4 . \quad (4.10)$$

Therefore we also have to transform the gamma matrices according to Appendix A.1. Hence, we obtain the action in Euclidean space-time:

$$iS_M \rightarrow -S_E . \quad (4.11)$$

By going to Euclidean space-time the complex, oscillating weight becomes real and has the form of the Boltzmann factor in classical statistical physics:

$$Z = \int [d\phi] e^{iS_M[\phi]} \rightarrow \int [d\phi] e^{-S_E[\phi]} . \quad (4.12)$$

The multi-dimensional integral in Euclidean space-time can now be solved with Monte Carlo techniques (cf. Section 7.1).

---

<sup>1</sup>For long distances or small energies the coupling constant of QCD  $\alpha_s$  is not a small number anymore. Therefore we cannot expand the theory in terms of the coupling constant  $\alpha_s$  and neglect the higher orders for a good approximation, because all orders may contribute. However, chiral perturbation theory also makes use of perturbative methods even in the low energy limit of QCD, but this ansatz is not valid for higher energies. Thus Lattice QCD provides a non-perturbative way to do calculations in the low energy limit of QCD.

Note that the Hamilton operator in both the Euclidean and in the Minkowski space-time stays the same, i.e., as long as one is interested in matrix elements and their energy eigenstates one always obtains the same results independently of the space-time metric. More problematic are quantities which are not projected on the eigenstates of the Hamiltonian, e.g., scattering matrix elements, but these are not discussed in this work.

## Outline

In this part we concentrate on Lattice QCD and follow the way how a lattice simulation is done. First we explain the ingredients of the simulation, stress the importance of chiral fermions and describe the generation of gauge configurations with Monte Carlo methods. But at this point one has not gained any physical results at all. After we have gauge configurations we want to calculate observables on them. Therefore we need propagators and interpolators. After we have expectation values for the physical quantities on each gauge configuration we have to cancel the discretization errors on the lattice, i.e., to perform chiral, infinite volume and continuum extrapolations. Since we work with a finite set of gauge configurations, we also have to add an error analysis. The results which we have obtained in that way can then be compared to experiments or other theoretical predictions.

In Chapter 5 we begin to introduce Lattice QCD where we want to solve QCD on a lattice via brute force, i.e., computing very high-dimensional integrals. This is typically done on large computer systems. But even there we have to restrict ourselves to finite degrees of freedom, i.e., we have to discretize the problem. Fortunately, we can use the discretization (i.e., the lattice spacing  $a$ ) as the regulator of the quantum field theory at the same time. The discretization of the space-time is therefore the most intuitive discretization which connects both, the numerical problems computing high-dimensional integrals and the theoretical needs (regularization) of a quantum field theory. Due to the fact that QCD is also a gauge theory we have also to discretize the gauge fields and to find a way to implement gauge invariance. Then, there are still various possibilities to calculate the derivative in the Dirac operator. At the end of the day, one finds that chiral symmetry, which is very important for the non-perturbative regime of QCD, is broken at first, but can be implemented in a different way.

Chiral fermions (Chapter 6) are much more time consuming than, e.g., Wilson fermions. However, we show how chiral fermions on the lattice has been rediscovered (Section 6.1) and that the additional chiral symmetry relativizes the efforts (Section 6.2). In Part III we are using Chirally Improved (CI) fermions and in Part IV we are using fixed-point (FP) fermions. These are fermions which approximately chiral symmetry properties and are much cheaper in terms of computer resources than exact chiral fermions. We introduce both fermions in Sections 6.3 and 6.4.

In Chapter 7, we give the basic ideas why we have to use Monte Carlo methods and why it is working for our problem. We discuss the properties of an algorithm which are required to generate suitable gauge configurations. From theory (Section 7.1) we come to a section for practitioner (Section 7.2), where the individual steps to create gauge configurations are explained separately. In our simulations we also apply some improvements discussed in Section 7.3.

Generating a lot of gauge configurations is only the first step. The ensuing analysis in Chapter 8 applied to every configuration determines the observables one is interested in. There are many different ways of doing that depending on, e.g., the lattice size, the fermion types or the way one puts the fermions on the lattice. In our case after the gauge configuration are generated we compute the propagators and store them (Section 8.1). This can be also done in different ways. We present here two types of propagators, the point-to-all and the all-to-all propagators. Then, we can combine the propagators to correlation functions (Section 8.2). We also discuss some important improvements as smearing and the variational method that we used in our calculations (Section 8.3). Due to the fact low-mode averaging (Section 8.4) and covariant operators (Section 8.5) become very important in Part IV we have put them in two additional improvement sections.

The final step before comparing the results to experiments or theoretical predictions is addressed in Chapter 9. Comparing lattice results with physical values requires to set the scale first. After that we can always convert our results in lattice units into energy or length units (Section 9.1). The analysis of the correlation functions is shown via two examples and the AWI mass in Section 9.2. Aiming for LECs we want to go another way as the brute force calculation of matrix elements. We want to use the finite size effects in our lattices and access the

$\epsilon$ -regime. There, the LECs can be obtained in a much cleaner way (Section 9.3).

By doing a calculation on a discrete space-time lattice we obviously make discretization errors which are hopefully under control. But at the end we have to remove them to get physical results. Additionally due to the restrictions in our computer resources we are not able to simulate at physical quark masses and volumes. But we know from chiral perturbation theory how these results, obtained at unphysical quark masses and volumes, should extrapolate to the physical ones (Section 9.4). After that we have to estimate the statistical and systematical errors for our results (Section 9.5).

# Chapter 5

## Discretizations

In order to put a theory on a lattice, one has to discretize space-time. This has two reasons:

1. We want to do a computer simulation. Therefore we have to cut the theory from an infinite number of degrees of freedom to a finite number.
2. Computing a quantity in a quantum field theory we always need a regularization. But most of the regularization methods used in perturbative QCD are not applicable on the lattice. In lattice gauge theory the lattice spacing  $a$  works as its regularization because it is a non-perturbative ultraviolet cutoff. At the same time the size of the lattice is applied for an infrared cutoff of the theory. Thus, the lattice itself is an important ingredient for the definition of the quantum field theory.

### 5.1 The lattice

The hypercubic lattice consists of sites and links. The sites are the points  $x$  separated by the lattice spacing  $a$ :

$$x_\mu = a(n_1, n_2, n_3, n_4) \quad \text{with} \quad n_\mu \in \{0, \dots, L_\mu - 1\}, \quad (5.1)$$

where  $L_i$  are the extensions of the lattice in the directions  $i = 1, \dots, 4$ . The links connect a site at point  $x$  with its neighboring site in  $\hat{\mu}$ -direction at point  $x + \hat{\mu}$ .  $\hat{\mu}$  is the vector of length  $a$  in direction  $\mu$ . The links are often denoted by  $(x, \mu)$ . On such a hypercubic lattice, the quark fields  $\bar{\psi}, \psi$  are located on the sites. Due to the fact that the gauge fields  $U_\mu(x)$  are orientated quantities they are lying on the links.

In an analogous way to the discretized space, momentum space has also discrete values only:

$$p_\mu = \frac{2\pi}{aL}(n_1, n_2, n_3, n_4) \quad \text{with} \quad n_\mu \in \{0, \dots, L_\mu - 1\}. \quad (5.2)$$

Here we are using periodic boundary conditions on the lattice, so that:

$$e^{ip_\mu x_\mu} = e^{ip_\mu(x_\mu + L_\mu)}. \quad (5.3)$$

We note that the lattice spacing  $a$  in the context of a quantum field theory also serves as a regulator, which makes the whole theory finite. This kind of regularization breaks the Euclidean space-time symmetries  $O(4)$  to the hypercubic group  $H(4)$ <sup>1</sup>. Furthermore, the translational invariance of the theory is only present in integer multiples of the lattice spacing  $a$ . However, in the continuum limit  $a \rightarrow 0$  all these symmetries have to be restored, independently of the choice of the lattice.

---

<sup>1</sup>In the hypercubic group only rotations about  $\pi/2$  and reflexions at the axes are incorporated, but discrete symmetries like parity and time-reversal are still intact. The choice of the lattice strongly influences the symmetries which can be restored in the continuum limit. Therefore more complicated lattices, e.g., a  $F_4$  lattice, can be used to incorporate more and more space-time symmetries.

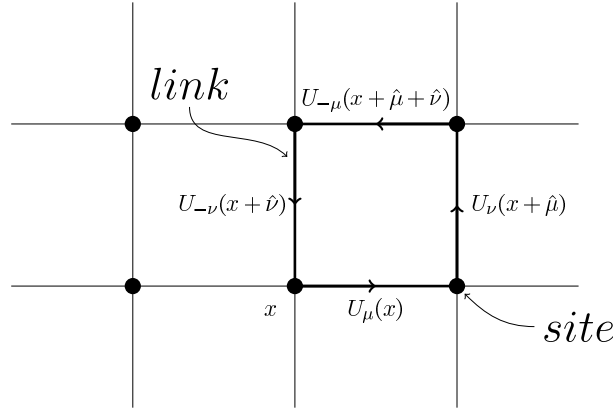


Figure 5.1: The gauge fields are put on the links of the lattice. In Eq. (5.12) we define the smallest loop consisting out of four links, the so-called plaquette.

## 5.2 The gauge action

The gauge field is a vector field. It has an index related to the space-time direction. Thus, it is natural to put it on the links of the lattice (cf. Fig. 5.1). The local gauge invariance of the continuum theory has to be reflected by the transformation properties of the lattice variables which describe the gauge field. At this point the gauge transporters are introduced which correspond to the path ordered exponentials of the gauge fields. On the link  $(x, \mu)$  the parallel transporter is denoted by  $U_\mu(x)$ . The  $U_\mu(x)$  are elements of the gauge group  $SU(3)$ . They are connected to the gauge fields  $A_\mu(x) = -igA_\mu^a(x)t^a$  via

$$U_\mu(x) = e^{aA_\mu(x)}. \quad (5.4)$$

Under gauge transformation  $\Lambda(x) \in SU(3)$  the parallel gauge transporters transform as

$$U_\mu(x) \rightarrow U'_\mu(x) = \Lambda(x)U_\mu(x)\Lambda^{-1}(x + \hat{\mu}). \quad (5.5)$$

This relation makes the parallel transporters useful for constructing gauge invariant terms which are located on different sites. In this context there exists also the following common notation:

$$U_{-\mu}(x) \equiv U_\mu^\dagger(x - \hat{\mu}) \rightarrow U'_{-\mu}(x) = \Lambda(x)U_{-\mu}(x)\Lambda^{-1}(x - \hat{\mu}). \quad (5.6)$$

The discretized gauge action is in general constructed as a sum of products of the parallel transporters along closed paths. Due to that fact there are several different discretizations of the gauge actions possible. Therefore we have to define the ordered product along a path  $\mathcal{P}$  of  $k$  links on the lattice connecting the points  $x_0$  and  $x_1$ :

$$P[U] = U_{\mu_0}(x_0)U_{\mu_1}(x_0 + \hat{\mu}_0) \dots U_{\mu_{k-1}}(x_1 - \hat{\mu}_{k-1}) = \prod_{(x,\mu) \in \mathcal{P}} U_\mu(x). \quad (5.7)$$

We now introduce a shorthand notation for such paths  $P[U]$  using an ordered list of the directions of the links of the path. We denote a path of length  $k$  on the lattice by

$$P[U] \equiv \langle l_1, l_2, \dots, l_k \rangle, \quad (5.8)$$

with the  $l_i$  giving the directions of the subsequent hops, i.e.,  $l_i \in \{\pm 1, \pm 2, \pm 3, \pm 4\}$ .

From (5.5) and (5.6) one can show that the product  $P[U]$  transforms according to:

$$P[U] \rightarrow P[U'] = \Lambda(x_0)P[U]\Lambda^{-1}(x_1). \quad (5.9)$$

We can now construct gauge invariant products of link variables through closing the path  $\mathcal{P}$  to get a loop  $\mathcal{L}$  and taking the trace over it:

$$L[U] = \text{tr} \left[ \prod_{(x,\mu) \in \mathcal{L}} U_\mu(x) \right]. \quad (5.10)$$

From (5.9) we derive:

$$L[U'] = \text{tr} \left[ \Lambda(x_0) \prod_{(x,\mu) \in \mathcal{L}} U_\mu(x) \Lambda^{-1}(x_0) \right] = L[U]. \quad (5.11)$$

Such loops of link variables are used for the construction of the gluon action. The easiest gluon action is the Wilson gauge action.

### 5.2.1 Wilson gauge action

In the Wilson gauge action we use the shortest, non-trivial loops consisting of four link variables, namely the plaquettes. The plaquette  $U_{\mu\nu}(x)$  is defined via<sup>2</sup>:

$$U_{\mu\nu}(x) = U_\mu(x) U_\nu(x + \hat{\mu}) U_{-\mu}(x + \hat{\mu} + \hat{\nu}) U_{-\nu}(x + \hat{\nu}) \equiv \langle \mu, \nu, -\mu, -\nu \rangle. \quad (5.12)$$

Wilson [42] defined the action for the pure  $SU(3)_C$  lattice gauge theory in terms of plaquettes as follows:

$$S_{\text{Wilson}}[U] = \beta \sum_x \sum_{1 \leq \mu \leq \nu \leq 4} \left( 1 - \frac{1}{3} \text{Re tr } U_{\mu\nu}(x) \right). \quad (5.13)$$

Using (5.4) to expand (5.12), the Campell-Baker-Hausdorff formula

$$\exp(A) \exp(B) = \exp \left( A + B + \frac{1}{2}[A, B] + \dots \right) \quad (5.14)$$

and finally

$$\begin{aligned} A_\mu(x + \hat{\nu}) &= A_\mu(x) + a \partial_\nu A_\mu(x) \\ A_\nu(x + \hat{\mu}) &= A_\nu(x) + a \partial_\mu A_\nu(x) \end{aligned}$$

we get a relation containing the field strength tensor:

$$U_{\mu\nu}(x) = \exp(a^2 F_{\mu\nu} + \mathcal{O}(a^3)). \quad (5.15)$$

When we expand the exponential in (5.15), take the trace and keep only the real part of it, we get:

$$\text{Re tr } U_{\mu\nu}(x) = 3 + \frac{a^4}{2} \text{tr } F_{\mu\nu} F^{\mu\nu} + \mathcal{O}(a^6). \quad (5.16)$$

Finally, we end up with

$$\begin{aligned} S_{\text{Wilson}}[U] &= -\beta \sum_x \sum_{1 \leq \mu \leq \nu \leq 4} \left( \frac{a^4}{6} \text{tr } F_{\mu\nu} F^{\mu\nu} + \mathcal{O}(a^6) \right), \\ &= -\frac{\beta a^4}{12} \sum_x \sum_{\mu\nu} (\text{tr } F_{\mu\nu} F^{\mu\nu} + \mathcal{O}(a^2)), \\ &\rightarrow -\frac{\beta}{12} \int d^4x (\text{tr } F_{\mu\nu} F^{\mu\nu}), \end{aligned} \quad (5.17)$$

where we get the continuum gauge action (2.7) for the so-called inverse coupling

$$\beta = \frac{6}{g^2}. \quad (5.18)$$

---

<sup>2</sup>also cf. Fig. 5.1.

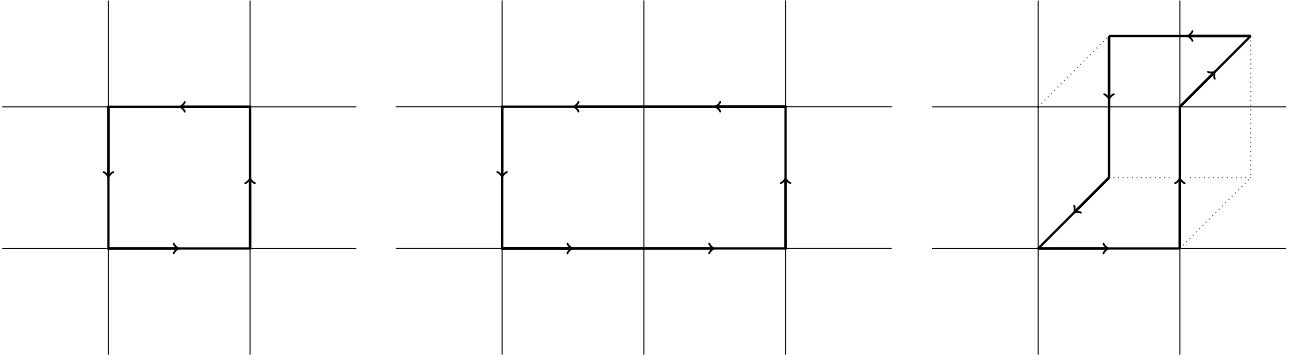


Figure 5.2: Here we plot the three contribution in the Lüscher-Weisz gauge action. On the left this is the plaquette (5.12) which also occurs in the Wilson gauge action. The figure in the middle is the rectangular (5.22) and on the right we have the parallelogram-like contribution (5.23).

### 5.2.2 Lüscher-Weisz gauge action

In Section 5.2.1 we make an order  $\mathcal{O}(a^2)$  discretization error. This can introduce problems in doing an extrapolation to the continuum limit. Because gauge invariance restricts the available dimension-four operator for the continuum gauge action to just one:

$$\text{tr } F_{\mu\nu}F_{\mu\nu} , \quad (5.19)$$

we also find higher dimensional operators in the trace over the plaquettes. These operators are responsible for the  $\mathcal{O}(a^2)$  discretization errors in (5.13). To remove these  $\mathcal{O}(a^2)$  errors and to get an action with  $\mathcal{O}(a^3)$  errors, one has to take into account additional higher-dimensional operators in the gauge action.

Here we introduce the Lüscher-Weisz gauge action which consists in addition to the Wilson gauge action in (5.13) of auxiliary loops (cf. Fig. 5.2):

$$S[U] = \beta_0 \sum_{\text{plaq}} \left[ 1 - \frac{1}{3} \text{Re}(\text{tr } U^{\text{plaq}}) \right] + \beta_1 \sum_{\text{rect}} \left[ 1 - \frac{1}{3} \text{Re}(\text{tr } U^{\text{rect}}) \right] + \beta_2 \sum_{\text{para}} \left[ 1 - \frac{1}{3} \text{Re}(\text{tr } U^{\text{para}}) \right] . \quad (5.20)$$

The  $\beta_0$  term is the Wilson action (5.12):

$$U^{\text{plaq}} = U_{\mu\nu}(x) , \quad (5.21)$$

the  $\beta_1$  term includes all  $2 \times 1$  rectangular loops:

$$\begin{aligned} U_{\mu\nu}^{\text{rect}}(x) &= U_{\mu}(x)U_{\nu}(x+a\hat{\mu})U_{\nu}(x+a\hat{\mu}+a\hat{\nu})U_{-\mu}(x+a\hat{\mu}+2a\hat{\nu})U_{-\nu}(x+2a\hat{\nu})U_{-\nu}(x+a\hat{\nu}) \\ &\equiv \langle \mu, \nu, \nu, -\mu, -\nu, -\nu \rangle , \end{aligned} \quad (5.22)$$

and the  $\beta_2$  term contains all  $1 \times 1 \times 1$  parallelograms:

$$\begin{aligned} U_{\mu\nu\xi}^{\text{para}} &= U_{\mu}(x)U_{\nu}(x+a\hat{\mu})U_{\xi}(x+a\hat{\mu}+a\hat{\nu})U_{-\mu}(x+a\hat{\mu}+a\hat{\nu}+a\hat{\xi})U_{-\nu}(x+a\hat{\nu}+a\hat{\xi})U_{-\xi}(x+a\hat{\xi}) \\ &\equiv \langle \mu, \nu, \xi, -\mu, -\nu, -\xi \rangle . \end{aligned} \quad (5.23)$$

Using suitable ratios<sup>3</sup> for  $\beta_0$ ,  $\beta_1$  and  $\beta_2$  the  $\mathcal{O}(a^2)$  discretization errors cancel and we get a gauge invariant gauge action with  $\mathcal{O}(a^3)$  discretization errors.

Although it is not shown here, this method can be used to avoid even  $\mathcal{O}(a^3)$  discretization errors by adding more and more closed loops and their corresponding coefficients. However, usually the other parts of a simulations have larger discretization errors which would cover the advantages of a gauge actions without cutoff effects, even if the perturbation theory for higher order would already exist.

<sup>3</sup>In particular we used Tadpole Improved Perturbation Theory [43] to determine  $\beta_0$ ,  $\beta_1$  and  $\beta_2$ .

### 5.2.3 Renormalization-group inspired improvement

A different approach to improve the gauge action without adding more and more additional terms to the Wilson action is inspired by renormalization group transformations (RGTs). In principle we want to use gauge actions without any discretization errors or cutoff effects. Such actions live along the renormalized trajectory of some RGT.

We want to relate the continuum theory of free fermions to a corresponding lattice theory by an exact RGT. This is achieved by defining lattice fermion fields as block averages of continuum fields integrated over hypercubes. The resulting lattice theory is then in all aspects equivalent to the underlying continuum theory, i.e., it is completely free of lattice artifacts. It also has an exact chiral symmetry.

After performing repeated RGTs the action undergoes specific modifications

$$S \xrightarrow{\text{RGT}} S' \xrightarrow{\text{RGT}} S'' \xrightarrow{\text{RGT}} \dots \xrightarrow{\text{RGT}} S^{(n)}. \quad (5.24)$$

We can write down the action in a general form, as a sum of all possible operators  $\Theta_\alpha[\bar{\psi}, \psi, U]$ , each multiplied with the corresponding coupling constant  $K_\alpha$ :

$$S(\bar{\psi}, \psi, U) = \sum_\alpha K_\alpha \Theta_\alpha[\bar{\psi}, \psi, U]. \quad (5.25)$$

The operators  $\Theta_\alpha[\bar{\psi}, \psi, U]$  can be classified in three different kinds:

- Operators are called relevant if the corresponding coupling constant becomes larger after each RGT step.
- Most of the operators belong to the second kind of operators, so-called irrelevant operators, i.e., their couplings go towards zero after a large number of RGT steps.
- The third kind of operators are called marginal operators. These operators<sup>4</sup> do not change under RGTs.

After a RGT the action can be again expanded in terms of  $\Theta_\alpha(\bar{\psi}', \psi', U')$ , now with new coupling constants  $K'_\alpha$ . Thus RGTs induce motions in the coupling constant space:

$$\{K_\alpha\} \xrightarrow{\text{RGT}} \{K'_\alpha\} \xrightarrow{\text{RGT}} \{K''_\alpha\} \xrightarrow{\text{RGT}} \dots \quad (5.26)$$

If we reproduce a point in the coupling constant space under a RGT, we call this a fixed point (FP) of the RGT:

$$\{K_\alpha^*\} \xrightarrow{\text{RGT}} \{K_\alpha^*\}. \quad (5.27)$$

Consider a lattice with lattice size  $L$  and lattice spacing  $a$  in each direction. We define a RGT where we perform a simple block transformation as in Fig. 5.3: We average two points in each directions to get one single point. Thus we get a coarser lattice with lattice size  $L' = L/2$  and lattice spacing  $a' = 2a$  in each direction. The action also changes according to (5.24). For large  $n$ , the action  $S^{(n)}$  contains only a few operators  $\Theta_\alpha[\bar{\psi}, \psi, U]$ , namely the relevant (and marginal) ones.

Let us now set the couplings of the relevant operators to zero by hand as they should be in a fixed point<sup>5</sup>. Then the only operators which remains after  $n$  RGT steps are the marginal ones. Those do not change under RGTs, in other words the action  $S^{(n)}$  does not change under further RGTs:

$$\dots \xrightarrow{\text{RGT}} S^{(n)} \approx S^{\text{FP}} \xrightarrow{\text{RGT}} S^{\text{FP}} \xrightarrow{\text{RGT}} \dots \quad (5.28)$$

The fixed-point action  $S^{\text{FP}}$  does not change under RGT, the action is exactly the same at different lattice spacings  $a, a', a'', \dots$ . Since also physics does not change under RGT, the FP action does not depend on the

<sup>4</sup>Actually, we do not have really marginal operators. The name is mainly coming from perturbation theory, where some operators do not move in leading order, but then move in the second order of perturbation theory. So they are not marginal. The best is to talk only about relevant and irrelevant operators.

<sup>5</sup>If we already sit on the fixed point then all the relevant operators have to have zero coefficients, or otherwise they would move, i.e., we would not be in the FP.

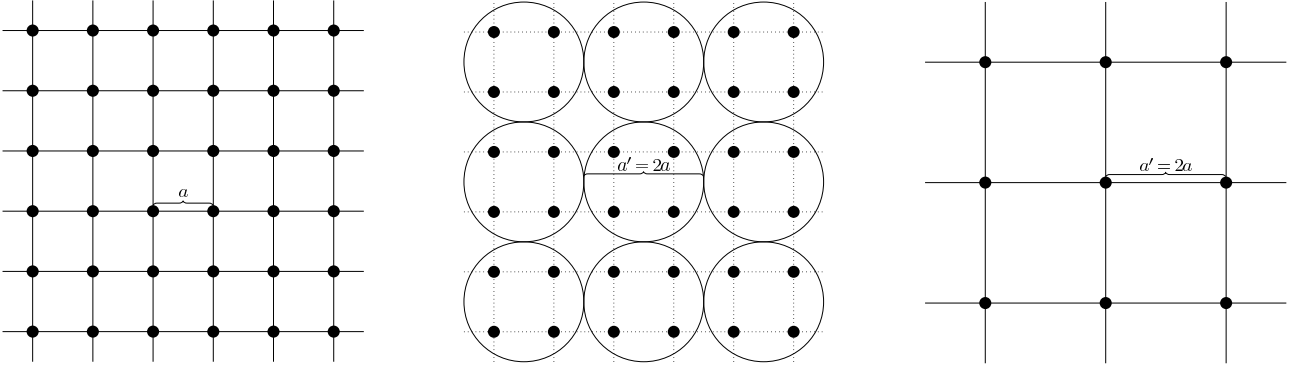


Figure 5.3: We demonstrate here the block transformation used in RGT. Several points of a fine lattice are merged to a single point on a coarser lattice.

cutoff of the regularization, i.e., it has no cutoff effects and is exact in classical physics. A detailed review on FP action can be found in [44].

In a numerical simulation, where we calculate the gauge action very often, the FP gauge action would not be feasible. But one can parametrize the solutions in terms of gauge loops<sup>6</sup> for  $S_{\text{gauge}}$  and fit the coefficients to:

$$S_{\text{gauge}}^{\text{FP}}(V) = \min_{\{U\}} (S_{\text{gauge}}^{\text{FP}}(U) + T_{\text{gauge}}(V, U)) , \quad (5.29)$$

where  $T_{\text{gauge}}(V, U)$  defines the gauge invariant averaging process from the fine  $U$  to the coarse field  $V$ :

$$T(V, U)_{\text{gauge}} = \sum_{x_B, \mu} \left( \mathcal{N}_\mu(x_B) - \frac{\kappa_g}{N} \text{Re tr} [V_\mu(x_B) Q_\mu^\dagger(x_B)] \right) , \quad (5.30)$$

where  $x_B$  are the coordinates of the coarse lattice after a RGT process.  $Q_\mu(x_B)$  is a  $3 \times 3$  matrix which represents a special averaging of products of link variables  $U_\mu(x)$  connecting the sites  $x_B$  and  $x_B + 2\hat{\mu}$  on the fine lattice. The term

$$\mathcal{N}_\mu(x_B) = \max_{W \in SU(3)} \left\{ \frac{\kappa_g}{N} \text{Re tr} [W Q_\mu^\dagger(x_B)] \right\} . \quad (5.31)$$

is a normalization which ensures the invariance of the partition function. The parameter  $\kappa_g$  is a positive constant, which can be fixed by optimizing the action to have a short interaction range<sup>7</sup>.

### 5.3 The Dirac operator

The fermionic part of the QCD action in the continuum is given by (2.2) and it transforms on the lattice into:

$$S_{\text{ferm}}[\psi, \bar{\psi}, A] \rightarrow S_{\text{ferm}}^{\text{lat}}[\psi, \bar{\psi}, U] = \sum_f \sum_{x, x'} a^4 \bar{\psi}^f(x) [D(x, x', U) + m^f] \psi^f(x') , \quad (5.32)$$

where  $D(x, x', U)$  is a matrix in color and spinor space. Furthermore it is diagonal in flavor space. Sometimes one rescales the quark fields such that the lattice spacing  $a$  disappears

$$\begin{aligned} S_{\text{ferm}}^{\text{lat}}[\psi, \bar{\psi}, U] &= \sum_f \sum_{x, x'} a^{\frac{3}{2}} \bar{\psi}^f(x) [aD(x, x', U) + am^f] a^{\frac{3}{2}} \psi^f(x') \\ &\longrightarrow \sum_f \sum_{x, x'} \bar{\psi}'^f(x) [D'(x, x', U) + m'^f] \psi'^f(x') \end{aligned} \quad (5.33)$$

<sup>6</sup>For parametrization of the FP gauge action the same gauge loops as for the Lüscher-Weisz gauge action in Section 5.2.2 are used (cf. Fig. 5.2).

<sup>7</sup>We refer the interested reader to [45] for the explicit form of the RG block transformation.

For practical reasons this is similar as to set the lattice spacing to  $a = 1$ , but keep in mind that the dimensions of the quantities are still important whenever we want to interpret the lattice data.

On the lattice we have to define the discretization of the derivative which is a non-trivial task. The naive discretization fails<sup>8</sup> as it produces doublers, i.e., additional mass degenerate states at each corner of the Brillouin zone.

A general discretization of the derivative acts on the quark fields at different sites. Thus the Dirac operator has to depend on the gauge fields through products of parallel transporters along paths connecting the quark fields located at different sites. This condition is equal to the gauge invariance of the fermion action in the continuum formulation (2.2).

In addition to gauge invariance the Dirac operator should have as many of the continuum properties as possible, i.e., the action should be invariant under charge conjugation  $\mathcal{C}$ , parity  $\mathcal{P}$ , rotations and translations. Furthermore the Dirac operator should be  $\gamma_5$ -hermitian:

$$D\gamma_5 = \gamma_5 D^\dagger, \quad (5.34)$$

### 5.3.1 Naive fermions

In the continuum the fermion action  $S_{\text{ferm}}[\psi, \bar{\psi}, 0]$  for a free fermion is given by the expression<sup>9</sup>

$$S_{\text{ferm}}[\psi, \bar{\psi}, 0] = \sum_f \int d^4x \bar{\psi}^f(x) [\gamma_\mu \partial_\mu(x) + m^f] \psi^f(x). \quad (5.35)$$

When formulating this action on the lattice we have to discretize the integral over space-time as well as the partial derivative, where we use a symmetric expression:

$$\partial_\mu \psi(x) \rightarrow \frac{1}{2a} (\psi(x + \hat{\mu}) - \psi(x - \hat{\mu})). \quad (5.36)$$

On the lattice we get for (5.35):

$$S_{\text{ferm}}[\psi, \bar{\psi}, 0] \rightarrow S_{\text{ferm}}^{\text{free}}[\psi, \bar{\psi}] = \sum_f a^4 \sum_{x,\mu} \bar{\psi}^f(x) \left[ \gamma_\mu \frac{\psi^f(x + \hat{\mu}) - \psi^f(x - \hat{\mu})}{2a} + m^f \psi^f(x) \right]. \quad (5.37)$$

One can easily see that  $S_{\text{ferm}}^{\text{free}}$  is not gauge invariant on the lattice. To get a gauge invariant action we have to make use of the parallel transporters  $U_\mu(x)$ . We can now generalize the free fermion action to the so-called naive fermion action describing fermions in an external gauge field  $U$ :

$$S_{\text{ferm}}^{\text{naive}}[\psi, \bar{\psi}, U] = \sum_f a^4 \sum_{x,\mu} \bar{\psi}^f(x) \left[ \gamma_\mu \frac{U_\mu(x) \psi^f(x + \hat{\mu}) - U_{-\mu}(x) \psi^f(x - \hat{\mu})}{2a} + m^f \psi^f(x) \right]. \quad (5.38)$$

Comparing this action with (5.32) we get the naive Dirac operator on the lattice:

$$D^{\text{naive}}(x, x', U) = \frac{1}{2a} \sum_\mu \gamma_\mu [U_\mu(x) \delta_{x+\hat{\mu}, x'} - U_{-\mu}(x) \delta_{x-\hat{\mu}, x'}] \quad (5.39)$$

<sup>8</sup>cf. Section 5.3.1

<sup>9</sup>cf. Eq. (2.2)

### 5.3.2 Wilson-type fermions

Before we discuss the Wilson fermion action, let us compute the Fourier transform of (5.39) for the free case, i.e.,  $A_\mu^a(x) = 0$  or  $U_\mu(x) = 1$ :

$$a^8 \sum_{x, x'} e^{-ipx} D^{\text{naive}}(x, x', 0) e^{-iqx'} , \quad (5.40)$$

$$= \frac{a^8}{2a} \sum_x e^{-i(p+q)x} \sum_\mu \gamma_\mu (e^{-iaq_\mu} - e^{iaq_\mu}) , \quad (5.41)$$

$$= -ia^3 V \delta^4(p+q) \sum_\mu \gamma_\mu \sin(aq_\mu) , \quad (5.42)$$

$$= ia^3 V \delta^4(p+q) \sum_\mu \gamma_\mu \sin(ap_\mu) , \quad (5.43)$$

$$= a^4 V \delta^4(p+q) \hat{D}^{\text{naive}}(p) , \quad (5.44)$$

where we have defined the Fourier transform of the naive Dirac operator as:

$$\hat{D}^{\text{naive}}(p) = \frac{i}{a} \sum_\mu \gamma_\mu \sin(ap_\mu) . \quad (5.45)$$

Now we calculate the inverse of  $\hat{D}^{\text{naive}}(p)$ , which has the correct continuum limit:

$$\hat{D}^{\text{naive}}(p)^{-1} = \frac{-ia \sum_\mu \gamma_\mu \sin(ap_\mu)}{\left(\sum_\mu \gamma_\mu \sin(ap_\mu)\right)^2} \xrightarrow{a \rightarrow 0} \frac{-i \sum_\mu \gamma_\mu p_\mu}{p^2} . \quad (5.46)$$

In the continuum the momentum space propagator for massless fermions has a pole at  $p_\mu = (0, 0, 0, 0)$ . This pole corresponds to the single fermion which is described by the continuum Dirac operator. However, on the lattice the situation is different. There the propagator for free fermions has additional poles, whenever one of the components is either  $p_\mu = 0$  or  $p_\mu = \pi/a$ . It is easy to see that this creates 15 unphysical poles, the so-called doublers.

Wilson has found a way to circumvent this issue in defining the fermion action as follows:

$$\begin{aligned} D^{\text{Wilson}}(x, x', U) &= \left(\frac{4}{a} + m\right) \delta_{x, x'} - \frac{1}{2a} \sum_\mu (\mathbb{1} - \gamma_\mu) U_\mu(x) \delta_{x+\hat{\mu}, x'} - \frac{1}{2a} \sum_\mu (\mathbb{1} + \gamma_\mu) U_{-\mu}(x) \delta_{x-\hat{\mu}, x'} , \\ &= D^{\text{naive}}(x, x', U) + \frac{4}{a} \delta_{x, x'} - \frac{1}{2a} \sum_\mu U_\mu(x) \delta_{x+\hat{\mu}, x'} - \frac{1}{2a} \sum_\mu U_{-\mu}(x) \delta_{x-\hat{\mu}, x'} , \\ &= D^{\text{naive}}(x, x', U) - \frac{a}{2} \sum_\mu \left( \frac{U_\mu(x) \delta_{x+\hat{\mu}, x'} - 2\delta_{x, x'} + U_{-\mu}(x) \delta_{x-\hat{\mu}, x'}}{a^2} \right) . \end{aligned} \quad (5.47)$$

The additional term is called Wilson term and it is proportional to the negative Laplace operator  $-\partial_\mu \partial_\mu$ . In the momentum space one finds:

$$\hat{D}^{\text{Wilson}}(p) = \hat{D}^{\text{naive}}(p) + m + \frac{1}{a} \sum_\mu (1 - \cos(ap_\mu)) . \quad (5.48)$$

The extra term, the so-called Wilson term, vanishes for components with  $p_\mu = 0$  and provides an additional contribution  $2/a$  for each component with  $p_\mu = \pi/a$ . This term acts like a mass term

$$m \rightarrow m + \frac{2l}{a} , \quad (5.49)$$

where  $l$  is the number of momentum components with  $p_\mu = \pi/a$ . In this way the unphysical doublers get an infinite large mass in the continuum limit and decouple from the theory. However, due to this extra term the Wilson Dirac operator breaks the chiral symmetry explicitly. The importance of chiral symmetry becomes more concrete in Chapter 6.

# Chapter 6

## Chiral fermions

In this work we make use of two kinds of Dirac operators, the chirally improved (CI) Dirac operator and the parametrized fixed-point (FP) Dirac operator. They have one property in common, namely they are tuned to satisfy chiral symmetry only approximately. We briefly try to explain the idea behind these operators. But before that, we start to discuss some more general features of chiral fermions on the lattice.

### 6.1 Chiral symmetry on the lattice

Chiral symmetry and its breaking are very important ingredients for the QCD phenomenology, especially in the low-energy regime. Although the Wilson Dirac operator (5.47) has the correct continuum limit and also avoids fermion doubling, we find that it violates chirality (2.27) even in the massless case. Nielsen and Ninomiya [46, 47] showed that this problem cannot be avoided without violating at least one of a set of conditions, which all seem to be basically important.

#### 6.1.1 Nielsen-Ninomiya No-Go theorem

The requested properties of a Dirac operator  $D$  on the lattice should be:

1. Locality: The Dirac operator  $D(x, y)$  has to decrease exponentially fast with  $e^{-M|x-y|}$ , where  $M$  is larger than any physical mass on the lattice (i.e.,  $M \sim a^{-1}$ , cutoff). Locality is required in order to ensure renormalizability and therefore that a consistent field theory is obtained.
2. Continuum limit: The Dirac operator has to have the correct naive continuum limit for  $a \rightarrow 0$ .
3. No doublers: The number of fermion species should be equal to that of the target continuum theory. The Fourier transform of the Dirac operator can be inverted for  $p \neq 0$ , i.e., it does not have any poles in the Brillouin zone beyond the expected ones.
4. Chiral symmetry:  $\gamma_5 D + D \gamma_5 = 0$ . This implies that the fermion action is chirally invariant.

The Nielsen-Ninomiya theorem claims that these conditions cannot be satisfied simultaneously. Violating one of the conditions 1 - 3 somehow would cause severe theoretical problems. In the case of Wilson fermions (5.47), where we want to hold these conditions fixed, the lattice Dirac operator breaks chirality explicitly (condition (4)). In QCD this also creates serious technical problems and in chiral gauge theories it has even blocked progress from the start:

- Due to the additive mass renormalization the bare quark mass has to be fine tuned. The interested reader is referred to [48]. We also discuss this in Section 9.2.2 and in Appendix C.5.

- Fluctuations of the Dirac operator eigenvalues restrict the computation of the Dirac propagator for light quark masses. Even the massive Dirac operator  $D^{(m)}$  can have eigenvalues  $\lambda \sim 0$ . The more the eigenvalues of the massless Dirac operator fluctuate, the larger the bare quark mass  $m$  has to be in order to avoid a break down in the inversion of the Dirac operator.
- Operators of different chiral representations are mixed.

### 6.1.2 Ginsparg-Wilson equation

Even though the Nielsen-Ninomiya No-Go theorem is correct, the solution to all these problems was published by Ginsparg and Wilson [49] in 1982. They suggested to introduce a weaker condition for the chirality on the lattice than condition (4), the so-called Ginsparg-Wilson equation:

$$\gamma_5 \mathcal{D} + \mathcal{D} \gamma_5 = a \mathcal{D} \gamma_5 2R \mathcal{D} . \quad (6.1)$$

In (6.1) the Dirac operator<sup>1</sup>  $\mathcal{D}$  is the massless lattice Dirac operator,  $a$  is the lattice spacing and  $R$  is a local matrix which is proportional to a  $\mathbf{1}$  in spinor space<sup>2</sup>. In the continuum limit  $a \rightarrow 0$  the equation (6.1) is equal to condition (4) and for this reason chiral symmetry can even be restored on the lattice without violating the Nielsen-Ninomiya No-Go theorem.

Although the Ginsparg-Wilson equation (6.1) was already proposed in 1982, it was never applied for Lattice QCD, because no explicit solution was known. Finally, it was forgotten until 1998, when Hasenfratz, Laliena and Niedermayer in [50] and Neuberger in [51, 52] suggested that chiral symmetry may also be preserved in Lattice QCD. Although both constructions of their Dirac operators, which are chiral in the continuum limit, are very complicated they all satisfy the Ginsparg-Wilson equation (6.1), which circumvents the Nielsen-Ninomiya No-Go theorem in this way.

We can always transform the Dirac operator  $\mathcal{D}$ :

$$D = \sqrt{2R} \mathcal{D} \sqrt{2R} , \quad (6.2)$$

and the fields  $\bar{\Psi}, \Psi$ :

$$\bar{\psi} = \bar{\Psi} \frac{1}{\sqrt{2R}} \quad \psi = \frac{1}{\sqrt{2R}} \Psi , \quad (6.3)$$

which is often very helpful to derive relations in a simpler way. We can then use:

$$\gamma_5 D + D \gamma_5 = a D \gamma_5 D , \quad (6.4)$$

where the fermion action  $S_{\text{ferm}}^{\text{lat}}[\psi, \bar{\psi}, U] = S_{\text{ferm}}^{\text{lat}}[\Psi, \bar{\Psi}, U]$  stays the same<sup>3</sup>. In some constructions of a lattice Dirac operator,  $R$  is set to a constant from the beginning, e.g.,  $R = \frac{1}{2}$ . The more general case  $2R \neq 1$  is discussed in Appendix D.

Note that the net effect of the extra term on the right hand side is like a contact term for the anti-commutator of the propagator  $D^{-1}$  with  $\gamma_5$ . If we multiply (6.4) with  $D^{-1}$  from both sides we obtain:

$$D^{-1} \gamma_5 + \gamma_5 D^{-1} = a \gamma_5 , \quad (6.5)$$

or equivalently:

$$\mathcal{D}^{-1} \gamma_5 + \gamma_5 \mathcal{D}^{-1} = a \gamma_5 2R . \quad (6.6)$$

<sup>1</sup>In this Chapter we strictly distinguish between  $\mathcal{D}$  and  $D$ , where the matrix  $R$  is local or a constant, respectively. In all the other chapters we explicitly denote, what Dirac operator we are using.

<sup>2</sup>Also the inverse of  $R$  is in contrast to the Dirac operator a ultra-local matrix (cf. Section 6.4).

<sup>3</sup>Note that we have here different measures in the path integrals. Although the fermionic action does not change, the partition functions differ from each other.

### 6.1.3 Neuberger's overlap projection

Neuberger presented in [51] the overlap Dirac operator and has shown in [52] that it is also a solution of the Ginsparg-Wilson equation (6.4).

Any massless Dirac operator  $\widehat{D}^{(0)}$ , not suffering from the fermion doubling problem can be inserted into the following overlap construction:

$$aD_{\text{ov}} = \mathbb{1} - A(\gamma_5 A \gamma_5 A)^{-1/2}, \quad A = \mathbb{1} - a\widehat{D}^{(0)}. \quad (6.7)$$

The so-called Neuberger or overlap operator  $D_{\text{N}} = D_{\text{ov}}$  respects the simplified Ginsparg-Wilson relation (6.4) with  $2R = \mathbb{1}$ .

If  $\widehat{D}^{(0)}$  is  $\gamma_5$ -hermitian, then so is  $A$ , i.e.,  $\gamma_5 A \gamma_5 = A^\dagger$ , and the inverse square root of  $\gamma_5 A \gamma_5 A = A^\dagger A$  in (6.7) is well-defined. The convergence of an approximation to  $A(A^\dagger A)^{-1/2}$  is the deciding factor for the computer time needed and this depends on the quality<sup>4</sup> of the original Dirac operator  $\widehat{D}^{(0)}$ . Then it is easy to see that  $D_{\text{ov}}$  obeys the Ginsparg-Wilson equation (6.4):

$$\begin{aligned} aD_{\text{ov}}^\dagger D_{\text{ov}} &= a^{-1} \gamma_5 \left( \mathbb{1} - A(A^\dagger A)^{-1/2} \right) \gamma_5 \left( \mathbb{1} - A(A^\dagger A)^{-1/2} \right), \\ &= a^{-1} \left[ \mathbb{1} - \gamma_5 A(A^\dagger A)^{-1/2} \gamma_5 - A(A^\dagger A)^{-1/2} + \mathbb{1} \right], \\ &= D_{\text{ov}}^\dagger + D_{\text{ov}}, \\ \Rightarrow D_{\text{ov}} &= D_{\text{GW}}. \end{aligned} \quad (6.8)$$

Because of the construction in Eq. (6.7) the operator  $D_{\text{ov}}$  is no longer ultra-local, which can be shown for all Ginsparg-Wilson Dirac operators (cf. [53]). However, locality has to be preserved to obtain a renormalizable quantum field theory. The Dirac operator satisfies the following constraint:

$$|D(x, y)| \leq A e^{-M|x-y|}, \quad (6.9)$$

where the constants  $A$  and  $M$  are independent of the gauge field. If  $M \sim a^{-1}$  is a fixed distance on the lattice, the Dirac operator is still local in the continuum limit  $a \rightarrow 0$ . In [54] it is shown that  $D_{\text{ov}}$  is local (with exponentially decaying tails) if the gauge field is sufficiently smooth at the scale of the cutoff.

The overlap improvement can also be applied for the CI Dirac operator  $D_{\text{CI}}$  or the parametrized FP Dirac operator  $D_{\text{FP}}$  discussed in Sections 6.3 and 6.4, respectively. In this way the exact chiral symmetry which was lost due to the parametrizations in the CI and FP Dirac operators can be recovered again. Eq. (6.7) is therefore more like a projection of a non-chiral Dirac operator onto a solution of the Ginsparg-Wilson equation (6.4).

### 6.1.4 Chiral transformations on the lattice

Lüscher proposed in [55] a modification of the standard infinitesimal chiral transformations in the continuum<sup>5</sup>:

$$\delta^a \psi_f = i t_{ff}^a \epsilon \gamma_5 \left( \mathbb{1} - \frac{a}{2} D \right) \psi_{f'}, \quad \delta^a \bar{\psi}_f = i \bar{\psi}_{f'} \left( \mathbb{1} - \frac{a}{2} D \right) \gamma_5 t_{f'f}^a \epsilon, \quad (6.10)$$

where  $D$  is a massless Dirac operator satisfying (6.4) and  $\epsilon$  is an infinitesimal parameter. For finite  $a$  the lattice fermion action (5.32) with  $m^f = 0$  is invariant under these transformations and therefore the chiral rotations in (6.10) allow us to define chiral symmetry also on the lattice.

To implement chiral symmetry on the lattice one can also define  $\hat{\gamma}_5$  via:

$$\gamma_5 D + D \gamma_5 - a D \gamma_5 D = \gamma_5 D + D \hat{\gamma}_5 = 0, \quad \hat{\gamma}_5 = \gamma_5 (\mathbb{1} - a D) \quad (6.11)$$

<sup>4</sup>The approximation of the square root in Eq. (6.7) numerically converges the faster, the more chirality is already implemented in the massless Dirac operator  $\widehat{D}^{(0)}$ .

<sup>5</sup>cf. Section 2.3.3

and use it to introduce the projectors  $\hat{P}_L$  and  $\hat{P}_R$ :

$$\hat{P}_L = \frac{\mathbb{1} + \hat{\gamma}_5}{2}, \quad \hat{P}_R = \frac{\mathbb{1} - \hat{\gamma}_5}{2}. \quad (6.12)$$

Due to (6.4) one finds  $(\hat{\gamma}_5)^2 = \mathbb{1}$  and

$$\hat{P}_R^2 = \hat{P}_R, \quad \hat{P}_L^2 = \hat{P}_L, \quad \hat{P}_R \hat{P}_L = \hat{P}_L \hat{P}_R = 0, \quad \hat{P}_R + \hat{P}_L = \mathbb{1}. \quad (6.13)$$

Using the definitions in (2.23) for  $P_L, P_R$  and in (6.12) for  $\hat{P}_L, \hat{P}_R$  one can easily show that:

$$D\hat{P}_R = P_L D, \quad D\hat{P}_L = P_R D. \quad (6.14)$$

We can use  $\hat{\gamma}_5$  to write down the transformations in (6.10) in an asymmetric way:

$$\delta^a \psi_f = i t_{ff'}^a \epsilon \hat{\gamma}_5 \psi_{f'}, \quad \delta^a \bar{\psi}_f = i \bar{\psi}_{f'} \gamma_5 t_{f'f}^a \epsilon. \quad (6.15)$$

One can easily check that the action is also invariant under these transformations.

Based on the last equations we can write the lattice action in the form:

$$\bar{\psi} D \psi = \bar{\psi}_L D \psi_L + \bar{\psi}_R D \psi_R = \bar{\psi} \left( P_R D \hat{P}_L + P_L D \hat{P}_R \right) \psi, \quad (6.16)$$

where we redefine the continuum definition (2.23) on the lattice as follows:

$$\bar{\psi}_L = \bar{\psi} P_R, \quad \bar{\psi}_R = \bar{\psi} P_L, \quad \psi_L = \hat{P}_L \psi, \quad \psi_R = \hat{P}_R \psi. \quad (6.17)$$

According to Eq. (6.16) we transform the mass term into this language:

$$m(\bar{\psi}_L \psi_R + \bar{\psi}_R \psi_L) = m \bar{\psi} (P_R \hat{P}_R + P_L \hat{P}_L) \psi = m \bar{\psi} \left( \mathbb{1} - \frac{a}{2} D \right) \psi. \quad (6.18)$$

Therefore a massive Ginsparg-Wilson Dirac operator can be written in the form:

$$D^{(m)} = D^{(0)} + m \left( \mathbb{1} - \frac{a}{2} D^{(0)} \right) \equiv \bar{m} D^{(0)} + m \mathbb{1}, \quad (6.19)$$

where we define for later purposes

$$\bar{m} = 1 - \frac{a}{2} m. \quad (6.20)$$

### 6.1.5 Covariant densities and currents

In [56, 57] Kikukawa and Yamada present a way to find the chirally covariant vector and axialvector currents in the overlap construction with Wilson kernel. The more general case, which can also be used in numerical simulations, can be found in [58].

The exact global symmetries in (6.15) imply the existence of covariant densities and covariant conserved currents, which transform the same way as in the continuum. Inspired by the introduction of the mass into the Dirac operator in Eq. (6.18) we define a covariant scalar and pseudoscalar density in a similar way:

$$S^a = \bar{\psi} \left( \mathbb{1} - \frac{a}{2} D \right) t^a \psi, \quad P^a = \bar{\psi} \gamma_5 \left( \mathbb{1} - \frac{a}{2} D \right) t^a \psi. \quad (6.21)$$

We show in Appendix C.2 that these densities satisfy the same relations as their continuum counterparts.

For the vector and axialvector currents it is not so easy to find conserved currents which transform covariantly. In [58] the authors propose the following covariant and conserved currents (cf. Appendix C.3):

$$V_\mu^a(x) = \bar{\psi} \left( P_R K_\mu(x) \hat{P}_L + P_L K_\mu(x) \hat{P}_R \right) t^a \psi, \quad A_\mu^a(x) = \bar{\psi} \left( P_R K_\mu(x) \hat{P}_L - P_L K_\mu(x) \hat{P}_R \right) t^a \psi, \quad (6.22)$$

and give also a numerical procedure to obtain the kernel function  $K_\mu(x)$  on the lattice defined in Eq. (C.36). Note that in addition to their global covariance the currents in (6.22) are also invariant under a local axial

and vector transformation as defined in Eqs. (C.15) and (C.16). The fact that the action is a scalar under these transformations implies also that it is  $\mathcal{O}(a)$  improved since the mixing of the action density with higher dimensional operators is forbidden by the symmetries. The spectral quantities are therefore automatically  $\mathcal{O}(a)$  improved.

Although having now covariant currents and densities, Eqs. (6.21) and (6.22) are not related to each other by a Ward identity. However, we can also define scalar and pseudoscalar densities which are invariant under local transformations (C.15) and (C.16) and also satisfying the Ward identities [58]:

$$\begin{aligned} S^a(x) &= \bar{\psi} \left[ \frac{1}{2} E(x) \left( \mathbf{1} - \frac{a}{2} D \right) + \frac{1}{4} \left( \mathbf{1} - \frac{a}{2} D \right) (E(x) + \hat{\gamma}_5 E(x) \hat{\gamma}_5) \right] t^a \psi, \\ P^a(x) &= \bar{\psi} \left[ \frac{1}{2} E(x) \gamma_5 \left( \mathbf{1} - \frac{a}{2} D \right) + \frac{1}{4} \left( \mathbf{1} - \frac{a}{2} D \right) (\hat{\gamma}_5 E(x) + E(x) \hat{\gamma}_5) \right] t^a \psi, \end{aligned} \quad (6.23)$$

where

$$(E(x))_{yz} = \delta_{yx} \delta_{xz}. \quad (6.24)$$

Although Eqs. (6.21) and (6.23) look very complicated one can replace them up to contact terms and prefactors by the naive densities. This is discussed in Appendix C.3.

It is advantageous to work with scalar and pseudoscalar densities and conserved currents which transform covariantly under the global transformations in Eqs. (C.10) and (C.11). These  $dim = 3$  operators are again automatically  $\mathcal{O}(a)$  improved, because they cannot mix with any  $dim = 4$  operators.

For a generalization of the equations in this section to Dirac operators satisfying Eq. (6.1) the interested reader is referred to Appendices C and D.

## 6.2 Consequences of the Ginsparg-Wilson equation

We summarize in this Section some of the most important consequences of the Ginsparg-Wilson equation (6.4), which are frequently used in the rest of this work.

### 6.2.1 Spectrum of a Ginsparg-Wilson Dirac operator

The corresponding eigenvalue equation is

$$Dv_\lambda = \lambda v_\lambda. \quad (6.25)$$

We also require  $\gamma_5$ -hermiticity (5.34) for the Dirac operator. For a  $\gamma_5$ -hermitian Dirac operator one can show that its eigenvalues are either real or come in complex conjugate pairs. Furthermore real eigenvalues can have non-vanishing chirality  $v_r^\dagger \gamma_5 v_r \neq 0$  or

$$v_\lambda^\dagger \gamma_5 v_\lambda = 0, \quad \text{unless } \lambda \in \mathbb{R}. \quad (6.26)$$

Combining  $\gamma_5$ -hermiticity and the Ginsparg-Wilson equation one finds for the eigenvalues of the massless Dirac operator  $D$ :

$$\lambda + \lambda^* = a\lambda\lambda^*, \quad (6.27)$$

which is the equation of a circle in the complex plane with  $\lambda = x + iy$ :

$$\left( x - \frac{1}{a} \right)^2 + y^2 = \frac{1}{a^2}. \quad (6.28)$$

The so-called Ginsparg-Wilson circle has its center at  $(1/a, 0)$  in the complex plane and a radius of  $1/a$  (cf. plot on the lhs. in Fig. 6.1). Since the circle intersects the real axis at two points, the real eigenvalues are not only sitting at zero, as in the continuum, but also at  $\lambda = 2/a$ , i.e., not only zero eigenvalues, but also  $\lambda = 2/a$  eigenvalues can have non-vanishing chirality on the lattice.

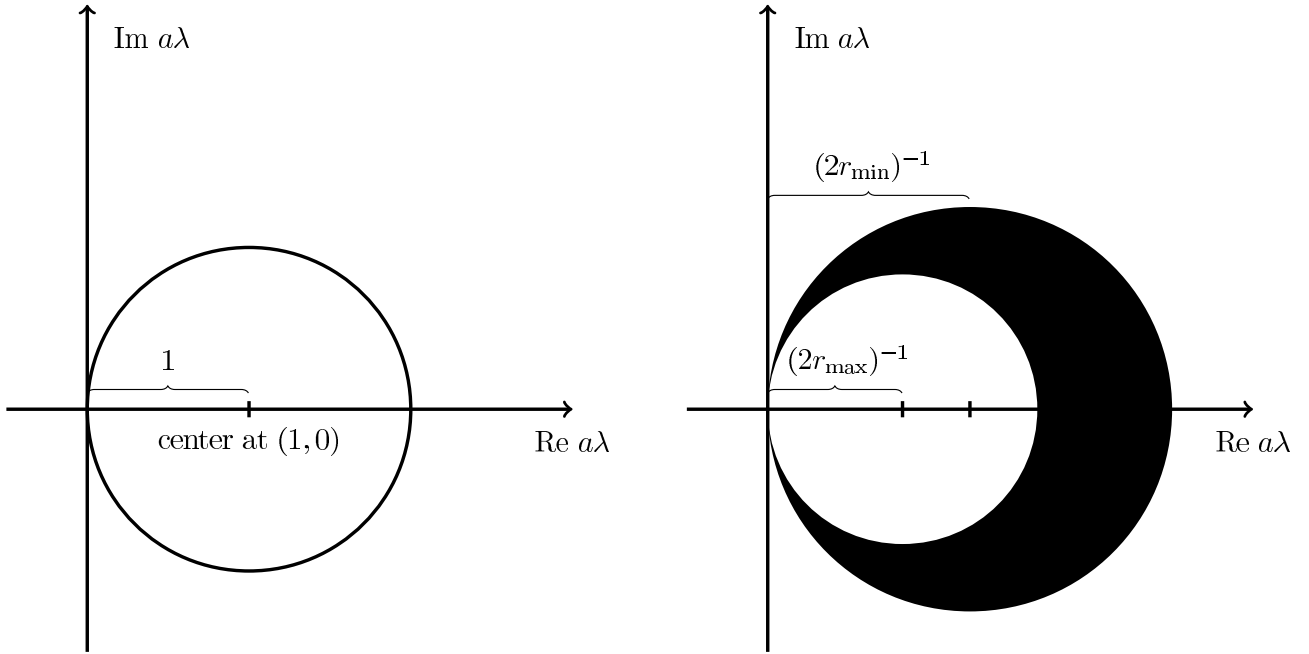


Figure 6.1: In the left figure we plot the Ginsparg-Wilson circle with  $R = \frac{1}{2}$ , while on the right hand side the spectrum for  $R \neq \text{const.}$  is confined between two circles with radii  $(2ar_{\min})^{-1}$  and  $(2ar_{\max})^{-1}$  centered at  $([2ar_{\min}]^{-1}, 0)$  and  $([2ar_{\max}]^{-1}, 0)$  respectively.

If  $2R \neq 1$  one can rescale the Dirac operator  $\mathcal{D}$  using (6.2) and the eigenvalues of  $D$  lie on the Ginsparg-Wilson circle again. Alternatively, the eigenvalues of  $\mathcal{D}$  are restricted to lie between two circles of radii  $(2ar_{\min})^{-1}$  and  $(2ar_{\max})^{-1}$  centered at  $([2ar_{\min}]^{-1}, 0)$  and  $([2ar_{\max}]^{-1}, 0)$  respectively, where  $r_{\min}$  and  $r_{\max}$  are the smallest and largest eigenvalues of operator  $R$ , respectively (cf. plot on the rhs. in Fig. 6.1).

The spectrum of a massive Dirac operator is not only shifted by the lattice mass  $am$ , but also the radius depends on  $m$ . If we solve (6.19) for the massless Dirac operator and apply  $\gamma_5$ -hermiticity again, which is also valid for the massive Dirac operator, and use the Ginsparg-Wilson equation (6.4) we obtain for the massive eigenvalue spectrum:

$$\bar{m}(\lambda + \lambda^* - 2m) = a(\lambda\lambda^* - m(\lambda + \lambda^*) + m^2) \quad \text{for all } m < 2/a, \quad (6.29)$$

where  $\bar{m} = 1 - \frac{1}{2}am$  and  $\lambda = x + iy$  again. This also corresponds to a circle equation plotted in Fig. 6.2:

$$\left(x - \frac{1 + \frac{1}{2}am}{a}\right)^2 + y^2 = \left(\frac{1 - \frac{1}{2}am}{a}\right)^2. \quad (6.30)$$

## 6.2.2 Topology

In [50] it is shown that the solutions of the Ginsparg-Wilson relation satisfy the index theorem on the lattice: the zero modes of  $D$  are chiral and the associated index is a topological invariant which represents the topological charge on the lattice.

Consider Eq. (6.4) and assume the hermiticity property in Euclidean space-time in Eq. (5.34). Then, as it is shown in Section 6.2.1 the spectrum of the massless Dirac operator  $D$  lies on a circle with radius  $1/a$  around the point  $z = (1/a, 0)$  in the complex plane and has the following properties.

- The real modes  $\lambda = 0$  and  $\lambda = 2/a$  are chiral (i.e., the corresponding eigenvectors are also eigenvectors of  $\gamma_5$  with  $\pm 1$  eigenvalues).

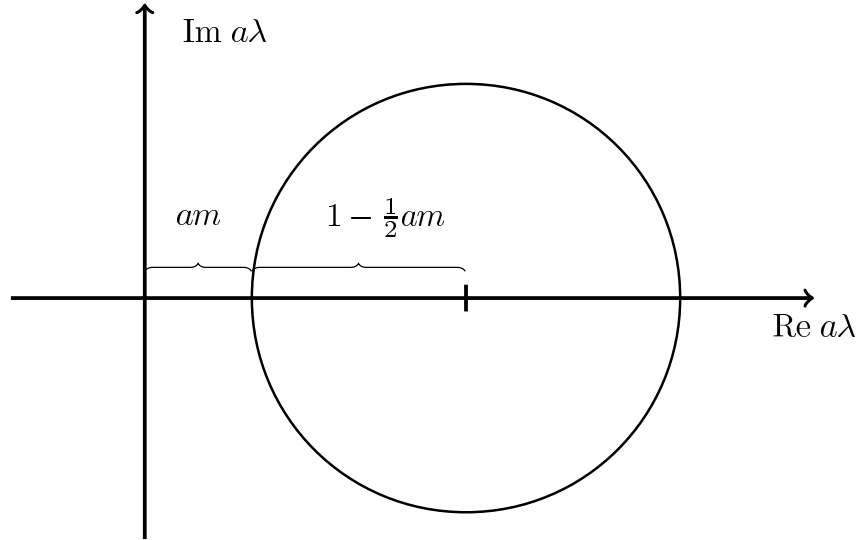


Figure 6.2: We show here the spectrum of the massive Dirac operator with  $2R = 1$ . The spectrum is not only shifted by  $am$ , but the radius of the circle is also scaled by the mass via  $1 - \frac{1}{2}am$ .

- If  $v_\lambda$  is an eigenvector with a complex eigenvalue  $\lambda$ , then  $v_{\lambda^*} = \gamma_5 v_\lambda$  is also one and they are orthogonal to each other:  $v_\lambda^\dagger \gamma_5 v_\lambda = 0$ .

Define the fermionic density

$$q(x) = -\frac{1}{2} \text{tr}_{D,C} (\gamma_5 D(x, x)) , \quad (6.31)$$

where  $\text{tr}_{D,C}$  is the trace over all Dirac and color indices. Consider now

$$\sum_x q(x) = -\frac{1}{2} \text{tr} (\gamma_5 D) = \frac{1}{2} \text{tr} (\gamma_5 (2 - D)) = \frac{1}{2} \text{tr} \sum_\lambda (2 - \lambda) (v_\lambda^\dagger \gamma_5 v_\lambda) , \quad (6.32)$$

where  $\text{tr}$  denotes the trace in all the indices. In the second step we add  $\text{tr} \gamma_5 = 0$  to the trace. Using the orthogonality properties discussed above only the  $\lambda = 0$  modes contribute giving

$$\sum_x q(x) = n_+ - n_- , \quad (6.33)$$

where  $n_\pm$  are the number of zero modes of the Dirac operator with positive/negative chirality. The index of  $D$  is, therefore, a sum over  $x$  of the pseudoscalar density  $q(x)$ . It can be shown [59, 60, 61, 62] that on smooth configurations the gluonic quantity  $q(x)$  is the continuum topological charge density

$$q(x) = -\frac{1}{32\pi^2} \epsilon^{\mu\nu\alpha\beta} \text{tr} F_{\mu\nu}(x) F_{\alpha\beta}(x) = \text{index}(D) . \quad (6.34)$$

This is the Atiyah-Singer index theorem on the lattice. We discuss its continuum version in Section 2.4.2. We can use Eq. (6.33) to determine the topological charge of a gauge field whenever we are using an exact Ginsparg-Wilson Dirac operator.

### 6.2.3 The chiral condensate

The chiral condensate  $\langle \bar{\psi}^f(x) \psi^f(x) \rangle$  is not invariant under chiral transformations and is thus breaking chiral symmetry. It can serve as an order parameter for spontaneous chiral symmetry breaking (cf. Section *Phase diagram of QCD* at the beginning of Part I). Furthermore the chiral condensate is also important in chiral

perturbation theory, where it plays the role of a low energy constant in the effective chiral Lagrangian (cf. Section 3.2), which can only be determined via experiments or lattice calculations.

Having chirality implemented on the lattice, it becomes possible to study also spontaneous chiral symmetry breaking on the lattice. With the lattice formulation of a scalar density (6.21) we write the chiral condensate  $\Sigma^{\text{lat}}$  depending on the quark mass  $m$  and the Volume  $V$ :

$$\Sigma^{\text{lat}}(m, V) = - \left\langle \bar{\psi}^f(x) \left( \mathbb{1} - \frac{a}{2} D^{(0)} \right) \psi^f(x) \right\rangle . \quad (6.35)$$

We can use the translational invariance of the lattice, because the chiral condensate is independent of  $x$  and after performing the integration over the fermion fields we get:

$$\Sigma^{\text{lat}}(m, V) = \frac{1}{V} \sum_x \left\langle \left( \mathbb{1} - \frac{a}{2} D^{(0)} \right) G^{(m)}(x, x) \right\rangle_U , \quad (6.36)$$

where  $G^{(m)} \equiv (D^{(m)})^{-1}$  is the massive Dirac propagator. If we use (6.19) we obtain:

$$\Sigma^{\text{lat}}(m, V) = \frac{1}{mV} \sum_x \left\langle G^{(m)}(x, x) - \frac{a}{2} \mathbb{1} \right\rangle_U . \quad (6.37)$$

To obtain from this the order parameter of chiral symmetry breaking we have to take the infinite volume limit  $V \rightarrow \infty$ . After that we also have to remove the explicit breaking of chiral symmetry through the mass term, i.e., we have to take the limit  $m \rightarrow 0$ . As a result we get the bare chiral condensate at a fixed UV cutoff  $a^{-1}$ :

$$\Sigma^{\text{bare}} = \lim_{m \rightarrow 0} \lim_{V \rightarrow \infty} \Sigma^{\text{lat}}(m, V) . \quad (6.38)$$

The physical chiral condensate is renormalization scheme dependent and is usually given in the  $\overline{\text{MS}}$ -scheme. It is obvious that the whole calculation is a numerically very demanding approach which needs huge computer time. In Section 9.3 we also discuss another approach to determine the quark condensate  $\Sigma$  which is at least computationally more promising.

### 6.3 The chirally improved Dirac operator

If we expand the most general lattice Dirac operator  $D$  in a basis of simple operators, the Ginsparg-Wilson equation turns into a system of coupled quadratic equations for the expansion coefficients [63, 64]. The expansion of  $D$  allows a natural cutoff and the remaining quadratic equations can be solved numerically. The procedure allows us to find Dirac operators which obey the Ginsparg-Wilson equation with arbitrary precision. For a more detailed discussion the interested reader is referred to [63].

#### First step

Typically the derivative term on the lattice is discretized by the following nearest neighbor expression<sup>6</sup>:

$$\frac{1}{2} \sum_{\mu=1}^4 \gamma_{\mu} [U_{\mu}(x) \delta_{x+\hat{\mu}, y} - U_{-\mu}(x) \delta_{x-\hat{\mu}, y}] . \quad (6.39)$$

However, it is compatible with all the symmetries to discretize the derivative using higher order terms, e.g.,

$$\frac{1}{4} \sum_{\mu=1}^4 \gamma_{\mu} [U_{\mu}(x) U_{\mu}(x + \hat{\mu}) \delta_{x+2\hat{\mu}, y} - U_{-\mu}(x) U_{-\mu}(x - \hat{\mu}) \delta_{x-2\hat{\mu}, y}] , \quad (6.40)$$

and there are many more possibilities one can think of. Thus an ansatz for the most general Dirac operator  $D$  must allow for a superposition of all the possible discretizations for the derivative term.

<sup>6</sup>Here we are using convention (5.32) again.

In order to remove the doublers one also needs a term which can distinguish between  $p_\mu = 0$  (physical modes) and  $p_\mu = \pi/a$  (doublers) in momentum space. Such a term is provided by the standard Wilson term. Because of symmetry reasons this term has to come with  $\mathbf{1}$  in spinor space. Again, we allow for all possible terms. We generalize  $D$  further, by including all terms also for the remaining elements  $\Gamma_\alpha$  of the Clifford algebra (cf. Appendix A.1), i.e., tensors, axialvectors and the pseudoscalar. Thus the emerging lattice Dirac operator has the following form:

$$D = \sum_{\alpha=1}^{16} \Gamma_\alpha \sum_{p \in \mathcal{P}^\alpha} c_p^\alpha \langle l_1, l_2, \dots, l_{|p|} \rangle, \quad (6.41)$$

where we use the notation defined in Section 5.2. To each generator  $\Gamma_\alpha$  of the Clifford algebra we assign a set  $\mathcal{P}^\alpha$  of paths  $p$ , each  $p$  given by some ordered set of links  $\langle l_1, l_2, \dots, l_{|p|} \rangle$  (cf. Eq. (5.8)) where  $|p|$  denotes the length of the path  $p$ . Each path is weighted with some complex weight  $c_p^\alpha$ .

### Second step

The second step is to impose on  $D$  the symmetries which we want to maintain: Translation and rotation invariance and invariance under charge conjugation  $\mathcal{C}$  and parity  $\mathcal{P}$ . In addition we require that  $D$  is  $\gamma_5$ -hermitian. When implementing all these symmetries we find that paths in our ansatz (6.41) become grouped together where all paths in a group come with the same coefficient up to sign factors [63].

When we insert our expanded Dirac operator  $D$  into the Ginsparg-Wilson equation (6.4), we get a system of coupled quadratic equations for the expansion coefficients of  $D$ . Due to the fact that we would get an infinite number of coupled quadratic equations we truncate the expansion of  $D$  and find solutions for the finite number of coupled equations which can be solved and stored on present computer systems. We call the solution, the chirally improved Dirac operator  $D_{\text{CI}}$ . However, the truncation of the expansion only respects the Ginsparg-Wilson relation approximately. An unfortunate consequence is that the lattice index theorem does not hold for this operator. The chirality of the real modes of  $D_{\text{CI}}$  is no longer an integer  $\pm 1$ , but distributed over the range  $[-1, 1]$ . Furthermore we get an additive mass renormalization (cf. 9.2.2).

## 6.4 The parametrized fixed-point Dirac operator

The FP Dirac operator satisfies the Ginsparg-Wilson relation exactly. However, it has a very complex structure and is therefore difficult to use for lattice simulations. Consider the RG transformations in QCD as already discussed in Section 5.2.3 only for the fermionic action  $S_{\text{ferm}}$ :

$$e^{-S'_{\text{ferm}}[\bar{\chi}, \chi, V]} = \int [dU][d\bar{\psi}][d\psi] e^{-(S_{\text{ferm}}[\bar{\psi}, \psi, U] + T_{\text{ferm}}[\bar{\chi}, \chi, V; \bar{\psi}, \psi, U])}. \quad (6.42)$$

The averaging function for the fermions  $T_{\text{ferm}}[\bar{\chi}, \chi; \bar{\psi}, \psi, U]$  can be chosen in the following form:

$$T_{\text{ferm}}[\bar{\chi}, \chi, V; \bar{\psi}, \psi, U] = \sum_{x_B, y_B} (\bar{\chi}_{x_B} - \sum_x \bar{\psi}_x \omega_{x, x_B}^\dagger) (\kappa_f)_{x_B y_B} (\chi_{y_B} - \sum_y \omega_{y_B, y} \psi_y), \quad (6.43)$$

where  $\omega_{x, x_B}$  describes the averaging process in a local neighborhood of the coarse lattice point  $x_B$  and

$$(\kappa_f)_{x_B y_B} = \kappa_f \delta_{x_B y_B} \quad (6.44)$$

can be used for optimizing issues. As in (5.29) we have to solve a minimization problem to get the fixed-point fermion action:

$$S_{\text{ferm}}^{\text{FP}}(V) = \min_{\bar{\psi}, \psi} (S_{\text{ferm}}^{\text{FP}}(U) + T_{\text{ferm}}(V, U)), \quad (6.45)$$

The minimizing fields in (6.45) are given by:

$$\psi_0(\chi)_x = \kappa_f \sum_{y, y_B} A_{x, y}^{-1} \omega_{y, y_B}^\dagger \chi_{y_B}, \quad (6.46)$$

$$\bar{\psi}_0(\bar{\chi})_x = \sum_{y, y_B} \bar{\chi}_{y_B} \omega_{y_B, y} A_{y, x}^{-1}, \quad (6.47)$$

where

$$A(U)_{x,y} = \mathcal{D}_{\text{FP}}(U)_{x,y} + \kappa_f \sum_{z_B} \omega^\dagger(U, V)_{x,z_B} \omega(V, U)_{z_B,y} . \quad (6.48)$$

For the fixed-point Dirac operator  $\mathcal{D}_{\text{FP}}$  in  $S_{\text{ferm}}$  one obtains:

$$\mathcal{D}_{\text{FP}}(V)_{x_B,y_B} = \kappa_f \delta_{x_B,y_B} - \kappa_f^2 \sum_{x,y,z_B} \omega(V, U)_{x_B,x} [\mathcal{D}_{\text{FP}}(U)_{x,y} + \kappa_f \omega^\dagger(U, V)_{x,z_B} \omega(V, U)_{z_B,y}]^{-1} \omega^\dagger(U, V)_{y,y_B} . \quad (6.49)$$

We can also get a FP equation for the propagator using Wick's theorem in (B.5) on the coarse lattice:

$$\langle \chi \bar{\chi} \rangle = \mathcal{D}_{\text{FP}}(V)^{-1} , \quad \langle \psi \bar{\psi} \rangle = \mathcal{D}_{\text{FP}}(U)^{-1} . \quad (6.50)$$

We can shift the variables  $\chi, \bar{\chi}$  introducing

$$\phi = \chi - \omega \psi \quad \text{and} \quad \bar{\phi} = \bar{\chi} - \bar{\psi} \omega^\dagger \quad (6.51)$$

and integrate over  $\phi, \bar{\phi}$  and  $\psi, \bar{\psi}$ . We obtain:

$$\langle \chi \bar{\chi} \rangle = \frac{1}{\kappa_f} + \omega \langle \psi \bar{\psi} \rangle \omega^\dagger , \quad (6.52)$$

or written in a different form:

$$\mathcal{D}_{\text{FP}}(V)_{x_B,y_B}^{-1} = \frac{1}{\kappa_f} \delta_{x_B,y_B} + \sum_{x,y} \omega(V, U)_{x_B,x} \mathcal{D}_{\text{FP}}(U)_{x,y}^{-1} \omega(U, V)_{y,y_B}^\dagger . \quad (6.53)$$

Inserting the FP Dirac operator from Eq. (6.53) in the Ginsparg-Wilson equation (6.6) we obtain the operator  $R$ :

$$R_{\text{FP}}(V)_{x_B,y_B} = \frac{1}{\kappa_f} \delta_{x_B,y_B} + \sum_{x,y} \omega(V, U)_{x_B,x} R_{\text{FP}}(U)_{x,y} \omega(U, V)_{y,y_B}^\dagger . \quad (6.54)$$

In a numerical simulation, where we need to evaluate the matrix-vector product very frequently, there is no way to calculate a Dirac operator using the FP equations (6.49). One can, however, parametrize the solutions in terms of a certain number of fermion offsets and paths for  $\mathcal{D}_{\text{FP}}$ , fit the coefficients to Eq. (6.49) and obtain an approximate solution,  $\mathcal{D}_{\text{FP}}^{\text{param}}$ . While the  $\mathcal{D}_{\text{FP}}$  is no longer an ultra-local operator, the operator  $R_{\text{FP}}$  has a far simpler structure. Due to the fact that Eq. (6.54) is a linear equation the hypercubic operator  $R_{\text{FP}}$  is strictly zero outside of the hypercube. However, as for the Dirac operator  $\mathcal{D}_{\text{FP}}$  one also has to find a parametrization for the operator  $R_{\text{FP}}$  and fit the coefficients to Eq. (6.54), where we obtain  $R_{\text{FP}}^{\text{param}}$ .

The parametrized FP Dirac operator  $\mathcal{D}_{\text{FP}}^{\text{param}}$  being applicable for simulations is an approximation to the exact operator<sup>7</sup>. It has only a finite number of couplings, but is computationally not too expensive. As for the chirally improved Dirac operator<sup>8</sup>  $D_{\text{CI}}$  the lattice index theorem does also not hold for the parametrized fixed-point Dirac operator  $\mathcal{D}_{\text{FP}}^{\text{param}}$  and we also get an additive mass renormalization (cf. Section 9.2.2).

<sup>7</sup>Because of its ultra-locality and in contrast to the parametrized FP Dirac operator  $\mathcal{D}_{\text{FP}}^{\text{param}}$  the parametrized operator  $R_{\text{FP}}^{\text{param}}$  is exact.

<sup>8</sup>By construction  $\mathcal{D}_{\text{FP}}^{\text{param}}$  and  $D_{\text{CI}}$  are approximately satisfying Eq. (6.1) and Eq. (6.4), respectively.

# Chapter 7

## Ensemble creation

A numerical simulation in lattice field theory has the goal to calculate the expectation values of some functionals  $A[\psi, \bar{\psi}, U]$  which depend on fermion fields  $\psi, \bar{\psi}$  and gauge configurations  $U$ . This is given by path integrals as:

$$\langle A \rangle = Z^{-1} \int [d\psi][d\bar{\psi}][dU] e^{-S[\psi, \bar{\psi}, U]} A[\psi, \bar{\psi}, U], \quad Z = \int [d\psi][d\bar{\psi}][dU] e^{-S[\psi, \bar{\psi}, U]}. \quad (7.1)$$

$S[\psi, \bar{\psi}, U]$  is the lattice action and for a LQCD simulation it looks like:

$$S = \beta S_g[U] + \sum_f \bar{\psi} D^{(m_f)} \psi, \quad (7.2)$$

where  $D^{(m)}$  is the massive Dirac operator. If one integrates out the fermion fields the effective action  $S$  can be written as<sup>1</sup>:

$$S_{\text{eff}}[D, U] \simeq \beta S_g[U] - \sum_f \ln \det D^{(m_f)} = \beta S_g[U] + S_f[D^{(m_f)}, U]. \quad (7.3)$$

For a so-called quenched simulation the determinant in (7.3) is set to a constant<sup>2</sup>.

Although we do not write the summation over the lattice sites explicitly, you can find it in both the gauge action  $S_g[U]$  and the fermion action  $S_f[D, U]$ . Since the problem size to find the exact solution of the integral in (7.1) is too large, it is known that only a very small region in the configuration space will substantially contribute. Dealing with such situations requires Monte Carlo simulations with importance sampling.

### 7.1 Monte Carlo integration

The basic theorem of simple Monte Carlo integration is:

$$\frac{1}{V} \int_V d^D x f(\vec{x}) \approx \langle f \rangle \pm \sqrt{\frac{\langle f^2 \rangle - \langle f \rangle^2}{N}}, \quad (7.4)$$

$$\langle f \rangle = \frac{1}{N} \sum_{i=1}^N f(\vec{x}_i), \quad \langle f^2 \rangle = \frac{1}{N} \sum_{i=1}^N f(\vec{x}_i)^2. \quad (7.5)$$

The  $N$  points  $\vec{x}_1, \dots, \vec{x}_N$  are chosen independently and randomly with a uniform probability distribution in a  $D$ -dimensional volume  $V$ . Eq. (7.4) is justified by the law of large numbers and the central limit theorem, i.e., in the limit  $N \rightarrow \infty$  one gets an exact solution of the integral.

---

<sup>1</sup>cf. Appendix B.1

<sup>2</sup>In the quenched approximation we neglect the fermionic part of the action or equivalently set the quark masses to infinity, i.e., this part contributes infinitely less to the action.

### 7.1.1 Importance sampling

Simple Monte Carlo integration works best for flat functions but has problems, if the integrand is sharply peaked or rapidly oscillating. Therefore in lattice simulations one applies importance sampling which greatly improves the efficiency of the Monte Carlo integration.

The idea is to find a function  $g(\vec{x}) > 0$  which satisfies

$$f(\vec{x}) = g(\vec{x})h(\vec{x}) , \quad (7.6)$$

where  $\int_V d^D x g(\vec{x}) = 1$  and  $h(\vec{x})$  is as close as possible to a constant. Then the integral in (7.4) can be evaluated by

$$\frac{1}{V} \int_V d^D x f(\vec{x}) \approx \frac{1}{N} \sum_{i=1}^N h(\vec{x}_i) , \quad (7.7)$$

where the  $\vec{x}_i$  are now chosen with probability density  $g(\vec{x})$ .

The expectation value of an operator  $A[\psi, \bar{\psi}, U]$  on the lattice is calculated as follows<sup>3</sup>:

$$\langle A \rangle = Z^{-1} \int [dU] e^{-S_{\text{eff}}[U]} A[U] . \quad (7.8)$$

This is an integral over all possible sets of link variables  $U_\mu(x)$  of the lattice:

$$[dU] \equiv \prod_{x, \alpha, \mu} dU_\mu^\alpha(x) . \quad (7.9)$$

Therefore we apply importance sampling to choose the link variables with a probability distribution of

$$P[U] = C e^{-S_{\text{eff}}[U]} \equiv w , \quad (7.10)$$

where  $C$  is introduced as a normalization factor<sup>4</sup> to get also the required probability property  $\sum_U P[U] = 1$ . We can identify the probability distribution  $w$  with the function  $g$  in equation (7.6).

Our algorithm has to choose configurations  $U_i$  with the probability  $P[U_i]$ . Then if we compute on these gauge configurations some operators  $A[U_i]$ , we get for (7.8):

$$\langle A \rangle \approx \frac{1}{N} \sum_{i=1}^N A[U_i] . \quad (7.11)$$

### 7.1.2 Markov chains

Stochastic processes:

A stochastic process is a sequence of events  $X_t$ ,  $t = 1, 2, \dots$  governed by probabilistic laws. Consider a system which can be in one of  $R$  discrete states  $s_1, s_2, \dots, s_R$  and which moves via an event  $X$  from one state to another. Then the probability to find the system in a state  $s$  after  $t$  steps is denoted by  $P(X_1, \dots, X_{t-1} | X_t)$  and may depend on the previous states of the system and possibly also on  $t$  (see [65]).

A stochastic process is called stationary if the probability remains unchanged throughout shifts in time, i.e., the probability distribution of  $(X_t, X_{t+j_1}, \dots, X_{t+j_n})$  is the same as that of  $(X_{t+h}, X_{t+h+j_1}, \dots, X_{t+h+j_n})$  for any  $h$ . For such processes the mean  $E(X_t) = \mu$  and the variance  $E((X_t - \mu)^2) = \sigma^2$  are independent of  $t$ .

<sup>3</sup>Compare this to Eq. (2.10) in the continuum. In this section we have already integrated over the fermion fields and obtain the effective action  $S_{\text{eff}}$ .

<sup>4</sup>The normalization factor  $C$  is not important in our case, because as we discuss below we are only interested in the change of the probability in our simulations, i.e., the normalization factor is the same for all probabilities  $P[U]$  and is therefore always canceled.

A Markov chain is a stochastic process which generates a sequence of states with probabilities depending only on the current state of the system (see [65]). If the current state is  $s_i$ , then the chain moves to state  $s_j$  at the next step with transition probability  $p_{ij}$ . The transition probabilities has to fulfill strong ergodicity, i.e., it must be possible with a non-vanishing probability  $p_{ij}$  to go from every state  $s_i$  to every other state  $s_j$ :

$$P[U_i \rightarrow U_j] \equiv p_{ij} > 0 \quad \text{for all } i, j = 1, \dots, R. \quad (7.12)$$

The condition (7.12) ensures that every state can be reached from any other state in the system. Furthermore, the transition probability has to be normalized

$$\sum_{\{U_j\}} P[U_i \rightarrow U_j] \equiv \sum_j p_{ij} = 1. \quad (7.13)$$

The idea is to start with a arbitrary configuration and then construct a stochastic sequence of configurations that follows an equilibrium distribution  $P[U]$ , where  $P[U]$  is the probability to find the configuration  $U$  in the system. This is done with a so-called Markov chain. Starting from an arbitrary configuration  $U_1$  we get

$$U_1 \longrightarrow U_2 \longrightarrow \dots \longrightarrow U_N. \quad (7.14)$$

If the Markov chain is supposed to follow an stationary distribution  $P[U]$ , we have to find an algorithm which has to fulfill the detailed balance condition.

#### Detailed balance:

If an algorithm satisfies detailed balance one gets the correct probability distribution:

$$w_i p_{ij} = w_j p_{ji}. \quad (7.15)$$

Note that detailed balance guarantees the fixed-point condition:

$$\sum_j w_j p_{ji} = \sum_j w_i p_{ij} = w_i. \quad (7.16)$$

This condition is sufficient (but not necessary) to generate a fixed probability distribution.

In the language of gauge configurations (7.16) means

$$\sum_{\{U_j\}} P[U_j] P[U_j \rightarrow U_i] = \sum_{\{U_j\}} P[U_i] P[U_i \rightarrow U_j] = P[U_i]. \quad (7.17)$$

### 7.1.3 The Metropolis algorithm

One simply way of implementing detailed balance is the Metropolis algorithm [66], where we select a candidate state  $s_j$  at random and then accept it with transition probability

$$p_{ij}^{\text{acc}} = \min \left( 1, \frac{w_j}{w_i} \right) \equiv \min \left( 1, \frac{P[U_j]}{P[U_i]} \right) \quad (7.18)$$

or otherwise keep the initial state  $s_i$  as the next step in the Markov chain.

It is easy to see that (7.18) satisfies the detailed balance condition:

$$w_i p_{ij}^{\text{acc}} = w_j p_{ji}^{\text{acc}} = w_i \quad \text{for } \frac{w_j}{w_i} \geq 1, \quad (7.19)$$

$$w_i p_{ij}^{\text{acc}} = w_j p_{ji}^{\text{acc}} = w_j \quad \text{for } \frac{w_j}{w_i} < 1. \quad (7.20)$$

## A Metropolis sweep

In [67] it is described that if we have two Markov steps  $P_1$  and  $P_2$  which both have the desired fixed point distribution (7.17), but are not necessarily ergodic (7.12), then the composition of the two steps  $P_2 \circ P_1$  is a Markov step that also has the desired fixed point and it may be ergodic.

This result allows to sweep through a lattice performing single site Metropolis updates. Each single site update has the desired fixed point. Therefore the entire sweep of the lattice has the desired fixed point also and furthermore it is ergodic, although it does not satisfy detailed balance in general.

## Overrelaxation

In the Metropolis algorithm a candidate configuration  $U'$  is always accepted if it does not change the action and so the probability  $P[U] = P[U']$ . The idea is to find a candidate configuration  $U'$  which has the same probability weight as the valid configuration  $U$  and thus is automatically accepted. The advantage in doing so is that we can speed up the motion through configuration space. Therefore we get a shorter autocorrelation length in the Markov chain<sup>5</sup>. However, the overrelaxation algorithm alone is not ergodic. Therefore one has to combine the overrelaxation steps with other updating algorithms, such as Metropolis steps.

## 7.2 Running a simulation

The simulation consists of several steps, which are equally important. To start a Markov chain Monte Carlo algorithm one needs an initial configuration  $U_1$ . Next one has to create a Markov chain which has to reach equilibrium first. This step is called thermalization or equilibration. Technically this is the same as to wait for the stochastic process becoming stationary. As soon as the system is in equilibrium one can use the ensuingly created configurations to compute expectation values of operators. Due to the Markov chain two consecutive configurations  $U_i$  and  $U_{i+1}$  are usually strongly correlated, which would introduce artificially small statistical errors. Therefore, one has to determine the autocorrelation first, to use only largely independent configurations.

### 7.2.1 Initializing

To start a Markov chain it is possible to use any configuration. But using just a random configuration (hot start) or all link variables set to unity (cold start) would elongate the thermalization. In our simulation runs we start always from Yang-Mills configurations. Here we start either hot or cold and create a Markov chain using only the gauge part of the configurations. This is equal to using a quenched configuration to start with.

During the simulations it becomes necessary to split up the run into several subsequent runs. However, in this stage we always start with the last configuration which was created. This does not disrupt the Markov chain as long as one does not change the run parameters. In the initializing stage of a simulation we can only run one line of a Markov chain, because we always need the previous configuration to get a new one.

### 7.2.2 Thermalization

Here we have to consider whether we did enough steps in the Markov chain, so that it becomes a stationary process. Only after this check is satisfied all subsequently generated configurations in the Markov chain are also thermalized. One way to check this would be to start with both a hot and a cold configuration, and compare the behavior of some observables. If they produce the same values within statistical errors we are in equilibrium. In dynamical simulations this would be too expensive in terms of computer time and one has to estimate the beginning of the equilibrated phase in a different way.

In general how fast the system approaches the equilibrium depends on the updating algorithm and on lattice specific parameters like the gauge coupling  $\beta$ , the size of the lattice and the type of the action used. A

<sup>5</sup>cf. Section 7.2.4

rough estimate can be obtained from some quantities, e.g., the plaquette and its autocorrelation length. If the autocorrelation length stays the same and does not change after several steps in the Markov chain, then this could indicate that the stochastic process is stationary and the system has approached the equilibrium.

In practice, thermalization is a subtle issue requiring careful treatment. Whenever possible, it is preferred to initialize a Markov chain with an already thermalized configuration from a previous run of the Markov chain. However, if one starts a simulations it is a very difficult task to find the first thermalized configuration exactly. Due to the fact that one is always constraint by available computer resources one often has to use results from previous runs with the same action and lattice size.

### 7.2.3 Production runs

One has two choices to reach equilibrium and speed up the generation of independent configurations:

1. Increasing the number of processors speeds up the creation of configuration, because on every single node the computer has to handle a smaller local volumes and therefore the memory requirements are smaller. Unfortunately, it is not always possible to go to a larger number of processors. This could have different reasons which are lying in the computer system or in the implementation of the algorithm. For instance if the speed of the algorithm does not scale with the number of processors due to the need of more communication we would need a larger amount of our limited budget.
2. One finds a sensible parallelization for the code which does not have to be the largest possible parallelization and split the run into several lines which can be executed independently. Because we have started with a thermalized configuration we are still in equilibrium. In this way if the code would not scale with the numbers of CPUs within one run we are still able to scale with the over-all budget, i.e., we obtain in the same time from each production line independent results and have therefore managed to speed up the production by a factor depending on the number of the different lines.

### 7.2.4 Autocorrelation

We have an ensemble of  $N$  (thermalized) configurations  $\{U_i\}$  which look as if they are drawn from some probability distribution  $P[U]$ , but were actually produced in sequential order by a Markov chain. The Markov process introduces serial autocorrelations [67] into the ensemble which increases the true variance of the estimate. This implies that estimates of the variance will underestimate the true variance, which can in fact be much larger. In other words, our error bars are too small if our data is correlated.

Consider the autocorrelation of some quantities  $X_i$  measured on a sequence of successive configurations  $U_i$  from a Markov chain. Without loss of generality we may assume  $\langle X \rangle = 0$ . The variance of the estimator is the sample average  $\overline{X}$  which is

$$\sigma_{\overline{X}}^2 = \frac{1}{N^2} \sum_{m,n=1}^N X_m X_n = \frac{1}{N^2} \left[ \sum_{m=1}^N X_m^2 + 2 \sum_{m=1}^{N-1} \sum_{n=m+1}^N X_m X_n \right] = \frac{\sigma_X^2}{N} \left( 1 + \frac{2}{N} \sum_{m=1}^{N-1} \sum_{n=m+1}^N \frac{X_m X_n}{X_m X_m} \right). \quad (7.21)$$

and if we introduced the autocorrelation function

$$C_X(t) = \frac{X_m X_{m+t}}{X_m X_m} \quad (7.22)$$

this becomes

$$\begin{aligned} \sigma_{\overline{X}}^2 &= \frac{\sigma_X^2}{N} \left( 1 + \frac{2}{N} \sum_{m=1}^{N-1} \sum_{n=m+1}^N C_X(n-m) \right) = \frac{\sigma_X^2}{N} \left( 1 + \frac{2}{N} \sum_{k=1}^{N-1} (N-k) C_X(k) \right), \\ &= \frac{\sigma_X^2}{N} \left( 1 + 2 \sum_{k=1}^{N-1} C_X(k) - \frac{2}{N} \sum_{k=1}^{N-1} k C_X(k) \right). \end{aligned} \quad (7.23)$$

In the case of a Markov chain,  $C_X(k)$  falls exponentially with  $k$ , and for sufficiently large  $N$  we have

$$\sigma_{\bar{X}}^2 \rightarrow \frac{\sigma_X^2}{N} (1 + 2\tau_X^{\text{int}}) , \quad (7.24)$$

where we have defined the integrated autocorrelation function

$$\tau_X^{\text{int}} = \sum_{k=1}^{\infty} C_X(k) . \quad (7.25)$$

This result tells us that on average  $1 + 2\tau_X^{\text{int}}$  correlated measurements are needed to reduce the variance of  $\bar{X}$  by the same amount as a single truly independent measurement. In practice, the Markov chain updating method has to be tuned to reduce the autocorrelation of the analyzed quantities to negligible levels. Note that  $\tau_X^{\text{int}}$  can drastically vary for different observables and thus it is a good advice to compute the integrated autocorrelation function for several different observables.

## 7.3 Improvements

After the ensembles are generated we are still not ready to start with the analysis. Here we discuss some improvements for the gauge configurations.

### 7.3.1 Pruning

The consecutive gauge configurations in a Markov chain are very strongly correlated. Using such strongly correlated configurations in the analysis would artificially decrease the statistical error. Therefore one uses the trick of pruning, whereas we first have to estimate the autocorrelation length  $\tau_A$  of some observable on these configurations. How this is done one finds in Section 7.2.4. From the autocorrelation length one derives the length of the Markov chain which feels the impact of a previous configuration. Pruning means now to skip  $n - 1$  configurations from the Markov chain and keep only every  $n$ -th for the analysis, where  $n \sim \tau_A$ . This procedure has two advantages, but also one caveat:

1. The autocorrelation length of the pruned configurations is much smaller and so are the statistical errors including the autocorrelations.
2. The amount of produced data which has to be stored is reduced to a feasible amount. Also the amount of analysis is reduced.
3. The autocorrelation time depends on the observable. Pruning too much would mean to waste configurations which are already independent from each other for a certain observable. A good strategy is to calculate the autocorrelation for those observables one is interested in and uses the obtained  $\tau_A$  as an upper limit for pruning. We discuss this also in Section 9.5.4.

### 7.3.2 Smearing of gauge configuration

In the analysis we are mainly interested in the long distance (IR) behavior of correlation functions<sup>6</sup>, but in gauge theories there are typically very strong short distance (UV) fluctuations in the gauge fields. Smearing the whole gauge configuration helps to improve the correlator signal by suppressing these short distance fluctuations.

Smearing means in this context to replace the links of a gauge configuration through averages over short paths connecting the endpoints of the link. The propagators and the correlators are then constructed on the smeared configurations. There are many different ways to do the smearing. However, if the smearing is kept local the long distance behavior is not affected in the continuum limit.

---

<sup>6</sup>cf. Section 8.2

Every CI gauge configuration is stored as the HYP smeared configuration, because of the advantages described above. For the FP configurations we also apply smearing for the FP gauge configurations, but this is more complicated, because there we use both, the APE smearing [68] and a RG inspired smearing [69], which enter in the different parametrization steps [70].

### HYP smearing

In [71] one finds the so-called HYP-smearing, which is a non-differential way of smearing. The fat links of the hypercubic blocking (HYP) are constructed in three steps. At the final level the blocked link  $V_\mu(x)$  is constructed via projected APE blocking [68] from a set of decorated links  $\tilde{V}_{\mu;\nu}(x)$  as

$$V_\mu(x) = \text{Proj}_{SU(3)} \left[ (1 - \alpha_1)U_\mu(x) + \frac{\alpha_1}{6} \sum_{\pm\nu \neq \mu} \tilde{V}_{\nu;\mu}(x) \tilde{V}_{\mu;\nu}(x + \hat{\nu}) \tilde{V}_{\nu;\mu}^\dagger(x + \hat{\mu}) \right], \quad (7.26)$$

where  $U_\mu(x)$  is the original thin link and the index  $\nu$  in  $\tilde{V}_{\mu;\nu}(x)$  indicates that the fat link at location  $i$  and direction  $\mu$  is not decorated with staples extending in direction  $\nu$ . The decorated links  $\tilde{V}_{\mu;\nu}(x)$  are constructed with a modified projected APE blocking from an other set of decorated links,  $\bar{V}_{\mu;\rho,\nu}(x)$  as

$$\tilde{V}_{\mu;\nu}(x) = \text{Proj}_{SU(3)} \left[ (1 - \alpha_2)U_\mu(x) + \frac{\alpha_2}{4} \sum_{\pm\rho \neq \nu, \mu} \bar{V}_{\rho;\nu,\mu}(x) \bar{V}_{\mu;\rho,\nu}(x + \hat{\rho}) \bar{V}_{\rho;\nu,\mu}^\dagger(x + \hat{\mu}) \right], \quad (7.27)$$

where the indices  $\rho, \nu$  indicate that the fat link  $\bar{V}_{\mu;\rho,\nu}(x)$  in direction  $\mu$  is not decorated with staples extending in the  $\rho$  or  $\nu$  directions. The decorated links  $\bar{V}_{\mu;\rho,\nu}(x)$  are constructed from the original thin links with a modified projected APE blocking step

$$\bar{V}_{\mu;\rho,\nu}(x) = \text{Proj}_{SU(3)} \left[ (1 - \alpha_3)U_\mu(x) + \frac{\alpha_3}{2} \sum_{\pm\eta \neq \rho, \nu, \mu} U_\eta(x) U_\mu(x + \hat{\eta}) U_\eta^\dagger(x + \hat{\mu}) \right]. \quad (7.28)$$

Here only the two staples orthogonal to  $\mu, \nu$  and  $\rho$  are used. With the construction in Eqs. (7.26)-(7.28) the fat link  $V_\mu(x)$  mixes thin links living only on the hypercubes attached to the original link  $U_\mu(x)$ . The parameters  $\alpha_1, \alpha_2$  and  $\alpha_3$  can be optimized to achieve the smoothest blocked link configuration. The construction in Eqs. (7.26)-(7.28) can also be iterated. Most of the positive effect, reducing the UV fluctuations, is achieved already after the first step.

### RG smearing

The basic idea of the RG smearing is to combine the effect of a minimization and a blocking step into one local transformation of the coarse gauge links. Therefore, the RG smearing consists of a minimization step from the configuration  $V$  to the configuration  $U[V]$  and a subsequent blocking step from the configuration  $U[V]$  to the configuration  $\tilde{V}[U[V]]$ .

The first step is an inverse blocking. In the inverse blocking we want to find the smoothest among the configurations that block back to the original configuration, which is in words the same as to find a solution to the RG fixed point equation (5.29):

$$S_{\text{FP}}(V) = \min_{\{U\}} (S_{\text{FP}}(U) + T(V, U)),$$

where  $T(V, U)$  is the blocking kernel. In the second step we perform a blocking transformation using the same kernel  $T$  as for the inverse blocking.

The result of the RG smearing is a configuration that has much smaller UV fluctuations than the original configuration. It however still encodes the same long-range properties as the initial configuration due to the properties of the RGT. As the HYP smearing it is a non-differential smearing and cannot be used in Hybrid Monte Carlo algorithms.

# Chapter 8

## Analysis

Generating gauge configurations is the first step in a lattice QCD simulation. The ensuing analysis is done in a completely self-contained second step using the stored gauge configurations from the first step. In the quenched approximation this is the most time-consuming part of the calculation. However, using dynamical fermions the production of independent gauge configurations is very expensive and so more and more groups justify with that also a more expensive analysis part.

Analysis means literally to break a complex problem down into smaller, independent parts. In our case this includes the calculation of the propagators and store them. Only after that we have the ingredients to obtain physical quantities from the lattice combing the information of both, gauge configurations and propagators into the correlators.

### 8.1 Propagators

A propagator gives the probability amplitude for a particle to travel from one site on the lattice to another. From the Wick theorem in Eq. (B.5) one gets:

$$\langle 0 | \psi(x) \bar{\psi}(y) | 0 \rangle_{\psi\bar{\psi}} = G(x, y) \equiv D^{-1}(x, y) . \quad (8.1)$$

On the lattice it would be far too time consuming to invert the whole Dirac operator  $D$ . Although the Dirac operator is a sparse matrix its inverse is not. So one would have to calculate and store the propagator from every source site, Dirac and color index to every sink site, Dirac and color index on the lattice. Both are technically not feasible problems which have to be solved by other methods.

#### 8.1.1 Point-to-all

Here we invert the Dirac operator on a source vector, which is located on a single site. We are using conjugate gradient (CG) methods on every Dirac and color index, which is also called dilution in Dirac and color indices:

$$\sum_{\substack{d,e \\ \beta,\gamma}} \sum_{y,z} D_{\alpha,\beta} G_{\beta,\gamma} G_{\gamma,\alpha_0} \eta_\alpha(x) = \eta_{\alpha_0}(x) = \delta^4(x - x_0) \delta_{\alpha\alpha_0} \delta_{cc_0} . \quad (8.2)$$

We get finally the propagator  $G_{c,c_0}^{\alpha,\alpha_0}(x, x_0)$  for the source at  $x_0$  and for all sink points  $x$ . As every site on the lattice, the source and the sink points have also Dirac and color indices,  $(\alpha_0, c_0)$  and  $(\alpha, c)$  respectively, which are connected via the propagator separately. Using the  $\gamma_5$ -hermiticity of the Dirac operator in (5.34) it is possible to get also the propagator starting from the sink and ending at the source:

$$G(x, x_0) = \gamma_5 G^\dagger(x_0, x) \gamma_5 . \quad (8.3)$$

In meson correlators this property is necessary to calculate closed loops of fermion lines which are needed for, e.g., non-flavor-diagonal meson correlators like they are used to do spectroscopy for  $\pi^\pm$  or  $\rho$  mesons.

The numerical costs are 12 (3 color  $\times$  4 Dirac indices) inversions per valence quark mass. These inversions are usually done via solving 12 linear equations with an iterative Krylov space solver. To improve the condition number of the inversions one can use the spectral decomposition of the Dirac operator.

### Spectral decomposition

Denote the right and left eigenvectors of the massive Dirac operator<sup>1</sup>

$$D \equiv D^{(m)} = \left(1 - \frac{1}{2}m\right)D^{(0)} + m \quad (8.4)$$

by

$$Dv_\lambda = \lambda v_\lambda, \quad w_\lambda^\dagger D = \lambda w_\lambda^\dagger; \quad (8.5)$$

From  $\gamma_5$ -hermiticity it follows that the left eigenvectors can be obtained from the right ones:

$$w_\lambda^\dagger = v_{\lambda^*}^\dagger \gamma_5, \quad \text{for complex eigenvalues,} \quad (8.6)$$

$$w_\lambda^\dagger = s_\lambda v_\lambda^\dagger \gamma_5, \quad \text{for real eigenvalues,} \quad (8.7)$$

where  $s_\lambda = \pm 1$ . The eigenvectors  $w_\lambda^\dagger$  can be chosen to fulfill the normalization condition

$$w_\lambda^\dagger v_{\lambda'} = \delta_{\lambda\lambda'}. \quad (8.8)$$

In particular, this fixes the sign factor of the modes with real eigenvalues:

$$v_\lambda^\dagger \gamma_5 v_\lambda = s_\lambda = \pm 1. \quad (8.9)$$

It is convenient to introduce the projectors

$$P_\lambda = v_\lambda w_\lambda^\dagger, \quad (8.10)$$

which due to (8.8) satisfy the projector relation  $P_\lambda^2 = P_\lambda$ . Then the Dirac operator can be written as

$$D = \sum \lambda P_\lambda. \quad (8.11)$$

Assume now that we know a few (smallest) eigenvalues and the corresponding right eigenvectors, and separate the spectral decomposition of the Dirac operator accordingly<sup>2</sup>:

$$D = \sum' \lambda P_\lambda + \sum'' \lambda P_\lambda. \quad (8.12)$$

Here we denote the sum over the eigenvectors with the smallest eigenvalues with  $\sum'$ , the so-called low-mode contribution of the Dirac operator. The sum over all the remaining eigenvectors is denoted by  $\sum''$  and called the high-mode contribution of the Dirac operator.

We introduce the projector to the high-lying modes:

$$P_h = \mathbb{1} - \sum' v_\lambda w_\lambda^\dagger = \mathbb{1} - \sum' P_\lambda, \quad (8.13)$$

If we already have the smallest eigenvalues and their corresponding eigenvectors, we can calculate instead of Eq. (8.2) the following:

$$D G_h \eta = P_h \eta, \quad (8.14)$$

where

$$G_h = \sum'' \frac{1}{\lambda} P_\lambda. \quad (8.15)$$

<sup>1</sup>For Dirac operators obeying Eq. (6.1) we have to use Eq. (D.9) here.

<sup>2</sup>We assume that the complex eigenvalues used explicitly are in complex conjugate pairs.

We then get the complete propagator via:

$$G = \sum' \frac{1}{\lambda} P_\lambda + \sum'' \frac{1}{\lambda} P_\lambda = G_l + G_h . \quad (8.16)$$

Because the propagator  $G_h$  does not contain small eigenvalues anymore the condition number for the inversion becomes smaller and the needed CG steps are drastically reduced although we get the same precision. However, instead of the larger condition number we have to add an Arnoldi algorithm which finds the lowest-lying eigenvalues and -vectors (cf. Chapter 12).

### 8.1.2 All-to-all

Calculating an all-to-all propagator on the lattice we have to use another method as that mentioned in the previous Section 8.1.1. In [72] one finds a method which uses random noise vectors and tries to minimize the errors of the Dirac propagator at least to the point where other errors, e.g., discretization errors become equally large.

The standard method of estimating the all-to-all quark propagator is by sampling the vector space stochastically. One generates an ensemble of random, independent noise vectors,  $\{\eta^{[1]}, \dots, \eta^{[N_r]}\}$ , with the property

$$\langle\langle \eta^{[r]}(x) \otimes \eta^{[r]}(y)^\dagger \rangle\rangle = \delta_{x,y} , \quad (8.17)$$

where  $\langle\langle \dots \rangle\rangle$  is the expectation value over the distribution of noise vectors. Each component of the noise vectors has modulus 1,

$$\eta_c^\alpha(x)^* \eta_c^\alpha(x) = 1 \quad (\text{no summation}) . \quad (8.18)$$

The solution vectors  $\psi^{[r]}$  are obtained in the usual way by using CG methods,

$$D\psi^{[r]}(x) = \eta^{[r]}(y) . \quad (8.19)$$

The quark propagator from any point  $x$  to any other point  $y$  is given by

$$G(x, y)_{\alpha, \alpha'} = \langle\langle \psi^{[r]} \otimes \eta^{[r]\dagger} \rangle\rangle_{\alpha, \alpha'} = \lim_{N_r \rightarrow \infty} \frac{1}{N_r} \sum_{r=1}^{N_r} \psi_c^{[r]}(x) \eta_{\alpha'}^{[r]}(y)^\dagger . \quad (8.20)$$

This method is noisy because we would need many samples to find a suitable signal. In [72] they propose to remove the random noise by diluting the noise vector in some set of variables  $i$  such that  $\eta = \sum_i \eta_i$ , resulting in an substantial reduction in the variance. Each diluted source is inverted, yielding  $N_d$  pairs of vectors,  $\{\psi_i, \eta_i\}$ :

$$D\psi_i^{[r]}(x) = \eta_i^{[r]}(y) , \quad (8.21)$$

which then gives an unbiased estimator of  $G$ ,

$$G(x, y) = \lim_{N_r \rightarrow \infty} \frac{1}{N_r} \sum_{r=1}^{N_r} \sum_{i=1}^{N_d} \psi_i^{[r]}(x) \otimes \eta_i^{[r]}(y)^\dagger . \quad (8.22)$$

The numerical costs are very high. For each valence quark mass we have to do  $N_r \times N_d$  inversions of the Dirac operator. On the other hand generating dynamical gauge configurations is even more expensive in terms of computer resources, so it makes sense to investigate the configurations more intensively than in the quenched approximation. Furthermore, it is easy to reduce the statistical noise in the propagators also in a later stage of the calculation without changing the analysis code. One only has to compute more noise vectors and therefore to increase  $N_r$ .

### Hybrid list

We also try to calculate as many of the low modes as possible exactly and correct the truncation with the noisy method described in the previous Section 8.1.2. Again we follow here mainly the ideas in reference [72].

We use the low-mode contribution  $G_l$  exactly and estimate  $G_h$  using the stochastic method:

$$G_l = \sum' \frac{1}{\lambda} v_\lambda w_\lambda^\dagger, \quad G_h = \langle\langle \psi^{[r]} \otimes \eta^{[r]\dagger} \rangle\rangle \quad (8.23)$$

with  $N_r$  noise vectors  $\{\eta^{[1]}, \dots, \eta^{[N_r]}\}$ . The solutions are given by

$$\psi^{[r]} = G_h \eta^{[r]} = D^{-1} \left( P_h \eta^{[r]} \right). \quad (8.24)$$

We now apply the idea of dilution to the stochastic estimation of  $G_h$ . Each random noise vector,  $\eta^{[r]}$ , that is generated will be diluted and orthogonalized with respect to the eigenvectors of the Dirac operator  $v_\lambda$ , so that it can be used to obtain  $\psi^{[r]}$ . In other words, we now have the following set of noise vectors:

$$\left\{ \left( \eta_1^{[1]}, \dots, \eta_1^{[N_r]} \right), \dots, \left( \eta_{N_d}^{[1]}, \dots, \eta_{N_d}^{[N_r]} \right) \right\}, \quad (8.25)$$

where the lower indices denote the dilution and the upper indices in squared brackets label the different noise samples. Note that the noise vectors are mutually orthogonal due to the dilution before an average over different random vectors are taken, i.e.:

$$\eta_i^{[r]}(x) \eta_j^{[s]\dagger}(y) = 0 \quad \text{for all } i \neq j. \quad (8.26)$$

This results in smaller variance than the standard method which mixes noise, as Eq. (8.17) shows.

The similarity in the structure of Eq. (8.16) and Eq. (8.20) suggests to construct the following hybrid list for the source and solution vectors:

$$m_i^{[r]} = \left\{ w_1, \dots, w_{N_{ev}}, P_h \eta_1^{[r]}, \dots, P_h \eta_{N_d}^{[r]} \right\}, \quad (8.27)$$

$$n_i^{[r]} = \left\{ \frac{v_1}{\lambda_1}, \dots, \frac{v_{N_{ev}}}{\lambda_{N_{ev}}}, \psi_1^{[r]}, \dots, \psi_{N_d}^{[r]} \right\}, \quad (8.28)$$

where the indices  $i$  run over  $N_{HL} = N_{ev} + N_d$  elements. The unbiased, variance reduced estimate of the all-to-all quark propagator for a single random noise vector is then given by

$$G(x, y) = \lim_{N_r \rightarrow \infty} \frac{1}{N_r} \sum_{r=1}^{N_r} \sum_{i=1}^{N_{HL}} n_i^{[r]}(x) \otimes m_i^{[r]\dagger}(y). \quad (8.29)$$

In contrast to point-to-all quark propagators we do not have to calculate the dependence of correlation functions on the propagators using the Wick theorem in Eq. (B.5). The differences in the implementation of the point-to-all and the all-to-all propagators are discussed in following Sections.

## 8.2 Correlators

This is, as the inversion of the Dirac operator, a self-contained part of the analysis. Here one makes use of both, the gauge configurations and the propagators, which were computed and stored in previous steps. The importance to study correlators at all, will be discussed in Section 9.2. Initially, we will explain what we are able to compute and give afterwards the motivation for it. I start to define a correlator:

$$C_{AB}(x_A, x_B) = \langle \mathcal{O}_A(x_A) \mathcal{O}_B^\dagger(x_B) \rangle, \quad (8.30)$$

where  $\langle \dots \rangle$  is a path integral over all gauge configurations  $U$  and quark fields  $\bar{q}, q$ .

A single correlator for a particle is constructed by the interpolator  $\mathcal{O}_A = \mathcal{O}_B$  which generates a particle state from the vacuum at  $x_B$  and annihilates it at  $x_A$  respectively. However, we discuss the general case where the  $\mathcal{O}_A$  and  $\mathcal{O}_B$  are independent interpolators<sup>3</sup>. In Section 9.2 we calculate in two successive examples the correlation functions first for non-flavor diagonal mesons and second for three-quark baryons explicitly.

<sup>3</sup>For a single correlator it would be enough to use  $\mathcal{O}_A = \mathcal{O}_B$ , but in Section 8.3.2 we need the general case, where  $\mathcal{O}_A$  and  $\mathcal{O}_B$  are different from each other.

### 8.2.1 Meson interpolators and correlators

A typical meson interpolator looks like:

$$\begin{aligned} \mathcal{O}_{(i)}^{f f'}(x) &= \sum_{\alpha, \alpha', c, c'} \delta_{cc'} \bar{q}_{\alpha}^f(x) \Gamma_{\alpha\alpha'}^{(i)} q_{\alpha'}^{f'}(x), \\ &= \bar{q}_{\alpha}^f(x) \Gamma_{\alpha\alpha'}^{(i)} q_{\alpha'}^{f'}(x) \quad (\text{using summation convention}), \end{aligned} \quad (8.31)$$

where  $\alpha, \alpha', c, c'$  and  $f, f'$  are Dirac, color and flavor indices and the  $\Gamma^{(i)}$  matrices are a representation of the Clifford algebra in Dirac space, respectively. To get an overlap with a physical state it has to have the same symmetries as the physical particle in terms of flavor, parity, charge conjugation, spin and so on. The conjugated interpolator of (8.31) reads as:

$$\begin{aligned} \left(\mathcal{O}_{(i)}^{f f'}(x)\right)^\dagger &= - \sum_{\alpha, \alpha', c, c'} \delta_{cc'} \left(q_{\alpha'}^{f'}(x)\right)^\dagger \left(\Gamma^{(i)}\right)_{\alpha'\alpha}^\dagger \left(\bar{q}_{\alpha}^f(x)\right)^\dagger, \\ &= - \sum_{\alpha, \alpha', c, c'} \delta_{cc'} \bar{q}_{\alpha'}^{f'}(x) \left(\gamma_4 \Gamma^{(i)} \gamma_4\right)_{\alpha'\alpha}^\dagger q_{\alpha}^f(x), \\ &= -s^{(i)} \sum_{\alpha, \alpha', c, c'} \delta_{cc'} \bar{q}_{\alpha'}^{f'}(x) \Gamma_{\alpha'\alpha}^{(i)} q_{\alpha}^f(x) = -s^{(i)} \mathcal{O}_{(i)}^{f' f}(x). \end{aligned} \quad (8.32)$$

The sign of the conjugated interpolator depends on (cf. Appendix A.1):

$$\left(\gamma_4 \Gamma^{(i)} \gamma_4\right)^\dagger = \gamma_4 \left(\Gamma^{(i)}\right)^\dagger \gamma_4 = s^{(i)} \Gamma^{(i)}. \quad (8.33)$$

Back to the general case, using two operators of the type in (8.31) we get for the correlator:

$$\begin{aligned} C_{AB}(x_A, x_B) &= \left\langle \mathcal{O}_{(i_A)}^{f_A f'_A}(x_A) \left(\mathcal{O}_{(i_B)}^{f_B f'_B}\right)^\dagger(x_B) \right\rangle = -s^{(i_B)} \left\langle \mathcal{O}_{(i_A)}^{f_A f'_A}(x_A) \mathcal{O}_{(i_B)}^{f'_B f_B}(x_B) \right\rangle \\ &= -s^{(i_B)} \left\langle \delta_{cc'} \bar{q}_{\alpha}^{f_A}(x_A) \Gamma_{\alpha\alpha'}^{(i_A)} q_{\alpha'}^{f'_A}(x_A) \delta_{dd'} \bar{q}_{\beta}^{f'_B}(x_B) \Gamma_{\beta\beta'}^{(i_B)} q_{\beta'}^{f_B}(x_B) \right\rangle \\ &= -s^{(i_B)} \delta_{f_A f'_A} \delta_{f_B f'_B} \Gamma_{\alpha\alpha'}^{(i_A)} \Gamma_{\beta\beta'}^{(i_B)} \left\langle q_{\alpha'}^{f'_A}(x_A) \bar{q}_{\alpha}^{f_A}(x_A) q_{\beta'}^{f'_B}(x_B) \bar{q}_{\beta}^{f_B}(x_B) \right\rangle \\ &\quad + s^{(i_B)} \delta_{f_A f'_B} \delta_{f_B f'_A} \Gamma_{\alpha\alpha'}^{(i_A)} \Gamma_{\beta\beta'}^{(i_B)} \left\langle q_{\beta'}^{f'_B}(x_B) \bar{q}_{\alpha}^{f_A}(x_A) q_{\alpha'}^{f'_A}(x_A) \bar{q}_{\beta}^{f_B}(x_B) \right\rangle. \end{aligned} \quad (8.34)$$

#### Using point-to-all propagators for mesons

We can integrate out all fermion fields from the correlation function using the Wick theorem (B.5) and perform a Fourier transformation on the sinks:

$$\hat{\mathcal{O}}_{(i_A)}^{f_A f'_A}(\vec{p}, t_A) = \sum_{\vec{x}_A} e^{-i\vec{p}\vec{x}_A} \mathcal{O}_{(i_A)}^{f_A f'_A}(\vec{x}_A, t_A). \quad (8.36)$$

We get for the projection to zero-momentum  $\vec{p} = 0$ :

$$\begin{aligned} \hat{C}_{AB}(t, x_B) &= s^{(i_B)} \Gamma_{\alpha\alpha'}^{(i_A)} \Gamma_{\beta\beta'}^{(i_B)} \times \\ &\left\{ \delta_{f_A f'_B} \delta_{f_B f'_A} \sum_{\vec{y}} \left\langle G_{\beta',\alpha}^{f_A}((\vec{x}_B, t_B), (\vec{x}_B + \vec{y}, t_B + t)) G_{\alpha',\beta}^{f_B}((\vec{x}_B + \vec{y}, t_B + t), (\vec{x}_B, t_B)) \right\rangle_U \right. \\ &\left. - \delta_{f_A f'_A} \delta_{f_B f'_B} \sum_{\vec{y}} \left\langle G_{\alpha',\alpha}^{f_A}((\vec{x}_B + \vec{y}, t_B + t), (\vec{x}_B + \vec{y}, t_B + t)) G_{\beta',\beta}^{f_B}((\vec{x}_B, t_B), (\vec{x}_B, t_B)) \right\rangle_U \right\}. \end{aligned} \quad (8.37)$$

where  $t = t_A - t_B$  and  $\langle \dots \rangle_U$  is now the path integral over all gauge configurations. Using the Wick theorem (B.5) we can do the integration over the fermion fields in an extra step. In the flavor-diagonal case we would need in the sum over  $\vec{y}$  the propagator  $G_{\alpha',\alpha}^{f_A}((\vec{x}_B + \vec{y}, t_B + t), (\vec{x}_B + \vec{y}, t_B + t))$ . If we have only point-to-all propagators we cannot calculate this, thus for this type of propagator we are restricted to flavor-non-diagonal mesons.

Omitting the flavor-diagonal case and using  $\gamma_5$ -hermiticity of the Dirac propagator (8.3) we get:

$$\begin{aligned} \hat{C}_{AB}(t, x_B) &= s^{(i_B)} \delta_{f_A f'_B} \delta_{f_B f'_A} \left( \gamma_5 \Gamma^{(i_A)} \right)_{\alpha\alpha'} \left( \Gamma^{(i_B)} \gamma_5 \right)_{\beta'\beta} \times \\ &\sum_{\vec{y}} \left\langle \left( G_{\alpha,\beta}^{f_A}((\vec{x}_B + \vec{y}, t_B + t), (\vec{x}_B, t_B)) \right)^* G_{\alpha',\beta'}^{f_B}((\vec{x}_B + \vec{y}, t_B + t), (\vec{x}_B, t_B)) \right\rangle_U, \end{aligned} \quad (8.38)$$

where  $(\dots)^*$  denotes complex conjugation. These correlation functions are even with point-to-all propagators calculable and can be used to compute all possible correlation functions using operators  $\mathcal{O}_{(i)}^{ff'}(x)$ , where  $f \neq f'$ .

### Using all-to-all propagators

To address correlation functions with flavor-diagonal meson operators or with operators which are not localized at a single lattice site one has to use all-to-all propagators. Following the construction of all-to-all propagators in Section 8.1.2 it is finally not necessary to make use of the Wick theorem (B.5) at all. All-to-all propagators eliminate this complication as both source and sink operators are constructed purely from local vectors and Eq. (8.31) changes into:

$$\left( \mathcal{O}_{jj'}^{[r,s]} \right)_{(i)}^{ff'}(x) = (\mathbf{m}_j^{[r]})^{f\dagger}(x) \Gamma^{(i)} (\mathbf{n}_{j'}^{[s]})^{f'}(x). \quad (8.39)$$

It is even possible that the  $\Gamma^{(i)}$  is space-dependent and contains gauge links  $U_\mu(x)$  or derivations which connect lattice sites  $x$  with  $y$ . The aim would be to get a larger overlap between the interpolators and the physical states. Here we have only used interpolators localized on a single site.

For a meson correlator at least two pairs of noise vectors,  $(\mathbf{m}^{[r]}, \mathbf{n}^{[r]})$  and  $(\mathbf{m}^{[s]}, \mathbf{n}^{[s]})$ , are needed to get the two independent noisy estimators in the correlation functions, which are then obtained from these interpolating operators sitting at different lattice sites [72]:

$$\begin{aligned} \hat{C}_{AB}(t, x_B) &= \sum_{\vec{y}} \left\langle \sum_{r < s} \sum_{jj'}^{N_{\text{HL}}} \left( \mathcal{O}_{jj'}^{[r,r]} \right)_{(i_A)}^{f_A f_A} (\vec{x}_B + \vec{y}, t_B + t) \left( \mathcal{O}_{j'j'}^{[s,s]} \right)_{(i_B)}^{f_B f_B} (\vec{x}_B, t_B) \right\rangle \\ &- \sum_{\vec{y}} \left\langle \sum_{r < s} \sum_{jj'}^{N_{\text{HL}}} \left( \mathcal{O}_{jj'}^{[r,s]} \right)_{(i_A)}^{f_A f_B} (\vec{x}_B + \vec{y}, t_B + t) \left( \mathcal{O}_{j'j'}^{[s,r]} \right)_{(i_B)}^{f_B f_A} (\vec{x}_B, t_B) \right\rangle. \end{aligned} \quad (8.40)$$

To increase the statistics we can also sum over  $x_B$  using the translation invariance of the lattice.

$$\hat{C}_{AB}(t) = \frac{1}{V} \sum_{x_B} \hat{C}_{AB}(t, x_B). \quad (8.41)$$

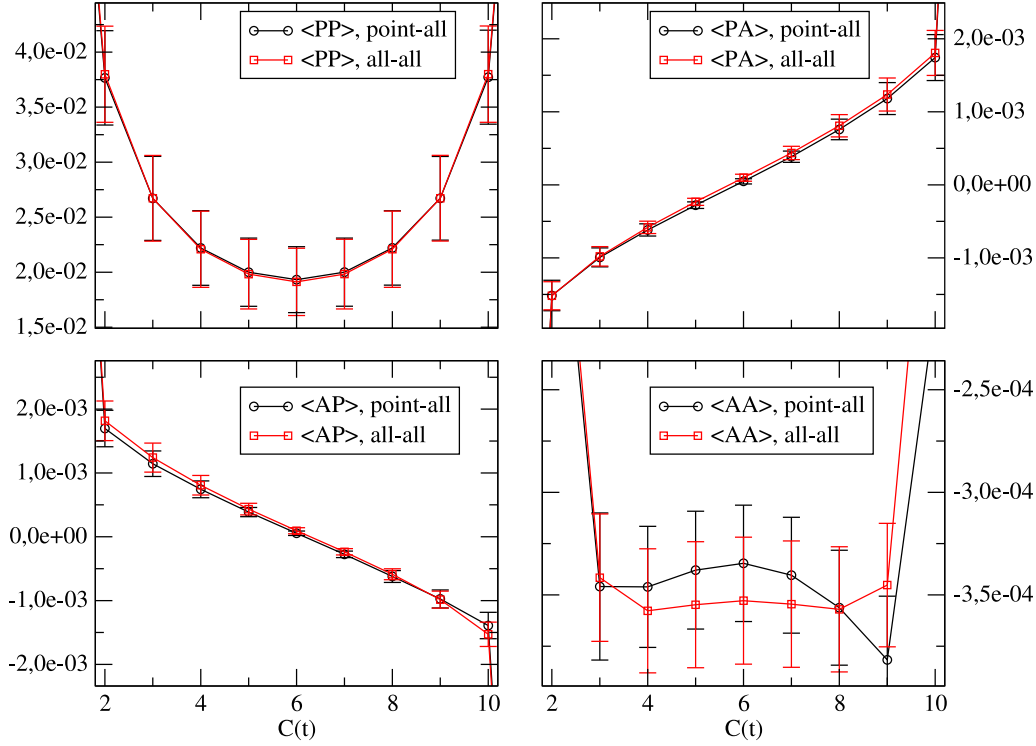


Figure 8.1: Here we show the difference between the same correlation functions obtained using all-to-all propagators with 5 noise vectors on 52 configurations and point-to-all propagators on 511 configurations. Due to the low-mode averaging in the point-to-all propagators we get quite the same signals for the  $\langle PP \rangle$  or the mixed  $\langle AP \rangle$ ,  $\langle PA \rangle$  correlators. We find that the  $\langle AA \rangle$  correlators are less fluctuating by using all-to-all propagators, although the noise stays the same compared to the noise of the correlators using point-to-all propagators with low-mode averaging.

This removes fluctuations which come primarily from the random noises in the all-to-all propagators. One can find a comparison of point-to-all and all-to-all propagators in Fig. 8.1. Furthermore, using translational invariance of the lattice as in Eq. (8.41) we only need to store the already Fourier transformed operators  $\left(\hat{\mathcal{O}}_{jj'}^{[r,s]} \right)_{(i_A)}^{f_A f_B}(t)$  and obtain the correlation functions through:

$$\hat{C}_{AB}(t) = \frac{1}{V} \sum_{t_B} \left\langle \sum_{r < s} \sum_{jj'}^{N_{HL}} \left(\hat{\mathcal{O}}_{jj}^{[r,r]} \right)_{(i_A)}^{f_A f_A}(t_B + t) \left(\hat{\mathcal{O}}_{j'j'}^{[s,s]} \right)_{(i_B)}^{f_B f_B}(t_B) - \left(\hat{\mathcal{O}}_{jj'}^{[r,s]} \right)_{(i_A)}^{f_A f_B}(t_B + t) \left(\hat{\mathcal{O}}_{j'j}^{[s,r]} \right)_{(i_B)}^{f_B f_A}(t_B) \right\rangle. \quad (8.42)$$

## 8.2.2 Baryon interpolators and correlators

For baryons we need at least a three quark operator. We start with an interpolator for a spin-1/2 baryon:

$$\left(\mathcal{O}_{(i)}^{f_1 f_2 f_3} \right)_{\alpha} (x) = \sum_{\alpha_i, c_i} \left(\Gamma_1^{(i)} \right)_{\alpha \alpha_1} \epsilon_{c_1 c_2 c_3} q_{\alpha_1}^{f_1}(x) \left[ q_{\alpha_2}^{f_2}(x) \left(\Gamma_2^{(i)} \right)_{\alpha_2 \alpha_3} q_{\alpha_3}^{f_3}(x) \right]. \quad (8.43)$$

Even in this simple operator we see that it have to be a color singlet where color indices  $c_1$ ,  $c_2$ ,  $c_3$  are antisymmetrized by  $\epsilon_{c_1 c_2 c_3}$ . In contrast to a meson interpolator the one for the baryon carries an additional spinor

index  $\alpha$  which indicates that baryons are fermions. The conjugated interpolator of (8.43) looks like:

$$\left(\mathcal{O}_{(i)}^{f_1 f_2 f_3}\right)_{\alpha}^{\dagger}(x) = s_1^{(i)} s_2^{(i)} \sum_{\alpha_i, c_i} \epsilon_{c_1 c_2 c_3} \left[ \bar{q}_{c_3}^{f_3}(x) \left(\Gamma_2^{(i)}\right)_{\alpha_3 \alpha_2} \bar{q}_{c_2}^{f_2}(x) \right] \bar{q}_{c_1}^{f_1}(x) \left(\Gamma_1^{(i)} \gamma_4\right)_{\alpha_1 \alpha}. \quad (8.44)$$

The sign of the conjugated interpolator depends only on the product of  $s_1^{(i)} s_2^{(i)}$  which are defined by<sup>4</sup>:

$$\left(\gamma_4 \Gamma_{1,2}^{(i)} \gamma_4\right)^{\dagger} = \gamma_4 \left(\Gamma_{1,2}^{(i)}\right)^{\dagger} \gamma_4 = s_{1,2}^{(i)} \Gamma_{1,2}^{(i)}. \quad (8.45)$$

### Parity

Under parity transformation  $\mathcal{P}$  (cf. Appendix A.4.1) the interpolator transforms as:

$$\begin{aligned} \left(\mathcal{O}_{(i)}^{f_1 f_2 f_3}\right)_{\alpha}^{\mathcal{P}}(x) &= \sum_{\alpha_i, c_i} \left(\Gamma_1^{(i)} \gamma_4\right)_{\alpha \alpha_1} \epsilon_{c_1 c_2 c_3} q_{c_1}^{f_1}(\mathcal{P}x) \left[ q_{c_2}^{f_2}(\mathcal{P}x) \left(\gamma_4 \Gamma_2^{(i)} \gamma_4\right)_{\alpha_2 \alpha_3} q_{c_3}^{f_3}(\mathcal{P}x) \right], \\ &= s_1^{(i)} s_2^{(i)} \sum_{\alpha_1} (\gamma_4)_{\alpha \alpha_1} \left(\mathcal{O}_{(i)}^{f_1 f_2 f_3}\right)_{\alpha_1}(\mathcal{P}x), \end{aligned} \quad (8.46)$$

where  $s_{1,2}^{(i)}$  are defined in (8.45).

After a projection to zero-momentum the change of the spatial vector  $\vec{x}$  into  $-\vec{x}$  is irrelevant because of the sum over all spatial components in the Fourier transformation. To project out a distinct positive or negative parity state we also have to multiply the interpolator with the parity projectors  $P^{\pm}$  which are defined as<sup>5</sup>

$$P^{\pm} = \frac{1}{2}(\mathbb{1} \pm \gamma_4). \quad (8.47)$$

We then consider the following parity projected interpolator:

$$\begin{aligned} \left(\hat{\mathcal{O}}_{(i)}^{f_1 f_2 f_3}\right)_{\alpha}^{\pm}(t) &= \frac{1}{2} \sum_{\vec{x}} \left( \left(\mathcal{O}_{(i)}^{f_1 f_2 f_3}\right)_{\alpha}(\vec{x}, t) \pm \left(\mathcal{O}_{(i)}^{f_1 f_2 f_3}\right)_{\alpha}^{\mathcal{P}}(\vec{x}, t) \right) \\ &= \begin{cases} \sum_{\vec{x}} \sum_{\alpha_i, c_i} \left(P^{\pm} \Gamma_1^{(i)}\right)_{\alpha \alpha_1} \epsilon_{c_1 c_2 c_3} q_{c_1}^{f_1}(\vec{x}, t) \left[ q_{c_2}^{f_2}(\vec{x}, t) \left(\Gamma_2^{(i)}\right)_{\alpha_2 \alpha_3} q_{c_3}^{f_3}(\vec{x}, t) \right] & \text{for } s_1^{(i)} s_2^{(i)} = 1 \\ \sum_{\vec{x}} \sum_{\alpha_i, c_i} \left(P^{\mp} \Gamma_1^{(i)}\right)_{\alpha \alpha_1} \epsilon_{c_1 c_2 c_3} q_{c_1}^{f_1}(\vec{x}, t) \left[ q_{c_2}^{f_2}(\vec{x}, t) \left(\Gamma_2^{(i)}\right)_{\alpha_2 \alpha_3} q_{c_3}^{f_3}(\vec{x}, t) \right] & \text{for } s_1^{(i)} s_2^{(i)} = -1. \end{cases} \end{aligned}$$

In the final result the signs are not important, thus we set them to one, i.e.,  $s_1^{(i)} s_2^{(i)} = 1$ .

### Using point-to-all propagators for baryons

Here we discuss only the point-to-all case and the interested reader is referred to one of the subsections in Section 8.2.1 where the application of all-to-all propagators in meson correlators is discussed in detail. The correlation functions for a spin-1/2 baryon consisting of three quarks reads:

$$\hat{C}_{AB}^{\pm}(t_A, x_B) = \left\langle \sum_{\alpha, \beta} \left(\hat{\mathcal{O}}_{(i_A)}^{f_1^A f_2^A f_3^A}\right)_{\alpha}^{\pm}(t_A) (\gamma_4)_{\alpha \beta} \left(\mathcal{O}_{(i_B)}^{f_1^B f_2^B f_3^B}\right)_{\beta}^{\dagger}(x_B) \right\rangle, \quad (8.48)$$

$$\begin{aligned} &= \sum_{\vec{x}_A} \sum_{\alpha_i, \beta_i} \sum_{c_i, d_i} \epsilon_{c_1 c_2 c_3} \epsilon_{d_1 d_2 d_3} \left(\Gamma_2^{(i_B)}\right)_{\beta_3 \beta_2} \left(\Gamma_1^{(i_B)} P^{\pm} \Gamma_1^{(i_A)}\right)_{\beta_1 \alpha_1} \left(\Gamma_2^{(i_A)}\right)_{\alpha_2 \alpha_3} \\ &\quad \left\langle q_{c_1}^{f_1^A}(x_A) \bar{q}_{d_1}^{f_1^B}(x_B) q_{c_2}^{f_2^A}(x_A) \bar{q}_{d_2}^{f_2^B}(x_B) q_{c_3}^{f_3^A}(x_A) \bar{q}_{d_3}^{f_3^B}(x_B) \right\rangle. \end{aligned} \quad (8.49)$$

<sup>4</sup>cf. Appendix A.1

<sup>5</sup>Note that parity is only well-defined for zero-momentum. Thus the parity projectors always have to be combined with a zero-momentum projection.

Unlike (8.30) we insert in (8.48) a  $\gamma_4$ -matrix between the two interpolating fields in order to get the parity  $P = +$  for  $\hat{C}_{AB}^+(t_A, x_B)$  and parity  $P = -$  for  $\hat{C}_{AB}^-(t_A, x_B)$ , but this is just a convention and does not change the physical content at all<sup>6</sup>. We introduce in the  $\langle \dots \rangle$  a abbreviated form of the indices via  $q_{\alpha_i}^{f_i^A}(x_A) = q_{A_i}$  and  $\bar{q}_{\beta_i}^{f_i^B}(x_B) = \bar{q}_{B_i}$  multi-indices, then:

$$\begin{aligned} \langle q_{A_1} \bar{q}_{B_1} q_{A_2} \bar{q}_{B_2} q_{A_3} \bar{q}_{B_3} \rangle &= \\ &= \delta_{f_1^A f_1^B} \left( \delta_{f_2^A f_2^B} \delta_{f_3^A f_3^B} \langle q_{A_1} \bar{q}_{B_1} q_{A_2} \bar{q}_{B_2} q_{A_3} \bar{q}_{B_3} \rangle - \delta_{f_2^A f_3^B} \delta_{f_3^A f_2^B} \langle q_{A_1} \bar{q}_{B_1} q_{A_2} \bar{q}_{B_3} q_{A_3} \bar{q}_{B_2} \rangle \right) \\ &+ \delta_{f_1^A f_2^B} \left( \delta_{f_2^A f_3^B} \delta_{f_3^A f_1^B} \langle q_{A_1} \bar{q}_{B_2} q_{A_2} \bar{q}_{B_3} q_{A_3} \bar{q}_{B_1} \rangle - \delta_{f_2^A f_1^B} \delta_{f_3^A f_3^B} \langle q_{A_1} \bar{q}_{B_2} q_{A_2} \bar{q}_{B_1} q_{A_3} \bar{q}_{B_3} \rangle \right) \\ &+ \delta_{f_1^A f_3^B} \left( \delta_{f_2^A f_1^B} \delta_{f_3^A f_2^B} \langle q_{A_1} \bar{q}_{B_3} q_{A_2} \bar{q}_{B_1} q_{A_3} \bar{q}_{B_2} \rangle - \delta_{f_2^A f_2^B} \delta_{f_3^A f_1^B} \langle q_{A_1} \bar{q}_{B_3} q_{A_2} \bar{q}_{B_2} q_{A_3} \bar{q}_{B_1} \rangle \right). \end{aligned} \quad (8.50)$$

Now we perform a Wick contraction as in (B.5), where we get a product of three point-to-all Dirac propagators:

$$\begin{aligned} \langle q_{A_1} \bar{q}_{B_1} q_{A_2} \bar{q}_{B_2} q_{A_3} \bar{q}_{B_3} \rangle &= \\ &\delta_{f_1^A f_1^B} \left( \delta_{f_2^A f_2^B} \delta_{f_3^A f_3^B} \langle G_{A_1;B_1} G_{A_2;B_2} G_{A_3;B_3} \rangle_U - \delta_{f_2^A f_3^B} \delta_{f_3^A f_2^B} \langle G_{A_1;B_1} G_{A_2;B_3} G_{A_3;B_2} \rangle_U \right) \\ &+ \delta_{f_1^A f_2^B} \left( \delta_{f_2^A f_3^B} \delta_{f_3^A f_1^B} \langle G_{A_1;B_2} G_{A_2;B_3} G_{A_3;B_1} \rangle_U - \delta_{f_2^A f_1^B} \delta_{f_3^A f_3^B} \langle G_{A_1;B_2} G_{A_2;B_1} G_{A_3;B_3} \rangle_U \right) \\ &+ \delta_{f_1^A f_3^B} \left( \delta_{f_2^A f_1^B} \delta_{f_3^A f_2^B} \langle G_{A_1;B_3} G_{A_2;B_1} G_{A_3;B_2} \rangle_U - \delta_{f_2^A f_2^B} \delta_{f_3^A f_1^B} \langle G_{A_1;B_3} G_{A_2;B_2} G_{A_3;B_1} \rangle_U \right). \end{aligned} \quad (8.51)$$

### Spin-3/2 baryons

Changing the matrices  $\Gamma_1^{(i)}$ ,  $\Gamma_2^{(i)}$  or the flavor content of the interpolator in (8.43) baryons with spin  $J = 3/2$  can also be obtained. These baryon operators have in addition to a free Dirac index  $\alpha$ , also a free Lorentz index  $\mu$  obtained either from  $\Gamma_1^{(i)}$  or from  $\Gamma_2^{(i)}$ , e.g.:

$$\left( \mathcal{O}_{(i)}^{f_1 f_2 f_3} \right)_{\alpha \mu} (x) = \sum_{\alpha_i, c_i} \left( \Gamma_1^{(i)} \right)_{\alpha \alpha_1} \epsilon_{c_1 c_2 c_3} q_{\alpha_1}^{f_1}(x) \left[ q_{c_2}^{f_2}(x) \left( \Gamma_2^{(i)} \right)_{\alpha_2 \alpha_3} q_{c_3}^{f_3}(x) \right]. \quad (8.52)$$

Usually those baryon interpolators are a mixture of both, spin-3/2 and spin-1/2 contributions. As in the parity case we need a projection to definite spin. We use the continuum formulation of a spin-3/2 projection for a Rarita-Schwinger field [73]:

$$P_{\mu\nu}^{3/2}(p) = \delta_{\mu\nu} \mathbb{1} - \frac{1}{3} \gamma_\mu \gamma_\nu - \frac{1}{3p^2} (\gamma \cdot p \gamma_\mu p_\nu + p_\mu \gamma_\nu \gamma \cdot p), \quad (8.53)$$

where  $p_\mu$  is the 4-momentum, in our case for zero-momentum given by  $p_\mu = (\vec{0}, m)$ :

$$P_{ij}^{3/2} = \delta_{ij} \mathbb{1} - \frac{1}{3} \gamma_i \gamma_j, \quad (8.54)$$

$$P_{4i}^{3/2} = P_{i4}^{3/2} = 0, \quad (8.55)$$

$$P_{44}^{3/2} = \mathbb{1} - \frac{1}{3} \mathbb{1} - \frac{2}{3} \mathbb{1} = 0. \quad (8.56)$$

The corresponding spin-1/2 state can be projected by applying the projection operator

$$P_{\mu\nu}^{1/2}(p) = \delta_{\mu\nu} \mathbb{1} - P_{\mu\nu}^{3/2}(p). \quad (8.57)$$

<sup>6</sup>One can also define the parity projector as  $P^\pm = \frac{1}{2}(\gamma_4 \pm \mathbb{1})$ , but this is very unusual, because it would mean that the proton and the neutron have negative parity.

or in our case

$$P_{ij}^{1/2} = \frac{1}{3}\gamma_i\gamma_j, \quad (8.58)$$

$$P_{4i}^{1/2} = P_{i4}^{1/2} = 0, \quad (8.59)$$

$$P_{44}^{1/2} = \mathbf{1}, \quad (8.60)$$

$$(8.61)$$

Combining the results for the spin projector with a zero-momentum Fourier transform we get the final result for an interpolating field with definite spin:

$$\left(\hat{\mathcal{O}}_{(i)}^{f_1 f_2 f_3}\right)_\alpha^{J=1/2}(t) = \sum_{\vec{x}} \sum_{\mu,\nu=1}^4 P_{\mu\nu}^{1/2} \left(\mathcal{O}_{(i)}^{f_1 f_2 f_3}\right)_\nu^\alpha(x), \quad (8.62)$$

$$\left(\hat{\mathcal{O}}_{(i)}^{f_1 f_2 f_3}\right)_\alpha^{J=3/2}(t) = \sum_{\vec{x}} \sum_{i,j=1}^3 P_{ij}^{3/2} \left(\mathcal{O}_{(i)}^{f_1 f_2 f_3}\right)_j^\alpha(x). \quad (8.63)$$

## 8.3 Improvements I

### 8.3.1 Smearing

In order to get clear and strong correlation signals, which allow a reliable analysis, we have to optimize the interpolating fields. The overlap can be improved considerably by providing more realistic spatial wave functions, which one gets, e.g., by smearing the source. There are various ways of smearing functions possible, but those we use have in common that the smeared source  $\varphi(y, z)$  (a  $12 \times 12$  matrix) is a gauge covariant expression built from a sum of paths from  $z$  to  $y$ . We have an operator  $\varphi$  which has to be hermitian:

$$\varphi(y, z)^\dagger = \varphi(z, y). \quad (8.64)$$

Note also that smearing takes place only within a timeslice:

$$\varphi(y, z) = \varphi(y, z)\delta_{y_0, z_0}. \quad (8.65)$$

The propagator with a smeared source  $\tilde{G}(y, z)$  is defined by

$$\sum_y D(x, y)\tilde{G}(y, z) = \varphi(x, z), \quad (8.66)$$

which can be expressed through the point-like propagator  $G(y, x)$  by:

$$\tilde{G}(y, z) = \sum_x G(y, x)\varphi(x, z). \quad (8.67)$$

We define

$$\tilde{v}_\lambda(z) = \sum_y \varphi(z, y)v_\lambda(y), \quad \tilde{w}_\lambda(z)^\dagger = \sum_y w_\lambda(y)^\dagger\varphi(y, z). \quad (8.68)$$

and get

$$\tilde{G} = G\varphi = \sum_\lambda \frac{1}{\lambda} v_\lambda w_\lambda^\dagger \varphi = \sum_\lambda \frac{1}{\lambda} v_\lambda \tilde{w}_\lambda^\dagger, \quad (8.69)$$

or

$$\tilde{G}(x, z) = \sum_\lambda \frac{1}{\lambda} v_\lambda(x)\tilde{w}_\lambda(z)^\dagger. \quad (8.70)$$

One can also define the propagator  $\tilde{G}$  which is smeared at both, the sink and the source:

$$\tilde{G}(x, z) = \varphi(x, y)\tilde{G}(y, z) = \sum_\lambda \frac{1}{\lambda} \tilde{v}_\lambda(x)\tilde{w}_\lambda(z)^\dagger. \quad (8.71)$$

### Jacobi smearing

A gauge covariant type of sources, which has a shape similar to a Gaussian, is obtained by Jacobi smearing [74, 75]:

$$\tilde{\eta}_c^\alpha(x) = \varphi_{cc_0}^{\alpha\alpha_0}(x, x_0)\eta_{c_0}^{\alpha_0}(x_0), \quad (8.72)$$

where

$$\eta_c^\alpha(x) = \delta_{\alpha\alpha_0}\delta_{cc_0}\delta_{xx_0} \quad (8.73)$$

and the smearing function is defined as

$$\varphi_{cc_0}^{\alpha\alpha_0}(x, x_0) = \delta_{\alpha\alpha_0} \sum_{n=0}^N \kappa^n (H^{(t_0)})_{cc_0}^n(x, x_0), \quad (8.74)$$

$$H_{c'c''}^{(t_0)}(x', x'') = \sum_{i=1}^3 \left[ U_i(x', t_0)_{c'c''} \delta_{x'+\hat{i}, x''} + U_{-i}(x', t_0)_{c'c''} \delta_{x'-\hat{i}, x''} \right]. \quad (8.75)$$

The operation connects different sites of the timeslice to the central site via gauge links. Therefore it is gauge covariant.

Jacobi smearing has two free parameters,  $N$  and  $\kappa$ , which can be used to adjust the width of the source. The width is defined by

$$\sigma^2 = \frac{\sum_{\vec{x}} |\vec{x} - \vec{x}_0|^2 \eta^\dagger(\vec{x}, t_0)\eta(\vec{x}_0, t_0)}{\eta^\dagger(\vec{x}, t_0)\eta(\vec{x}_0, t_0)}, \quad (8.76)$$

where  $|\dots|$  is taken as the minimum distance from  $\vec{x}$  to  $\vec{x}_0$  on a periodic lattice. To have a good overlap with physical states we try to extend the size of a smeared source to the size of the physical hadron tuning the two free parameters  $N$  and  $\kappa$ .

### 8.3.2 The variational method

In Part III we use the variational method [76, 77] to extract the masses of ground and excited states. Starting from a set of basis operators  $\mathcal{O}_i$ ,  $i = 1, \dots, N$ , which have the required symmetry properties, we compute the two-point correlation matrix

$$\hat{C}_{ij}(t) = \langle \hat{\mathcal{O}}_i(t) \mathcal{O}_j^\dagger(0) \rangle. \quad (8.77)$$

In Hilbert space these correlators have the decomposition<sup>7</sup>

$$\hat{C}_{ij}(t) = \sum_n \langle 0 | \hat{\mathcal{O}}_i | n \rangle \langle n | \mathcal{O}_j^\dagger | 0 \rangle e^{-tM_n}. \quad (8.78)$$

Using the factorization of the amplitudes one can show as in [77] that the eigenvalues  $\lambda^{(k)}(t)$  of the generalized eigenvalue problem

$$\hat{C}(t)\vec{v}^{(k)} = \lambda^{(k)}(t)\hat{C}(t_0)\vec{v}^{(k)}, \quad (8.79)$$

behave as

$$\lambda^{(k)}(t) = e^{-(t-t_0)M_k} [1 + \mathcal{O}(e^{-(t-t_0)\Delta M_k})], \quad (8.80)$$

where  $M_k$  is the mass of the  $k$ -th state and  $\Delta M_k$  is the difference to the masses of neighboring states. In (8.79) the eigenvalue problem is normalized with respect to a timeslice  $t_0 < t$ .

Not only the eigenvalues  $\lambda^{(k)}(t)$  are interesting, but also the eigenvectors of the generalized eigenvalue problem (8.79) contain additional information. If one plots the entries of the eigenvector as a function of  $t$ , one finds that they are essentially constant in the same range of  $t$ -values where plateaus of the effective mass (cf. Section 9.5.1) are seen. These plateaus can be used to optimize the interval for fitting the eigenvalues. Furthermore, the eigenvectors encode the information which linear combinations of the basis interpolators couple to which eigenvalue and thus provide a fingerprint of the corresponding states. Comparing these fingerprints for different values of the valence and sea quark masses is an important cross-check for the correct identification of the states.

<sup>7</sup>This is only true for the thermodynamic limit, where the lattice has a infinitely large extension in the time direction. For feasible lattices this is not true. This issue is discussed in Section 9.2 in greater detail. To understand the idea of the variational method it is sufficient to focus on (8.77) for the moment.

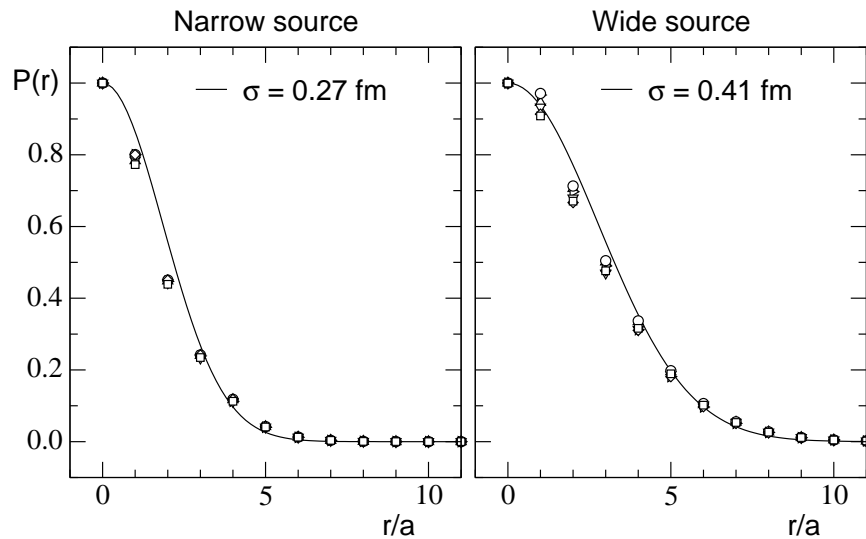


Figure 8.2: These are shapes of the narrow and wide smeared sources. Using both smearings in the variational method enlarges the basis of the interpolators with the correct quantum numbers. Furthermore it is possible that the two smearings are combined in an anti-symmetric way creating a node in the wavefunction. Such a node could be an indication for a radial excitation. The free parameters  $\kappa$  and  $N$  of the Jacobi smearing were adjusted such that the narrow source approximates a Gaussian with a half width (i.e., standard deviation) of 0.27 fm and the wide source a Gaussian with a half width of 0.41 fm.

### Narrow-wide smearing

To get a better signal we have just to extent the basis of operators used in (8.77). A simple way to enlarge the basis is the application of sources with different widths. Jacobi smearing<sup>8</sup> has two free parameters, the hopping parameter  $\kappa$  and the number of smearing steps  $N$ . They can be used to create sources and sinks with approximately Gaussian profiles of different widths. In Fig. 8.2 we show two such profiles  $P(r)$  as a function of the radius  $r$ . For mapping these profiles we use the definition

$$P(r) \propto \sum_{\vec{y}} \delta(|\vec{y}| - r) |\eta(\vec{y}, t_0)| . \quad (8.81)$$

Using narrow and wide sources as basis in the variational methods it is possible that both sources are combined anti-symmetrically. This gives us a node in the wavefunction which should have an improved overlap with radial excitations. In the search for excited baryons it is not excluded that some of the particles also possess a radial excitation of one of their valance quarks.

## 8.4 Improvements II - Low-mode averaging for meson correlators

The methods presented in this Section are also applicable for baryons, but using it in this work only for mesons we restrict ourselves to non-flavor-diagonal mesons. For flavor-diagonal mesons we would have to use all-to-all propagators anyhow.

So we want to calculate the meson correlator in (8.38) using the fact that we already have calculated some of the low-lying eigenmodes of the Dirac operator. These eigenmodes are responsible for large fluctuation in the propagators and therefore also in the correlators. Thus we split up the propagator according to Eq. (8.16) and

<sup>8</sup>We discuss Jacobi smearing in Section 8.3.1.

set  $s^{(i_B)} = 1$  in (8.38). We find that the meson correlator can be written in four parts [78, 79, 80]:

$$\begin{aligned} \hat{C}_{AB}(t, x_B) &= -\delta_{f_A f'_B} \delta_{f_B f'_A} \left( \gamma_5 \Gamma^{(i_A)} \right)_{\alpha\alpha'} \left( \Gamma^{(i_B)} \gamma_5 \right)_{\beta'\beta} \times \\ &\quad \sum_{\vec{y}} \left\langle \left( (G_l)_{\alpha,\beta}^{f_A}((\vec{x}_B + \vec{y}, t_B + t), (\vec{x}_B, t_B)) + (G_h)_{\alpha,\beta}^{f_A}((\vec{x}_B + \vec{y}, t_B + t), (\vec{x}_B, t_B)) \right)^* \right. \\ &\quad \left. \left( (G_l)_{\alpha',\beta'}^{f_B}((\vec{x}_B + \vec{y}, t_B + t), (\vec{x}_B, t_B)) + (G_h)_{\alpha',\beta'}^{f_B}((\vec{x}_B + \vec{y}, t_B + t), (\vec{x}_B, t_B)) \right) \right\rangle_U \\ &= \hat{C}_{AB}^{ll}(t, x_B) + \hat{C}_{AB}^{lh}(t, x_B) + \hat{C}_{AB}^{hl}(t, x_B) + \hat{C}_{AB}^{hh}(t, x_B). \end{aligned} \quad (8.82)$$

After we have replaced the  $G_l$  propagators as in Eq. (8.16) through their spectral decomposition these four parts individually read as:

$$\begin{aligned} \hat{C}_{AB}^{ll}(t, x_B) &= -\delta_{f_A f'_B} \delta_{f_B f'_A} \left( \Gamma^{(i_A)} \right)_{\alpha\alpha'} \left( \Gamma^{(i_B)} \right)_{\beta'\beta} \times \\ &\quad \sum_{\vec{y}} \left\langle \sum_{\lambda_A, \lambda_B} \frac{1}{\lambda_A \lambda_B} (w_{\lambda_B})_{\beta'}^{\dagger}(\vec{x}_B, t_B) (v_{\lambda_A})_{\beta}(\vec{x}_B, t_B) (w_{\lambda_A})_{\alpha}^{\dagger}(\vec{x}_B + \vec{y}, t_B + t) (v_{\lambda_B})_{\alpha'}(\vec{x}_B + \vec{y}, t_B + t) \right\rangle_U, \end{aligned} \quad (8.83)$$

$$\begin{aligned} \hat{C}_{AB}^{lh}(t, x_B) &= -\delta_{f_A f'_B} \delta_{f_B f'_A} \left( \Gamma^{(i_A)} \right)_{\alpha\alpha'} \left( \Gamma^{(i_B)} \right)_{\beta'\beta} \times \\ &\quad \sum_{\vec{y}} \left\langle \sum_{\lambda_A} \frac{1}{\lambda_A} (w_{\lambda_A})_{\alpha}^{\dagger}(\vec{x}_B + \vec{y}, t_B + t) (G_h)_{\alpha',\beta'}^{f_B}((\vec{x}_B + \vec{y}, t_B + t), (\vec{x}_B, t_B)) (v_{\lambda_A})_{\beta}(\vec{x}_B, t_B) \right\rangle_U, \end{aligned} \quad (8.84)$$

$$\begin{aligned} \hat{C}_{AB}^{hl}(t, x_B) &= -\delta_{f_A f'_B} \delta_{f_B f'_A} \left( \gamma_5 \Gamma^{(i_A)} \right)_{\alpha\alpha'} \left( \Gamma^{(i_B)} \gamma_5 \right)_{\beta'\beta} \times \\ &\quad \sum_{\vec{y}} \left\langle \sum_{\lambda_B} \frac{1}{\lambda_B} (w_{\lambda_B})_{\beta'}^{\dagger}(\vec{x}_B, t_B) (G_h^*)_{\alpha,\beta}^{f_A}((\vec{x}_B + \vec{y}, t_B + t), (\vec{x}_B, t_B)) (v_{\lambda_B})_{\alpha'}(\vec{x}_B + \vec{y}, t_B + t) \right\rangle_U, \end{aligned} \quad (8.85)$$

$$\begin{aligned} \hat{C}_{AB}^{hh}(t, x_B) &= -\delta_{f_A f'_B} \delta_{f_B f'_A} \left( \gamma_5 \Gamma^{(i_A)} \right)_{\alpha\alpha'} \left( \Gamma^{(i_B)} \gamma_5 \right)_{\beta'\beta} \times \\ &\quad \sum_{\vec{y}} \left\langle (G_h^*)_{\alpha,\beta}^{f_A}((\vec{x}_B + \vec{y}, t_B + t), (\vec{x}_B, t_B)) (G_h)_{\alpha',\beta'}^{f_B}((\vec{x}_B + \vec{y}, t_B + t), (\vec{x}_B, t_B)) \right\rangle_U. \end{aligned} \quad (8.86)$$

The correlators have the hermiticity property

$$\hat{C}_{AB}(t, x_B)^{\dagger} = \eta_1 \eta_2 \hat{C}_{BA}(t, x_B), \quad (8.87)$$

where we have introduced  $\eta_j \Gamma_j = \gamma_5 \Gamma_j^{\dagger} \gamma_5$  and have used the relation

$$v_{\lambda}(x)^{\dagger} X_j w_{\lambda}(z) = w_{\lambda^*}(x)^{\dagger} \gamma_5 X_j \gamma_5 v_{\lambda^*}(z) = \eta_j w_{\lambda^*}(x)^{\dagger} X_j v_{\lambda^*}(z). \quad (8.88)$$

Our choice of the Clifford algebra basis  $(\mathbb{1}, \gamma_{\mu}, \sigma_{\mu\nu}, \gamma_5, \gamma_{\mu} \gamma_5)$  gives  $\eta_S = \eta_P = \eta_A = 1$  and  $\eta_V = \eta_T = -1$ . One also has<sup>9</sup>

$$\hat{C}_{AB}^{hl}(t, x_B)^{\dagger} = \eta_1 \eta_2 \hat{C}_{BA}^{lh}(t, x_B). \quad (8.89)$$

<sup>9</sup>Note that for  $A \neq B$  the parts  $\hat{C}_{AB}^{lh}(t, x_B)$  and  $\hat{C}_{AB}^{hl}(t, x_B)$  are not directly related to each other.

### 8.4.1 Low-low averaging

For the low-low part of the correlation function  $\hat{C}_{AB}^{ll}(t, x_B)$  we have an all-to-all propagator in principle [78, 79, 80]. Thus we are able to use the translational invariance of our lattice to increase the statistics and at the same time to decrease the fluctuation at least in that part of the correlation function. We have to replace Eq. (8.83) by:

$$\begin{aligned} \hat{K}_{AB}^{ll}(t) &= \frac{1}{V} \sum_{x_B} \hat{C}_{AB}^{ll}(t, x_B) \\ &= -\delta_{f_A f'_B} \delta_{f_B f'_A} \left( \Gamma^{(i_A)} \right)_{\alpha\alpha'} \left( \Gamma^{(i_B)} \right)_{\beta'\beta} \frac{1}{V} \sum_{\vec{y}, \vec{x}_B, t_B} \\ &\quad \left\langle \sum_{\lambda_A, \lambda_B} \frac{1}{\lambda_A \lambda_B} (w_{\lambda_B})_{\beta'}^\dagger(\vec{x}_B, t_B) (v_{\lambda_A})_\beta(\vec{x}_B, t_B) (w_{\lambda_A})_\alpha^\dagger(\vec{x}_B + \vec{y}, t_B + t) (v_{\lambda_B})_{\alpha'}(\vec{x}_B + \vec{y}, t_B + t) \right\rangle_U, \end{aligned} \quad (8.90)$$

where  $V$  is the volume of the lattice. Now we call this low-low averaging of the correlation function in (8.82):

$$\hat{C}_{AB}(t, x_B) = \hat{K}_{AB}^{ll}(t) + \hat{C}_{AB}^{lh}(t, x_B) + \eta_1 \eta_2 \hat{C}_{BA}^{lh}(t, x_B)^\dagger + \hat{C}_{AB}^{hh}(t, x_B). \quad (8.92)$$

### 8.4.2 Low-high averaging

For the  $lh$  and  $hl$  parts one can also use the translational invariance of the lattice<sup>10</sup>:

$$\begin{aligned} \hat{K}_{AB}^{lh}(t, t_B) &= \frac{1}{V_s} \sum_{\vec{x}_B} \hat{C}_{AB}^{lh}(t, x_B), \\ &= -\delta_{f_A f'_B} \delta_{f_B f'_A} \left( \Gamma^{(i_A)} \right)_{\alpha\alpha'} \left( \Gamma^{(i_B)} \right)_{\beta'\beta} \times \\ &\quad \sum_{\vec{y}, \vec{x}_B} \left\langle \sum_{\lambda_A} \frac{1}{\lambda_A} (w_{\lambda_A})_\alpha^\dagger(\vec{x}_B + \vec{y}, t_B + t) (G_h)_{\alpha', \beta'}^{f_B}((\vec{x}_B + \vec{y}, t_B + t), (\vec{x}_B, t_B)) (v_{\lambda_A})_\beta(\vec{x}_B, t_B) \right\rangle_U, \\ &= -\delta_{f_A f'_B} \delta_{f_B f'_A} \left( \Gamma^{(i_A)} \right)_{\alpha\alpha'} \times \\ &\quad \sum_{\vec{y}} \left\langle \sum_{\lambda_A} \frac{1}{\lambda_A} (w_{\lambda_A})_\alpha^\dagger(\vec{y}, t_B + t) (\hat{G}_h^{\lambda_A})_{\alpha'}^{f_B}((\vec{y}, t_B + t), t_B; \Gamma^{(i_B)}) \right\rangle_U, \end{aligned} \quad (8.93)$$

Here  $V_s$  is the spatial volume of the lattice and

$$(\hat{G}_h^{\lambda_A})_\alpha^{f_B}((\vec{y}, t), t_B; \Gamma^{(i_B)}) = \sum_{\vec{x}_B} (G_h)_{\alpha, \beta'}^{f_B}((\vec{x}_B + \vec{y}, t), (\vec{x}_B, t_B)) \left( \Gamma^{(i_B)} \right)_{\beta'\beta} (v_{\lambda_A})_\beta(\vec{x}_B, t_B). \quad (8.94)$$

This is obtained by solving the equation

$$\sum_x D^{(m_{f_A})}(y, x) (\hat{G}_h^{\lambda_A})^{f_B}(x, t; \Gamma) = P_h^B \hat{\eta}(y, t, \lambda_A, \Gamma), \quad (8.95)$$

with the source

$$\hat{\eta}(y, t, \lambda_A, \Gamma) = \Gamma \delta_{y_0, t} v_{\lambda_A}(y). \quad (8.96)$$

In Eq.(8.95)  $P_h^B = 1 - P_l^B$  is the projector corresponding to the low modes of  $D^{(m_{f_B})}$ . For the low-high parts one needs to store  $(\hat{G}_h^{\lambda_A})^{f_B}(x, t; \Gamma)$ .

In the final correlator we can now replace the low-high contributions by the averaged ones:

$$\hat{C}_{AB}(t, x_B) = \hat{K}_{AB}^{ll}(t) + \hat{K}_{AB}^{lh}(t, t_B) + \eta_1 \eta_2 \hat{K}_{BA}^{lh}(t, t_B)^\dagger + \hat{C}_{AB}^{hh}(t, x_B). \quad (8.97)$$

<sup>10</sup>Note that one can do this also for the time directions and using also in the low-high case the 4d translational invariance of the lattice, but this would increase the already very high numerical and storage costs by another factor of  $L_4$ . However, using only the 3d translational invariance we need for every valence quark mass  $m_f$  and every  $\Gamma$  and every eigenvector  $v$  12 inversions of the subtracted Dirac operator  $P_h D$ .

### 8.4.3 Low-mode averaging in the smeared case

In a natural way one can also apply smearing techniques to the low-mode averaging. Here we will only discuss the smearing at the source, while the sinks are kept local. For smeared-smeared propagators the procedure is easy, because in that case we simply have to replace every local field or propagator by its smeared field or propagator, respectively. For the local-smeared case one has to pay attention more carefully.

In the local-smeared case we also need<sup>11</sup>

$$\gamma_5 \tilde{G}(x, y)^\dagger \gamma_5 = \sum_\lambda \frac{1}{\lambda} \tilde{v}_\lambda(y) w_\lambda(x)^\dagger \neq \tilde{G}(y, x). \quad (8.98)$$

But the correlator we want to calculate has the form

$$C(x, y) = \sum_{zz'} \text{tr} (G(x, z) \varphi(z, y) \Gamma_A \varphi(y, z') G(z', x) \Gamma_B) = \text{tr} \left( \tilde{G}(x, y) \Gamma_A \gamma_5 \tilde{G}(x, y)^\dagger \gamma_5 \Gamma_B \right). \quad (8.99)$$

This means that it is enough to know the propagator with the smeared source  $\tilde{G}(x, z)$  to obtain the correlator, again.

We get for the local-smeared, low-low part:

$$\begin{aligned} \hat{K}_{AB}^{ll}(t) &= \frac{1}{V} \sum_{x_B} \hat{C}_{AB}^{ll}(t, x_B) \\ &= -\delta_{f_A f'_B} \delta_{f_B f'_A} \left( \Gamma^{(i_A)} \right)_{\alpha\alpha'} \left( \Gamma^{(i_B)} \right)_{\beta'\beta} \frac{1}{V} \sum_{\vec{y}, \vec{x}_B, t_B} \\ &\quad \left\langle \sum_{\lambda_A, \lambda_B} \frac{1}{\lambda_A \lambda_B} (\tilde{w}_{\lambda_B})_{\beta'd}^\dagger(\vec{x}_B, t_B) (\tilde{v}_{\lambda_A})_\beta(\vec{x}_B, t_B) (w_{\lambda_A})_{\alpha c}^\dagger(\vec{x}_B + \vec{y}, t_B + t) (v_{\lambda_B})_{\alpha'c}(\vec{x}_B + \vec{y}, t_B + t) \right\rangle_U, \end{aligned} \quad (8.100)$$

and for the local-smeared, low-high part:

$$\begin{aligned} \hat{K}_{AB}^{lh}(t, t_B) &= \frac{1}{V_s} \sum_{\vec{x}_B} \hat{C}_{AB}^{lh}(t, x_B), \\ &= -\delta_{f_A f'_B} \delta_{f_B f'_A} \left( \Gamma^{(i_A)} \right)_{\alpha\alpha'} \left( \Gamma^{(i_B)} \right)_{\beta'\beta} \times \\ &\quad \sum_{\vec{y}, \vec{x}_B} \left\langle \sum_{\lambda_A} \frac{1}{\lambda_A} (w_{\lambda_A})_{\alpha c}^\dagger(\vec{x}_B + \vec{y}, t_B + t) (\tilde{G}_h)_{\alpha', \beta'}^{f_B}_{c, d}((\vec{x}_B + \vec{y}, t_B + t), (\vec{x}_B, t_B)) (\tilde{v}_{\lambda_A})_\beta(\vec{x}_B, t_B) \right\rangle_U, \\ &= -\delta_{f_A f'_B} \delta_{f_B f'_A} \left( \Gamma^{(i_A)} \right)_{\alpha\alpha'} \times \\ &\quad \sum_{\vec{y}} \left\langle \sum_{\lambda_A} \frac{1}{\lambda_A} (w_{\lambda_A})_{\alpha c}^\dagger(\vec{y}, t_B + t) (\tilde{G}_h^{\lambda_A})_{\alpha'}^{f_B}_{c}((\vec{y}, t_B + t), t_B; \Gamma^{(i_B)}) \right\rangle_U, \end{aligned} \quad (8.101)$$

where we define<sup>12</sup>:

$$(\tilde{G}_h^{\lambda_A})_{\alpha c}^{f_B}_{c'}((\vec{y}, t), t'; \Gamma) = \sum_{\vec{x}'} (G_h)_{\alpha, \beta'}^{f_B}_{\alpha', d}((\vec{x}' + \vec{y}, t), (\vec{z}', t')) \Gamma_{\beta'\beta} \varphi(z, x') (\tilde{v}_{\lambda_A})_\beta(\vec{x}', t'). \quad (8.102)$$

We can obtain  $\hat{G}$  similar to (8.95) by solving the equation

$$\sum_x D^{(m_{f_A})}(y, x) (\hat{G}_h^{\lambda_A})^{f_B}(x, t; \Gamma) = P_h^B \hat{\eta}(y, t, \lambda_A, \Gamma), \quad (8.103)$$

<sup>11</sup>Note that  $\tilde{G}$  is not  $\gamma_5$ -hermitian:  $\tilde{G}^\dagger = (G\varphi)^\dagger = \varphi G^\dagger = \gamma_5 \varphi G \gamma_5 \neq \gamma_5 (G\varphi) \gamma_5 = \gamma_5 \tilde{G} \gamma_5$ .

<sup>12</sup>We note that the smearing  $\varphi$  acts only in the spatial directions.

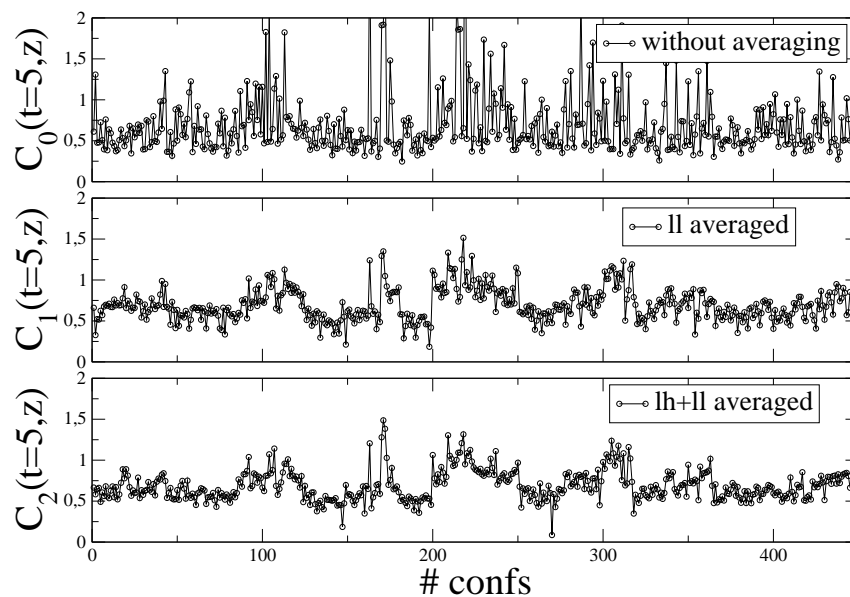


Figure 8.3: Here we compare three levels of low-mode averaging in the pseudoscalar channel. We plot the value of the pseudoscalar correlator for timeslice  $t = 5$  on  $\sim 440$  different  $8^3 \times 24$  dynamical FP gauge configurations first without any low-mode averaging, second only with low-low averaging and third with both, low-low and low-high averaging. We get a large reduction in the noise if we do low-low averaging, but only a minor improvement of the signal if we apply low-high in addition to low-low averaging.

with the source

$$\widehat{\eta}(y, t, \lambda_A, \Gamma) = \Gamma \delta_{y_0, t} \sum_{\vec{z}} \varphi(y, z) \widetilde{v}_{\lambda_A}(z). \quad (8.105)$$

The procedure is the following: the smeared eigenvector  $\widetilde{v}_{\lambda_A}(z)$  is restricted to the timeslice  $t$  of the source, smeared again on this timeslice and then multiplied by  $\Gamma$ . In the next step this vector is projected to the high modes of the basis of  $D^{(m_{f_B})}$ . Finally the Dirac operator  $D^{(m_{f_A})}$  is inverted on this source vector. This inversion has to be done on each  $\lambda_B$  and  $\Gamma$  to be used<sup>13</sup>.

#### 8.4.4 Comparison

In Fig. 8.3 we show the values of correlators on timeslice  $t = 5$  obtained on different gauge configurations. We get a very large improvement if we apply low-low averaging and a minor reduction of the noise if we also replace the local low-high contribution by the averaged one. Low-high averaging should become very useful for vector and axialvector currents, because there the low-low averaging has not the effect as for the pseudoscalar and the scalar densities<sup>14</sup>. In [81] they show to what extent the meson correlator can be approximated by using only the 200 lowest eigenmodes. These approximations of the pseudoscalar and the scalar densities are valid within a few percent, while the vector and axialvector currents cannot be approximated by using only the lowest-lying eigenmodes at all.

<sup>13</sup>The timeslice  $t$  used here does not need to coincide with the position of the source used in the  $hh$  part. In fact, it is even better to use the furthest timeslice to have a more independent estimator.

<sup>14</sup>This has still to be verified for our case. Because of limited computer resources we could not investigate the more expensive way of low-high averaging in greater detail for other channels.

## 8.5 Improvements III - Correlators using covariant operators

Covariant operators are  $\mathcal{O}(a)$  improved operators which satisfy the same relations as the operators in the continuum (cf. Section 6.1.5).

Although we can apply covariant operators for the CI fermions also, we only show it here for the FP fermions. The FP Dirac operator satisfy the original Ginsparg-Wilson equation (6.1). Therefore we have to take care for the operator  $R$  also in the covariant operators. For further details the interested reader is referred to Appendix D.

In the following we use the notation  $\langle \dots \rangle_{\text{cov}}$  for correlation functions of covariant currents (cf. (6.22)) and densities (cf. (6.21) and (6.23)), i.e.:

$$C_{AB}^{\text{cov}}(x_A, x_B) = \langle \mathcal{O}_A(x_A) \mathcal{O}_B^\dagger(x_B) \rangle_{\text{cov}} , \quad (8.106)$$

where in this case both operators  $\mathcal{O}_A$  and  $\mathcal{O}_B$  are either covariant currents or densities.

### 8.5.1 Using point-to-all propagators for covariant densities

We show now the implementation of the covariant scalar and pseudoscalar densities (cf. (D.21)) using point-to-all propagators. In the following we use:

$$M_f = \frac{1}{2\bar{m}_f} = \frac{1}{2} \frac{1}{1 - m_f/2} . \quad (8.107)$$

We have to calculate:

$$\begin{aligned} \hat{C}^{\text{cov}}(t, y) &= -M_f M_{f'} \sum_{\vec{x}} \sum_{x_2 y_1} (2R)^{-1}((\vec{x}, t), x_2) \Gamma G^{(m_f)}(x_2, y_1) (2R)^{-1}(y_1, y) \Gamma' G^{(m_{f'})}(y, (\vec{x}, t)) , \\ &- M_f M_{f'} n_{ff'} \sum_{\vec{x}} \sum_{x_2 y_2} (2R)^{-1}((\vec{x}, t), x_2) \Gamma G^{(m_f)}(x_2, y) (2R)^{-1}(y, y_2) \Gamma' G^{(m_{f'})}(y_2, (\vec{x}, t)) , \\ &- M_f M_{f'} n_{f'f} \sum_{\vec{x}} \sum_{x_1 y_1} (2R)^{-1}(x_1, (\vec{x}, t)) \Gamma G^{(m_f)}((\vec{x}, t), y_1) (2R)^{-1}(y_1, y) \Gamma' G^{(m_{f'})}(y, x_1) , \\ &- M_f M_{f'} n_{ff'} n_{f'f} \sum_{\vec{x}} \sum_{x_1 y_2} (2R)^{-1}(x_1, (\vec{x}, t)) \Gamma G^{(m_f)}((\vec{x}, t), y) (2R)^{-1}(y, y_2) \Gamma' G^{(m_{f'})}(y_2, x_1) , \end{aligned} \quad (8.108)$$

where

$$n_{ff'} = \frac{1}{2} \left( \frac{1 - m_{f'}/2}{1 - m_f/2} + \frac{1 + m_{f'}/2}{1 + m_f/2} \right) \quad \text{and} \quad \Gamma = \Gamma' = \mathbb{1} , \quad (8.109)$$

for a scalar-scalar correlator  $\hat{C}_{SS}^{\text{cov}}(t, y) = \sum_{\vec{x}} \langle S(x) S^\dagger(y) \rangle_{\text{cov}}$  and

$$n_{ff'} = \frac{1}{2} \left( \frac{1 - m_{f'}/2}{1 + m_f/2} + \frac{1 + m_{f'}/2}{1 - m_f/2} \right) \quad \text{and} \quad \Gamma = -\Gamma' = \gamma_5 , \quad (8.110)$$

for a pseudoscalar-pseudoscalar correlator  $\hat{C}_{PP}^{\text{cov}}(t, y) = \sum_{\vec{x}} \langle P(x) P^\dagger(y) \rangle_{\text{cov}}$ .

We also have to compute the sequential propagators  $H$ . While  $G^{(m)}(x, y) = (D^{(m)})^{-1}$ , the propagators  $H$  are defined as:

$$H^{(m)}(x, y) = \sum_z (D^{(m)})^{-1}(x, z) (2R)^{-1}(z, y) = \sum_z G^{(m)}(x, z) (2R)^{-1}(z, y) . \quad (8.111)$$

Note that  $H$  is not  $\gamma_5$ -hermitian:

$$\begin{aligned} \gamma_5 H^{(m)}(y, x)^\dagger \gamma_5 &= \sum_z \gamma_5 (G^{(m)}(y, z) (2R)^{-1}(z, x))^\dagger \gamma_5 \\ &= \sum_z \gamma_5 (2R)^{-1}(z, x)^\dagger (G^{(m)}(y, z))^\dagger \gamma_5 = \sum_z (2R)^{-1}(x, z) \gamma_5 (G^{(m)}(y, z))^\dagger \gamma_5 \\ &= \sum_z (2R)^{-1}(x, z) G^{(m)}(z, y) \neq \sum_z G^{(m)}(x, z) (2R)^{-1}(z, y) = H^{(m)}(x, y) . \end{aligned} \quad (8.112)$$

Using that operator  $(2R)^{-1}$  is a one in the Dirac indices we get:

$$\begin{aligned}
\hat{C}^{\text{cov}}(t, y) &= -M_f M_{f'} \sum_{\vec{x}z} \Gamma(2R)^{-1}((\vec{x}, t), z) H^{(m_f)}(z, y) \Gamma' \gamma_5 G^{(m_{f'})}((\vec{x}, t), y)^\dagger \gamma_5, \\
&- M_f M_{f'} n_{ff'} \sum_{\vec{x}z} \Gamma(2R)^{-1}((\vec{x}, t), z) G^{(m_f)}(z, y) \Gamma' \gamma_5 H^{(m_{f'})}((\vec{x}, t), y)^\dagger \gamma_5, \\
&- M_f M_{f'} n_{ff'} \sum_{xz} \delta_{tt_x} \Gamma(2R)^{-1}(z, (\vec{x}, t_x)) H^{(m_f)}((\vec{x}, t_x), y) \Gamma' \gamma_5 G^{(m_{f'})}(z, y)^\dagger \gamma_5, \\
&- M_f M_{f'} n_{ff'} n_{ff'} \sum_{xz} \delta_{tt_x} \Gamma(2R)^{-1}(z, (\vec{x}, t_x)) G^{(m_f)}((\vec{x}, t_x), y) \Gamma' \gamma_5 H^{(m_{f'})}(z, y)^\dagger \gamma_5.
\end{aligned} \tag{8.113}$$

We introduce the following terms:

$$f_G^1(t, \vec{x}) = f_G^1(x) = \Gamma' \gamma_5 G^{(m_{f'})}(x, y)^\dagger \gamma_5 \Gamma, \tag{8.114}$$

$$f_G^2(t, z) = \sum_x \delta_{tt_x} (2R)^{-1}(z, (\vec{x}, t_x)) G^{(m_f)}((\vec{x}, t_x), y), \tag{8.115}$$

$$f_G^3(t, \vec{x}) = \sum_z (2R)^{-1}((\vec{x}, t), z) G^{(m_f)}(z, y), \tag{8.116}$$

and obtain:

$$\begin{aligned}
\hat{C}^{\text{cov}}(t, y) &= -M_f M_{f'} \left[ \sum_{\vec{x}} f_H^3(t, \vec{x}) f_G^1(t, \vec{x}) + n_{ff'} \sum_{\vec{x}} f_G^3(t, \vec{x}) f_H^1(t, \vec{x}) \right. \\
&\quad \left. + n_{ff'} \sum_z f_H^2(t, z) f_G^1(z) + n_{ff'} n_{ff'} \sum_z f_G^2(t, z) f_H^1(z) \right].
\end{aligned} \tag{8.117}$$

All these steps can be avoided by using all-to-all propagators. A comparison of the methods obtained by using in the correlation functions different propagators for the same channel is given in Section 8.5.5.

### 8.5.2 Using low-mode averaging

For the low-low part we have  $G(x) = \sum_\lambda \frac{1}{\lambda} v_\lambda \otimes w_\lambda^\dagger$  and we calculate finally:

$$\begin{aligned}
\hat{C}_{ll}^{\text{cov}}(t, m_f m_{f'}) &= \frac{1}{V} \sum_{\vec{x}y} C_{ll}^{\text{cov}}(x, y), \\
&= - \sum_{\lambda\lambda'} \frac{M_f M_{f'}}{V \lambda \lambda'} \sum_{\vec{x}y x_2 y_1} w_{\lambda'}^{\dagger f'}(\vec{x}, t) (2R)^{-1}((\vec{x}, t), x_2) \Gamma v_\lambda^f(x_2) w_\lambda^{\dagger f}(y_1) (2R)^{-1}(y_1, y) \Gamma' v_{\lambda'}^{f'}(y) \\
&- \sum_{\lambda\lambda'} \frac{M_f M_{f'}}{V \lambda \lambda'} n_{ff'} \sum_{\vec{x}y x_2 y_2} w_{\lambda'}^{\dagger f'}(\vec{x}, t) (2R)^{-1}((\vec{x}, t), x_2) \Gamma v_\lambda^f(x_2) w_\lambda^{\dagger f}(y) (2R)^{-1}(y, y_2) \Gamma' v_{\lambda'}^{f'}(y_2) \\
&- \sum_{\lambda\lambda'} \frac{M_f M_{f'}}{V \lambda \lambda'} n_{ff'} \sum_{\vec{x}y x_1 y_1} w_{\lambda'}^{\dagger f'}(x_1) (2R)^{-1}(x_1, (\vec{x}, t)) \Gamma v_\lambda^f(\vec{x}, t) w_\lambda^{\dagger f}(y_1) (2R)^{-1}(y_1, y) \Gamma' v_{\lambda'}^{f'}(y) \\
&- \sum_{\lambda\lambda'} \frac{M_f M_{f'}}{V \lambda \lambda'} n_{ff'} n_{ff'} \sum_{\vec{x}y x_1 y_2} w_{\lambda'}^{\dagger f'}(x_1) (2R)^{-1}(x_1, (\vec{x}, t)) \Gamma v_\lambda^f(\vec{x}, t) w_\lambda^{\dagger f}(y) (2R)^{-1}(y, y_2) \Gamma' v_{\lambda'}^{f'}(y_2).
\end{aligned} \tag{8.119}$$

We introduce  $x = (\vec{x}, t + t_y)$ ,  $y = (\vec{y}, t_y)$  and  $t = t_x - t_y$ :

$$F_{1\lambda\lambda'}^{ff'}(t) = \delta_{tt_x} \frac{1 + n_{ff'}}{\lambda'} \sum_{\vec{x}z} w_{\lambda}^{\dagger f}(\vec{x}, t_x) (2R)^{-1}((\vec{x}, t_x), z) \Gamma' v_{\lambda'}^{f'}(z), \quad (8.120)$$

$$F_{2\lambda'\lambda}^{f'f}(t) = \delta_{tt_x} \frac{1}{\lambda} \sum_{\vec{x}z} w_{\lambda'}^{\dagger f'}(\vec{x}, t_x) (2R)^{-1}((\vec{x}, t_x), z) \Gamma v_{\lambda}^f(z), \quad (8.121)$$

$$F_{3\lambda'\lambda}^{f'f}(t) = \delta_{tt_x} \frac{n_{f'f}}{\lambda} \sum_{\vec{x}z} w_{\lambda'}^{\dagger f'}(z) (2R)^{-1}(z, (\vec{x}, t_x)) \Gamma v_{\lambda}^f(\vec{x}, t_x) \quad (8.122)$$

$$= \frac{n_{f'f}}{\lambda} \sum_{xz} \delta_{tt_x} w_{\lambda'}^{\dagger f'}(z) (2R)^{-1}(z, x) \Gamma v_{\lambda}^f(x). \quad (8.123)$$

Also:

$$\hat{C}_{ll}^{\text{cov}}(t; m_f m_{f'}) = -\frac{M_f M_{f'}}{V} \sum_{\lambda\lambda'} \sum_{t'} \left( F_{2\lambda'\lambda}^{f'f}(t+t') + F_{3\lambda'\lambda}^{f'f}(t+t') \right) F_{1\lambda\lambda'}^{ff'}(t'). \quad (8.124)$$

### 8.5.3 Using all-to-all propagators for covariant densities

As we already mentioned at the end of Section 8.1.2 from a theoretical point of view it is easier to use all-to-all propagators. Here we do not have to calculate the Wick contractions which would be a huge task on its own, before we are able to code the correlator itself. Using all-to-all propagators only demands to code the operators. For simplicity we still calculate the pseudoscalar and the scalar densities only after neglecting the contact terms (cf. Eq. (D.21)). We obtain

$$\begin{aligned} \left( P_{jj'}^{[r,s]} \right)^{ff'}(x) &= \frac{1}{1 - m_{f'}/2} \frac{1}{2} (\mathbf{m}_j^{[r]})^{f\dagger}(y) \left[ E(x)_{yz'} \frac{1}{2R_{z'z}} \right. \\ &\quad \left. + \frac{1}{2} \left( \frac{1 - m_{f'}/2}{1 + m_f/2} + \frac{1 + m_{f'}/2}{1 - m_f/2} \right) \frac{1}{2R_{yy'}} E(x)_{y'z} \right] \gamma_5 (\mathbf{n}_{j'}^{[s]})^{f'}(z), \end{aligned} \quad (8.125)$$

for the pseudoscalar case and

$$\begin{aligned} \left( S_{jj'}^{[r,s]} \right)^{ff'}(x) &= \frac{1}{1 - m_{f'}/2} \frac{1}{2} (\mathbf{m}_j^{[r]})^{f\dagger}(y) \left[ E(x)_{yz'} \frac{1}{2R_{z'z}} \right. \\ &\quad \left. + \frac{1}{2} \left( \frac{1 - m_{f'}/2}{1 - m_f/2} + \frac{1 + m_{f'}/2}{1 + m_f/2} \right) \frac{1}{2R_{yy'}} E(x)_{y'z} \right] (\mathbf{n}_{j'}^{[s]})^{f'}(z), \end{aligned} \quad (8.126)$$

for the scalar case. Using these operators we can again build and store correlation functions as they are needed in Eq. (8.42).

### 8.5.4 Using all-to-all propagators for conserved currents

We write the conserved current operators in Eq. (6.22) in a suitable form to use them in our all-to-all method in Section 8.1.2:

$$\left( (A_{\mu})_{jj'}^{[r,s]} \right)^{ff'}(x) = (\mathbf{m}_j^{[r]})^{f\dagger}(y) \left( P_R \mathcal{K}_{\mu}(x)_{yz} \hat{\mathcal{P}}_L - P_L \mathcal{K}_{\mu}(x)_{yz} \hat{\mathcal{P}}_R \right) (\mathbf{n}_{j'}^{[s]})^{f'}(z), \quad (8.127)$$

and

$$\left( (V_{\mu})_{jj'}^{[r,s]} \right)^{ff'}(x) = (\mathbf{m}_j^{[r]})^{f\dagger}(y) \left( P_R \mathcal{K}_{\mu}(x)_{yz} \hat{\mathcal{P}}_L + P_L \mathcal{K}_{\mu}(x)_{yz} \hat{\mathcal{P}}_R \right) (\mathbf{n}_{j'}^{[s]})^{f'}(z). \quad (8.128)$$

The most time consuming task is to determine the kernel  $\mathcal{K}_{\mu}(x)$  defined in (D.24). Therefore we have to discretize the gauge derivation of the Dirac operator:

$$\mathcal{K}_{\mu}(x) = -i \frac{\mathcal{D}^{(0)}(U^{(\alpha)}) - \mathcal{D}^{(0)}(U^{(-\alpha)})}{2\alpha_{\mu}(x)}, \quad (8.129)$$

where we have to build up the Dirac operator twice on the gauge configurations  $U^{(\alpha)}$  and  $U^{(-\alpha)}$ , where only one single link  $U_\mu(x)$  is replaced by:

$$U_\mu(x) \rightarrow U_\mu^{(\alpha)}(x) = e^{i\alpha_\mu(x)} U_\mu(x). \quad (8.130)$$

However, it is possible to replace all links within a timeslice at once, where we use a constant  $\alpha_\mu(t)$  for all links on a single timeslice  $t$ . Thus, we have to implement the following:

$$\left( (A_\mu)_{jj'}^{[r,s]} \right)^{ff'}(t) = \frac{1}{2} \sum_{\vec{x}} (\mathbf{m}_j^{[r]})^{f\dagger}(y) \left( \mathcal{K}_\mu(x) \hat{\Gamma}_5 - \gamma_5 \mathcal{K}_\mu(x) \right) (\mathbf{n}_{j'}^{[s]})^{f'}(z), \quad (8.131)$$

$$\begin{aligned} &= \frac{-i}{4\alpha_\mu(t)} \sum_{\vec{x}} (\mathbf{m}_j^{[r]})^{f\dagger}(y) \left\{ \left[ \mathcal{D}^{(0)}(U^{(\alpha)}) - \mathcal{D}^{(0)}(U^{(-\alpha)}) \right] \gamma_5 - \right. \\ &\quad \left. - \gamma_5 \left[ \mathcal{D}^{(0)}(U^{(\alpha)}) - \mathcal{D}^{(0)}(U^{(-\alpha)}) \right] + \right. \\ &\quad \left. - a \left[ \mathcal{D}^{(0)}(U^{(\alpha)}) - \mathcal{D}^{(0)}(U^{(-\alpha)}) \right] \gamma_5 2R(U^{(0)}) \mathcal{D}(U^{(0)}) \right\} (\mathbf{n}_{j'}^{[s]})^{f'}(z), \end{aligned} \quad (8.132)$$

and

$$\left( (V_\mu)_{jj'}^{[r,s]} \right)^{ff'}(t) = \frac{1}{2} \sum_{\vec{x}} (\mathbf{m}_j^{[r]})^{f\dagger}(y) \left( \mathcal{K}_\mu(x) - \gamma_5 \mathcal{K}_\mu(x) \hat{\Gamma}_5 \right) (\mathbf{n}_{j'}^{[s]})^{f'}(z), \quad (8.133)$$

$$\begin{aligned} &= \frac{-i}{4\alpha_\mu(t)} \sum_{\vec{x}} (\mathbf{m}_j^{[r]})^{f\dagger}(y) \left\{ \left[ \mathcal{D}^{(0)}(U^{(\alpha)}) - \mathcal{D}^{(0)}(U^{(-\alpha)}) \right] - \right. \\ &\quad \left. - \gamma_5 \left[ \mathcal{D}^{(0)}(U^{(\alpha)}) - \mathcal{D}^{(0)}(U^{(-\alpha)}) \right] \gamma_5 + \right. \\ &\quad \left. + a\gamma_5 \left[ \mathcal{D}^{(0)}(U^{(\alpha)}) - \mathcal{D}^{(0)}(U^{(-\alpha)}) \right] \gamma_5 2R(U^{(0)}) \mathcal{D}(U^{(0)}) \right\} (\mathbf{n}_{j'}^{[s]})^{f'}(z). \end{aligned} \quad (8.134)$$

Differently to the naive operators in Section 8.2, these covariant operators are very time consuming. However, using translational invariance of the lattice as in Eq. (8.41) we only need to store the already Fourier transformed operators  $\left( (A_\mu)_{jj'}^{[r,s]} \right)^{ff'}(t)$  and  $\left( (V_\mu)_{jj'}^{[r,s]} \right)^{ff'}(t)$  and obtain the correlation functions through Eq. (8.42).

### 8.5.5 Comparison

In this Section we have used various methods to calculate covariant densities or conserved currents. Correlators using those operators have a defined prefactor, i.e., in contrast to naive operators we exactly get  $Z = 1$ . In our case using only approximately chiral fermions we expect  $Z$ -factors close to 1.

For the densities we neglect contact terms, which only contributes to the short-ranged correlations. In this region the correlators are contaminated by higher excitations and do not provide useful information anyway. Due to the fact that neglecting the contact terms simplifies the calculation drastically, we can justify this systematical error. An additional complication for the FP fermions comes from the fact that the FP Dirac operator satisfies Eq. (6.1). In this case we have to handle the operator  $R$ , whereas for the CI Dirac operator, which obeys Eq. (6.4), the bare  $Z$ -factors for the naive density operators can be calculated analytically if one neglects contact terms (cf. Appendix C). The operator  $R$  increases the region where the contact terms would contribute and furthermore it is no longer possible to calculate the bare  $Z$ -factor analytically.

For the covariant point-to-all densities we need sequential propagators  $H$  (Eq. (8.111)) in addition to the propagators  $G$  (Eq. (8.1)). Therefore the difficulty in this method is to calculate the correlator in terms of  $G$  and  $H$  while it is relatively cheap to compute the correlator numerically. However, as seen in Section 8.4 low-mode averaging is unavoidable and this will again increase the computational efforts.

Although the theoretical derivation is much simpler for covariant densities using all-to-all propagators, we still neglect the contact terms to frequently save expensive matrix-vector multiplication with the operator  $R$ . Note that all-to-all propagators are using translational invariance and therefore include low-mode averaging implicitly.

For conserved currents the computational effort does not significantly change if we also include the contact terms. Due to the fact that the quark masses do not occur in the correlator, the correlators become simpler for those cases, where the correlators contain quarks with different masses.

# Chapter 9

## Data Modeling

In this Chapter we discuss several important steps of the analysis. One of the first measurements on gauge configurations is the scale setting. Due to the fact that the lattice spacing is created dynamically one has to guess the initial parameters of the simulation to get the wanted lattice spacing and is only able to verify it after the calculation is done. A second important step for non-exact Ginsparg-Wilson fermions is the determination of the additive mass renormalization, i.e., the masses in our action are shifted from the actually simulated quark masses. To extrapolate the results via chiral perturbation theory this mass shift has to be considered. The most important tools in data modeling are the correlation functions in which the physics is encoded. From them we can extract hadron masses or LECs. Finally one has to extrapolate every result from the lattice to physical points. Because of limited computer resources one has to make approximations which should be under control. Using these approximations allows us to get results which would not be feasible via brute force contrariwise. Therefore error estimation becomes also a very important to compare the results with experimental data afterwards.

### 9.1 Setting the scale

When we compute observables on the lattice they are given in lattice units  $a$ . Therefore, we have to determine the physical length of the lattice spacing  $a$ , before we can compare them to experiments or use them as non-perturbative input in perturbative calculations. This can be done via comparing observables on the lattice to hadronic masses, e.g., the vector meson  $\rho$  or the Nucleon  $N$  mass.

However, in our calculations we use the Sommer parameter  $r_0$  [82] to set the scale. This method involves the computation of the static quark/anti-quark potential  $V$  for different values of the inverse gauge coupling  $\beta$  which can be done very precisely. One defines a hadronic length-scale  $r(c)$  which depends on a dimensionless parameter  $c$  through:

$$-r^2 \frac{\partial V}{\partial r} \Big|_{r=r(c)} = c . \quad (9.1)$$

Choosing  $c = 1.65$  corresponds to  $r(1.65) = r_0 = 0.49$  fm [83, 84]. Now we have a dimension-assigned quantity  $r_0$  both in physical and in lattice units. Using this dependency connects every observable on the lattice to a physical dimension.

### 9.2 Two-point correlation functions in Hilbert space

We want to calculate the correlation function of two operators  $\mathcal{O}_A, \mathcal{O}_B$  on two different points on the lattice (cf. Eq. (8.30)):

$$C_{AB}(x_A, x_B) = \langle \mathcal{O}_A(x_A) \mathcal{O}_B(x_B) \rangle .$$

On the lattice every particle propagates in both directions of time. Let  $T \equiv aL_4$ , then it is:

$$\begin{aligned} \langle \mathcal{O}_A(\vec{x}_A, t_A) \mathcal{O}_B(\vec{x}_B, t_B) \rangle &= \lim_{T \rightarrow \infty} \mathcal{K}[\mathcal{O}_A, \mathcal{O}_B, T, t_A - t_B], \\ &= \lim_{T \rightarrow \infty} \frac{\text{tr} [\mathcal{O}_A e^{-(t_A - t_B)H} \mathcal{O}_B e^{-(T - t_A + t_B)H}]}{\text{tr} [e^{-TH}]}, \end{aligned} \quad (9.2)$$

Inserting of  $\mathbb{1} = \sum_n |n\rangle\langle n|$  between all operators, where all states  $|n\rangle$  are chosen to be eigenstates of the Hamilton operator, one gets:

$$\begin{aligned} \mathcal{K}[\mathcal{O}_A, \mathcal{O}_B, T, t] &= \frac{\sum_{i,j,k,l} \langle i | \mathcal{O}_A | j \rangle \langle j | e^{-tH} | k \rangle \langle k | \mathcal{O}_B | l \rangle \langle l | e^{-(T-t)H} | i \rangle}{\sum_i \langle i | e^{-TH} | i \rangle}, \\ &= \frac{\sum_{i,j} \langle i | \mathcal{O}_A | j \rangle \langle j | \mathcal{O}_B | i \rangle e^{-tE_j - (T-t)E_i}}{\sum_i e^{-TE_i}}, \\ &= \frac{\sum_{i,j} \langle i | \mathcal{O}_A | j \rangle \langle j | \mathcal{O}_B | i \rangle e^{-t(E_j - E_0) - (T-t)(E_i - E_0)}}{1 + e^{-T(E_1 - E_0)} + e^{-T(E_2 - E_0)} + \dots}, \end{aligned} \quad (9.3)$$

Here we factor out the ground state energy  $E_0$  due to the fact, that all energies can be defined as the energy difference to the ground state energy. Normalizing the expectation value by

$$Z^{-1} = (\text{tr} [e^{-TH}])^{-1} \quad (9.4)$$

is equally to normalize the unity operator to one, i.e.,  $\langle \mathbb{1} \rangle = 1$ .

Due to the dispersion relation

$$E(\vec{p}) = \sqrt{m^2 + \vec{p}^2},$$

the masses of the eigenstates are obtained by  $E(\vec{p} = 0) = m$ . Therefore, in spectroscopy we are mainly interested in the Fourier transform of (8.30):

$$\hat{C}_{AB}(t_A, x_B) = \sum_{\vec{y}} \langle \mathcal{O}_A(\vec{x}_B + \vec{y}, t_A) \mathcal{O}_B(\vec{x}_B, t_B) \rangle. \quad (9.5)$$

### 9.2.1 Hadron masses

To get hadron masses we have to compute the correlators and let them propagate in temporal direction. After a while one should see only the ground state in the the correlator, which can be measured via an exponential fit. We give in this Section two examples why and how we can get masses in this way.

#### Example I: flavor-non-diagonal mesons

In the special case of flavor-non-diagonal mesons and where  $\mathcal{O}_A = \mathcal{O}$  and  $\mathcal{O}_B = \mathcal{O}^\dagger$ ,  $\mathcal{K}[\mathcal{O}, \mathcal{O}^\dagger, T, t]$  can be expanded in the lowest energy states  $|a\rangle, |a'\rangle, \dots$ , which have a non-vanishing overlap with  $\mathcal{O}, \mathcal{O}^\dagger$ :

$$\begin{aligned} \mathcal{K}[\mathcal{O}, \mathcal{O}^\dagger, T, t] &= Z^{-1} \left( \langle 0 | \mathcal{O} | a \rangle \langle a | \mathcal{O}^\dagger | 0 \rangle e^{-tE_a} + \langle \bar{a} | \mathcal{O} | 0 \rangle \langle 0 | \mathcal{O}^\dagger | \bar{a} \rangle e^{-(T-t)E_a} \right) \\ &+ Z^{-1} \left( \langle 0 | \mathcal{O} | a' \rangle \langle a' | \mathcal{O}^\dagger | 0 \rangle e^{-tE_{a'}} + \langle \bar{a}' | \mathcal{O} | 0 \rangle \langle 0 | \mathcal{O}^\dagger | \bar{a}' \rangle e^{-(T-t)E_{a'}} \right) + \dots, \\ &= Z^{-1} |\langle a | \mathcal{O}^\dagger | 0 \rangle|^2 (e^{-tE_a} + e^{-(T-t)E_a}) \left( 1 + \frac{|\langle a' | \mathcal{O}^\dagger | 0 \rangle|^2 e^{-tE_{a'}} + e^{-(T-t)E_{a'}}}{|\langle a | \mathcal{O}^\dagger | 0 \rangle|^2 e^{-tE_a} + e^{-(T-t)E_a}} + \dots \right). \end{aligned} \quad (9.6)$$

Here we assume  $|\langle \bar{a} | \mathcal{O} | 0 \rangle|^2 = |\langle a | \mathcal{O}^\dagger | 0 \rangle|^2$ , which is at least valid in the case of meson spectra because of their invariance under charge conjugation  $C$ . All states  $|a\rangle, |a'\rangle, \dots$  have to be projected to the momentum eigenstates. Therefore we apply a Fourier transform which is denoted as in (8.36):

$$\hat{\mathcal{O}}(\vec{p}, t) = \sum_{\vec{y}} e^{-i\vec{p}\vec{y}} \mathcal{O}(\vec{y}, t). \quad (9.7)$$

Inserting this in (9.6) gives:

$$\hat{C}_{\vec{p}}(t, 0) = \langle \hat{\mathcal{O}}(\vec{p}, t) \mathcal{O}^\dagger(\vec{x}, 0) \rangle = \lim_{T \rightarrow \infty} \mathcal{K} [\hat{\mathcal{O}}, \mathcal{O}^\dagger, T, t] \quad (9.8)$$

$$\mathcal{K} [\hat{\mathcal{O}}, \mathcal{O}^\dagger, T, t] = \sum_{\vec{y}} e^{-i\vec{p}\vec{y}} \mathcal{K} [\mathcal{O}, \mathcal{O}^\dagger, T, t] . \quad (9.9)$$

To get the energies of the lowest state  $E_a$  from (9.9) as good as possible, one has to go to large  $T$  and at the same time one has to use operators which minimize the following ratio:

$$\frac{|\langle a' | \mathcal{O}^\dagger | 0 \rangle|^2}{|\langle a | \mathcal{O}^\dagger | 0 \rangle|^2} \quad (9.10)$$

This can be achieved by increasing the overlap of the operator  $\mathcal{O}^\dagger$  with the lowest state  $|a\rangle$  using smearing techniques or improved operators.

Thus one gets zero-momentum projected two point correlators:

$$\begin{aligned} \hat{C}_{\vec{0}}(t, (\vec{x}, 0)) \equiv \hat{C}(t, (\vec{x}, 0)) &= \langle \hat{\mathcal{O}}(\vec{0}, t) \mathcal{O}^\dagger(\vec{x}, 0) \rangle = \lim_{T \rightarrow \infty} \sum_{\vec{y}} \mathcal{K} [\mathcal{O}(y), \mathcal{O}^\dagger(x), T, t] , \\ &= A (e^{-mt} + e^{-m(T-t)}) + \dots = R(t) , \end{aligned} \quad (9.11)$$

where  $A$  and  $m$  are real constants for large  $T$ . In order to improve statistics we can symmetrize  $R(t)$  via:

$$R_S(t) = \frac{1}{2} \left[ \hat{C}(t, (\vec{x}, 0)) + \hat{C}(T-t, (\vec{x}, 0)) \right] . \quad (9.12)$$

### Example II: baryons

For baryon correlation functions we have a look at (8.48):

$$C^\pm = \langle \mathcal{O}^\pm \bar{\mathcal{O}} \rangle ,$$

where  $\bar{\mathcal{O}} \equiv \mathcal{O}^\dagger \gamma_4$  and  $\mathcal{O}^\pm = P^\pm \mathcal{O}$  the parity projected baryon operator. Due to the fact that the interpolating baryon fields are a mixture of both parity states, Eq. (9.3) changes into:

$$\begin{aligned} \mathcal{K} [\mathcal{O}^\pm, \bar{\mathcal{O}}, T, t] &= \frac{\sum_{i,j,k,l} \langle i | \mathcal{O}^\pm | j \rangle \langle j | e^{-tH} | k \rangle \langle k | \bar{\mathcal{O}} | l \rangle \langle l | e^{-(T-t)H} | i \rangle}{\sum_i \langle i | e^{-TH} | i \rangle} , \\ &= \frac{\sum_{i,j,k,l} \langle i | \mathcal{O}^\pm | j \rangle \langle j | e^{-tH} | k \rangle \langle k | \bar{\mathcal{O}}^+ + \bar{\mathcal{O}}^- | l \rangle \langle l | e^{-(T-t)H} | i \rangle}{\sum_i \langle i | e^{-TH} | i \rangle} , \\ &= \frac{\sum_{i,j} \langle i | \mathcal{O}^\pm | j \rangle \langle j | \bar{\mathcal{O}}^+ | i \rangle e^{-tE_j^+ - (T-t)E_i^+} + \sum_{k,l} \langle k | \mathcal{O}^\pm | l \rangle \langle l | \bar{\mathcal{O}}^- | k \rangle e^{-tE_l^- - (T-t)E_k^-}}{\sum_m e^{-TE_m}} . \end{aligned} \quad (9.13)$$

We expand  $\mathcal{K} [\mathcal{O}^\pm, \bar{\mathcal{O}}, T, t]$  into the lowest energy states  $|a\rangle, \dots$  and  $|b\rangle = \mathcal{P}|a\rangle, \dots$  with the opposite parity<sup>1</sup>, which have only non-vanishing overlap with  $\mathcal{O}^+$  and  $\mathcal{O}^-$ , respectively. As in the meson example we have already

<sup>1</sup>We choose  $|a\rangle$  to be a positive parity state.

factored out the ground state energy  $E_0$ . We get two cases:

$$\begin{aligned}
\mathcal{K} [\mathcal{O}^+, \bar{\mathcal{O}}, T, t] &= Z^{-1} \left( \langle 0 | \mathcal{O}^+ | a \rangle \langle a | \bar{\mathcal{O}}^+ | 0 \rangle e^{-tE_a} + \langle \bar{a} | \mathcal{O}^+ | 0 \rangle \langle 0 | \bar{\mathcal{O}}^+ | \bar{a} \rangle e^{-(T-t)E_a} \right) \\
&+ Z^{-1} \left( \langle 0 | \mathcal{O}^+ | b \rangle \langle b | \bar{\mathcal{O}}^+ | 0 \rangle e^{-tE_b} + \langle \bar{b} | \mathcal{O}^+ | 0 \rangle \langle 0 | \bar{\mathcal{O}}^+ | \bar{b} \rangle e^{-(T-t)E_b} \right) \\
&+ Z^{-1} \left( \langle 0 | \mathcal{O}^+ | a \rangle \langle a | \bar{\mathcal{O}}^- | 0 \rangle e^{-tE_a} + \langle \bar{a} | \mathcal{O}^+ | 0 \rangle \langle 0 | \bar{\mathcal{O}}^- | \bar{a} \rangle e^{-(T-t)E_a} \right) \\
&+ Z^{-1} \left( \langle 0 | \mathcal{O}^+ | b \rangle \langle b | \bar{\mathcal{O}}^- | 0 \rangle e^{-tE_b} + \langle \bar{b} | \mathcal{O}^+ | 0 \rangle \langle 0 | \bar{\mathcal{O}}^- | \bar{b} \rangle e^{-(T-t)E_b} \right) + \dots .
\end{aligned} \tag{9.14}$$

$$\begin{aligned}
\mathcal{K} [\mathcal{O}^-, \bar{\mathcal{O}}, T, t] &= Z^{-1} \left( \langle 0 | \mathcal{O}^- | a \rangle \langle a | \bar{\mathcal{O}}^+ | 0 \rangle e^{-tE_a} + \langle \bar{a} | \mathcal{O}^- | 0 \rangle \langle 0 | \bar{\mathcal{O}}^+ | \bar{a} \rangle e^{-(T-t)E_a} \right) \\
&+ Z^{-1} \left( \langle 0 | \mathcal{O}^- | b \rangle \langle b | \bar{\mathcal{O}}^+ | 0 \rangle e^{-tE_b} + \langle \bar{b} | \mathcal{O}^- | 0 \rangle \langle 0 | \bar{\mathcal{O}}^+ | \bar{b} \rangle e^{-(T-t)E_b} \right) \\
&+ Z^{-1} \left( \langle 0 | \mathcal{O}^- | a \rangle \langle a | \bar{\mathcal{O}}^- | 0 \rangle e^{-tE_a} + \langle \bar{a} | \mathcal{O}^- | 0 \rangle \langle 0 | \bar{\mathcal{O}}^- | \bar{a} \rangle e^{-(T-t)E_a} \right) \\
&+ Z^{-1} \left( \langle 0 | \mathcal{O}^- | b \rangle \langle b | \bar{\mathcal{O}}^- | 0 \rangle e^{-tE_b} + \langle \bar{b} | \mathcal{O}^- | 0 \rangle \langle 0 | \bar{\mathcal{O}}^- | \bar{b} \rangle e^{-(T-t)E_b} \right) + \dots .
\end{aligned} \tag{9.15}$$

Now we can use:

$$\begin{aligned}
\langle 0 | \mathcal{O}^- | a \rangle &= \langle 0 | \mathcal{O}^+ | b \rangle = 0 , \\
\langle a | \bar{\mathcal{O}}^- | 0 \rangle &= \langle b | \bar{\mathcal{O}}^+ | 0 \rangle = 0 ,
\end{aligned}$$

where  $\mathcal{O}^\pm$  annihilates and  $\bar{\mathcal{O}}^\mp$  creates a particle with parity  $P = \pm$ . Furthermore it is:

$$\begin{aligned}
\langle \bar{a} | \mathcal{O}^+ | 0 \rangle &= \langle \bar{b} | \mathcal{O}^- | 0 \rangle = 0 , \\
\langle 0 | \bar{\mathcal{O}}^+ | \bar{a} \rangle &= \langle 0 | \bar{\mathcal{O}}^- | \bar{b} \rangle = 0 ,
\end{aligned}$$

where  $\mathcal{O}^\pm$  creates and  $\bar{\mathcal{O}}^\mp$  annihilates an anti-particle with parity  $P = \mp$ . One can also show that:

$$\begin{aligned}
A^+ &\equiv \langle 0 | \mathcal{O}^+ | a \rangle \langle a | \bar{\mathcal{O}}^+ | 0 \rangle = \langle \bar{a} | \mathcal{O}^- | 0 \rangle \langle 0 | \bar{\mathcal{O}}^- | \bar{a} \rangle > 0 , \\
-A^- &\equiv \langle 0 | \mathcal{O}^- | b \rangle \langle b | \bar{\mathcal{O}}^- | 0 \rangle = \langle \bar{b} | \mathcal{O}^+ | 0 \rangle \langle 0 | \bar{\mathcal{O}}^+ | \bar{b} \rangle < 0 .
\end{aligned}$$

Finally we find:

$$\mathcal{K} [\mathcal{O}^+, \bar{\mathcal{O}}, T, t] = Z^{-1} \left( A^+ e^{-tE_a} - A^- e^{-(T-t)E_b} \right) + \dots , \tag{9.16}$$

$$\mathcal{K} [\mathcal{O}^-, \bar{\mathcal{O}}, T, t] = Z^{-1} \left( -A^- e^{-tE_b} + A^+ e^{-(T-t)E_a} \right) + \dots . \tag{9.17}$$

This is the result for the periodic boundary conditions in the temporal direction. But for spectroscopy one usually uses anti-periodic boundary condition to simulate the fermionic characteristics of the quarks. Boundary conditions in the temporal direction are introduced via:

$$\mathcal{K}^{(\epsilon)} [\mathcal{O}^\pm, \bar{\mathcal{O}}, T, t] = \sum_{n \in \mathbb{Z}} (-1)^{n\epsilon} \mathcal{K} [\mathcal{O}^\pm, \bar{\mathcal{O}}, T, t + nT] , \tag{9.18}$$

where  $\epsilon = 0, 1$  denotes periodic and anti-periodic boundary conditions, respectively. After neglecting all states propagating more often than once around the lattice, i.e., it is  $0 < t < T$ , we get:

$$\mathcal{K}^{(\epsilon)} [\mathcal{O}^+, \bar{\mathcal{O}}, T, t] = Z^{-1} \left( A^+ e^{-tE_a} - (-1)^\epsilon A^- e^{-(T-t)E_b} \right) + \dots , \tag{9.19}$$

$$\mathcal{K}^{(\epsilon)} [\mathcal{O}^-, \bar{\mathcal{O}}, T, t] = Z^{-1} \left( -A^- e^{-tE_b} + (-1)^\epsilon A^+ e^{-(T-t)E_a} \right) + \dots . \tag{9.20}$$

Thus one gets zero-momentum projected two point correlators like [85]:

$$\begin{aligned}
\hat{C}^\pm(t, (\vec{x}, 0)) &= \langle \hat{\mathcal{O}}^\pm(\vec{0}, t) \bar{\mathcal{O}}(\vec{x}, 0) \rangle = \lim_{T \rightarrow \infty} \mathcal{K}^{(\epsilon)} [\hat{\mathcal{O}}^\pm, \bar{\mathcal{O}}, T, t] , \\
&= \pm A^\pm \exp[-m^\pm t] \mp (-1)^\epsilon A^\mp \exp[-m^\mp(T-t)] + \dots = R^\pm(t) ,
\end{aligned} \tag{9.21}$$

where  $A^\pm$  and  $m^\pm$  are real constants for large  $T$ . In order to improve statistics we can use:

$$R_S^\pm(t) = \frac{1}{2} \left[ \hat{C}^\pm(t, (\vec{x}, 0)) + (-1)^\epsilon \hat{C}^\mp(T-t, (\vec{x}, 0)) \right]. \quad (9.22)$$

Using both periodic and anti-periodic boundary conditions in the time direction would allow combinations of correlators which would only depend on one parity state. Therefore one can use a larger interval in the temporal direction to find longer effective mass plateaus, if one has a good overlap with the ground state. However, for small lattices the extend in the time direction would also be too small to satisfy still the thermodynamic limit  $T \rightarrow \infty$  using periodic boundary conditions, i.e., the simulated temperature would give non-negligible effects. For anti-periodic boundary conditions, which are the usually ones in spectroscopy due to the fermionic nature of the quarks, these effects are more suppressed.

### 9.2.2 AWI mass

If we consider a non-singlet axial transformation as in (C.10) for the expectation value of a local operator  $\mathcal{O}(y)$  on the lattice (cf. Eq. (7.1)) we get<sup>2</sup>:

$$\left\langle i \frac{\delta_A^{1,2} \mathcal{O}(y)}{\delta \epsilon(x)} \right\rangle - \langle \mathcal{O}(y) \partial_\mu^* A_\mu^{1,2}(x) \rangle + 2m \langle \mathcal{O}(y) P^{1,2}(x) \rangle = 0, \quad (9.23)$$

where the first term only gives a contribution for  $y$  close to  $x$  and the other terms come in via the axial transformation of the action as shown in (C.54).

In the calculation we also choose an arbitrary operator  $\mathcal{O}$  which has adequate overlap with both,  $A_\mu^{1,2}(x)$  and  $P^{1,2}(x)$ , and compute the ratio:

$$m^{\text{AWI}} = m = \frac{\langle \mathcal{O}(y) \partial_\mu^* A_\mu^{1,2}(x) \rangle}{2 \langle \mathcal{O}(y) P^{1,2}(x) \rangle}, \quad (9.24)$$

where  $x$  has to be sufficiently far away from  $y$ .

In this way the AWI mass  $m_{\text{AWI}} = m^{\text{bare}}$  is the bare mass which occurs in the Lagrangian for  $u$  and  $d$  quark mass ( $m = m_u = m_d$ ), respectively. For GW-like fermions and using covariant densities and currents the AWI mass and  $m$  are exactly the same.

### Additive mass renormalization

We want to do QCD simulations with only approximate GW-like fermions. Due to this approximation we have a non-zero additive mass renormalization like in the Wilson case [48]. In this section we only discuss the case  $a = 1, 2$ .

Bochicchio et al. found for Wilson fermions a slightly different operator identity as in (C.56):

$$\partial_\mu^* A_\mu^a(x) = 2mP^a(x) + X^a(x), \quad (9.25)$$

where  $X^a(x)$  contains all chiral symmetry breaking terms of the Wilson Dirac operator. One finds that in the continuum limit only  $\dim = 3$  or  $\dim = 4$  operators contribute. With an analysis of the allowed quantum numbers we can write:

$$X^a(x) = \overline{X}^a(x) - 2m_0 P^a(x) - (Z_A - 1) \partial_\mu^* A_\mu^a(x), \quad (9.26)$$

where in  $\overline{X}^1(x)$  all operators of higher dimension are included whose contributions vanish in the continuum limit  $a \rightarrow 0$ . The prefactors  $m_0$  and  $Z_A$  are at first not known. Later, we can identify them with a mass shift  $m_0$  or renormalization constant  $Z_A$  for the axialvector current. Using GW fermions, conserved currents and covariant densities all terms in (9.26) vanish:

$$m_0 = 0, \quad Z_A = 1 \quad \text{and} \quad \overline{X}^a(x) = 0.$$

---

<sup>2</sup>For the flavor singlet axial transformation we would get an additional contribution of the measure due to the fact that the measure is not invariant under this transformation (axial anomaly, cf. Section 2.5.2).

We have to modify this statement if one only applies naive currents and densities together with GW fermions:

$$m_0 = 0, \quad Z_P \neq Z_A \neq 1 \quad \text{and} \quad \overline{X}^a(x) = 0. \quad (9.27)$$

However, using approximately chiral fermions we also get a different AWI mass  $m^{\text{AWI}}$ :

$$Z_A \partial_\mu^* A_\mu^a(x) = 2(m - m_0)P^a(x) + \overline{X}^a(x), \quad (9.28)$$

which gives instead of (9.24):

$$\frac{1}{Z_P}(m - m_0) = \frac{Z_{\mathcal{O}} Z_A \langle \mathcal{O}(y) \partial_\mu^* A_\mu^a(x) \rangle}{2Z_{\mathcal{O}} Z_P \langle \mathcal{O}(y) P^a(x) \rangle} - \frac{Z_{\mathcal{O}} \langle \mathcal{O}(y) \overline{X}^a(x) \rangle}{2Z_{\mathcal{O}} Z_P \langle \mathcal{O}(y) P^a(x) \rangle} \xrightarrow{a \rightarrow 0} \frac{Z_A \langle \mathcal{O}(y) \partial_\mu^* A_\mu^a(x) \rangle}{2Z_P \langle \mathcal{O}(y) P^a(x) \rangle} = \frac{Z_A}{Z_P} m^{\text{AWI}}, \quad (9.29)$$

where the operator  $\overline{X}^a(x)$  is a higher dimensional operator and vanishes therefore in the continuum limit.

The AWI mass  $m^{\text{AWI}}$  has by definition no additive mass renormalization. So if we compare the AWI mass  $m^{\text{AWI}}$  with  $m$  used in the simulation we get for the slope of the chiral extrapolation [86]:

$$Z = \frac{m^{\text{AWI}}}{m - m_0} = \frac{1}{Z_A}, \quad (9.30)$$

and can determine the additive mass renormalization  $m_0$  by writing  $m^{\text{AWI}}$  as a function of  $m$ :

$$m^{\text{AWI}}(m) = Z_A^{-1}(m - m_0) \quad \text{with} \quad m^{\text{AWI}}(m_0) = 0. \quad (9.31)$$

All these steps can also be done for the CI and FP fermions which are only approximately chiral invariant fermions. With these fermions we also get a mass shift  $m_0$  which is very small compared to Wilson fermions<sup>3</sup>, but not negligible. We need to know the additive mass renormalization for the CI and the FP fermions, e.g., to interpret the hadron spectrum correctly or to estimate how large the quark masses have to be in our simulation not getting exceptional configurations in a subsequent run.

### 9.3 LECs from "unphysical" regimes

In Section 3.3 we have already discussed finite volume effects. To obtain masses or matrix elements we need a sufficiently large box size in order to keep the systematical errors coming from the finite size as small as possible. The situation is quite different for LECs. Although we can determine LECs also on lattices with a large physical volume there exists also another approach. In the  $\epsilon$ - or  $\delta$ -regime one utilizes the fact that in those regimes NLO predictions are less contaminated by higher order effects and so the LECs can be determined by fitting less parameters in principle.

However, using a small finite box does not mean that those calculations in the  $\epsilon$ - or  $\delta$ -regime are, e.g., cheaper in terms of the computer time. Contrariwise, one faces additional problems which can be neglected in spectroscopy at all. Lattice simulations both in the  $\epsilon$ - and the  $\delta$ -regime require very small quark masses. Due to the fact that the spectrum of a Ginsparg-Wilson Dirac operator is bounded from below and that this ensures stability of the dynamical simulations it is highly desirable to preserve chiral symmetry at finite lattices. In addition to small quark masses there is also another reason that makes those regimes particularly challenging. In the region, where  $m\Sigma V \sim O(1)$ , one expects large fluctuations of the low-lying modes, which can induce large uncertainties on the observables. These can be, however, substantially reduced by adopting the low-mode averaging technique in Section 8.4.

For a brief introduction on the determination of LECs from lattice simulations in general the interested reader is referred to [87] and the references therein.

<sup>3</sup>Due to the fact that the CI or FP fermions have good chiral properties, but not exact chirality, the size of the mass shift of the CI or FP fermions is small. While for the Wilson fermions the operator  $X$  can be written explicitly, this is very difficult for the CI and the FP fermions. Nevertheless both,  $X_{\text{CI}}$  and  $X_{\text{FP}}$ , also mix with the pseudoscalar density and the derivative of the axialvector, because of quantum number considerations, plus with operators of higher dimensions.

### 9.3.1 Meson correlators in the $\epsilon$ -regime - The bare $\Sigma$

The bare quark condensate  $\Sigma$  can be extracted by matching density correlators in the  $\epsilon$ -regime with the NLO predictions. In [32] Hasenfratz and Leutwyler show the corresponding relations for the  $O(4)$  spin model which can be matched to the massless  $SU(2)_F$  theory. For the pseudoscalar-pseudoscalar correlators we derive:

$$\frac{T}{2V} \hat{C}_{PP}^{\text{cov}}(t) = a_I + b_I h_1\left(\frac{t}{T}\right) + c_I h_2\left(\frac{t}{T}\right) + d_I h_3\left(\frac{t}{T}\right) + e_I \left( \delta\left(\frac{t}{T}\right) - 1 \right), \quad (9.32)$$

where the kinematic functions are defined by

$$h_1(\tau) = \frac{1}{2} \left[ \left( \tau - \frac{1}{2} \right)^2 - \frac{1}{12} \right], \quad (9.33)$$

$$h_2(\tau) = \frac{1}{24} \left[ \tau^2 (1 - \tau)^2 - \frac{1}{30} \right], \quad (9.34)$$

$$h_3(\tau) = h_1^2(\tau) + \sum'_n \left\{ \frac{\cosh q_n(\tau - 1/2)}{2q_n \sinh q_n/2} \right\}^2, \quad (9.35)$$

and  $q_n$  stands for

$$q_n = 2\pi T \left[ \sum_{\mu=1}^3 \left( \frac{n_\mu}{L_\mu} \right) \right]^{\frac{1}{2}}. \quad (9.36)$$

The sum in Eq. (9.35) runs over all integers  $n = (n_1, n_2, n_3)$  on the lattice except for  $(0, 0, 0)$  denoted by the prime. Here we compare a  $O(4)$  spin model with the  $SU(2)$  flavor theory, where the magnetization in the first model corresponds to the quark mass in the latter.

In the  $O(4)$  spin model with magnetization or equally in the massive  $SU(2)$  flavor theory the constants  $a_I, \dots, e_I$  in Eq. (9.32) are given through<sup>4</sup>:

$$a_I = a_\perp = \Sigma^2 \left\{ \rho_1^2 \eta + 2\rho_2 \left( \frac{1}{F^2 L^2} \right)^2 \right\}, \quad (9.37)$$

$$b_I = \frac{T^2}{V} b_\perp = \Sigma^2 \frac{\xi^2}{F^2 L^2} (1 - \eta) \left\{ 1 + \frac{\beta_1}{F^2 L^2} \right\}, \quad (9.38)$$

$$c_I = \left( \frac{T^2}{V} \right)^2 c_\perp = \Sigma^2 \xi^4 \left( \frac{1}{F^2 L^2} \right)^2 [1 + (2 + u^2)\eta], \quad (9.39)$$

$$d_I = \left( \frac{T^2}{V} \right)^2 d_\perp = \frac{3}{2} \Sigma^2 \xi^4 \left( \frac{1}{F^2 L^2} \right)^2 \eta, \quad (9.40)$$

$$e_I = \frac{1}{V} e_\perp = 2\Sigma^2 \left( \frac{1}{F^2 L^2} \right)^2 [\rho_2 - (1 - \eta)\rho_3], \quad (9.41)$$

where

$$\rho_1 = 1 + \frac{3}{2} \frac{\beta_1}{F^2 L^2} - \frac{3}{8} \left( \frac{1}{F^2 L^2} \right)^2 \left[ \beta_1^2 - 2\beta_2 - \frac{1}{4\pi^2} \ln(\Lambda_M L) \right], \quad (9.42)$$

$$\rho_2 = \frac{3}{4} \left[ \beta_2 + \frac{1}{8\pi^2} \ln(\Lambda_\Sigma L) \right], \quad (9.43)$$

$$\rho_3 = \frac{3}{4} \beta_2 + \frac{1}{8\pi^2} \ln(\Lambda_F L) - \frac{1}{32\pi^2} \ln(\Lambda_M L), \quad (9.44)$$

$$\eta = \frac{1}{4} - \frac{1}{96} u^2 + \mathcal{O}(u^4), \quad (9.45)$$

$$u = 2\rho_1 m \Sigma V. \quad (9.46)$$

<sup>4</sup>Without magnetization both the parallel and the perpendicular components of the spin fields are the same, because there is no privileged direction. Therefore we can average over the components of the spin fields. Considering the massive case we are only using the perpendicular components or equally the pseudoscalar density.

are defined in [32] explicitly and  $\xi = T/L$ ,  $\beta_1$  and  $\beta_2$  are known shape coefficients of the lattice.  $\Lambda_M$  and  $\Lambda_F$  are renormalization group invariant scales, which corresponds to the LECs  $L_3$  and  $L_4$  in Eq. (3.26), respectively.

We can combine  $a_I$  and  $e_I$  for timeslices  $t \neq 0$  to cancel the  $\rho_2$ :

$$a'_I = a_I - e_I = \Sigma^2 \left\{ \rho_1^2 \eta + 2(1 - \eta) \rho_3 \left( \frac{1}{F^2 L^2} \right)^2 \right\}, \quad (9.47)$$

and obtain:

$$\frac{T}{2V} \hat{C}_{PP}^{\text{cov}}(t) = a'_I + b_I h_1\left(\frac{t}{T}\right) + c_I h_2\left(\frac{t}{T}\right) + d_I h_3\left(\frac{t}{T}\right), \quad \text{for } t \neq 0. \quad (9.48)$$

Using covariant pseudoscalar densities we can obtain  $\Sigma^2$  from the amplitude of the correlator via a single parameter fit<sup>5</sup>.

### 9.3.2 Meson correlators in the $\epsilon$ -regime - The bare $F$

The pseudoscalar decay constant in the chiral limit  $F$  can also be extracted by matching current correlators in the  $\epsilon$ -regime with the NLO predictions. In [88] we find:

$$\frac{T}{2} \hat{C}_{AA}^{\text{cov}}(t) = a + b h_1\left(\frac{t}{T}\right) + c h_2\left(\frac{t}{T}\right) + \mathcal{O}(\epsilon^6), \quad (9.49)$$

where the functions  $h_1$  and  $h_2$  are defined in Eqs. (9.33) and (9.34). In  $SU(2)$  the coefficients are given by<sup>6</sup>:

$$a = \gamma_a = F_\pi^2 \left[ 1 - \frac{1}{4} I(u) - \frac{1}{2} \frac{\beta_1 \xi}{F_\pi^2 L^2} \left( 1 - \frac{3}{4} I(u) \right) + \mathcal{O}(\epsilon^6) \right], \quad (9.50)$$

$$b = F_\pi^2 \frac{u^2 I(u)}{8} \frac{\xi}{F_\pi^2 L^2}, \quad (9.51)$$

$$c = F_\pi^2 \left( 1 - \frac{1}{8} I(u) \right) \left( \frac{\xi}{F_\pi^2 L^2} \right)^2, \quad (9.52)$$

where  $F_\pi$  is the pseudoscalar decay constant, the integral function

$$I(u) = \frac{8Y'(u)}{uY(u)}, \quad (9.53)$$

are given by the Bessel function  $Y(u)$  and  $u$  is defined in Eq. (9.46).

Fitting the covariant axialvector-axialvector correlator to the form in Eq. (9.49), we can extract  $F_\pi^2$  from the amplitude. To obtain  $F$  out of  $F_\pi$  we have to use the ChPT formula in [89]:

$$F_\pi = F \left[ 1 + \frac{M_\pi^2}{16\pi^2 F^2} \ln \frac{\Lambda_F^2}{M_\pi^2} \right], \quad (9.54)$$

where we can apply the Gell-Mann-Oakes-Renner relation in Eq. (3.25) to cancel  $M_\pi^2$ :

$$M_\pi^2 = \frac{2m\Sigma}{F^2}. \quad (9.55)$$

Therefore we have to solve the following equation with respect to  $F$  numerically:

$$F_\pi - F - \frac{2m\Sigma}{16\pi^2 F^3} \ln \frac{F^2 \Lambda_F^2}{2m\Sigma} = 0. \quad (9.56)$$

<sup>5</sup>We have to insert the resulting  $\Sigma$  recursively into the fit again, which relatively fast converges to a constant  $\Sigma$ .

<sup>6</sup>Note, that we apply these  $N_f = 2$  formulas also for the  $N_f = 2 + 1$  case. We treat the excitations containing the strange quark as all the other non-Goldstone-boson excitations whose effects are coded in the low energy constants. This is certainly the source for a systematical error, which should become negligible if  $m_{ud} \ll m_s$ .

### 9.3.3 Quark condensate from the eigenvalue distribution

At LO in the  $\epsilon$ -expansion, the partition function at fixed topology is equivalent to the one of a chiral Random Matrix Theory (RMT) as discussed in Section 4.2. It follows that RMT reproduces the same microscopic spectral density  $\rho_S^\nu(\xi, \mu)$  as the chiral effective theory, where  $\xi = \alpha\Sigma V$ ,  $\mu = m\Sigma V$  and  $i\alpha$  are the eigenvalues of the continuum Dirac operator. Moreover, it is possible to extract the probability distributions of the low-lying eigenvalues [37, 41, 90]:

$$\rho_S^\nu(\xi, \mu) = \sum_{k=1}^{\infty} p_k^\nu(\xi, \mu). \quad (9.57)$$

By matching the low-lying spectrum with these expectations

$$\langle \alpha_{\nu k} \rangle^{\text{QCD}\Sigma V}(\mu) = \langle \xi_{\nu k} \rangle^{\text{RMT}}(\mu) = \int_0^\infty d\xi_k \xi_k p_k^\nu(\xi_k, \mu), \quad (9.58)$$

one can then extract the low-energy constant  $\Sigma$ .

Similarly, we can compare RMT with the lattice results by considering the shape of the distributions of the  $k$ -th eigenvalue in the topological sector  $\nu$ :

$$\langle \Delta \xi_{\nu k} \rangle^{\text{RMT}}(\mu) = \sqrt{\langle \xi_{\nu k}^2 \rangle - \langle \xi_{\nu k} \rangle^2} = \langle \Delta \alpha_{\nu k} \rangle^{\text{QCD}\Sigma V}(\mu). \quad (9.59)$$

It is also possible to compare the cumulative distributions of the eigenvalues:

$$c_{\nu k}(\xi_{\nu k}) = \int_0^{\xi_{\nu k}} d\xi'_k p_k^\nu(\xi'_k, \mu) = \int_0^{\alpha_{\nu k} \Sigma V} d\alpha'_k p_k^\nu(\alpha'_k, \mu) = c_{\nu k}(\alpha_{\nu k}) \Sigma V. \quad (9.60)$$

Note that using these methods for approximately chiral fermions have a drawback. Due to the fact that the index theorem does not hold for approximately chiral fermions we cannot exactly determine the topological sector  $\nu$ . This problem is addressed in Section 13.3.1.

### 9.3.4 The pion decay constant from the rotator spectrum

In the  $\delta$ -regime (cf. Section 3.3.4) one considers a lattice where

$$\frac{T}{4\pi F^2 L^3} = \frac{\xi}{4\pi F^2 L^2} > 1. \quad (9.61)$$

so that the low-lying rotator spectrum can be measured. This spectrum is given by an  $O(4)$  rotator having in LO a mass gap which is not disturbed by higher excitations (cf. Section 3.3.5)

$$m_{\text{gap}} = \frac{3}{2F^2 L^3}, \quad (9.62)$$

Determining this mass gap can be used to calculate  $F$ . Note, however, that for a small box size one expects non-negligible corrections to this LO result [91].

## 9.4 Extrapolations

Doing a LQCD simulations we have to discretize space-time and truncate the infinite volume of the universe to a small finite volume. Therefore we take special care in the previous chapters to have these unavoidable approximations under control. We are using lattices, gauge actions and Dirac operators which have small discretization errors, so that it becomes easier to extrapolate our lattice spacing to zero  $a \rightarrow 0$ . This is the continuum limit. When we choose the lattice size in our calculations we have to go to sizes where the truncation of the volume does not change the physical content of the theory. However, at the end of the day we have to correct the finite size effects by extrapolating the volume to infinity  $V \rightarrow \infty$ . A numerical problem occurs going to very small quark masses. The easiest way to circumvent this is to do the calculations with larger quark masses than with those which are realized in nature. Doing this for several unphysical heavy quark masses one can use chiral perturbation theory to extrapolate to the chiral limit  $m_q \rightarrow 0$ .

### 9.4.1 Scaling analysis

The lattice spacing  $a$  is not only the discretization error of our calculations, but also the regulator of our quantum field theory. Without a finite lattice spacing  $a$  we would get UV-divergences which would not allow us to compute physical quantities, i.e., all results would be infinite. As in every quantum field theory the regulator has to be removed from the theory and the physical quantities must not depend on the regulator at the end of the day.

The lattice spacing  $a$  is not a parameter which can be set like the quark mass or the volume of the lattice. Its size is produced more or less dynamically. So one has to measure the lattice spacing of a simulation after generating gauge configurations with the same parameters (cf. Section 9.1). However, the lattice spacing is driven by the gauge coupling  $\beta$ , where the limit  $a \rightarrow 0$  corresponds to  $\beta \rightarrow \infty$  and vice versa.

On the lattice one usually works with small discretization errors, but they are still there and contaminate the results. A typical  $a \rightarrow 0$  extrapolation is done on several lattices all with a different lattice spacing  $a$ , but the same physical volume  $V$ , i.e., if we make the lattice spacing smaller we have to increase the lattice points in very direction to stay in the same physical volume. This is very important in order to be not fooled by other effects, but this in turn is increasing also the costs for the simulation.

### 9.4.2 Infinite volume corrections

Our lattices have all finite volumes introducing errors if it is too small. Therefore one has to study the dependence of the results on the lattice size and extrapolate to infinite volume  $V \rightarrow \infty$  removing these errors. In [92] effects from interaction around the torus have been studied, which lead to exponential corrections to the mass. The leading contribution comes from the smallest hadron mass and is  $\mathcal{O}(e^{-m_\pi L})$ . Therefore it is important for spectroscopy<sup>7</sup> to satisfy the relation  $m_\pi L > 4$  allowing to ignore finite size effects.

Working in the Euclidean space-time and taking the limit  $V \rightarrow \infty$  has also a different meaning. Enlarging the lattice in time direction  $T \rightarrow \infty$  is connected to a lowering of the simulated temperature. Thus, ideally one would perform the so-called thermodynamic limit first and put the continuum extrapolation  $a \rightarrow 0$  to second place to be sure that we are not simulating quark-gluon plasma (cf. beginning of Part I). However, in a real simulation of today this cannot always be done.

### 9.4.3 Chiral extrapolations

Because of numerical difficulties LQCD simulations are always done for unphysically large quark masses. Also this error has to be removed. Actually we are interested in physical quark masses, but due to the fact that the theory for higher quark masses is known, we can save very much of the confined computer time. The extrapolations have to follow formulas predicted by ChPT. Therefore we have to use several masses of valence quark masses.

We have to distinguish three different ChPTs. If we are in the quenched approximation the sea quark masses are set to infinity and we have to apply quenched ChPT. The second case is where the sea quark masses are equal to the valence quark masses  $m_{\text{sea}} = m_{\text{valence}}$ . In this case the number of valence quark masses is restricted, because typical dynamical simulations are done for 2 or 2 + 1 flavors and so we have at maximum two valence quark masses which obeys  $m_{\text{sea}} = m_{\text{valence}}$ . If the valence and sea quark masses do not coincide this is the so-called partially quenched case. The simulation is done with  $m_{\text{sea}}$  and in the analysis one also inverts the Dirac operator for quark masses  $m \equiv m_{\text{valence}} \neq m_{\text{sea}}$ . Now one can perform the chiral limit  $m \rightarrow 0$  using the partially quenched ChPT. In Fig. 9.1 the regions are shown schematically where we have to make use of partially quenched chiral perturbation theory.

<sup>7</sup>Hadron spectroscopy is done in the  $p$ -regime (cf. Section 3.3).

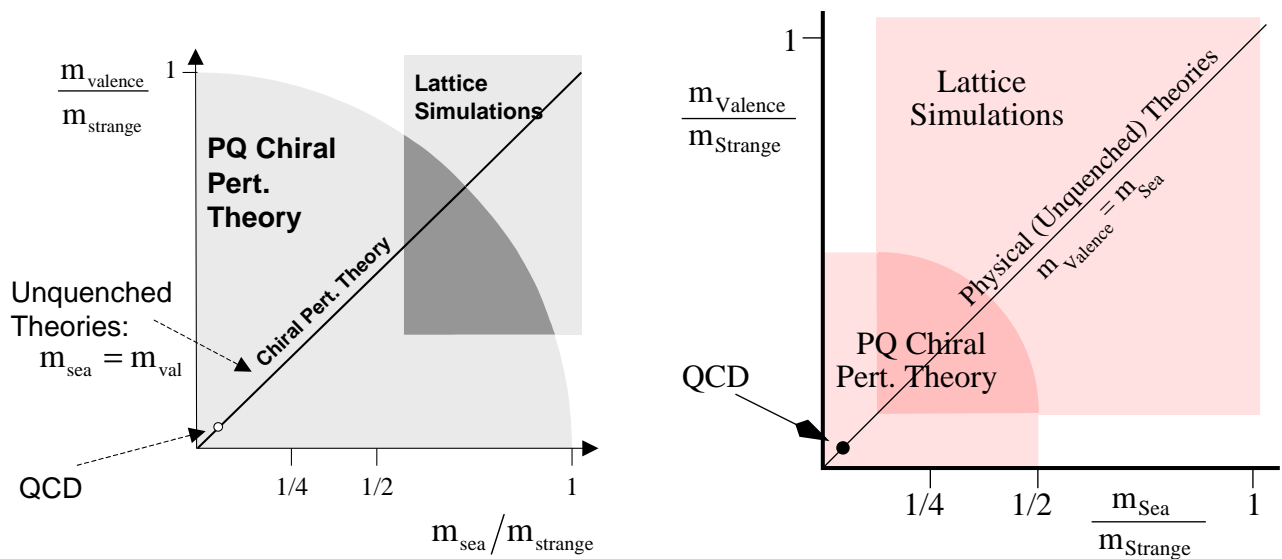


Figure 9.1: Schematic representation of the space of partially quenched theories for light quarks. On the lhs. the approximate range of simulations is shown as they were typical for the year 2000. The rhs. is an update from the year 2006 from the same author. These figures are taken from [93, 94], respectively.

## 9.5 Interpreting the data and its errors

### 9.5.1 Effective masses

Due to the fact that the correlation functions always contain higher excited states one has to find an interval  $t \in [t_{\min}, t_{\max}]$  with  $t_{\min}$  high enough such that only the lowest mass contribution dominates. Therefore, before fitting with an exact form, we compute the so-called effective masses:

$$m_{\text{eff}}(t) = \ln \frac{R(t)}{R(t+1)}, \quad (9.63)$$

where the definition of  $R(t)$  can be found in (9.11) or (9.21). A plot of the parameter  $m_{\text{eff}}$  vs.  $t$  will then show a plateau if only a single mass, the lowest one, controls the correlator.

If the lattice size in the time direction is too small the interval where one can find a plateau is disturbed by the backwards propagating particle. Taking into account both the forward and backward propagating particle one can do the following:

$$m_0(t) = \ln \frac{R(t)}{R(t+1)}, \quad m_{n+1}(t) = m_0(t) - \ln \frac{e^{-Tm_n(t)} + e^{(2t+2)m_n(t)}}{e^{-Tm_n(t)} + e^{2tm_n(t)}}, \quad (9.64)$$

$$m_{\text{eff}}(t) = m_{n+1}(t), \quad \text{if } |m_{n+1}(t) - m_n(t)| < \epsilon. \quad (9.65)$$

For a correlation function like in (9.11) this recursive method makes it much easier to identify the plateau.

If one wants to calculate the masses of excited states, both determinations of the fit range are not suitable. Therefore one uses the variational method, which is described in Section 8.3.2. There the excited states are separated by the diagonalization of a correlation matrix. For every obtained eigenvalue one can then use the effective mass methods again, because every eigenvalue contains a different ground state which can be identified with the mass of an excited state afterwards.

### 9.5.2 Least square fits

To fit a function  $f(x_i; \theta)$  as close as possible to some data points  $(x_i; \bar{y}_i \pm \sigma_i)$  one can use the method of least square fits:

Let  $\bar{y}_i$  be  $N$  independent measurement at known points  $x_i$ . Assume the data points are Gaussian-like distributed around the average  $f(x_i; \boldsymbol{\theta})$  with a variance of  $\sigma_i^2$ , where  $\boldsymbol{\theta} = (\theta_1, \dots, \theta_n)$  is a vector of the  $n$  different and unknown parameters. One has to find  $\bar{\boldsymbol{\theta}}$  which fits the data points best. Therefore the function  $\chi^2$  is introduced:

$$\chi^2(\boldsymbol{\theta}) = \sum_{i=1}^N \frac{(\bar{y}_i - f(x_i; \boldsymbol{\theta}))^2}{\sigma_i^2}. \quad (9.66)$$

If the measurements  $\bar{y}_i$  are independent from each other one gets via minimizing of  $\chi^2$  in the parameters  $\boldsymbol{\theta}$  the ensemble averages  $\bar{\boldsymbol{\theta}}$ . For simple fit function  $f(x_i; \boldsymbol{\theta})$  one can even derive the optimal parameters  $\boldsymbol{\theta}$  analytically.

In the limit of an infinite number of measurements and if the theoretical predictions  $\mathbf{f}(\bar{\boldsymbol{\theta}})$  are valid, then the ensemble average of  $\mathbf{y}$  is given by the ensemble average of  $\boldsymbol{\theta}$ :

$$\bar{\mathbf{y}} = \mathbf{f}(\bar{\boldsymbol{\theta}}), \quad (9.67)$$

where we set for independent measurements [95]:

$$\bar{\boldsymbol{\theta}} = \bar{\boldsymbol{\theta}} \pm \boldsymbol{\sigma}_\theta \quad \text{with} \quad \boldsymbol{\sigma}_\theta^2 = \sum_j \left( \frac{\partial \boldsymbol{\theta}}{\partial \bar{y}_j} \right)^2 \sigma_j^2. \quad (9.68)$$

### Goodness-of-fit tests

In order to estimate, how good the data points agree with the theoretical predictions, we have to determine the degrees of freedoms  $\nu$  first:

$$\nu = N - n. \quad (9.69)$$

Here  $N$  is the number of measurements and  $n$  is the dimension of  $\boldsymbol{\theta}$ , the degrees of freedom in parameter space. To estimate the goodness-of-fit we have to normalize  $\chi^2$  by the number of degrees of freedom  $\nu$ , i.e., we accept the fit only in fitting ranges, where

$$\chi^2/\text{d.o.f.} = \frac{\chi^2}{\nu} \sim 1. \quad (9.70)$$

### Correlated fits

If the measurements are not independent anymore, i.e., it exists a non-diagonal covariance matrix:

$$V_{ij} = \frac{1}{N-1} (\bar{y}_i \bar{y}_j - \bar{y}_i \bar{y}_j) = \frac{1}{N(N-1)} \sum_{s=1}^N (y_i^s - \bar{y}_i) (y_j^s - \bar{y}_j), \quad (9.71)$$

where  $y_i^s$  is the  $s$ -th sample within the  $i$ -th measurement, correlated fits are necessary. Again one obtains the least square estimates by minimizing the following:

$$\chi^2(\boldsymbol{\theta}) = (\bar{\mathbf{y}} - \mathbf{f}(\boldsymbol{\theta}))^T V^{-1} (\bar{\mathbf{y}} - \mathbf{f}(\boldsymbol{\theta})), \quad (9.72)$$

where  $\bar{\mathbf{y}} = (\bar{y}_1, \dots, \bar{y}_N)^T$  is the vector over all measurements and  $\mathbf{f}(\boldsymbol{\theta})$  the corresponding vector for the most optimal parameters. It is:

$$0 = \left. \frac{\partial \chi^2}{\partial \boldsymbol{\theta}} \right|_{\boldsymbol{\theta}=\bar{\boldsymbol{\theta}}} = 2 \frac{\partial \mathbf{f}(\bar{\boldsymbol{\theta}})}{\partial \boldsymbol{\theta}} V^{-1} [\mathbf{f}(\bar{\boldsymbol{\theta}}) - \bar{\mathbf{y}}]. \quad (9.73)$$

We find the minimum at  $\boldsymbol{\theta} = \bar{\boldsymbol{\theta}}$ .

For correlated measurements we get in a linear approximation [96]:

$$\bar{\theta}_i = \bar{\theta}_i \pm \sqrt{\Delta_{ii}} \quad \forall i = 1, \dots, n, \quad (9.74)$$

where

$$\Delta_{ij} = 4 \sum_{lm} H_{il}^{-1} \frac{\partial \mathbf{f}(\bar{\theta})}{\partial \bar{\theta}_l} V^{-1} \frac{\partial \mathbf{f}(\bar{\theta})}{\partial \bar{\theta}_m} H_{mj}^{-1}, \quad (9.75)$$

and  $H_{ij}$  is the so-called Hesse matrix:

$$H_{ij} = \left. \frac{\partial^2 \chi^2}{\partial \theta_i \partial \theta_j} \right|_{\theta=\bar{\theta}}. \quad (9.76)$$

For accepted fit ranges using (9.70) it is also:

$$\bar{\theta}_i = \bar{\theta}_i \pm \sqrt{2H_{ii}^{-1}} \quad \forall i = 1, \dots, n. \quad (9.77)$$

### 9.5.3 Error estimation for smaller data sets

The best estimate for a secondary quantity<sup>8</sup> can be obtained from the average over all samples, but not from the average over all subsamples<sup>9</sup>. If the subsamples are too small, one uses some techniques to estimate the magnitude of errors in the secondary quantities.

#### Jackknife

Let  $A$  be a primary quantity and  $A_1, A_2, \dots, A_N$  are the independent measurements of  $A$ , then it is:

$$\bar{A} = \frac{1}{N} \sum_{s=1}^N A_s. \quad (9.78)$$

The best estimate of the secondary quantity  $y \equiv y(A)$  is

$$\bar{y} = y(\bar{A}). \quad (9.79)$$

We define the so-called Jackknife averages:

$$A_s^{(J)} = \frac{1}{N-1} \sum_{\substack{i=1 \\ i \neq s}}^N A_i. \quad (9.80)$$

We get the so-called Jackknife estimates for the secondary quantity via:

$$\bar{y}^{(J)} = \frac{1}{N} \sum_{s=1}^N y_s^{(J)} = \frac{1}{N} \sum_{s=1}^N y(A_s^{(J)}). \quad (9.81)$$

The error of the Jackknife averages is:

$$\sigma^2(\bar{y}^{(J)}) = \frac{N-1}{N} \sum_{s=1}^N \left( y_s^{(J)} - \bar{y}^{(J)} \right)^2. \quad (9.82)$$

Note that for primary quantities we get back the usual definition of the variance:

$$\begin{aligned} \sigma^2(\bar{A}^{(J)}) &= \frac{N-1}{N} \sum_{s=1}^N \left( A_s^{(J)} - \bar{A}^{(J)} \right)^2, \\ &= \frac{1}{N(N-1)} \sum_{s=1}^N \left( A_s - \bar{A} \right)^2. \end{aligned} \quad (9.83)$$

We get as a final result:

$$\bar{y} = \bar{y} \pm \sigma(\bar{y}^{(J)}). \quad (9.84)$$

<sup>8</sup>A secondary quantity is a function of primary quantities, which themselves are determined directly from the measurement. They are depending on primary averages, which can be directly measured. Note that the averaging of primary and secondary averages do not commute with each other typically, i.e., we obtain the secondary quantity via  $\bar{y} = y(\bar{A})$  and it is  $y(\bar{A}) \neq \bar{y}(A)$ .

<sup>9</sup>Subsamples are disjoint subsets of all samples.

## Bootstrap

A generalization of the jackknife method is called bootstrap, in which a large number  $N_B$  (typically  $\mathcal{O}(1000)$ ) of bootstrap ensembles are each created by selecting  $N$  members (with replacement) from the original ensemble  $\{A_i\}$ . The secondary quantity  $y \equiv y(A)$  is then evaluated on the bootstrap ensembles to yield  $N_B$  bootstrap replicates  $y_s^{(B)}$ . The bootstrap estimate of the variance of  $y$  across ensembles is given by:

$$\sigma^2(\bar{y}^{(B)}) = \frac{1}{N_B} \sum_{s=1}^{N_B} \left( y_s^{(B)} - \bar{y}^{(B)} \right)^2, \quad (9.85)$$

where

$$\bar{y}^{(B)} = \frac{1}{N_B} \sum_{s=1}^{N_B} y_s^{(B)}. \quad (9.86)$$

For the final result we get again:

$$\bar{\bar{y}} = \bar{y}^{(B)} \pm \sigma(\bar{y}^{(B)}). \quad (9.87)$$

### 9.5.4 Binning

After obtaining the errors either with Jackknife or with Bootstrap we only know the statistical errors in the data. We do not know if the input data were still correlated. Therefore we build averages of different sizes of the data and use these averages as input for the error analysis. If the errors obtained again with Jackknife or Bootstrap grow faster than  $\sqrt{m}$ , where  $m$  is the bin size, then we probably have used correlated data.

To solve this issue we replace our data by the averages of  $m$  data points and shorten our statistics. However, obtaining the statistical errors in that way also includes the autocorrelation of the data points and gives therefore more reliable error estimates. Using instead of the original data the averages of  $m$  data points as the input data is called Binning.

This is also the logical consequence of Pruning (cf. Section 7.3.1). If we prune our data too rigorously, we probably waste configurations which are already independent for observables with smaller autocorrelations. In that case Pruning would even increase the statistical error because we throw away statistics unnecessarily. However, combing Pruning and Binning helps us for both reasons, not wasting independent configurations for certain observables and obtaining sensible error estimates without autocorrelation.

## Part III

# LQCD with chirally improved fermions

In this part of the work we want to discuss results obtained with the chirally improved Dirac operator in the quenched approximation. The aim of the first project is to calculate the masses of baryons in the baryon octet and decuplet. In the second project we go a step further and try to predict whether there is a pentaquark  $\Theta^+(1540)$ , which should be the lightest exotic baryon with strangeness  $S = 1$ . My contribution to these projects was the writing and optimizing of the analysis code, where we mainly made use of already generated quenched gauge configurations.

## Excited baryons

We calculate the Dirac propagators using multi-mass Bi-CGSTAB solvers and combine different baryon interpolators to get also the excited states from the variational method. We use a very simple ansatz to model radial excitations on the lattice by combining two sources with two different smearing widths. At the end of the day we are even able to make predictions for excited baryons which have not been listed in the particle data book [17] yet.

## Pentaquark

In this project we implement interpolating fields for the pentaquark on the lattice. We compare interpolators which have already been used by other lattice groups to new ones never considered before in lattice calculations. We give a brief survey of quark models and our considerations for the quantum numbers of the  $\Theta^+(1540)$  baryon.

## Chapter 10

# The baryon spectrum in the quenched approximation

The reproduction of the hadron mass spectrum from first principles is an important challenge for lattice QCD. Ground state spectroscopy on the lattice is by now a well understood problem and impressive agreement with experiments has been achieved. However, the lattice study of excited states [1, 2, 9, 85, 97, 98, 99, 100, 101, 102, 103, 104, 105, 106, 107, 108, 109, 110, 111, 112, 113, 114, 115, 116, 117, 118] is not as advanced. The reason for this is threefold: Firstly, the masses of excited states have to be extracted from subleading exponentials in the spectral decomposition of two-point functions. Secondly, the construction of hadron interpolators which have a good overlap with the wave functions of excited states is much more challenging than for the ground state. Finally, excited states need a larger volume not to feel the boundaries. We are using 2.4 fm boxes in spatial directions which could still squeeze the extended wave function of a excited state. A infinite volume extrapolation is not known for these excited states.

Concerning the first issue, the extraction of the signal from the subleading exponential, several approaches such as constrained fitting or the maximum entropy method can be found in the literature [119, 120]. Here we apply the variational method [76, 77], where not only a single correlator is analyzed, but a matrix of correlators is used. This matrix is built from several different interpolators, all with the quantum numbers of the desired state. The variational method also incorporates in a natural way a solution to the second issue, the wave function of the excited states: One uses a set of basis interpolators which is large enough to span ground and excited states and the variational method finds the optimal combinations of them. In principle, no prior knowledge of or assumption about the composition of the physical hadron state has to be used.

However, the variational method can succeed only if the basis set of hadron interpolators is rich enough to span ground and excited states. On the other hand, the basis should also be constructed such that it can be implemented numerically in an efficient way without the need for many different quark sources. In this article we use a twofold strategy for building our basis interpolators: We use interpolators with different Dirac structures and furthermore compose them using different types of smearing for the individual quarks. In particular, we apply different amounts of Jacobi smearing [74, 75] and in this way create narrow and wide sources. A combination of these allows for spatial wave functions with nodes, which are essential for a good overlap with excited states.

Following a first test of the outlined strategy [1, 2, 110, 112], we focus in detail on the results obtained for baryons. In Section 8.3.2 we collect the basic equations for the implementation of the variational method. We detail the construction of our sources and give an overview of the parameters of our numerical simulation in Appendix G. Here we discuss effective mass plots, the eigenmodes of the correlation matrix, as well as the baryon masses and their chiral extrapolations.

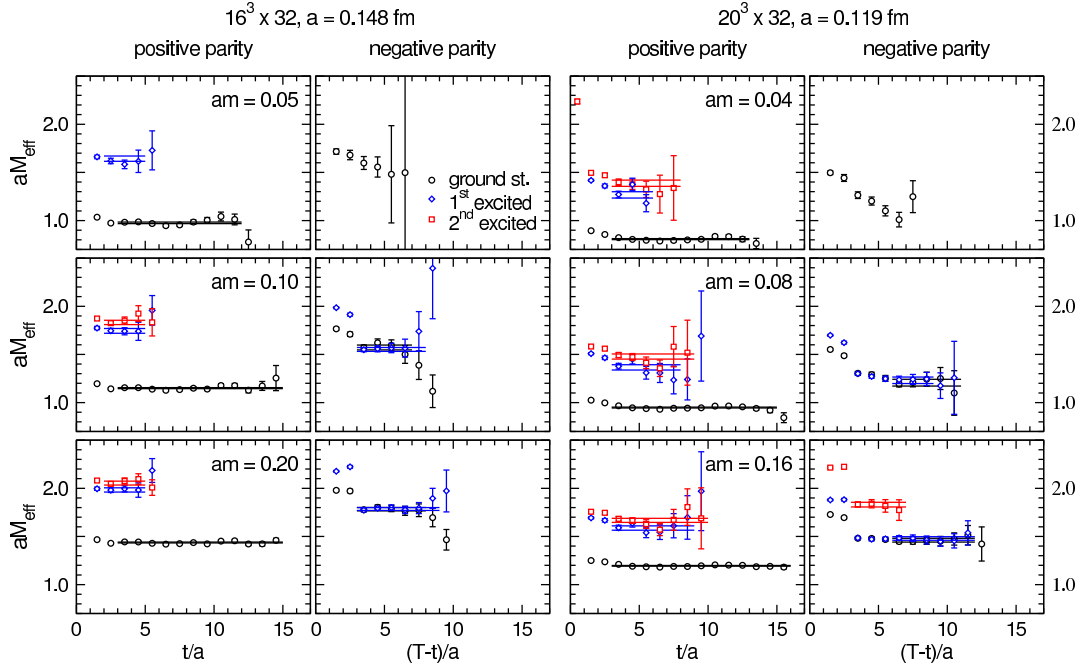


Figure 10.1: Effective mass plots for nucleon ground and excited states. We compare the results from our coarse ( $16^3 \times 32$ ,  $a = 0.148$  fm,  $am_q = 0.05, 0.1, 0.2$  top to bottom), and fine ( $20^3 \times 32$ ,  $a = 0.119$  fm,  $am_q = 0.04, 0.08, 0.16$ ) lattices. The solid lines are the results from correlated fits of the eigenvalues. They represent the fit results plus and minus the corresponding error.

## 10.1 Computing the baryon masses

We have summarized the parameters of this simulation in Appendix G. There, one can find the corresponding characteristics for the used lattices and the baryon interpolators. After choosing an interpolator one has to project it to definite parity and for the  $\Delta$  and  $\Omega$  baryons also to definite spin. We build the correlation matrix  $\hat{C}_{ij}(t)$  from interpolators with correct quantum numbers and use the variational method to obtain the energy levels of the sought-after baryon. We use antiperiodic boundary conditions in the temporal direction and periodic ones in the spatial directions on our lattice and so we can use both correlation functions  $\hat{C}_{ij}^+(t)$  and  $\hat{C}_{ij}^-(t)$  to obtain the energy levels of the interpolator. The positive parity states are obtained from the correlator at small  $t$  running forward in time, while the negative parity states are found at large time arguments, propagating backward in time with  $T - t$ . How this is done in detail is shown in Section 9.2.1. We also symmetrize the correlation matrix<sup>1</sup> by replacing  $\hat{C}_{ij}(t)$  by  $\hat{C}_{ij}(t) = [\hat{C}_{ij}(t) + \hat{C}_{ji}(t)]/2$  before diagonalization to further increase the statistics.

## 10.2 Effective masses, eigenvectors and fit ranges

In Fig. 10.1 we compare the effective mass plots for positive and negative parity nucleons  $N$  from our two lattices at different values of the bare quark mass;  $am = 0.05, 0.1, 0.2$  for  $16^3 \times 32$  and  $am = 0.04, 0.08, 0.16$  for

<sup>1</sup>The correlation matrix should be symmetric within the statistical errors. We use this fact explicitly.

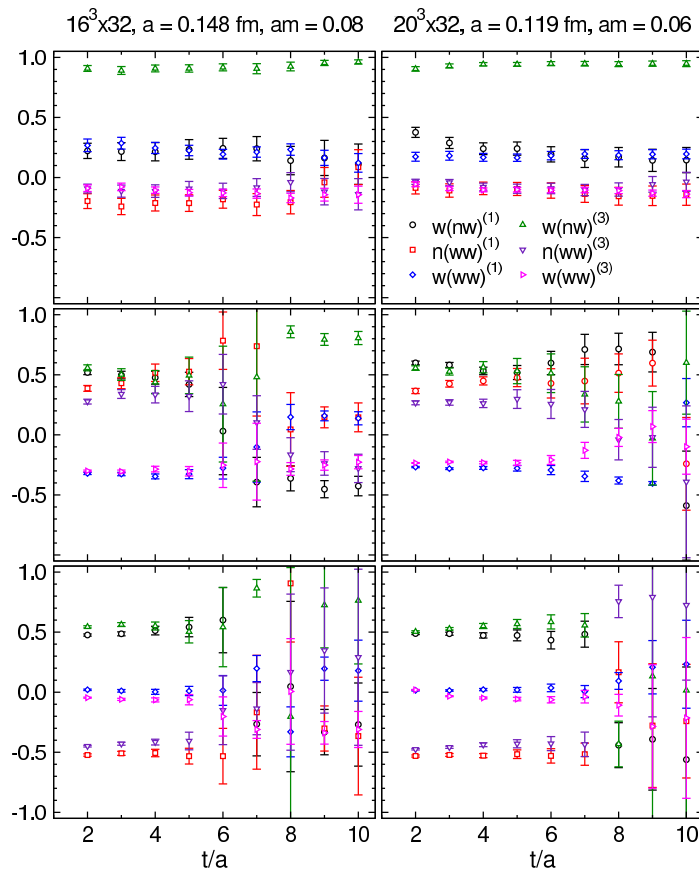


Figure 10.2: Eigenvectors for nucleon ground and excited positive parity states. From top to bottom we show the eigenvector components of ground, first and second excited state.

$20^3 \times 32$ . These numbers were chosen such that they give rise to approximately equal pion masses for the two lattice spacings used. The plots also contain the nucleon masses in lattice units as obtained from a correlated fit of the eigenvalues of the correlation matrix (horizontal bars giving the central values plus and minus the statistical error). The figure shows clear long plateaus for the ground state masses, while the signals for excited states have larger error bars and shorter plateaus. Furthermore the quality of the data decreases as the quarks become lighter, which is well known in lattice spectroscopy.

Another important piece of information comes from the eigenvectors. In Fig. 10.2 we show the six entries of the lowest three eigenvectors corresponding to ground, first and second excited state (top to bottom) in the positive parity nucleon channel. Again we compare the results for our two lattice sizes using quark mass values which give rise to essentially the same pion mass. For each value of  $t$  the respective eigenvectors are normalized to unit length.

It is interesting to note that the eigenvectors depend only weakly on  $t$  (actually this can be shown from the generalized eigenvalue problem). The entries form plateaus which are very long for the ground states but also for the excited states often contain 4 to 8 values of  $t$ . Typically these plateaus extend at least over the same number of  $t$ -values as the effective mass plateaus, i.e., often they are even longer by one or two points.

As in the case of effective masses, the formation of the eigenvector plateaus indicates that the channel is dominated by a single state. Thus, the eigenvector plateaus provide an important tool for the reliable identification of the  $t$ -intervals, where the eigenvalues can be used for a fit. Indeed, sometimes it is the eigenvectors which prevent one from fitting quasi-plateaus in the effective mass. Due to relatively large statistical errors in the effective masses, the data sometimes resemble a plateau and it is only the absence of a plateau in the corresponding eigenvectors which allows us to conclude that a quasi-plateau is not conclusive. We implement this strategy and now fit the eigenvalues only where we see also eigenvector plateaus.

We finally remark that the values for the eigenvectors are almost exactly the same for the two values of the cutoff we consider (in Fig. 10.2 the left hand side plots are for  $a = 0.148$  fm, the right hand side is for  $a = 0.119$ ). Although the entries of the eigenvectors cannot be expected to scale (they are linear combinations of matrix elements of our interpolators with the physical states), it is reassuring for the application of the method that no large discrepancies are observed.

### 10.3 Nucleon

For the nucleon we use the following three interpolator<sup>2</sup>:

$$N^{(i)} = \epsilon_{abc} \Gamma_1^{(i)} u_a (u_b^T \Gamma_2^{(i)} d_c - d_b^T \Gamma_2^{(i)} u_c). \quad (10.1)$$

For positive parity the combination of the six operators  $n(w\bar{w})^{(1)}$ ,  $w(w\bar{n})^{(1)}$ ,  $w(w\bar{w})^{(1)}$ ,  $n(w\bar{w})^{(3)}$ ,  $w(w\bar{n})^{(3)}$ ,  $w(w\bar{w})^{(3)}$ , (the upper index denotes the choice of Dirac structures according to Table G.3) gives the strongest signal. For negative parity we use the  $4 \times 4$  correlation matrix built from  $n(n\bar{n})^{(1)}$ ,  $w(n\bar{n})^{(1)}$ ,  $n(n\bar{n})^{(2)}$ ,  $w(n\bar{n})^{(2)}$ . Of course, these combinations are used for all quark masses. For the positive parity ground state we can determine its mass for all our quark masses. For the excited nucleon states of positive parity the combined assessment of effective masses and eigenvector plateaus do not allow for a trustworthy extraction of the corresponding nucleon masses for the two smallest quark masses.

We identify two excited states of positive parity which have not very different masses for the whole quark mass region where we see a signal. This is consistent with our previous observation on a smaller lattice [110, 112, 1, 2]. These are two physically distinct states since they are observed in different eigenvalues of the correlation matrix and the corresponding eigenvectors are orthogonal. Some additional efforts are required to properly identify the nature of our quenched excited states. We follow the strategy of Ref. [110, 112, 1, 2], i.e., we trace the states from the heavy quark region towards the physical limit.

In the heavy quark region, where we obtain the best signals, the quenching and chiral symmetry effects are less important and the naive quark picture is adequate. Then we know a-priori, that there must be two approximately degenerate excited states of positive parity. The first one is a member of the  $\mathbf{56}_{\text{FS}}$ -plet and the second one belongs to the  $\mathbf{70}_{\text{FS}}$ -plet. In the excited  $\mathbf{56}_{\text{FS}}$ -plet state, as well as in the ground state  $\mathbf{56}_{\text{FS}}$ -plet, all possible quark pairs have positive parity. Then it follows that the signal from the ground state  $\mathbf{56}_{\text{FS}}$ -plet, as well as from the excited  $\mathbf{56}_{\text{FS}}$ -plet state, can be seen with those interpolators that contain two-quark subsystems of positive parity (these are the ones with  $i = 1, 3$  from the Table G.3). On the other hand, the positive parity  $\mathbf{70}_{\text{FS}}$ -plet state contains both positive and negative parity two-quark subsystems, and can be seen with the  $i = 2$  interpolator, where the diquark has negative parity. This picture is confirmed in the heavy quark limit of our results. If we construct our correlation matrix with the  $i = 1$  and/or  $i = 3$  interpolators, we find both the ground state and two excited states of positive parity, while only one state is observed with the  $i = 2$  interpolator. This state corresponds to the first positive parity excited state.

But there is still another explanation for the  $N(1710)$  resonance. In [121] Diakonov, Petrov and Polyakov predict a pentaquark state in the flavor antidecuplet. For their model they have to fix the parameters with the nucleon states in this antidecuplet. In their article they recommend the  $N(1710)$  to be in the antidecuplet and thus also being a pentaquark. This is not taken into account in our calculations here. In their considerations the  $N(1710)$  has an quark content of  $uuds\bar{s}$  and would be classified as a non-exotic pentaquark<sup>3</sup>. Using this

<sup>2</sup>cf. Table G.3 for  $\Gamma_1^{(i)}$  and  $\Gamma_2^{(i)}$  with  $i = 1, 2, 3$

<sup>3</sup>Exotic pentaquarks have an antiquark of a different flavor as the other quarks.

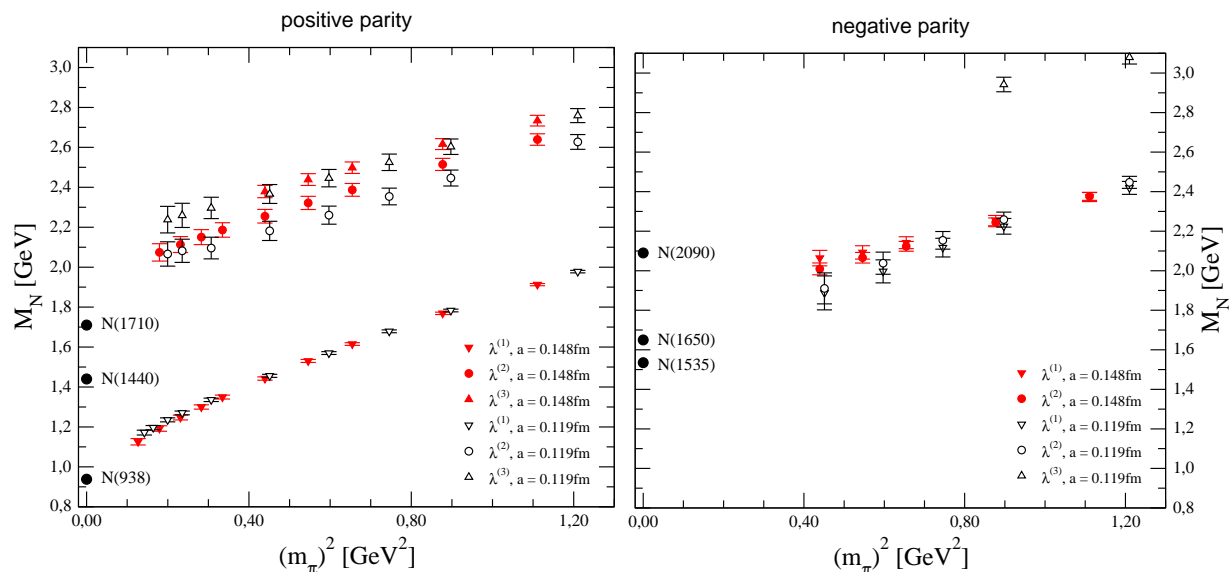


Figure 10.3: Ground and excited state nucleon masses versus  $m_\pi^2$  for our two lattices. Filled symbols are used for  $16^3 \times 32$ ,  $a = 0.148$  fm, open symbols for  $20^3 \times 32$ ,  $a = 0.119$  fm. The left hand side plot shows the positive parity states, the right hand side is for negative parity. The experimental data are included as filled circles.

identification Diakonov, Petrov and Polyakov have been able to calculate the masses of the other flavor antidecuplet masses, which fit very well into the baryon spectrum. However, in the light quark sector a universal experimental evidence of pentaquarks is still missing (cf. Chapter 11).

Using the fingerprint from the eigenvectors, we are able to trace these states from the heavy quark region, where their physical nature can be safely identified, to the light quark region (down to  $m_\pi = 450$  MeV), where they still remain approximately degenerate. Clearly these signals, extrapolated to the physical region, remain essentially higher than the experimental states  $N(1440)$  and  $N(1710)$  (cf. Fig. 10.3).

The discrepancy between our results and the experimental numbers is probably partly due to quenching, where a significant part of chiral physics is absent. Also finite volume effects cannot be excluded (our physical volume is 2.4 fm and large finite volume effects can be anticipated for excited states [103, 106, 113, 116]).

Note that the perturbative gluon exchange between valence quarks, characteristic for the naive constituent quark model, is adequately represented in the quenched calculation. The discrepancy of our results with the experimental ones hints that it is the chiral physics, partly missing in quenched QCD, that could shift both positive parity excited states (and especially  $N(1440)$ , the so-called Roper state) down [122, 123, 124].

state	Mass [MeV]	$I(J^P)$	status
$N(938)$	938	$\frac{1}{2}(\frac{1}{2}^+)$	***
$N(1440)$	1420 to 1470	$\frac{1}{2}(\frac{1}{2}^+)$	****
$N(1535)$	1525 to 1545	$\frac{1}{2}(\frac{1}{2}^-)$	****
$N(1650)$	1645 to 1670	$\frac{1}{2}(\frac{1}{2}^-)$	****
$N(1710)$	1680 to 1740	$\frac{1}{2}(\frac{1}{2}^+)$	***
$N(2090)$	$\sim 2090$	$\frac{1}{2}(\frac{1}{2}^-)$	*

Table 10.1: Here we list the nucleon and its excitations with spin-1/2 from [17].

Our results for the nucleons are presented in Fig. 10.3. The left plot is for positive parity, the right for negative parity. Filled symbols are used for the  $16^3 \times 32$ ,  $a = 0.148$  fm lattice, open symbols for  $20^3 \times 32$ ,  $a = 0.119$  fm. The filled circles represent the experimental masses. The experimental values are taken from [17] and are listed

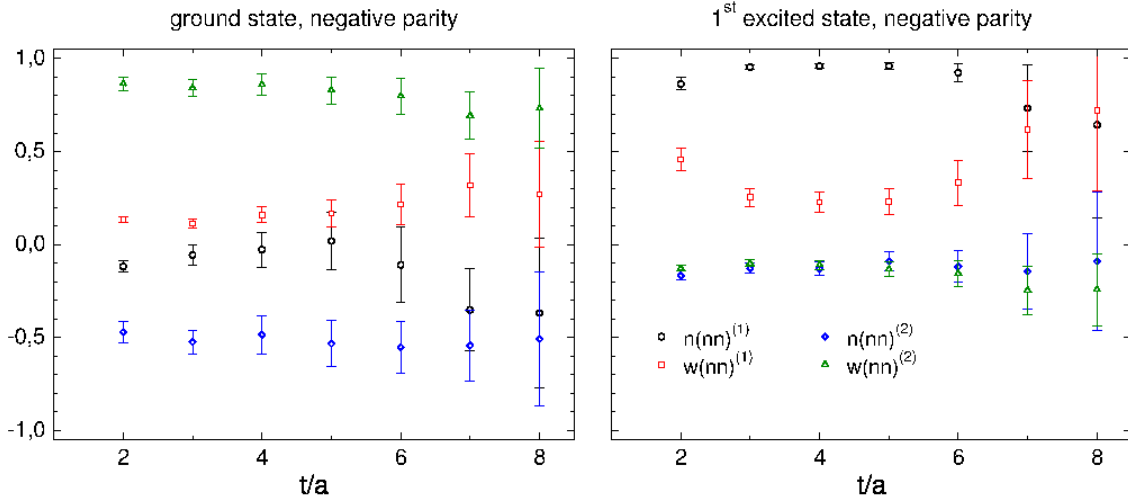


Figure 10.4: Eigenvectors for nucleon ground and first excited negative parity states. The data are for our  $20^3 \times 32$  lattice at  $am = 0.06$ .

in Table 10.1.

The results for the positive parity ground state (left plot, downward pointing triangles) agree well with the experimental value (for the chiral extrapolation of our data see Section 10.7). Furthermore, the data show almost no cutoff effects. For the first excited state (circles) the results for the two values of the cutoff differ by about one sigma, while for the second excited state (upward pointing triangles) the two data sets agree. However, both excited states extrapolate to values about 20-30% larger than the experimental numbers.

For negative parity we mainly fit ground and first excited states. Only for the two largest quark masses on the finer lattice we can extract the second excited mass. We find that the lowest two states are nearly degenerate, but extrapolate to the physical masses within error bars (cf. Section 10.7). Cutoff effects are clearly seen only for small quark masses. Since the negative parity ground and first excited state are nearly degenerate, we have checked that they are indeed different by inspecting the eigenvectors and following their behavior down from the heavy quark region. Entries of the eigenvectors at quark mass  $am = 0.06$  are shown for our  $20^3 \times 32$  lattice in Fig. 10.4. In contrast to the positive parity excited states, the negative parity states fit the experimental data well. This is expected since the negative parity states have the mixed flavor-spin symmetry  $\mathbf{70}_{\text{FS}}$  and experience only small chiral effects [122, 123, 124].

## 10.4 $\Sigma$ and $\Xi$

The  $\Sigma$  and  $\Xi$  resonances which belong to the flavor-octet are structurally identical to the nucleon: only one and two, respectively, of the light quarks are replaced by a strange quark. We use the interpolators:

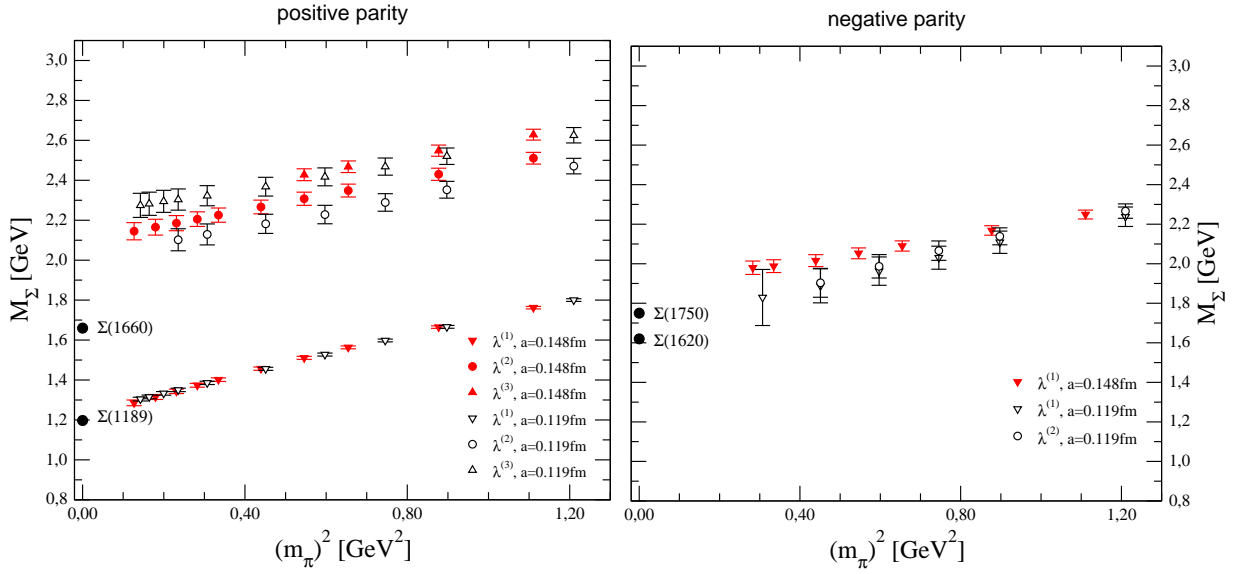
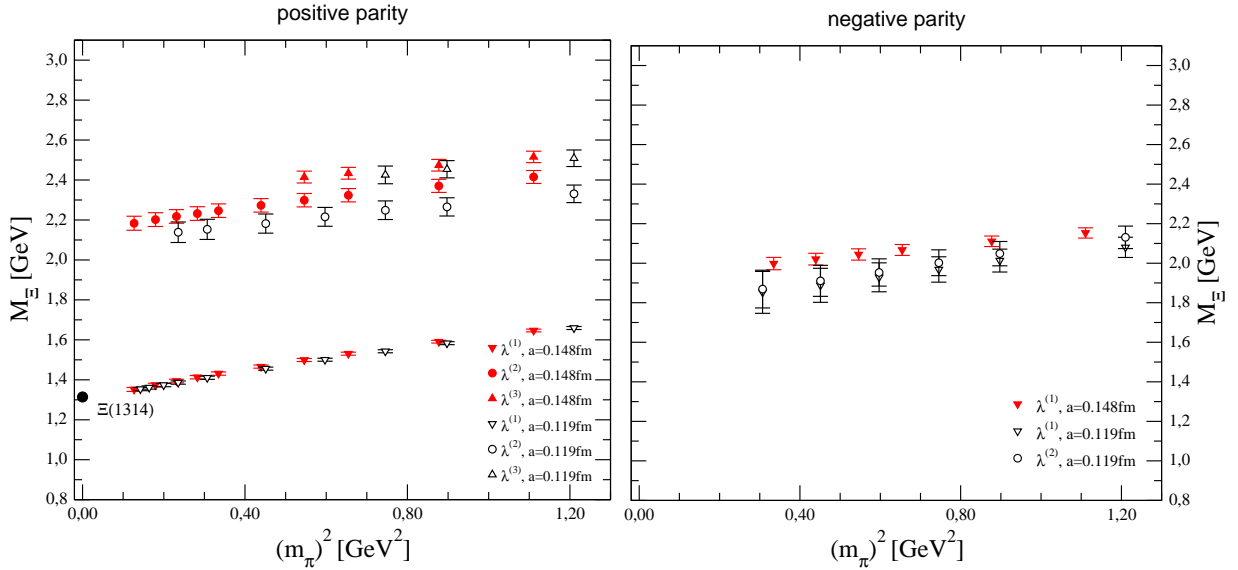
$$\Sigma^{(i)} = \epsilon_{abc} \Gamma_1^{(i)} u_a (u_b^T \Gamma_2^{(i)} s_c - s_b^T \Gamma_2^{(i)} u_c) \quad (10.2)$$

and

$$\Xi^{(i)} = \epsilon_{abc} \Gamma_1^{(i)} s_a (s_b^T \Gamma_2^{(i)} u_c - u_b^T \Gamma_2^{(i)} s_c). \quad (10.3)$$

Consequently, their analysis and also the results are only a variation of what has been found for the nucleon system. We use the same combination of interpolators in the  $6 \times 6$  (for positive parity) and  $4 \times 4$  (negative parity) correlation matrices as we did for the nucleons.

We present our results for the octet  $\Sigma$  in Fig. 10.5 and  $\Xi$  masses in Fig. 10.6. As for the nucleon system, the positive parity  $\Sigma$  and  $\Xi$  ground states are compatible with the experimental numbers and essentially no

Figure 10.5: Same as Fig. 10.3, now for  $\Sigma$ .Figure 10.6: Here we plot now the ground and excited state  $\Xi$  masses versus  $m_\pi^2$  for our two lattices.

cutoff effects are visible. In the case of the  $\Xi$  baryon only the ground state is experimentally well settled (cf. Table 10.2). Concerning the excited positive parity states, only the first excited states show notable cutoff effects, while the masses of the second excited states from the two lattices are compatible within error bars. For the  $\Sigma$ , where at least the first excited state is classified, our data extrapolate to a number which is about 20% larger than the experimental result, similar as in the nucleon case.

For negative parity, we find two nearly degenerate states which show clear cutoff effects for the smaller quark masses. For the  $\Sigma$  the data are compatible with the known states. For the negative parity  $\Xi$  our data extrapolate to two states near 1800 MeV (see also the discussion in Section 10.7).

state	Mass [MeV]	$I(J^P)$	status
$\Sigma$	1189	$1(\frac{1}{2}^+)$	****
$\Xi$	1314	$\frac{1}{2}(\frac{1}{2}^+)$	****
$\Sigma(1620)$	1620	$1(\frac{1}{2}^-)$	**
$\Sigma(1660)$	1630 to 1690	$1(\frac{1}{2}^+)$	***
$\Sigma(1750)$	1730 to 1800	$1(\frac{1}{2}^-)$	***

Table 10.2: Here we list the  $\Sigma$  and its excitations with spin-1/2 from [17]. The quantum numbers for  $\Xi$  are only known for the ground state.

## 10.5 $\Lambda$

state	Mass [MeV]	$I(J^P)$	status
$\Lambda$	1115	$0(\frac{1}{2}^+)$	****
$\Lambda(1405)$	$1406.5 \pm 4.0$	$0(\frac{1}{2}^-)$	****
$\Lambda(1600)$	1560 to 1700	$0(\frac{1}{2}^+)$	***
$\Lambda(1670)$	1660 to 1680	$0(\frac{1}{2}^-)$	***

Table 10.3: The  $\Lambda$  with spin-1/2 and its excitations from [17].

For  $\Lambda$  we have considered two different kinds of interpolators: one which is a pure flavor singlet

$$\Lambda_1 = \epsilon_{abc} \Gamma_1^{(1)} u_a (d_b^T \Gamma_2^{(1)} s_c - s_b^T \Gamma_2^{(1)} d_c) + \text{cyclic permutations of } u, d, s \quad (10.4)$$

and one which has mainly overlap with a flavor octet

$$\Lambda_8^{(i)} = \epsilon_{abc} \left\{ \Gamma_1^{(i)} s_a (u_b^T \Gamma_2^{(i)} d_c - d_b^T \Gamma_2^{(i)} u_c) + \Gamma_1^{(i)} u_a (s_b^T \Gamma_2^{(i)} d_c) - \Gamma_1^{(i)} d_a (s_b^T \Gamma_2^{(i)} u_c) \right\}. \quad (10.5)$$

For the flavor singlet  $\Lambda_1$  we are mainly interested in the ground states in both parity channels. We have therefore used only a single interpolator, the one where all quarks are smeared narrowly  $n(nn)$  (choosing a different smearing combination does not change the results).

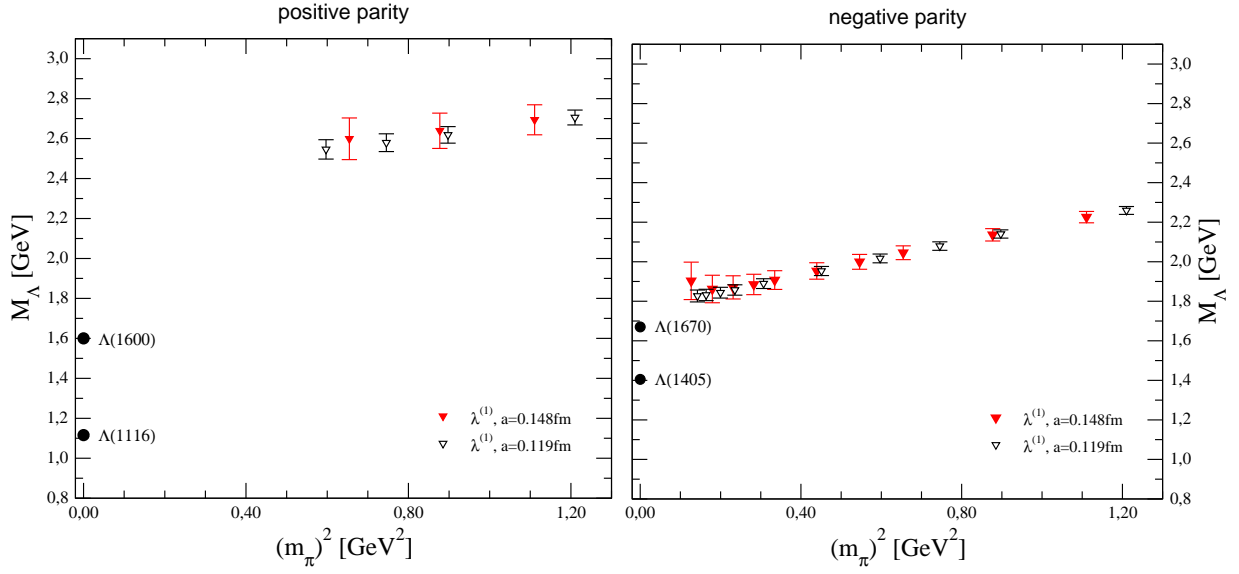
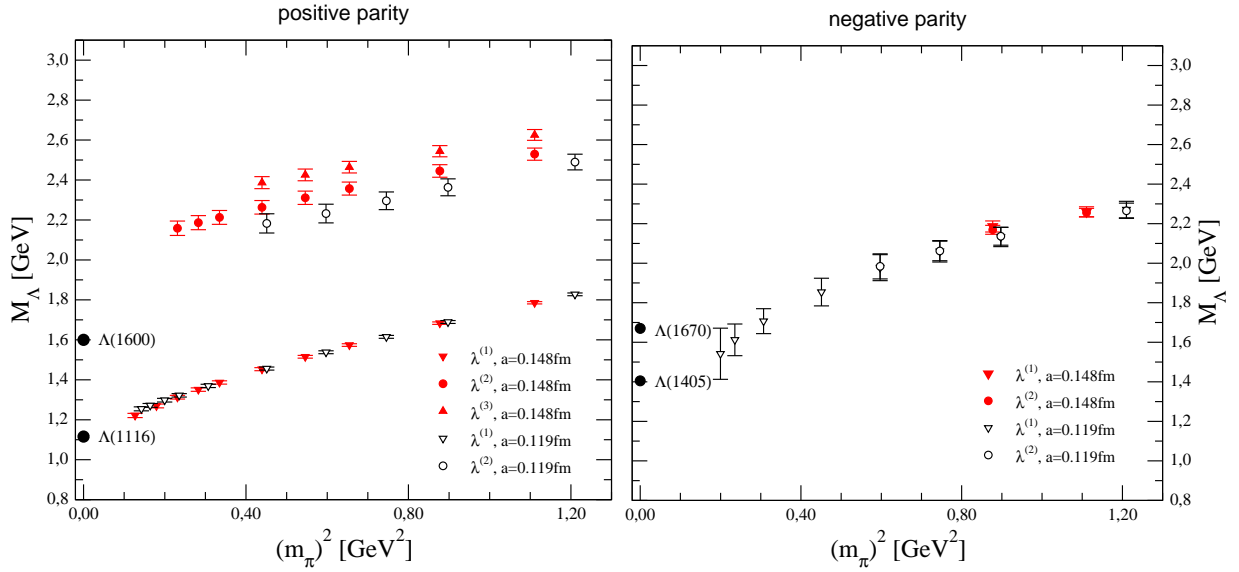
For the flavor octet  $\Lambda_8$  we obtain results which are similar to the results of the other flavor octet baryons. Even the same combination of sources used for  $N$ ,  $\Sigma$  and  $\Xi$  turns out to be the optimal one also for the  $\Lambda_8$  octet channel.

The interesting observation is that while the negative parity flavor-singlet state extrapolates to a mass which is essentially higher than  $\Lambda(1405)$ , but consistent with previous quenched lattice results, the flavor-octet negative parity ground state signal is consistent with the  $\Lambda(1405)$ . Within the simple quark model picture the negative parity pair  $\Lambda^{1/2^-}(1405)$  and  $\Lambda^{3/2^-}(1520)$  is a flavor-singlet. However, starting from the early Dalitz' work [125] it is also understood that at least a significant part of  $\Lambda(1405)$  could be due to  $\overline{K}N$  physics [17]. The  $\overline{K}N$  bound state system can couple to the flavor-octet interpolator and our results hint at the  $\overline{K}N$  nature of  $\Lambda(1405)$ . It would be very interesting to study also the  $\Lambda^{3/2^-}(1520)$  resonance and to see whether it is a flavor-singlet or flavor-octet state. But this has not been included in this study.

## 10.6 $\Delta^{\frac{3}{2}}$ and $\Omega^{\frac{3}{2}}$

As already discussed in the previous Section, our interpolators for  $\Delta^{\frac{3}{2}}$  and  $\Omega^{\frac{3}{2}}$  have to be spin projected to obtain correlators of states with definite quantum numbers:

$$\Delta_\mu = P_{\mu\nu}^{3/2} \epsilon_{abc} u_a (u_b^T C \gamma_\nu u_c) \quad (10.6)$$

Figure 10.7: Ground and excited state masses obtained from our  $\Lambda$  singlet interpolator.Figure 10.8: Ground and excited state masses obtained from our  $\Lambda$  octet interpolators.

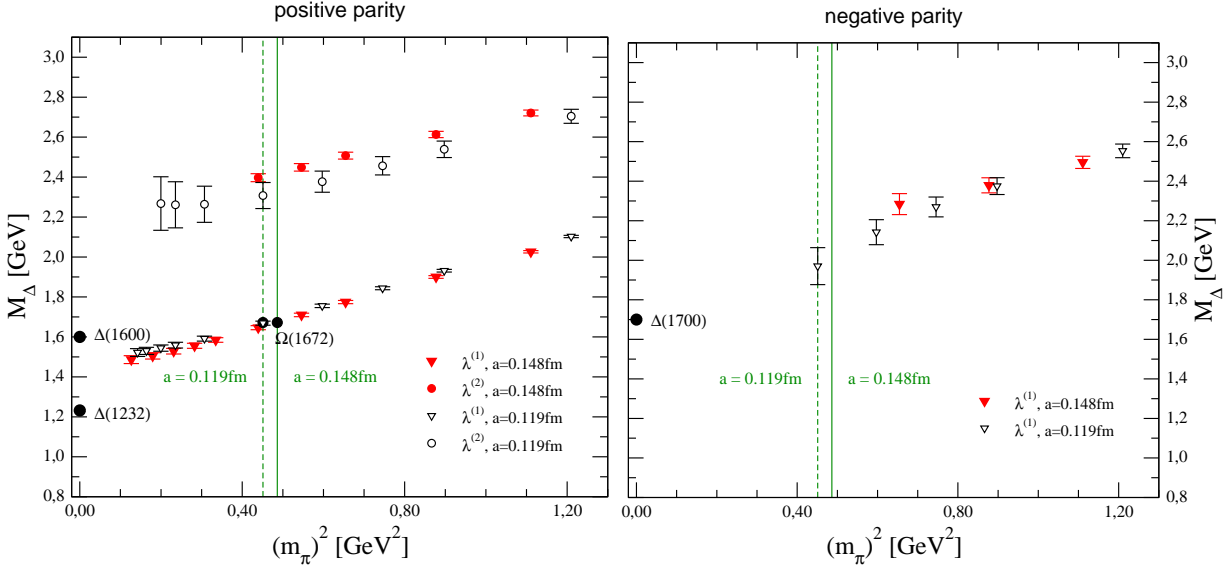
and

$$\Omega_\mu = P_{\mu\nu}^{3/2} \epsilon_{abc} s_a (s_b^T C \gamma_\nu s_c). \quad (10.7)$$

After the spin-3/2 projection we are left with a set of eight interpolators which differ only in the smearing combination of the quarks. From these we have chosen different subsets and found that the dependence on the chosen subset is only marginal. In the end, we decided to use the combinations  $n(nn)$ ,  $w(nn)$ ,  $n(nw)$ ,  $w(nw)$ ,  $n(ww)$ ,  $w(ww)$  for both parity channels.

In Fig. 10.9, we present the results for the  $\Delta^{\frac{3}{2}}$  and  $\Omega^{\frac{3}{2}}$  masses. The positive parity states are shown in the left plot, the right plot is for negative parity. The vertical lines in both plots mark the values of  $m_\pi^2$  corresponding

state	Mass [MeV]	$I(J^P)$	status
$\Delta(1232)$	1231 to 1233	$\frac{3}{2}(\frac{3}{2}^+)$	***
$\Delta(1600)$	1550 to 1700	$\frac{3}{2}(\frac{3}{2}^+)$	***
$\Omega$	1672	$0(\frac{3}{2}^+)$	****
$\Delta(1700)$	1640 to 1750	$\frac{3}{2}(\frac{3}{2}^-)$	****
$\Delta(1940)$	1940	$\frac{3}{2}(\frac{3}{2}^-)$	*

Table 10.4: Is is shown the spin-3/2  $\Delta$  and  $\Omega$  baryons from [17].Figure 10.9:  $\Delta$  masses  $M_\Delta$  versus  $m_\pi^2$ . The vertical lines mark the values of  $m_\pi^2$  corresponding to the physical strange quark mass.

to the physical strange quark mass, which has been determined from a fit to the  $K$ -meson mass in a separate calculation on the two lattices. At these values of the pion mass we extract the masses for the  $\Omega^{\frac{3}{2}}$  resonance from our results for the  $\Delta^{\frac{3}{2}}$ . It is remarkable that the ground state  $\Omega^{\frac{3}{2}}$  lies right on top of the experimental value.

The results for the positive parity ground states of  $\Delta^{\frac{3}{2}}$  show significant discrepancies with the experimental results. However, this is not unexpected and has already been observed by other groups [97, 99, 100, 101, 104]. The Roper-like state,  $\Delta(1600)$ , is not reproduced either. In both cases the most probable explanation would be a lack of the proper chiral dynamics in quenched QCD. Given the fact that the  $\Omega$  ground state is perfectly reproduced, we conclude that the missing chiral dynamics becomes especially important at the quark masses below the strange quark mass.

On the negative parity side we have only been able to fit the ground state reliably and only on the fine lattice our data reach the strange quark mass such that the mass of the negative parity  $\Omega^{\frac{3}{2}}$  can be determined. Extrapolation to the physical limit is consistent with  $\Delta(1700)$ .

## 10.7 Chiral extrapolations for the fine lattice

Where the data are sufficient, we perform a chiral extrapolation of our results. For excited states the form of the chiral extrapolation is not known from chiral perturbation theory and we extrapolate linearly in  $m_\pi^2$ :

$$M = Am_\pi^2 + B \quad (10.8)$$

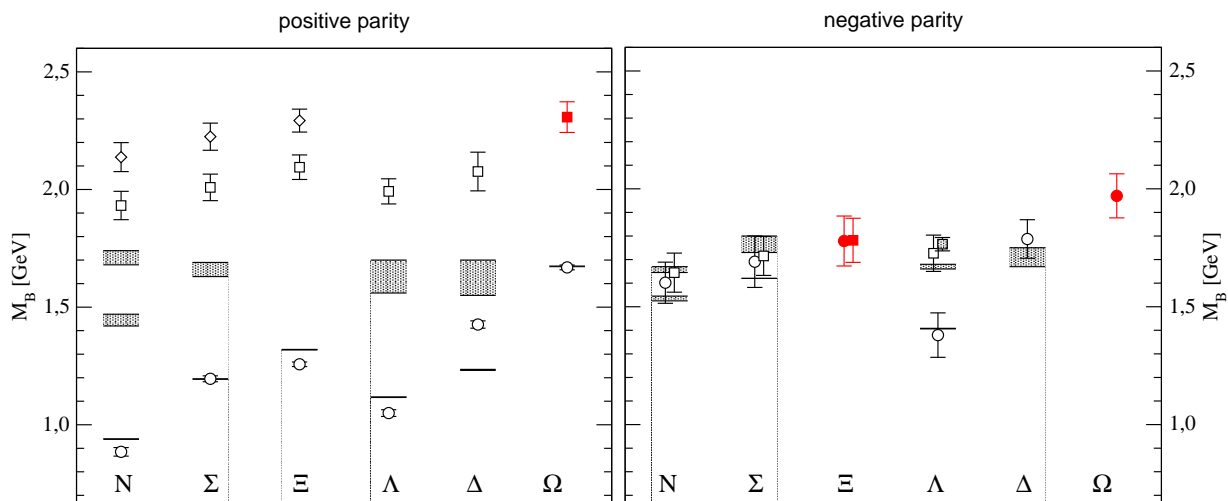


Figure 10.10: Chiral extrapolation of our results. The left plot is for positive parity, the right for negative parity. The horizontal bars represent the experimental numbers (where known), indicating also the error. For our results we use circles for ground states, squares and diamonds for the first and second excited states respectively. The shaded square symbol for the excited  $\Lambda$  represents the chiral limit of the data from the singlet interpolator. Filled symbols are used for those states where no corresponding state is listed by the particle data group [17].

Since in this paper the focus is on the excited states, the extrapolation for the ground states is also kept simple. We use second order polynomials in  $m_\pi$  there, which is the structure of the leading terms in quenched chiral perturbation theory [126]:

$$M = Am_\pi^2 + Bm_\pi + C. \quad (10.9)$$

Since for some of the states we still observe cutoff effects, we extrapolated only the data from the finer lattice.

For positive parity the results of the chiral extrapolation are presented in the left plot of Fig. 10.10. We remark, that the numbers for the  $\Omega$  are obtained by an interpolation to the strange quark mass. While the ground states come out reasonably well for a quenched calculation, the results for the excited states are systematically 20% - 25% above the experimental numbers (where known). The most likely explanation is that quenching removes some important piece of chiral physics, which is actually responsible for the proper mass of excited positive parity states. Significant finite volume effects cannot be ruled out either.

For negative parity states (right plot of Fig. 10.10) the results are compatible with the experimental numbers (where known), although the statistical errors are larger. Also here we cannot exclude that cutoff effects push our numbers up a little bit, but from the comparison of the results on our two lattices we estimate that this effect is not larger than the statistical error. Again the result for  $\Omega$  is obtained from an interpolation to the strange quark mass. One may expect that quenching effects are essentially smaller for the negative parity channel states than for the positive parity excited states. This is expected a-priori, since all low-lying negative parity states are in the mixed flavor-spin symmetry class of a  $\mathbf{70}_{\text{FS}}$ -plet and hence are affected by the chiral dynamics only slightly (except for the  $\Lambda(1405)$ ) [122, 123, 124].

## 10.8 Predictions

In some of the channels, we have analyzed corresponding baryons which are not yet classified in the particle data book [17]. For four of these channels we believe that our data are strong enough to quote the final results as a prediction: The first excited positive parity  $\Omega$  state, the negative parity  $\Omega$  ground state, and the ground and first excited negative parity  $\Xi$  states. The two  $\Omega$  states are included in this list since at the strange quark mass the chiral dynamics is less important and also our results do not need to be extrapolated to the chiral limit.

state	Mass [MeV]
$\Omega$ , positive parity, first excited state	2300(70)
$\Omega$ , negative parity, ground state	1970(90)
$\Xi$ , negative parity, ground state	1780(90)
$\Xi$ , negative parity, first excited state	1780(110)

Table 10.5: Collection of our final results for some states not classified by the Particle Data Group [17].

Concerning the two negative parity  $\Xi$  states we believe that the good results of the structurally very similar negative parity nucleons and  $\Sigma$  baryons justify the prediction of the mass of the negative parity ground and first excited state in the  $\Xi$  channel. Our final numbers for the masses of the four states are listed in Table 10.5.

# Chapter 11

## The pentaquark

All known hadrons can be considered as a combination of two or three quarks, but there is no theory which excludes the existence of particles composed by more than three valence quarks. Particles which are bound states of 3 quarks and additional particles are called exotic baryons. In [121] Diakonov, Petrov and Polyakov predicted a pentaquark which consists out of four quarks and one antiquark and is supposed to have a very narrow decay width. The possible discovery of this pentaquark called  $\Theta^+(1540)$  by the LEPS Collaboration at SPring-8 [128] has initiated great interest in exotic baryons. Since then, there has been a large number of experiments that have confirmed this result [127, 129, 130, 131, 132, 133, 134, 135, 136, 137], but also about the same number that could not confirm it [138, 139, 140, 141, 142, 143, 144, 145]. Presently the experimental situation is still highly unsettled [146, 147, 148]. Because of the discrepancy in the results of the experiments several quark models have been developed to explain the experimental data.

Also lattice QCD has not been able to give a conclusive answer so far to the question whether there might exist a bound  $\Theta^+$  state or not [149, 150, 151, 152, 153, 154, 155, 156, 157, 158]. To confirm or disprove the existence of the  $\Theta^+$  by lattice calculations is a huge challenge in both men and computer power. But if a clear conclusion can be reached and will eventually be experimentally confirmed, this would give a substantial boost to lattice QCD. Therefore, many lattice groups have started to work on this problem. In this Chapter we discuss our results using some interpolators which have not been tested by other groups on the lattice yet [5].

We start with a brief survey of the proposed quark models for the pentaquark in chronological order. First we discuss the quark soliton model and its origin to show the reason why one should believe that model. Diakonov, Petrov and Polyakov have used this model in [121] to propose a new exotic baryon, the  $\Theta^+$ . After that we consider a model where Jaffe and Wilczek in [159] introduce a force between diquarks which is attractive and explore the possibility to describe with their model the pentaquark  $\Theta^+$ . Also Glozman uses in [160] such a force in his model to make predictions about a possible  $\Theta^+$ . In addition, we present our considerations about the quantum numbers of the pentaquark.

Starting to calculate a particle mass one has to choose an interpolating field which has the correct quantum numbers, i.e., it has to follow the same symmetry properties as the particle one is interested in. However, this is not so easy for the  $\Theta^+$ . Due to the fact that the  $\Theta^+$  could not be confirmed experimentally, we do not exactly know what quantum numbers we have to hold fixed as this is the case, e.g., for nucleons (cf. Chapter 10).

In our calculations we perform a qualitative study using different types of spin- $\frac{1}{2}$  operators with possible quantum numbers of the  $\Theta^+$ . We compute all cross correlators and use the variational method [76, 77] to extract the lowest lying eigenvalues. These are used to create effective mass plots for a comparison to the  $n$ - $K$  scattering state which we compute separately on the same lattice.

### 11.1 Quark models

Here, we summarize the quark models which have partially induced the search for the  $\Theta^+$  pentaquark.

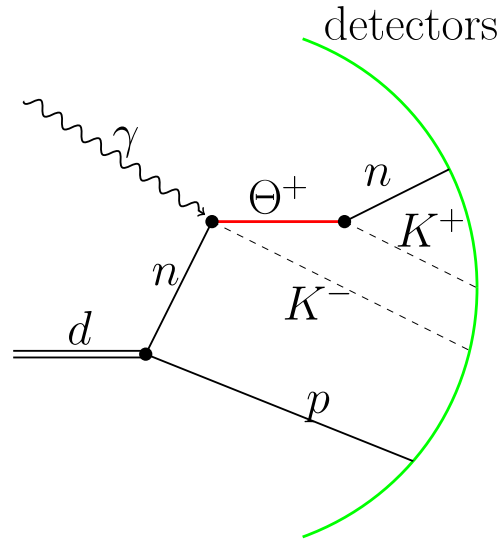


Figure 11.1: This is a schematic plot of an experiment searching for the  $\Theta^+$  pentaquark at CLAS [127]. The  $\Theta^+$  baryon is an intermediate state of a bound excited neutron state  $n$ , which decays into a neutron  $n$  and a  $K^+$  meson.

### 11.1.1 Chiral soliton model

The most important success of the chiral soliton model [161, 162], in which nucleons can be viewed as solitons of the pion field (the so-called Skyrmions<sup>1</sup>), is the classification of light baryons. The topological stability of the solitons is interpreted as the conservation of baryon number  $\mathcal{B}$ . The generalization to hyperons in [163, 164] makes the success of the chiral soliton idea even more impressive.

The chiral soliton models of baryons can successfully explain the relations between octet and decuplet baryons. In these models all baryons appear as various rotational excitations of the same object. The two lowest rotational states of chiral solitons are the octet with spin-1/2 and the decuplet with spin-3/2. The next rotational state is the antidecuplet with spin-1/2, where most of its properties can be predicted from symmetry considerations only.

In the two flavor case the next excitations would lie very high and would be cigar-shaped, i.e., they are very hard to observe [121]. In the three flavor case, the radiation by the soliton includes the Goldstone bosons of  $SU(3)$ , the  $K$  and  $\eta$  mesons, which are substantially heavier than pions. Hence, such radiation is to some extent suppressed. Therefore, the antidecuplet baryons may not necessarily have widths comparable to their masses. It is thus expected that a relatively light and narrow antidecuplet of baryons exists.

There is only a single unknown parameter (a specific  $SU(3)$  moment of inertia) which can be fixed by identifying the nucleon-like member of the antidecuplet with the observed  $N(1710)$  resonance (cf. Fig. 11.2). The calculated decay modes of the  $N(1710)$  are found to be in reasonable agreement with the existing data. At least it seems that the standard description of this state as a member of an octet, is in trouble with the data. Therefore the antidecuplet idea would even fit better (cf. Ref. [121]).

Using the chiral soliton model Diakonov, Petrov and Polyakov [121] have predicted an exotic  $\Theta^+$  (having positive parity, spin 1/2, isospin 0 and strangeness  $\mathcal{S} = +1$ )<sup>2</sup> with a relatively low mass of about 1530 MeV and total width of less than 15 MeV and the authors mentioned that until the year 1997 this region of masses has been avoided careful searches in the past.

<sup>1</sup>The Skyrmion [162] models the nucleon as a topological soliton in a non-linear  $SU(2)_F$  pion field.

<sup>2</sup>The  $\Theta^+$  was used to be called  $Z^+$  in the beginning of its research. Also in [121] it was still called  $Z^+$  and they predicted that it has a mass of 1530 MeV. The first positive experimental results found a resonance at a mass of 1540 MeV, which is now also listed in the particle data book [17].

### 11.1.2 Diquark model - Jaffe & Wilczek

Jaffe and Wilczek propose in [159] that the  $\Theta^+$  baryon should be a bound state of four quarks and an antiquark, containing two highly correlated  $ud$ -pairs and an  $\bar{s}$ -quark. The four quarks are bound into two spin zero, color and flavor  $\bar{\mathbf{3}}$  diquarks  $[ud]$ , i.e., they are in  $\mathbf{1}_S$ ,  $\bar{\mathbf{3}}_C$  and  $\bar{\mathbf{3}}_F$ .

$$\begin{aligned} 2_S \otimes 2_S &= 3_S \oplus 1_S , \\ 3_C \otimes 3_C &= 6_C \oplus \bar{\mathbf{3}}_C , \\ 3_F \otimes 3_F &= 6_F \oplus \bar{\mathbf{3}}_F . \end{aligned} \quad (11.1)$$

The diquarks obey Bose statistics, but may be expected to experience a repulsive Pauli blocking interaction at short distances. Because they are not color singlets they cannot be observed as free particles, but being bound states within a hadron is allowed as a start. In order to form a singlet together with the antiquark, the two diquarks must combine to a color  $\mathbf{3}_C$ .

$$\bar{\mathbf{3}}_C \otimes \bar{\mathbf{3}}_C = 6_C \oplus \mathbf{3}_C .$$

Since the  $\mathbf{3}_C$  is the antisymmetric part of  $\bar{\mathbf{3}}_C \otimes \bar{\mathbf{3}}_C$ , the diquark-diquark wavefunction must be antisymmetric with respect to the rest of its labels. The spin is symmetric and also fixed:

$$1_S \otimes 1_S = 1_S . \quad (11.2)$$

For  $[ud][ud]$  only space labels remain, so that the lightest state must have a wavefunction antisymmetric under space exchange ( $\vec{x} \rightarrow -\vec{x}$ ), i.e., it must have negative parity. When combined with the antiquark, the resulting  $q^4\bar{q}$  state therefore has positive parity and consequently the same quantum numbers as in the soliton picture.

### 11.1.3 Diquark model - Glozman

In [160] the  $\Theta^+$  pentaquark is described within the chiral constituent quark model. Color-orbital and flavor-spin quantum numbers are fixed through  $\bar{\mathbf{15}}_{CO}$  and  $\mathbf{21}_{FS}$ :

$$6 \otimes 6 = \bar{\mathbf{15}} \oplus \mathbf{21} , \quad (11.3)$$

$$(3 \odot 2) \otimes (3 \odot 2) = (6^1 \oplus 3^3) \oplus (6^3 \oplus 3^1) , \quad (11.4)$$

which gives two combinations of diquarks:

$$d_1 = 6_C, 1_O, \bar{\mathbf{3}}_F, 1_S \quad L = 1; S = 0; J = 1; P = - , \quad (11.5)$$

$$d_2 = \bar{\mathbf{3}}_C, 3_O, \bar{\mathbf{3}}_F, 1_S \quad L = 0; S = 0; J = 0; P = + , \quad (11.6)$$

and

$$d_1 = 6_C, 1_O, 6_F, 3_S \quad L = 1; S = 1; J = 0, 1, 2; P = - , \quad (11.7)$$

$$d_2 = \bar{\mathbf{3}}_C, 3_O, 6_F, 3_S \quad L = 0; S = 1; J = 1; P = + . \quad (11.8)$$

Within this picture the flavor-spin interaction between valence quarks inverts the  $(1s)^4$  and  $(1s)^3(1p)$  levels of the four-quark subsystem and consequently the lowest-lying pentaquark is a positive parity,  $I = 0$ ,  $J = 1/2$  state of the flavor antidecuplet, similar to the soliton model prediction. Contrary to the soliton model, however, the quark picture predicts its spin-orbit partner with  $J = 3/2$ , since the coupling of  $L = 1$  tetraquark (one of the diquarks is in a  $p$ -wave) with the strange antiquark produces both  $J = 1/2$  and  $J = 3/2$  states.

### 11.1.4 Diquark-triquark model - Karliner & Lipkin

In [165] Karliner and Lipkin propose another way to combine the quarks in a  $\mathbf{3}_C$   $ud$ -diquark  $d_1$  coupled to  $\mathbf{3}_C$   $ud\bar{s}$ -triquark in a relative  $p$ -wave, where we denote the  $ud$ -diquark within the  $ud\bar{s}$ -triquark as  $d_2$ :

$$d_1 = \bar{\mathbf{3}}_C, 3_O, \bar{\mathbf{3}}_F, 1_S \quad L = 0; S = 0; J = 0; P = + , \quad (11.9)$$

$$d_2 = 6_C, 3_O, \bar{\mathbf{3}}_F, 3_S \quad L = 0; S = 1; J = 1; P = + , \quad (11.10)$$

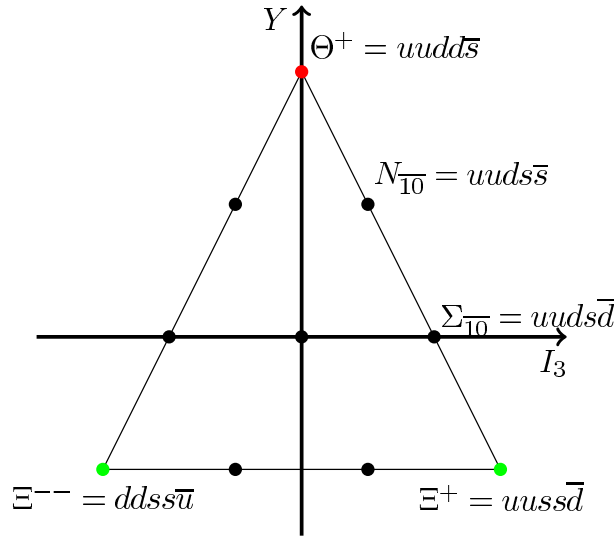


Figure 11.2: In [121] Diakonov, Petrov and Polyakov interpret the  $\Theta^+$  as an antidecuplet baryon with strangeness  $\mathcal{S} = +1$ . Identifying other baryons beside the  $\Theta^+$  as a member of the  $\overline{\mathbf{10}}_F$  would also increase the probability for the existence of the  $\Theta^+$  baryon if they can be found. The multiplets are always drawn in the  $Y$ - $I_3$ -plane, where  $Y = \mathcal{B} + \mathcal{S}$  is the sum of the baryon number  $\mathcal{B}$  and the strangeness and  $I_3$  is the third component of the isospin vector.

Combing the  $d_2$  diquark with the antiquark to a triquark, one gets:

$$t = 3_C, 2_O, \overline{6}_F, 2_S \quad L = 1; S = \frac{1}{2}; J = \frac{1}{2}, \frac{3}{2}; P = - \tag{11.11}$$

The difference of the diquark-triquark model compared to the soliton model and the diquarks model is that the pentaquark here is a negative parity state.

## 11.2 The Quantum Numbers of the Pentaquark

Before we present any pentaquark result we also want to discuss our considerations for the quantum numbers of a pentaquark with strangeness  $\mathcal{S} = +1$ .

### 11.2.1 Flavor

We want to find a pentaquark state with strangeness  $\mathcal{S} = +1$  and charge  $C = +1e$ . Thus we have to construct the responding flavor multiplet for  $SU(3)_F$ . It is easy to show that the claimed pentaquark can only be in the antidecuplet  $\overline{\mathbf{10}}_F$ , i.e., every other symmetry class<sup>3</sup> would result in a different strangeness  $\mathcal{S}$  or charge  $C$ .

$$\begin{array}{|c|c|c|} \hline \square & \square & \square \\ \hline \square & \square & \square \\ \hline \end{array} \Rightarrow \text{quark content: } uudd\bar{s}$$

This is also the minimal quark composition of an object with baryon number  $\mathcal{B} = 1$  and positive strangeness  $\mathcal{S} = +1$ .

<sup>3</sup>All possible  $SU(3)$  Young tableaus can be found in Section E.3.1

### 11.2.2 Isospin

The isospin quantum number of the pentaquark depends only on the tetra-quark which is built by the  $u$  and  $d$  quarks in it. There is only a sole possibility for the tetra-quark particle to form a pentaquark in the  $SU(3)_F$  antidecuplet  $\overline{10}_F$ :

$$\begin{array}{c} \begin{array}{|c|c|} \hline u & u \\ \hline d & d \\ \hline \end{array}, \quad \begin{array}{|c|c|} \hline u & d \\ \hline d & u \\ \hline \end{array}, \quad \begin{array}{|c|c|} \hline d & u \\ \hline u & d \\ \hline \end{array} \Rightarrow \text{isospin } I=0 \text{ particle.} \end{array}$$

$$\begin{array}{|c|c|} \hline a & b \\ \hline c & d \\ \hline \end{array} = (\epsilon^{ac}\epsilon^{bd} + \epsilon^{ad}\epsilon^{bc})q_a q_b q_c q_d$$
(11.12)

The isospin of a pentaquark can only be  $I = 0$  and its wave function is lying in the  $SU(2)_I$  singlet. The apparent absence of the  $I_3 = +1, \Theta^{++}$  in  $K^+p$  experiments argues also against  $I = 1$ .

### 11.2.3 Color

The pentaquark has to form a color singlet like all the other physical particles. There are three different projectors into the color singlet [160]:

$$\begin{array}{|c|c|} \hline a & b \\ \hline c & \bar{e} \\ \hline d & \bar{e} \\ \hline \end{array} \Rightarrow (\epsilon^{acd}\delta_e^b + \epsilon^{bcd}\delta_e^a)q_a q_b q_c q_d \bar{q}^e$$
(11.13)

$$\begin{array}{|c|c|} \hline a & c \\ \hline b & \bar{e} \\ \hline d & \bar{e} \\ \hline \end{array} \Rightarrow (\epsilon^{abd}\delta_e^c + \epsilon^{cbd}\delta_e^a)q_a q_b q_c q_d \bar{q}^e$$
(11.14)

$$\begin{array}{|c|c|} \hline a & d \\ \hline b & \bar{e} \\ \hline c & \bar{e} \\ \hline \end{array} \Rightarrow (\epsilon^{abc}\delta_e^d + \epsilon^{dbc}\delta_e^a)q_a q_b q_c q_d \bar{q}^e$$
(11.15)

### 11.2.4 Spin

Since there are no experimental predictions for the spin of the pentaquark we only know that the quarks are fermions and thus we are allowed to handle the spin structure within the  $SU(2)_S$  group. For the pentaquark the spins can be arranged in the following ways:

$$\begin{array}{|c|c|c|c|c|} \hline & & & & \\ \hline \end{array} \Rightarrow \text{spin-}\frac{5}{2} \text{ particle}$$

$$\begin{array}{|c|c|c|c|c|c|} \hline \uparrow & \uparrow & \uparrow & \uparrow & \uparrow & \uparrow \\ \hline \end{array}$$
(11.16)

$$\begin{array}{|c|c|c|c|} \hline & & & \\ \hline & & & \\ \hline & & & \\ \hline \end{array} \Rightarrow \text{spin-}\frac{3}{2} \text{ particle}$$

$$\begin{array}{|c|c|c|c|} \hline \uparrow & \uparrow & \uparrow & \uparrow \\ \hline \downarrow & & & \\ \hline \end{array}$$
(11.17)

$$\begin{array}{|c|c|c|} \hline & & \\ \hline & & \\ \hline & & \\ \hline \end{array} \Rightarrow \text{spin-}\frac{1}{2} \text{ particle}$$

$$\begin{array}{|c|c|c|} \hline \uparrow & \uparrow & \uparrow \\ \hline \downarrow & \downarrow & \\ \hline \end{array}$$
(11.18)

Because the  $\Theta^+$  is the lightest pentaquark most of the models predict that it is a spin- $\frac{1}{2}$  particle. In our calculation we are also using this assumption.

## 11.2.5 Orbital

We want to calculate the pentaquark on the lattice. At the moment we can only work with  $s$ -wave propagators, in the near future there will also be  $p$ -wave propagators available. Assuming there are only  $s$ - or  $p$ -wave excitations in the pentaquark, then we are in the  $SU(2)_O$ :

$$\begin{array}{|c|c|c|c|} \hline & & & \\ \hline \end{array} \Rightarrow \text{parity } P = \pm , \quad (11.19)$$

$$\begin{array}{|c|c|c|} \hline & & \\ \hline \end{array} \Rightarrow \text{parity } P = \pm , \quad (11.20)$$

$$\begin{array}{|c|c|} \hline & \\ \hline \end{array} \Rightarrow \text{parity } P = \pm . \quad (11.21)$$

Depending on the excitations of the quarks within the pentaquark, it could be either a positive or a negative parity state. Since all experimental searches for the pentaquark have failed, one should include always both possible parity states in lattice calculations.

## 11.3 Details of our lattice calculation

### 11.3.1 Lattice interpolators

We considered the following interpolating fields as basis for our correlation matrix:

- Currents suggested by Csikor/Fodor [149]:

$$I_{0/1} = \epsilon_{abc} [u_a^T C \gamma_5 d_b] [u_e \bar{s}_e i \gamma_5 d_c \mp (u \leftrightarrow d)] . \quad (11.22)$$

Here the diquark and the triquark have the quantum numbers:

$$u_a^T C \gamma_5 d_b - d_a^T C \gamma_5 u_b = \bar{3}_C, 3_O, \bar{3}_F, 1_S \quad L = 0; S = 0; J = 0; P = + , \quad (11.23)$$

$$u_e \bar{s}_e i \gamma_5 d_c - d_e \bar{s}_e i \gamma_5 u_c = 3_C, 4_O, \bar{6}_F, 2_S \quad L = 0; S = \frac{1}{2}; J = \frac{1}{2}; I = 0; P = - , \quad (11.24)$$

$$u_e \bar{s}_e i \gamma_5 d_c + d_e \bar{s}_e i \gamma_5 u_c = 3_C, 4_O, 15_F, 2_S \quad L = 0; S = \frac{1}{2}; J = \frac{1}{2}; I = 1; P = - . \quad (11.25)$$

This interpolator has only overlap with a  $J = \frac{1}{2}$  state. The lowest mass that Csikor/Fodor find has negative parity and is an isospin singlet. In their analysis in [149] they found a mass of  $1539 \pm 50$  MeV for their  $I^P = 0^-$  state and identified it as the  $\Theta^+$ .

- Currents suggested by Sasaki [150]:

$$\Theta_+^1 = \epsilon_{abc} \epsilon_{aef} \epsilon_{bgh} (u_e^T C d_f) (u_g^T C \gamma_5 d_h) C \bar{s}_c^T , \quad (11.26)$$

$$\left( \begin{array}{l} u_e^T C d_f = \bar{3}_C, 1_O, \bar{3}_F, 3_S \quad L = 1; S = 1; J = 0; P = - \\ u_g^T C \gamma_5 d_h = \bar{3}_C, 3_O, \bar{3}_F, 1_S \quad L = 0; S = 0; J = 0; P = + \end{array} \right) ,$$

$$\Theta_{+,\mu}^2 = \epsilon_{abc} \epsilon_{aef} \epsilon_{bgh} (u_e^T C \gamma_5 d_f) (u_g^T C \gamma_5 \gamma_\mu d_h) C \bar{s}_c^T , \quad (11.27)$$

$$\left( \begin{array}{l} u_e^T C \gamma_5 d_f = \bar{3}_C, 3_O, \bar{3}_F, 1_S \quad L = 0; S = 0; J = 0; P = + \\ u_g^T C \gamma_5 \gamma_\mu d_h = \bar{3}_C, 1_O, \bar{3}_F, 1_S \quad L = 1; S = 0; J = 1; P = - \end{array} \right) ,$$

$$\Theta_{-,\mu}^3 = \epsilon_{abc} \epsilon_{aef} \epsilon_{bgh} (u_e^T C d_f) (u_g^T C \gamma_5 \gamma_\mu d_h) C \bar{s}_c^T . \quad (11.28)$$

$$\left( \begin{array}{l} u_e^T C d_f = \bar{3}_C, 1_O, \bar{3}_F, 3_S \quad L = 1; S = 1; J = 0; P = - \\ u_g^T C \gamma_5 \gamma_\mu d_h = \bar{3}_C, 1_O, \bar{3}_F, 1_S \quad L = 1; S = 0; J = 1; P = - \end{array} \right) ,$$

One can rewrite the color structure of Eqs. (11.26)-(11.28):

$$\epsilon_{abc} \epsilon_{aef} \epsilon_{bgh} = (\delta_{be} \delta_{cf} - \delta_{bf} \delta_{ce}) \epsilon_{bgh} , \quad (11.29)$$

$$= \delta_{cf} \epsilon_{egh} - \delta_{ce} \epsilon_{fgh} . \quad (11.30)$$

One sees very easily that the relative sign in the color projector differs from that one proposed by Glozman in [160]. However, it is expected to have overlap with the color singlet on the lattice, too.

The analysis in [150] gives a null-result for a positive parity state and favors the  $\Theta^+$  pentaquark in a  $J^P = \frac{1}{2}^-$  state.

- Currents which are suggestions by L. Ya. Glozman [160], however, using only  $s$ -wave quarks instead of a mixture of  $s$ -wave and  $p$ -wave quarks in (11.31) and (11.32):

$$I_\mu = (\delta_{ae}\delta_{bg} + \delta_{be}\delta_{ag})\epsilon_{gcd} \begin{pmatrix} u_a^T C u_b \\ \frac{1}{\sqrt{2}}(u_a^T C d_b + d_a^T C u_b) \\ d_a^T C d_b \end{pmatrix} \begin{pmatrix} d_c^T (C\gamma_\mu) d_d \\ \frac{1}{\sqrt{2}}(u_c^T (C\gamma_\mu) d_d + d_c^T (C\gamma_\mu) u_d) \\ u_c^T (C\gamma_\mu) u_d \end{pmatrix} C\bar{s}_e^T, \quad (11.31)$$

$$\begin{pmatrix} d_1 = 6_C, 1_O, 6_F, 3_S & L = 1; S = 1; J = 0; P = - \\ d_2 = \bar{3}_C, 3_O, 6_F, 3_S & L = 0; S = 1; J = 1; P = + \end{pmatrix},$$

and

$$I = (\delta_{ae}\delta_{bg} + \delta_{be}\delta_{ag})\epsilon_{gcd} \begin{pmatrix} u_a^T (C\gamma_\mu\gamma_5) u_b \\ \frac{1}{\sqrt{2}}(u_a^T (C\gamma_\mu\gamma_5) d_b + d_a^T (C\gamma_\mu\gamma_5) u_b) \\ d_a^T (C\gamma_\mu\gamma_5) d_b \end{pmatrix} \begin{pmatrix} d_c^T (C\gamma_\mu) d_d \\ \frac{1}{\sqrt{2}}(u_c^T (C\gamma_\mu) d_d + d_c^T (C\gamma_\mu) u_d) \\ u_c^T (C\gamma_\mu) u_d \end{pmatrix} C\bar{s}_e^T, \quad (11.32)$$

$$\begin{pmatrix} d_1 = 6_C, 1_O, 6_F, 3_S & L = 1; S = 1; J = 1; P = - \\ d_2 = \bar{3}_C, 3_O, 6_F, 3_S & L = 0; S = 1; J = 1; P = + \end{pmatrix}.$$

- Other currents related to suggestions by L. Ya. Glozman [160], using only  $s$ -wave quarks and a factor  $(\delta_{ae}\delta_{bg} - \delta_{be}\delta_{ag})$  instead the factor  $(\delta_{ae}\delta_{bg} + \delta_{be}\delta_{ag})$  in (11.33) and (11.34):

$$I_\mu = (\delta_{ae}\delta_{bg} - \delta_{be}\delta_{ag})\epsilon_{gcd}[u_a^T (C\gamma_\mu\gamma_5) d_b - d_a^T (C\gamma_\mu\gamma_5) u_b][u_c^T (C\gamma_5) d_d - d_c^T (C\gamma_5) u_d] C\bar{s}_e^T, \quad (11.33)$$

$$\begin{pmatrix} d_1 = \bar{3}_C, 1_O, \bar{3}_F, 1_S & L = 1; S = 0; J = 1; P = - \\ d_2 = \bar{3}_C, 3_O, \bar{3}_F, 1_S & L = 0; S = 0; J = 0; P = + \end{pmatrix},$$

and

$$I_\nu = (\delta_{ae}\delta_{bg} - \delta_{be}\delta_{ag})\epsilon_{gcd} \begin{pmatrix} u_a^T (C\sigma_{\mu\nu}) u_b \\ \frac{1}{\sqrt{2}}(u_a^T (C\sigma_{\mu\nu}) d_b + d_a^T (C\sigma_{\mu\nu}) u_b) \\ d_a^T (C\sigma_{\mu\nu}) d_b \end{pmatrix} \begin{pmatrix} d_c^T (C\gamma_\mu) d_d \\ \frac{1}{\sqrt{2}}(u_c^T (C\gamma_\mu) d_d + d_c^T (C\gamma_\mu) u_d) \\ u_c^T (C\gamma_\mu) u_d \end{pmatrix} C\bar{s}_e^T, \quad (11.34)$$

$$\begin{pmatrix} d_1 = \bar{3}_C, 1_O, 6_F, 3_S & L = 1; S = 1; J = 2; P = - \\ d_2 = \bar{3}_C, 3_O, 6_F, 3_S & L = 0; S = 1; J = 1; P = + \end{pmatrix}.$$

While the interpolating fields (11.22) to (11.28) have already been used in other lattice calculations the interpolators (11.31) to (11.34) have been tested on the lattice by our group first.

Note that we do not have the resources to produce  $p$ -waves. Therefore, the Glozman interpolators in (11.31)-(11.34) cannot be reproduced in a proper way. Furthermore, we have to adjust the color projectors in (11.33) and (11.32) which also gives the interpolating fields other color quantum numbers as proposed by Glozman. However, all considered operators have in principle overlap with a 5-quark state, which consists out of four light quarks and one heavier strange antiquark. Putting this combination on a lattice, we expect to have a reasonable large overlap with the  $\Theta^+$ , although we might miss its exact quantum numbers.

### 11.3.2 Spin and parity projection

In order to get only spin-1/2 pentaquarks, we have to project our interpolators to definite spin. This is done using the spin projection operator for a Rarita-Schwinger field. The corresponding spin-1/2 state can be projected

by applying the projection operator defined in (8.57) and (8.53). In Section 8.2.2 we show that choosing the temporal components of the Lorentz indices at zero momentum is sufficient to get only spin-1/2 contributions.

Our baryon correlators are also projected to definite parity using the projection operator  $P^\pm = \frac{1}{2}(1 \pm \gamma_4)$ . We have antiperiodic boundary conditions in the temporal direction and thus we obtain two matrices of correlators:

$$\hat{C}_{ij}^+(t) = Z_{ij}^+ e^{-tE^+} + Z_{ij}^- e^{-(T-t)E^-}, \quad (11.35)$$

when we project with  $P^+$  and

$$\hat{C}_{ij}^-(t) = -Z_{ij}^- e^{-tE^-} - Z_{ij}^+ e^{-(T-t)E^+}, \quad (11.36)$$

when we use  $P^-$  as shown in [85]. These two matrices are combined to

$$\hat{C}(t) = \frac{1}{2} \left( \hat{C}^+(t) - \hat{C}^-(T-t) \right), \quad (11.37)$$

to improve the statistics. The parity channel of the  $\Theta^+$  is not known. There are conflicting theoretical predictions and no conclusive experimental data. Thus we look at both channels.

## 11.4 Analysis

For the interpolators (11.31)-(11.34)  $p$ -wave quarks<sup>4</sup> would be required. Since we do not have  $p$ -wave sources we had to adjust the color structure in the interpolators (11.33) and (11.34) to obtain a signal at all<sup>5</sup>. By doing so one immediately sees that the interpolator (11.33) becomes, up to a constant factor, the same as the operator (11.27). Performing a small test simulation on a few configurations, we find that the interpolator (11.32) is numerically the same as interpolator (11.26). Therefore we exclude the interpolators (11.26) and (11.27) from our analysis.

The interpolator (11.33) contains two diquarks with  $I = 0$  and so it has isospin  $I = 0$ . In contrast the interpolators (11.31), (11.32) and (11.34) are linear combinations of two diquarks with  $I = 1$ . Thus they are a mixture of isospin  $I = 0$  and  $I = 2$  states.

We also have to exclude the interpolators (11.22) because the cross correlations between them and the other interpolating fields are more complex and thus more demanding in computation.

We use the remaining five interpolators to calculate a cross correlation matrix  $\hat{C}_{ij}(t)$  which is then inserted into the generalized eigenvalue problem as in Section 8.3.2. Ordering the five eigenvalues according to their absolute value the largest eigenvalue in the positive parity channel should give the  $\Theta^+$  mass if  $\Theta^+$  is a positive parity particle. The second largest eigenvalue in the negative parity channel should give the  $\Theta^+$  mass, where the largest eigenvalue corresponds to the  $n$ - $K$  scattering state at rest.

The parameters of our calculation are collected in table G.1.

## 11.5 Results

The results of our calculations are shown in Fig. 11.4, where we plot the effective masses of the two lowest lying states of both parity channels obtained with the cross-correlation technique (cf. Section 8.3.2). These states are approaching a possible plateau very slowly as we expected, since states consisting of five quarks are very complicated and therefore should contain a large number of excited states which have to die out before the effective mass reaches a plateau. We use in addition to the cross-correlation technique Jacobi smeared Gaussian quark sources for all our quarks to improve the signal for the lowest lying states.

The lower dashed horizontal line in the negative parity channel is the sum of the nucleon and kaon mass at rest in the ground state obtained from a separate calculation on the same lattice. Since we project the final

<sup>4</sup>Quarks with an orbital  $p$ -wave excitation in their spatial wave functions.

<sup>5</sup>We changed the color factor  $(\delta_{ae}\delta_{bg} + \delta_{be}\delta_{ag})$  into  $(\delta_{ae}\delta_{bg} - \delta_{be}\delta_{ag})$ .

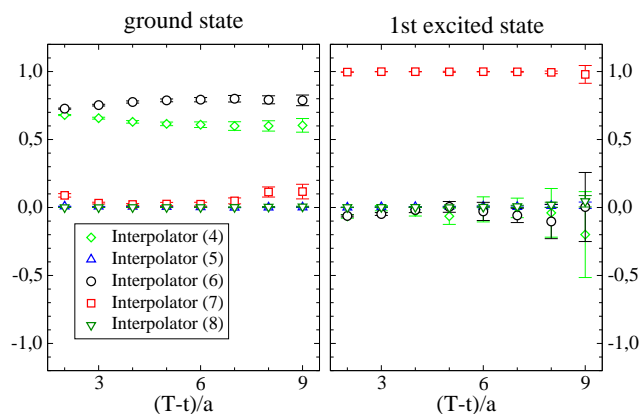


Figure 11.3: Plot of the eigenvector components for  $am_q = 0.08$  which corresponds to the pion mass  $m_\pi = 0.66$  GeV. The left hand side plot shows the eigenvector components of the negative parity ground state, the right hand side plot is for the negative parity first excited state. The eigenvectors are obviously stable and different. Thus, we conclude that we observe two independent states.

state to zero momentum a scattering state can also be a two particle state where the two particles have the same but antiparallel momentum, i.e.,  $\vec{p}_n = -\vec{p}_K$ . We use the relativistic  $E$ - $p$ -relation to calculate the energy of such states,

$$E = \sqrt{p^2 + m_n^2} + \sqrt{p^2 + m_K^2}, \quad (11.38)$$

where the smallest momentum is  $2\pi/L \approx 700$  MeV on our lattice. In Fig. 11.4 this energy is represented by the upper solid horizontal line.

In contrast to similar calculations we performed for ordinary mesons and baryons we do not find clean mass plateaus in this case. This implies also that we cannot perform any systematic chiral extrapolation. The signals we get are compatible with  $n$ - $K$  continuum states, but do not unambiguously identify them. For the latter we would have needed results for different volumes, which would have been very expensive. Furthermore, we are not interested in identifying such a continuum state, but only want to know whether there is any indication for a novel bound state.

In the negative parity channel we find effective mass plateaus which are consistent with the lowest  $n$ - $K$  scattering states. We find that the second state is noisy but within errors consistent with the energy in Eq. (11.38). Therefore, it is most likely that we do not observe a  $\Theta^+$  state in the negative parity channel. Naturally, if the  $\Theta^+$  were broad, which implies that it would mix strongly with the continuum, our conclusion would be weakened. However, for the  $\Theta^+$  this possibility is excluded experimentally.

From the composition of the eigenvectors, shown in Fig. 11.3, we conclude that the two lowest-lying states are really independent of each other. One can also see that some of the interpolators which have not been used in previous studies actually give large contributions to the low-lying states.

In the positive parity channel one expects to find either a bound  $\Theta^+$  or an excited  $n$ - $K$  scattering state. For such an excited state there are several possibilities, e.g.,  $n^*$ - $K$ , or  $n$ - $K$  with relative angular momentum, and so on.

On the positive parity side, we also show the two lowest lying states obtained from our calculation. Both of them are too heavy to have anything to do with the  $\Theta^+$ . They probably correspond to excited  $n$ - $K$  scattering states. If there would be a signal belonging to the  $\Theta^+$  it is supposed to lie below the solid line in Fig. 11.4 assuming that the chiral extrapolation of the  $\Theta^+$  does not lead to dramatic effects below our smallest quark mass. (A serious chiral extrapolation would require cleaner mass plateaus as noted above.)

## 11.6 What is still missing?

Due to a lack of computer resources we could not compute what would have been needed for either a clear identification or a null-result of the  $\Theta^+$ . In this Section we show a program of what is done by other groups to get further access to the properties of the  $\Theta^+$ .

### 11.6.1 Width of the $\Theta^+(1540)$

One of the curious features in the predictions by Diakonov, Petrov and Polyakov in [121] is the small width of the  $\Theta^+(1540)$  of less than 25 MeV. A small width is equal to a long lifetime because of the Heisenberg uncertainty principle. But the  $\Theta^+(1540)$  occurs in experiments as an intermediate particle which decays in a neutron  $n$  and a  $K^+$  meson. The channel to the  $n$ - $K$  scattering state is not suppressed because it does not involve any quark pair production and thus it is expected that the  $\Theta^+$  should have a very wide decay width of several hundreds of MeV. Michael in [166] even claims that a narrow pentaquark above  $n$ - $K$  threshold is not possible in QCD at all.

In [167] Lüscher proposes a way to determine the decay width from the scattering phase shifts  $\delta(k)$  for different momenta  $k$  calculated on the lattice where one particle decays into two particles with masses  $m_1$  and  $m_2$ . One uses here the fact that these phase shifts can be fitted to a Breit-Wigner model:

$$\tan \delta(k) = \frac{\Gamma/2}{E_0 - W(k)}, \quad \text{with} \quad W(k) = \sqrt{m_1^2 + k^2} + \sqrt{m_2^2 + k^2}, \quad (11.39)$$

where  $\Gamma$  and  $E_0$  are the parameters of the fit and  $W(k)$  is the two-particle energy on the lattice carrying momentum  $k$ . We can identify the fit parameter  $\Gamma$  with the decay width of the particle.

If the decay width is very narrow, it may be difficult to extract its width from the two-particle energy spectrum in finite volume. Only if the spectrum is determined very precisely, it is possible to use this technique. However, this is not possible for our data, i.e., the size and the statistics of our  $12^3 \times 24$  lattice data are too small.

### 11.6.2 Determination of the $n$ - $K$ scattering state

If there is a bound state it does not depend on the finite volume extrapolation  $V \rightarrow 0$ . In the case where we have two particles on the lattice, the situation is different. The result for their masses is strongly related to the volume in which they still feel the presence of each other.

On the lattice one has to determine the volume dependence of a particle to exclude that it is a two-particle state and vice versa. It was advocated in [156] to study the volume dependence of the spectral weights. If it is a one particle state, the spectral weight for the correlator constructed with point source and zero momentum point sink has essentially no volume dependence. On the other hand, if it is a two-particle scattering state with relatively weak interaction, it is inversely proportional to the spacial volume from the normalization factor. In our case we have only the resources for one single lattice. Therefore we are not able to determine the volume dependence of the  $\Theta^+$ .

### 11.6.3 $p$ -waves

In (11.33) and (11.34) we have to change the color structure from  $\delta_{ae}\delta_{bg} + \delta_{be}\delta_{ag}$  into  $\delta_{ae}\delta_{bg} - \delta_{be}\delta_{ag}$ . The remaining interpolators still have overlap with a pentaquark state, but for the other color structure it is believed that the overlap is much more enhanced. In order to get there a signal at all, we would have to use a  $p$ -wave for at least one out of the 5 quarks.

There is a possibility to implement  $p$ -waves on the lattice by applying in a covariant derivative to create a node in the wavefunction. But also this would exceed the computer resources we have access to within this project. For these derivatives we would need all-to-all propagators probably, but this is usually not done for quenched configurations.

### 11.6.4 Boundary conditions

The question is how to identify the pentaquark signal in the correlator, because the correlator at large Euclidian time is dominated by the ground state, the  $n$ - $K$  scattering state. In [168] a new method is developed which uses that a scattering state is sensitive to the spacial boundary condition (BC), while a compact one-particle state is expected to be insensitive. Practically, one calculates the correlator for two spacial boundary conditions: (1) periodic BC (PBC) for all  $u$ -,  $d$ - and  $s$ -quarks, (2) hybrid BC (HBC) where antiperiodic BC for  $u$ -,  $d$ -quarks and periodic BC for  $s$ -quark are used. Now, with PBCs, all of  $\Theta^+$ ,  $n$  and  $K$  are subject to periodic, spacial BCs, while with HBCs  $\Theta^+ = uudd\bar{s}$  remains subject to periodic BCs (it contains an even number of  $u$ - and  $d$ -quarks),  $n = udd$  and  $K^+ = \bar{s}u$  are subject to antiperiodic BC (they contain an odd number of  $u$ - and  $d$ -quarks).

Therefore, the energies of  $n$ - $K$  states are shifted, if we compare PBC with HBC, due to the momentum of  $n$  and  $K$ , while there is no energy shift for  $\Theta^+$ . In this way, the different behavior between the  $n$ - $K$  scattering state and the  $\Theta^+$  can be used to identify either the  $\Theta^+$  or the  $n$ - $K$  scattering state.

However, also this method is not feasible within our limited computer resources, because this would mean to calculate all the Dirac propagators with the lighter masses again, but now using the HBCs.

### 11.6.5 Dynamical simulations

In all simulations in the quenched approximation we neglect fermion loops and thus, we do not necessarily reproduce the real world out of our results. Especially the spectroscopy of positive parity excited baryons is very sensitive to this. We show this also in the previous Chapter 10 and we conclude for baryons that the excited positive parity states always come out 20% - 25% above the experimental results, because of the quenched approximation, where we miss a significant part of chiral physics. All published quenched lattice calculations are facing the same problem, that they cannot estimate the effect which arises from quenching. Differently to the excited baryons we do not have settled experimental results with which we can compare our results. Therefore, we are not able to estimate the quenching effects at all.

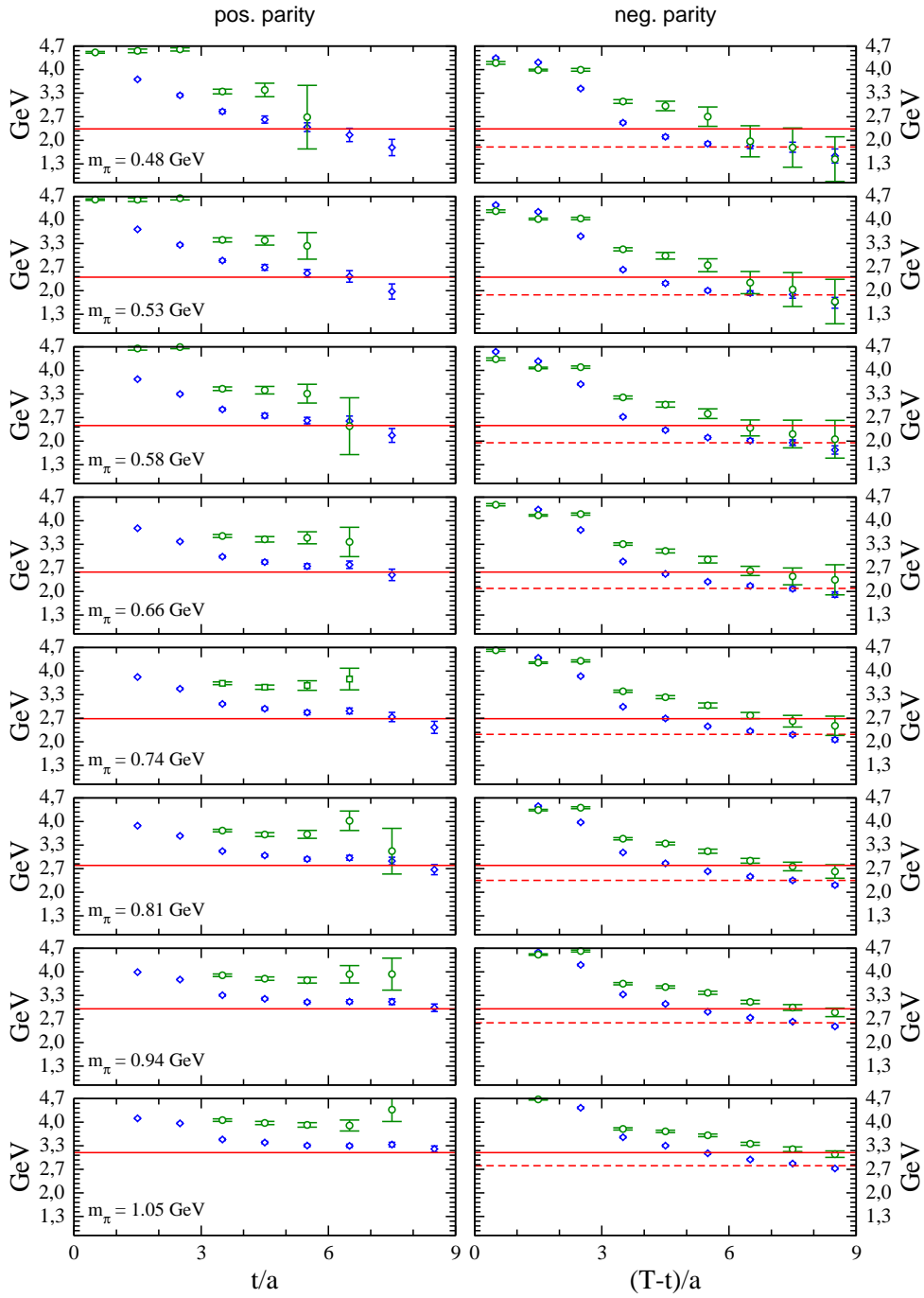


Figure 11.4: Results from cross-correlation of our final set of interpolating fields, i.e., (11.28), (11.31), (11.32), (11.33) and (11.34). We show effective masses for the two lowest-lying eigenvalues computed according to Eq. (9.63). The dashed line represents  $M_n + M_K$  obtained from a separate calculation on the same lattice. The solid line is the energy for the smallest momentum calculated according to Eq. (11.38). For all our quarks we use Jacobi smeared Gaussian sources.

## Part IV

# LQCD with 2+1 flavors using the fixed-point action

These projects were done within the BGR collaboration, especially together with the Bern group around Prof. Dr. Peter Hasenfratz and Dr. Ferenc Niedermayer. One of our first tasks was to port and to optimize an existing code running already on the Hitachi SR8000 in Munich onto the new SGI Altix 4700 system in Garching ranked on 10th place in the Top500 list from June 2007 (cf. TOP500 Supercomputing Sites). On this system it is possible to do dynamical simulations on larger lattices with even smaller pion masses.

## Algorithm

In Chapter 12 we describe the algorithm for our dynamical simulation of quarks with  $2 + 1$  flavors. Due to a special smearing step in the gauge update, which requires a projection to  $SU(3)_C$ , we are not able to use the state-of-the-art algorithm, a variant of a Hybrid Monte Carlo (HMC) algorithm. Therefore we have to use nested accept/reject steps in the generation of gauge configurations. We use some improvements to enlarge the acceptance rate of the algorithm and make the numerical simulation more stable. However, the gauge update was already very well tested in the quenched approximation and we still find a very good chiral behavior, which allows to simulate very small quark masses. Furthermore our dynamical algorithm applying the FP action does not suffer from large cutoff effects and is about  $\mathcal{O}(10)$  times cheaper than a full QCD simulation using the overlap operator.

The main task was to optimize the matrix-vector multiplication on the new HPC system in Garching/Munich, using the large cache there more efficiently, and improving the parallelization and communications issues. The matrix-vector multiplication is the efficiency limiting operation there, because it occurs in nearly all steps of our algorithm. Although the algorithm was already presented in [169] it was necessary to implement many parts of it on the new machine in Garching again.

## LECs

Beside the algorithmic issues we also want to address physics. Due to the fact that we have up to now only an algorithm which depends on the square of the lattice volume ( $V^2$  algorithm), we are restricted to smaller volumes. However, we can reach very small quark masses and thus, we are able to reach the  $\epsilon$ - and  $\delta$ -regime (cf. Section 3.3). There we have, compared to the  $p$ -regime, very easily access to low energy constants of the effective chiral Lagrangian. While the  $\epsilon$ -regime is subject to more and more lattice calculations, the  $\delta$ -regime is a nearly untouched field, which holds different NLO low energy constants readily, which can only hardly be seen in the  $\epsilon$ -regime.

Our first project was aiming for the  $\delta$ -regime. On a relatively small, asymmetric  $8^3 \times 24$  lattice we claim to already be in the  $\delta$ -regime. We find rotator excitations which allow us to determine the low energy constant  $F$  as a first test.

In the second part of the project we use a symmetric lattice in the  $\epsilon$ -regime to find the low energy constant  $\Sigma$  of the chiral perturbation theory via comparing our lattice results with RMT predictions. We also examine the correlation functions, where we can again obtain the bare chiral condensate  $\Sigma$  with a different method and finally determine the pion decay constant  $F$ .

## Chapter 12

# Algorithm for dynamical fermions

We want to do a dynamical simulation with quarks of  $2 + 1$  flavors. The action in this case looks like:

$$S(U; \bar{u}, u, \bar{d}, d, \bar{s}, s) = \beta S_g(U) + \bar{u}D^{(m_{ud})}u + \bar{d}D^{(m_{ud})}d + \bar{s}D^{(m_s)}s, \quad (12.1)$$

where  $\beta$  is the inverse coupling (5.18),  $S_g$  is the FP gauge action (5.29) and  $D^{(m_{ud})}$ ,  $D^{(m_s)}$  are the massive parametrized FP Dirac operators (6.49) for the two degenerate light  $u$ -,  $d$ -quarks and the heavier  $s$ -quark, respectively. After integrating out the fermion fields shown in Appendix B we obtain determinants in the path integral, which we write into the exponential, and thus derive an effective action, which we again denote as  $S$  in the following and which only depends on the gauge configurations:

$$\begin{aligned} S(U) &\simeq \beta S_g(U) - 2 \ln (\det D^{(m_{ud})}) - \ln (\det D^{(m_s)}) \\ &= \beta S_g(U) - \ln (\det D^\dagger(m_{ud})D^{(m_{ud})}) - \ln (\det D^{(m_s)}). \end{aligned} \quad (12.2)$$

The Dirac operator is a large matrix and would be very expensive to calculate its determinant repeatedly after changing the gauge field  $U$ . We shall estimate the determinant stochastically, which introduces fluctuations. A large part of these fluctuations are coming from the UV-modes. The idea is now to reduce the fluctuations in the UV-modes (Reduction) and also to treat the low-lying eigenmodes exactly (Subtraction). Using Reduction and Subtraction we can improve the condition number of inversion of the Dirac operator tremendously, which at the same time makes it computationally much easier to compute the stochastic estimator. Furthermore we apply relative gauge fixing and discuss two ways of a determinant breakup in the stochastic estimator to improve the acceptance rate of our Monte Carlo algorithm. Although we get a stable and working algorithm it scales with the square of the volume ( $V^2$  algorithm), which is inferior to a Hybrid Monte Carlo algorithm ( $\sim V$  algorithm). However, one should note that changing the topological charge is very expensive with the Hybrid Monte Carlo [170], while working in a fixed topological sector [171] is certainly unclean.

We recapitulate the steps of the algorithm as already published in [169] and add some new algorithmic improvements of the current code which also have to be implemented on the SGI Altix 4700 system in Garching. The code has been modified such that we are able to use several different ways of parallelizations. Therefore the most time consuming part of the code, i.e., the matrix-vector multiplication, has to be tuned and improved such that an efficient parallelization is possible.

### 12.1 Update

As discussed in Chapter 7 we have to calculate the difference between the actions of the valid and the competitor configuration  $U, U'$ , respectively.

$$\Delta S = \beta(S'_g - S_g) - \ln \left( \det \frac{D'^\dagger(m_{ud})D'(m_{ud})}{D^\dagger(m_{ud})D(m_{ud})} \right) - \ln \left( \det \frac{D'(m_s)}{D(m_s)} \right), \quad (12.3)$$

$$= \beta(S'_g - S_g) - \ln \left( \det \frac{D'^\dagger(m_{ud})D'(m_{ud})}{D^\dagger(m_{ud})D(m_{ud})} \right) - \ln \left( \det \frac{\sqrt{D'^\dagger(m_s)D'(m_s)}}{\sqrt{D^\dagger(m_s)D(m_s)}} \right), \quad (12.4)$$

where the gauge actions  $S_g, S'_g$  and the Dirac operators  $D, D'$  are calculated on the configurations  $U, U'$ , respectively.

First we update the gauge part of the action in (12.2) with a Metropolis update in order to obtain a new competitor configuration  $U'$ , starting from the valid configuration  $U$ . Next we have to deal with the fermionic part of (12.2), which is more complicated because of the determinant ratios. An exact calculation of the determinant ratios would be too time consuming. One basic approach is to compute the determinant ratio stochastically. Usually one introduces the matrix  $\Omega$  via

$$\Omega(m) = A'(m)^{-1}A(m) , \quad (12.5)$$

where  $A(m_{ud}) = D(m_{ud})$  and  $A(m_s) = \sqrt{D(m_s)}$  and which gives the difference in the action in the following form:

$$\Delta S = \beta \Delta S_g + \ln [\det \Omega^\dagger(m_{ud})\Omega(m_{ud})] + \ln [\det \Omega^\dagger(m_s)\Omega(m_s)] , \quad (12.6)$$

where  $\Delta S_g = S'_g - S_g$ . Furthermore one can rewrite the determinant as an Gaussian integral:

$$\begin{aligned} \det (\Omega^\dagger \Omega)^{-1} &= \int D\eta^\dagger D\eta e^{-\eta^\dagger \Omega^\dagger \Omega \eta} \\ &= \int D\eta^\dagger D\eta e^{-\eta^\dagger \eta} e^{-(\eta^\dagger \Omega^\dagger \Omega \eta - \eta^\dagger \eta)} \\ &= \int D\eta^\dagger D\eta e^{-\eta^\dagger \eta} e^{-\Delta S_f} . \end{aligned} \quad (12.7)$$

Eq. 12.7 suggests a stochastic estimator for the determinant by taking a c-number random Gaussian noise vector  $\eta$  and calculate

$$\Delta S_f = \eta^\dagger (\Omega^\dagger \Omega - \mathbb{1}) \eta . \quad (12.8)$$

It can be shown that this procedure satisfies detailed balance [172]. One gets a stochastic estimator for the change in the action:

$$\Delta S \simeq \beta \Delta S_g + \eta_{ud}^\dagger [\Omega^\dagger(m_{ud})\Omega(m_{ud}) - \mathbb{1}] \eta_{ud} + \eta_s^\dagger [\Omega^\dagger(m_s)\Omega(m_s) - \mathbb{1}] \eta_s . \quad (12.9)$$

In the following sections we discuss improvements in the update algorithm which increase the acceptance rate for a competitor configurations. Dropping one of these improvements would drive the acceptance rate due to large fluctuations in the stochastic estimator down to nearly zero.

## 12.2 Reduction

The UV modes contribute little to the action individually, but due to the fact that there are so many of them, they dominate the fluctuations. To reduce the fluctuations we transform the Dirac operator  $D \rightarrow D_r$  such that the UV modes of the so-called reduced Dirac operator  $D_r$  are condensed into a small patch in the complex eigenvalue plane. We choose  $D_r$  such that the change in the determinant  $\det(D/D_r)$  is calculable analytically (non-stochastically).

Let in following  $x$  be a matrix. Then the reduced matrix  $x_r$  looks like

$$x_r = (1 + x)e^{-\varphi(x)} , \quad (12.10)$$

where  $\varphi(x)$  is a power series of  $N$ -th order without a constant term:

$$\varphi(x) = \sum_{n=1}^N a_n x^n . \quad (12.11)$$

If we choose  $a_n = (-1)^{n+1}/n$  we obtain

$$x_r = (1 + x)e^{-\varphi(x)} = 1 + \mathcal{O}(x^{N+1}) , \quad (12.12)$$

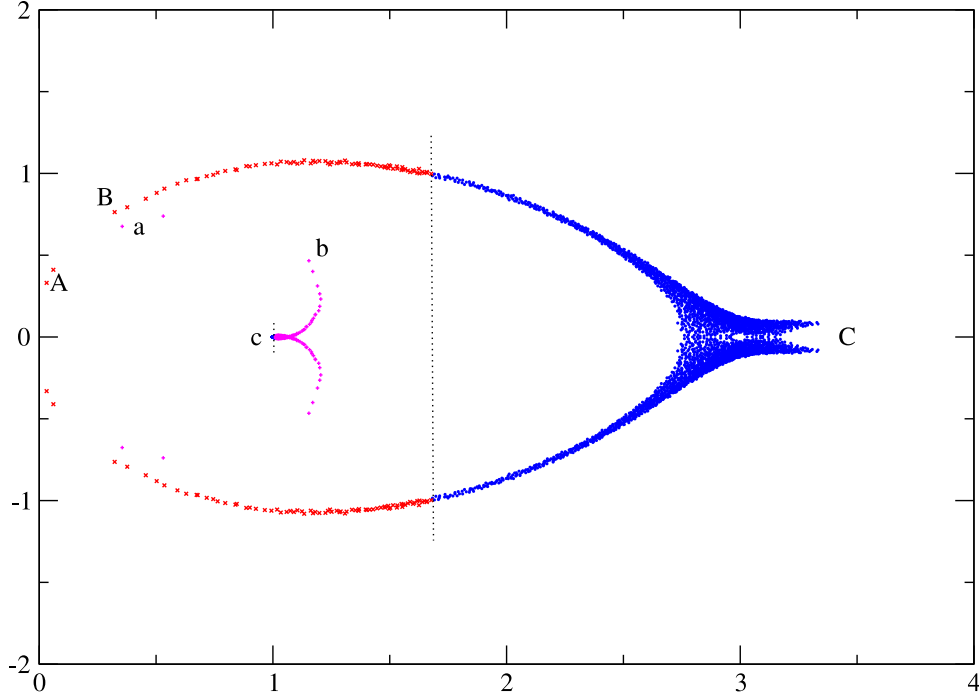


Figure 12.1: The eigenvalue spectrum of the FP Dirac operator on a single  $4^4$  gauge configuration as you can find it in [169]. The points of the larger Batman like figure correspond to the original Dirac operator, whose UV eigenvalues are located at  $(c, 0)$  in the complex plane. The points of the smaller wing-shape structure in the center represent the corresponding eigenvalues of the reduced Dirac operator  $D_r/c$ . Sections marked by  $A$ ,  $B$  and  $C$  on the original spectrum are mapped to sections  $a$ ,  $b$  and  $c$  after reduction.

and if the eigenvalues of  $x$  are close to zero, the eigenvalues of the reduced matrix are condensed at 1.

If we rescale  $D \rightarrow D/c$  and choose  $c \approx 2.8$ , where we approximately find the center of mass of the UV eigenvalues, we concentrate nearly all UV eigenvalues in a single point and thus reduce the fluctuations in the UV modes drastically. In Fig. 12.1 we show this for a 4th order power series in the reduction on a  $4^4$  lattice. We also see that the Reduction acts mainly on the UV eigenvalues  $\lambda_{UV}$  with  $|\lambda_{UV}/c - 1| \ll 1$ .

We define the reduced Dirac operator as:

$$D_r = D e^{-\sum_{n=1}^N a_n (D/c-1)^n}, \quad (12.13)$$

where we are able to calculate  $\det(D/D_r)$  analytically if we can calculate the  $n$ -th power of traces  $\text{tr}(D/c-1)^n$ .

$$\begin{aligned} \det D_r &= \det D e^{-\sum_{n=1}^N a_n \text{tr}(D/c-1)^n} \\ &= \det D e^{-\sum_{n=0}^N \alpha_n \text{tr} D^n}. \end{aligned} \quad (12.14)$$

For  $n = 0$  we get a constant term. Due to the fact that we only consider the difference between two actions, the constant term is always canceled. As  $n$  increases, the computing time and the complexity of the code to do the trace calculations increase rapidly. As a trade-off between computer resources and reducing the UV fluctuations we choose - as for the  $4^4$  lattice in Fig. 12.1 - also  $N = 4$  for our calculation on the larger lattices.

Using the reduced Dirac operator we can rewrite the action in the following way:

$$\begin{aligned} S &= \beta S_g(U) + S_{\text{UV}} \\ &- \ln \det D_r^{(m_{ud})\dagger} D_r^{(m_{ud})} - \ln \det D_r^{(m_s)} , \end{aligned} \quad (12.15)$$

where

$$S_{\text{UV}} = -2 \sum_{n=0}^4 \alpha_n \text{tr} \left( D^{(m_{ud})} \right)^n - \sum_{n=0}^4 \alpha_n \text{tr} \left( D^{(m_s)} \right)^n , \quad (12.16)$$

and the  $\alpha_n$ ,  $n = 0, \dots, 4$  are defined by Eq. 12.14. As already mentioned above in the change of the action  $\Delta S = S' - S$  one finds that the constant terms for  $n = 0$  are canceled and can thus be neglected in the calculation also.

## 12.3 Subtraction

Theoretical arguments suggest that much of the important infrared physics in hadronic interactions is encoded in the low-lying eigenmodes. In addition small eigenvalues create numerical problems if we invert the Dirac operator. This suggests to calculate the small eigenvalues and its eigenvectors and treat them exactly. We shall denote the subtracted Dirac operator by  $D_s$ , where we replace the small eigenvalues by the constant  $c \approx 2.8$  (center of mass of the UV eigenvalues). We pick up the discussion from Section 8.1.1 and write for Eq. (8.12):

$$D_s = c \sum' P_\lambda + \sum'' \lambda P_\lambda , \quad (12.17)$$

where we have replaced the low-lying eigenvalues  $\lambda$  by a constant  $c = \mathcal{O}(1)$ . One has

$$D = D_s - Q , \quad (12.18)$$

where

$$Q = \sum' (c - \lambda) P_\lambda . \quad (12.19)$$

Observe that the operator

$$D_s - c = - \sum'' (c - \lambda) P_\lambda \quad (12.20)$$

does not contain the small eigenvalues hence

$$(D_s - c)Q = Q(D_s - c) = 0 \quad (12.21)$$

and

$$(D - c)^n = (D_s - c - Q)^n = (D_s - c)^n + (-Q)^n , \quad \text{for } n > 0 . \quad (12.22)$$

Consequently, for any analytic function  $F$  we have<sup>1</sup>

$$F(D - c) = F(D_s - c) + F(-Q) - F(0) = F(D_s - c) + \sum' (F(\lambda - c) - F(0)) P_\lambda , \quad (12.23)$$

or if we shift all input variables by the constant  $c$ , we can write

$$F(D) = F(D_s) + \sum' (F(\lambda) - F(c)) P_\lambda . \quad (12.24)$$

For the determinant we have

$$\det \left( \frac{1}{c} D \right) = \left( \prod' \frac{\lambda}{c} \right) \det \left( \frac{1}{c} D_s \right) . \quad (12.25)$$

The stochastic estimator for  $\det D_s$  is expected to fluctuate much less than that for  $\det D$  because the lowest modes are absent in  $D_s$ .

<sup>1</sup>These equations can be easily checked on eigenvectors corresponding either to the low- or high-lying eigenvalues.

### 12.3.1 Combining Subtraction and Reduction

We want to subtract now the reduced Dirac operator from Eq. (12.13). For the reduced and subtracted Dirac operator  $D_{rs}$  we get:

$$D_{rs} = D e^{-\sum_n a_n (D/c-1)^n} + \sum' \left( c - \lambda e^{-\sum_n a_n (\lambda/c-1)^n} \right) P_\lambda . \quad (12.26)$$

Using the relation (12.25) we get finally:

$$\det D_r = \det D_{rs} \prod' \frac{\lambda}{c} e^{-\sum_n a_n (\lambda/c-1)^n} . \quad (12.27)$$

Using the reduced and subtracted Dirac operator we can rewrite the action in the following way:

$$\begin{aligned} S &= \beta S_g(U) + S_{UV} + S_{IR} \\ &- \ln \det D_{rs}^{(m_{ud})\dagger} D_{rs}^{(m_{ud})} - \ln \det D_{rs}^{(m_s)} \end{aligned} \quad (12.28)$$

where we can determine the IR correction  $S_{IR}$  to the action analytically again:

$$S_{IR} = 2 \sum' \left( -\ln \frac{|\lambda_{ud}|}{c} + \sum_{n=1}^4 a_n \left( \frac{\lambda_{ud}}{c} - 1 \right)^n \right) + \sum' \left( -\ln \frac{|\lambda_s|}{c} + \sum_{n=1}^4 a_n \left( \frac{\lambda_s}{c} - 1 \right)^n \right) . \quad (12.29)$$

## 12.4 Relative gauge fixing

The fluctuations in the stochastic estimator are increased by increasing the distance of the valid and the competitor gauge configuration. While we are not interested in a gauge fixed configuration in general, we use the fact that all gauge copies of our competitor configuration are equivalent. We use for the algorithm that gauge copy which is in the configuration space closest to the valid configuration. Therefore one can reduce this distance by fixing the gauge [173]. We use the condition in [169] to transform the competitor configuration  $U' \rightarrow U''$ :

$$\max_{\{U'\}} \sum_{x,\mu} \text{Re tr} \{ U'_\mu(x) U_\mu^\dagger(x) \} . \quad (12.30)$$

We are using  $U''$  only as long as we need it calculating the determinant ratios. After that we, of course, use the original competitor gauge configuration  $U'$  again.

## 12.5 Determinant breakup

For simplicity we go back to the notation of the Dirac operators as in Section 12.1. We now want to write the Dirac operator  $A$  as a product of operators  $A_i$ , helping to reduce the fluctuation of the stochastic estimator:

$$A = A_1 \times A_2 \times \dots \times A_l . \quad (12.31)$$

Thus we can write the stochastic estimator (12.8) as a sum of  $l$  terms:

$$\Delta S_f \simeq \sum_{i=1}^l \eta_i^\dagger \left( \Omega_i^\dagger \Omega_i - \mathbf{1} \right) \eta_i , \quad (12.32)$$

where  $\Omega_i = A_i'^{-1} A_i$ .

We achieve a reduction of the fluctuation in the determinant if every summand of (12.32) is close to zero. We use two different methods which are realizing the determinant breakup into smaller pieces.

### 12.5.1 Ladder method

The first method is the mass shifting or ladder method. Consider the real interval  $[0, \mu_l]$  which is divided into  $l$  intervals  $[\mu_{i-1}, \mu_i]$ ,  $i = 1, \dots, l$ . We have to start with small bins which become bigger until  $A(\mu_l) \approx 1$ , where  $A(\mu) = \frac{A+\mu}{c+\mu}$ . We get

$$\frac{1}{c}A = \frac{A(\mu_0)}{A(\mu_1)} \times \frac{A(\mu_1)}{A(\mu_2)} \times \dots \times \frac{A(\mu_{l-1})}{A(\mu_l)} \times A(\mu_l), \quad (12.33)$$

where  $\mu_0 = 0$ . Thus a single term  $A_i$  is then the ratio<sup>2</sup>

$$A_i = \frac{A(\mu_{i-1})}{A(\mu_i)} = \frac{A + \mu_{i-1}}{c + \mu_{i-1}} \frac{c + \mu_i}{A + \mu_i} \quad (12.34)$$

$$= \left(1 + \frac{\mu_i - \mu_{i-1}}{c + \mu_{i-1}}\right) \left(1 - \frac{\mu_i - \mu_{i-1}}{A + \mu_i}\right). \quad (12.35)$$

For the two degenerated  $u$ - and  $d$ -quarks or the 2-flavor case we use the reduced and subtracted Dirac operator

$$A(\mu) = \left( \frac{D_s^{(m_{ud})} + \mu}{c + \mu} \right)_r \quad (12.36)$$

$$= \frac{D_s^{(m_{ud})} + \mu}{c + \mu} \exp \left[ -\varphi \left( \frac{D_s^{(m_{ud})} + \mu}{c + \mu} - \mathbb{1} \right) \right], \quad (12.37)$$

where the function  $\varphi(x)$  is defined in (12.11) and we use (12.24) to get:

$$\frac{D_s^{(m_{ud})} + \mu}{c + \mu} = \frac{D^{(m_{ud})} + \mu}{c + \mu} + \sum' \left( 1 - \frac{\lambda^{(m_{ud})} + \mu}{c + \mu} \right) P_\lambda. \quad (12.38)$$

Thus we have to compute

$$\begin{aligned} \Omega_i \eta_i &= A_i'^{-1} A_i \eta_i = \frac{A'(\mu_i)}{A'(\mu_{i-1})} \frac{A(\mu_{i-1})}{A(\mu_i)} \eta_i = \\ &= \left( 1 - \frac{\mu_i - \mu_{i-1}}{c + \mu_i} \right) \left( 1 + \frac{\mu_i - \mu_{i-1}}{c + \mu_{i-1}} \right) \left( 1 + \frac{\mu_i - \mu_{i-1}}{D_s^{(m_{ud})'} + \mu_{i-1}} \right) \left( 1 - \frac{\mu_i - \mu_{i-1}}{D_s^{(m_{ud})} + \mu_i} \right) \times \\ &\exp \left[ \varphi \left( \frac{D_s^{(m_{ud})} + \mu_i}{c + \mu_i} - \mathbb{1} \right) - \varphi \left( \frac{D_s^{(m_{ud})} + \mu_{i-1}}{c + \mu_{i-1}} - \mathbb{1} \right) + \varphi \left( \frac{D_s^{(m_{ud})'} + \mu_{i-1}}{c + \mu_{i-1}} - \mathbb{1} \right) - \varphi \left( \frac{D_s^{(m_{ud})'} + \mu_i}{c + \mu_i} - \mathbb{1} \right) \right] \eta_i \end{aligned} \quad (12.39)$$

For the  $s$ -quark or the 1-flavor case it is even a bit more complicated:

$$A(\mu) = \sqrt{\left( \frac{D_s^{(m_s)} + \mu}{c + \mu} \right)_r} \quad (12.40)$$

$$= \sqrt{\frac{D_s^{(m_s)} + \mu}{c + \mu}} \exp \left[ -\frac{1}{2} \varphi \left( \frac{D_s^{(m_s)} + \mu}{c + \mu} - \mathbb{1} \right) \right]. \quad (12.41)$$

Therefore we have to find an approximation of the square root for the  $s$ -quark stochastic estimator (cf. Section 12.5.3).

<sup>2</sup>In this form we can calculate  $A_i$  with only one inversion step instead of one inversion and one additional matrix-vector multiplication step.

### 12.5.2 $N$ th-root method

In the second method we split up the Dirac operator  $A$  in a product of  $l$  terms:

$$\frac{1}{c}A = \prod_{i=1}^l A_i, \quad (12.42)$$

where all  $A_i$  are defined as the same:

$$A_i = \left(\frac{A}{c}\right)^{\frac{1}{l}}. \quad (12.43)$$

For the 2-flavor case we have again:

$$A_i = \left(\frac{D_s^{(m_{ud})}}{c}\right)^{\frac{1}{l}} \exp \left[ -\frac{1}{l} \varphi \left( \frac{D_s^{(m_{ud})}}{c} - \mathbf{1} \right) \right], \quad (12.44)$$

where we can use (12.24) to get the  $A_i$  depending on  $D^{(m_{ud})}$ . Then, we have to compute

$$\Omega_i \eta_i = A_i'^{-1} A_i \eta_i = \left[ \left( D_s^{(m_{ud})'} \right)^{-1} D_s^{(m_{ud})} \right]^{\frac{1}{l}} \exp \left[ \frac{1}{l} \varphi \left( \frac{D_s^{(m_{ud})'}}{c} - \mathbf{1} \right) - \frac{1}{l} \varphi \left( \frac{D_s^{(m_{ud})}}{c} - \mathbf{1} \right) \right] \eta_i. \quad (12.45)$$

In contrast to the ladder method the 1-flavor case has the same form as the 2-flavor case:

$$\begin{aligned} A_i &= \left( \sqrt{\frac{D_s^{(m_s)}}{c} \exp \left[ -\varphi \left( \frac{D_s^{(m_s)}}{c} - \mathbf{1} \right) \right]} \right)^{\frac{1}{l}}, \\ &= \left( \frac{D_s^{(m_s)}}{c} \right)^{\frac{1}{2l}} \exp \left[ -\frac{1}{2l} \varphi \left( \frac{D_s^{(m_s)}}{c} - \mathbf{1} \right) \right]. \end{aligned} \quad (12.46)$$

In both cases, in the 2-flavor and in the 1-flavor case, one has to find an approximation for the roots, but one does not need to fine-tune some parameters as, e.g., the intervals  $[\mu_{i-1}, \mu_i]$  in the ladder method. If one uses the reduced and subtracted Dirac operator and find the center of mass of the UV eigenvalues at  $(c, 0)$  in the complex plane, then most eigenvalues of  $D_{rs}/c$  are very close to one. It follows that then even for the square root  $l = 2$  the eigenvalues of  $D_{rs}/c$  are already closer to one than before. If we take a larger number for  $l$  then the situation is even more improved. However, increasing  $l$  is accompanied by increasing the number of matrix-vector multiplications and therefore one still has to trade-off numerical stability with the computational costs. Note that both, the ladder method and the  $N$ th-root method, can also be used together.

### 12.5.3 Approximation of roots

In both methods, the ladder method and the  $N$ th-root method, one has to calculate a root of the Dirac operator. This can be done in many different ways. In the first runs we used a Taylor series in  $(D/c - 1)$  to find the result of the square root in the ladder method. At the moment we are using the  $N$ th-root method for the  $s$ -quark contribution of the stochastic estimator and have replaced the Taylor expansion by a rational approximation of the roots. For a detailed review of the approximations the interested reader is referred to [174].

## 12.6 Nested Accept/Reject steps

In order to improve the acceptance rate further we use the cheaper parts of the action (12.2) more often. It is convenient to rewrite the action in a different form

$$\begin{aligned}
S &= (\beta + \delta\beta)S_g(U) \\
&+ [S_{UV}^g - \delta\beta S_g(U)] \\
&+ [S_{UV} - S_{UV}^g + S_{IR}^{\text{appr}}] \\
&+ [S_{IR} - S_{IR}^{\text{appr}} - \ln \det D_{rs}^{(m_{ud})\dagger} D_{sr}^{(m_{ud})} - \ln \det D_{rs}^{(m_s)}].
\end{aligned} \tag{12.47}$$

This is the same action as in Eq. (12.2), but now with respect to the coded algorithm<sup>3</sup>. Every line in (12.47) represents a different step in our algorithm, which is repeated depending on their computational expense:

### 1. Gauge update

The gauge update is a standard Metropolis local update with the fixed point gauge action at coupling  $\beta_{\text{eff}} = \beta + \delta\beta$ . The parameter  $\delta\beta$  mimics the missing fermion part of the action and is chosen to maximize the acceptance rate in the subsequent 1st accept/reject (A/R) step. We update  $4n_p$  gauge links with Metropolis by visiting  $n_p \leq V_s$  consecutive lattice sites.

### 2. The 1st accept/reject step

The gauge configuration created as discussed above is accepted/rejected with the action  $S_{UV}^g - \delta\beta S_g(U)$ , where  $S_{UV}^g$  is a good gauge approximation to the reduction contribution  $S_{UV}$  in Eq. (12.16). The function  $S_{UV}^g$  is represented by different gauge loops with fitted coefficients on the smeared configuration. Calculating  $S_{UV}^g$  is fast and can be done without building up the Dirac operator [169]. The deviation between  $S_{UV}^g$  and the exact Reduction  $S_{UV}$  will be corrected in the 2nd accept/reject step below. The combination of gauge updates and the 1st A/R step is repeated  $N^{\text{1st}}$  times.

### 3. The 2nd accept/reject step

In this step the Dirac operator is built on the competitor configuration  $U'$ , the traces are calculated for the exact reduction, and a certain number of the lowest eigenvalues and eigenvectors are determined. The proposed configuration is accepted/rejected with the action  $S_{UV} - S_{UV}^g + S_{IR}^{\text{appr}}$ . The first term corrects the small error we made in the 1st A/R step in approximating the traces in  $S_{UV}$  with gauge loops. The last term  $S_{IR}^{\text{appr}}$  is an approximation to the contribution of the low-lying eigenvalues to the determinant  $S_{IR}$  in Eq. 12.29.  $N_{\text{ev}}$  eigenvalues and the corresponding  $S_{IR}$  are only calculated for  $m_{ud}$  using an Arnoldi algorithm. The eigenvalues for  $m_s$  are determined from these, using leading order perturbation theory. The combination of the gauge updates, the 1st A/R steps and the 2nd A/R steps is repeated  $N^{\text{2nd}}$  times.

### 4. The 3rd accept/reject step

The cycle described above is followed by a final, stochastic accept/reject step with the action  $S_{IR} - S_{IR}^{\text{appr}} - \ln \det D_{rs}^{(m_{ud})\dagger} D_{sr}^{(m_{ud})} - \ln \det D_{rs}^{(m_s)}$ . The first part corrects the small error we made in calculating the contribution of the low-lying eigenvalues of  $D^{(m_s)}$  to the determinant in the 2nd A/R step. The second term gives the stochastic estimator of the subtracted, reduced, 2+1 flavor determinant. With this closing A/R step the algorithm becomes exact.

These steps are repeated and the accepted configurations that have managed to go through all three filters form a Markov chain corresponding to the 2+1 flavor action in (12.2) and also satisfy detailed balance.

## 12.7 Matrix-vector multiplications

In nearly all parts of our algorithm we have to multiply the Dirac operator with a vector of dimension  $12 \times V$  and thus this is due to the frequency of occurrence the most time consuming part of the algorithm. We explain in this Section the optimization tricks we are using as a real life example for code optimization.

<sup>3</sup>The meaning of the different terms will be explained in the rest of this Section.

### 12.7.1 Implementation of matrix-vector multiplication on a HPC system

Due to the fact that the Leibniz Computing Center in Garching was buying a new machine which has replaced the old SR 8000 Hitachi system, we have to transfer the already running code to the new SGI Altix 4700 system with Intel Itanium2 Montecito Dual Core processors (1.6 GHz, Level 3 Cache  $L_3 = 9$  MB, ccNUMA network).

#### Numerical costs

The parametrized fixed-point Dirac operator  $D_{\text{FP}}(x, y)$  has non-zero matrix elements if  $y$  is in the hypercube of  $x$ . Therefore a matrix-vector multiplication with the FP Dirac operator

$$w_c^\alpha(x) = \sum_{y, \beta, d} D_{\alpha, \beta}^{c, d}(x, y) v_\beta^d(y), \quad (12.48)$$

needs:

- We get  $4 + 2 + 2$  flops for every complex fused multiply-add operation and for the complex add to the result vector.
- Due to the offset of the Dirac operator living on a hypercube there are only 81 entries in the Dirac operator non-vanishing each having 12 color-Dirac indices.
- Calculating the whole  $12 \times V$  dimensional vector  $w$  we have to do this for every entry, where  $V$  is the volume of the lattice and equal with the number of sites.

Altogether this gives for a single matrix-vector multiplication:

$$\text{Costs} = 8 \times 81 \times 144 \times V \text{ Flops}. \quad (12.49)$$

In most of the cases we use the massive Dirac operator defined in (6.19):

$$D^{(m)} = \left(1 - \frac{1}{2}m\right) D + \frac{1}{2}mR^{-1}.$$

The operator  $R^{-1}$  is diagonal in Dirac space, i.e., the numerical costs of obtaining  $R^{-1}v$  is 25% of those for the  $Dv$ . The numerical costs for the massive Dirac operator are:

$$\text{Costs}^{\text{massive}} = 8 \times 81 \times 180 \times V \text{ Flops}. \quad (12.50)$$

#### Constraints

We want to compute the matrix-vector multiplication in parallel on several processors. Therefore we need data composition which is organized in our case as follows: The Dirac operator  $D$  and its offset, calculated once for a single gauge configuration  $U$ , and the vectors  $v$ ,  $w$  in Eq. (12.48) are distributed over all processors. Due to the fact that the Dirac operator lives on the hypercube we have to communicate the boundaries of the vectors.

To decrease the memory request we use the  $\gamma_5$ -hermicity of the FP Dirac operator, i.e., we store only an offset of 41 instead of 81 and build the rest out of  $D^\dagger = \gamma_5 D \gamma_5$ . Using this technique we nearly half the memory needs for the system. However, we have to do more floating point calculations, but in exchange we can make use of a faster memory access (cf. Section 12.7.1).

First we can only parallelize for  $N_4 = L_t/3$  processors at maximum in temporal direction. The reason for this constraint is the building subroutine of the Dirac operator, which also has to determine the traces for the Reduction. Only after the Dirac operator is built we can remap the indices and also parallelize with  $N_4 = L_t$  processors in the temporal direction.

In the gauge update we are using a very effective smearing, which removes UV fluctuations on the gauge configuration. This smearing also needs to know the values on the next-to-next neighboring sites. Therefore we also get constraints for the number of used processors for parallelizing the gauge update (cf. [175]).

### Matrix-vector multiplication with the FP Dirac operator

On our 4d lattice with the sizes  $L_i$ ,  $i = 1, \dots, 4$  and a volume of  $V = \prod_i L_i$  we distribute the vectors over all  $N = \prod_i N_i$  processors, where  $N_i$  is the number of processors sharing the  $i$ -th direction. We introduce global and local coordinates on each processor, which are denoted as  $y_i$  and  $x_i^{(n)}$ , respectively:

$$y_i = x_i^{(n)} + n_i \times \frac{L_i}{N_i} = x_i^{(n)} + n_i \times l_i, \quad (12.51)$$

where

$$y = (y_1, y_2, y_3, y_4), \quad \text{with } 0 \leq y_i^{(n)} \leq L_i - 1, \quad (12.52)$$

$$x^{(n)} = (x_1, x_2, x_3, x_4)^{(n)}, \quad \text{with } 0 \leq x_i^{(n)} \leq l_i - 1, \quad (12.53)$$

and  $l_i$  are the local sizes in the  $i$ -th direction on a processor and

$$n = (n_1, n_2, n_3, n_4), \quad \text{with } 0 \leq n_i \leq N_i - 1, \quad (12.54)$$

is the processor number. We also introduce a second kind of local coordinates  $z$ , which we need for the boundaries:

$$z^{(n)} = (z_1, z_2, z_3, z_4)^{(n)}, \quad \text{with } 0 \leq z_i^{(n)} \leq l_i + 1. \quad (12.55)$$

We get the dependency of  $y$  on  $z^{(n)}$  if we set  $z_i^{(n)} = x_i^{(n)} + 1$ :

$$z_i^{(n)} = y_i + 1 - n_i \times l_i. \quad (12.56)$$

Note that in contrast to  $y$  and  $x_i^{(n)}$  the local coordinates  $z^{(n)}$  do not map all the sites unambiguously, because the sites on the boundaries are also mapped on the neighboring processors. In addition to that it is still possible not to parallelize a direction  $i$  at all. Then  $z_i^{(n)}$  and  $x_i^{(n)}$  are the same in the  $i$ -th direction<sup>4</sup>.

### Indexing the coordinates

In the code we do not use vectors like shown above, instead we apply only 1d arrays, which are indexed as following:

$$\begin{aligned} y &= y_1 + L_1(y_2 + L_2(y_3 + L_3 y_4)), \\ x^{(n)} &= x_1 + l_1(x_2 + l_2(x_3 + l_3 x_4)), \\ z^{(n)} &= z_1 + L'_1(z_2 + L'_2(z_3 + L'_3 z_4)), \end{aligned} \quad (12.57)$$

where

$$L'_i = \begin{cases} L_i & \text{if we do not parallelize the } i\text{-th direction} \\ l_i + 2 & \text{if we parallelize the } i\text{-th direction} \end{cases}.$$

Using these indexing one sees immediately that transferring the boundary sites in the fourth direction means to send/receive a continuous address region. Therefore we only have to initiate two single send/receive processes transferring the boundary sites from the processor  $n = (0, 0, n_3, n_4)$  to  $n^{(\pm 4)} = (0, 0, n_3, n_4 \pm 1)$ . The situation is more complicated for the other directions, because the boundary sites do not use a connected address region there and therefore one naively has to send/receive several packages to transfer all boundary sites.

A HPC system is usually trimmed to have a network with a huge bandwidth and also a comparable small latency. However, if we would always initiate a send/receive process for every package, the latencies would be added up to a large fraction of time used for the matrix-vector multiplication. Therefore one uses derived datatypes which combine the boundary sites to only one large package which can then be transferred at once. Although the packing of the data also needs time, one has to pay the latency of initializing a send/receive process only once.

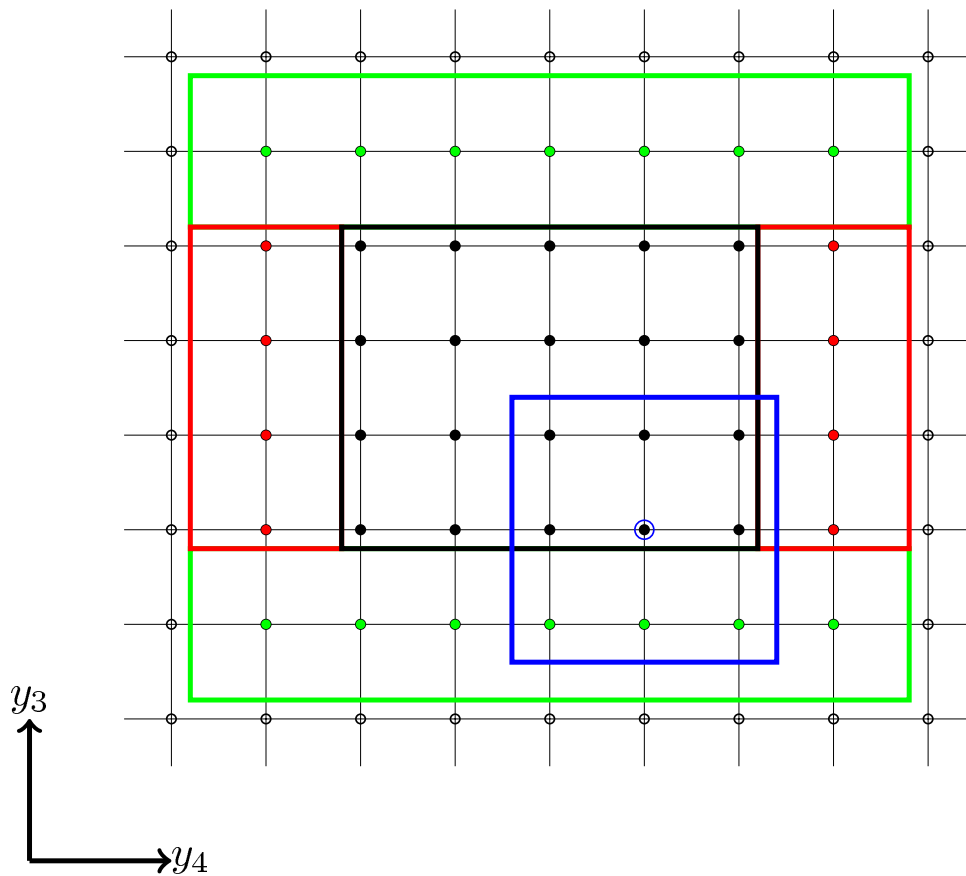


Figure 12.2: We plot here a lattice which is parallelized in two directions. The black filled circles are distributed to one processor  $n$ . But calculating the Dirac operator always needs the neighboring sites. So the processor  $n$  has to receive the boundary sites from the neighboring processors. This is done firstly in one direction, here in the  $y_4$  direction (red filled circles). After that one receives the boundary sites from the neighbors in the second direction (green filled circles,  $y_3$  direction). Here one also receives the boundary sites from the processors at the corners, i.e., from the processors  $(0, 0, n_3 + 1, n_4 + 1)$ ,  $(0, 0, n_3 + 1, n_4 - 1)$ ,  $(0, 0, n_3 - 1, n_4 + 1)$  and  $(0, 0, n_3 - 1, n_4 - 1)$ .

**Example** In Fig. 12.2 we show a part of our lattice in two dimensions, where every point represents all the sites in the  $y_1$  and  $y_2$  directions. In this example we show the case where we only parallelize in the third and the fourth direction. The sites within the black rectangular which are plotted as filled black circles are the sites where the vector  $v$  is distributed on the processor  $n = (0, 0, n_3, n_4)$ . The sites within the red rectangular, which are plotted as filled red circles, are the boundary sites of the vector in the fourth direction, which have to be received from the neighboring processors in the fourth direction  $n^{(\pm 4)} = (0, 0, n_3, n_4 \pm 1)$ . We also have to send the boundary sites to the neighboring processor, but this is not shown here. We also parallelize in the third direction and therefore we have to receive the sites of the vector within the green rectangular from the neighboring processors in the third direction  $n^{(\pm 3)} = (0, 0, n_3 \pm 1, n_4)$ . Those sites are plotted as filled green circles<sup>5</sup>. The sites which are plotted as empty black circles are not interesting, because our Dirac operator acts only on the next-neighbor sites. The blue rectangular denotes the sites which are needed to calculate the Dirac operator on the site which is plotted with a blue circle. Only after receiving the boundaries on every processor we can calculate the matrix-vector product on every black filled circle.

In terms of coordinates the data decomposition in Fig. 12.2 has the parameters  $l_4 = 5$ ,  $l_3 = 4$ ,  $n_1 = n_2 = 0$  and

<sup>4</sup>This was implemented only for one direction, which is only parallelized after the others are fully parallelized.

<sup>5</sup>We explain here the full Dirac operator with an offset of 81.

the Dirac operator has the following coordinates:

$$\begin{aligned} x^{(n)} &= (x_1, x_2, 0, 3) = x_1 + x_2 L_1 + 12 L_1 L_2 , \\ z^{(n)} &= (x_1, x_2, 1, 4) = x_1 + x_2 L_1 + L_1 L_2 + 24 L_1 L_2 , \\ y &= (x_1, x_2, 4n_3, 3 + 5n_4) = x_1 + x_2 L_1 + 4n_3 L_1 L_2 + 3 L_1 L_2 L_3 + 5n_4 L_1 L_2 L_3 . \end{aligned}$$

It is easy to see that the indices of the boundaries in the third directions are not continuous. Therefore one has to use MPI derived datatypes to minimize the latencies. For every communication between two processors one has to initialize a MPI connection and to send/receive data packets. But if the packets are too small, most of the time is spent by initializing the MPI connection and the huge bandwidth on the Altix communication network is not used. Working with MPI derived datatypes merges the non-continuous data into continuous ones, which has to be sent/received only once. Therefore the packets are larger and the bandwidth becomes important. Hiding the latencies was the main reason to rewrite the matrix-vector multiplication for the new architecture. In Table 12.1 one finds how the matrix-vector multiplication scales with different ways of parallelizations now.

### Memory requirements of the Dirac operator

We are using an  $\gamma_5$ -hermitian Dirac operator which lives on the hypercube. Therefore it costs:

$$Mem = 12 \times V \times 12 \times 81 \times 16 \text{ Bytes} \quad (12.58)$$

to keep one Dirac operator in memory. As discussed above we distribute the volume  $V$  of the lattice to all used cores and get:

$$Mem_{loc} = 12 \times V_{loc} \times 12 \times 81 \times 16 \text{ Bytes} . \quad (12.59)$$

Using the  $\gamma_5$ -hermiticity of the Dirac operator

$$D(x, y) = \gamma_5 D^\dagger(y, x) \gamma_5 , \quad (12.60)$$

helps us to decrease  $Mem_{loc}$  further, because one only needs to store an offset of 41. Therefore, we can still obtain all entries of the Dirac operators, but use only the half of them memory:

$$Mem_{loc}^{half} = 12 \times V_{loc} \times 12 \times 41 \times 16 \text{ Bytes} . \quad (12.61)$$

If we want to use instead of the memory the L3 cache on the Altix system (9 MB), we have to parallelize the application to meet the following constraint:

$$Mem_{loc}^{half} \lesssim 8 - 9 \text{ MB} . \quad (12.62)$$

This determine the minimum number of cores we have to use. For a  $12^4$  lattice we need to use  $\sim 230$  cores to come into the L3 cache. As shown in Fig. 12.3 this constraint corresponds to a linear curve, which allows us to estimate the applicability of the matrix-vector multiplication on the system.

## 12.7.2 Benchmarking

The most time consuming part in the code is used for matrix-vector multiplications. We list the scaling of our matrix-vector product in its final version compiled with the Intel Fortran Compiler, Version 9.1 in Table 12.1. A recompilation of the code with the newer Intel Fortran Compiler, Version 10.1 does not seem to bring a further improvement. However, all the runs were done with the 9.1 Version of the Intel Fortran Compiler. We see that there is super-scaling for very large number of used cores. This is due to the fact that at some point the local problem fits into the 9 MB L2 cache of the Itanium2 cores.

Unfortunately Amdahl's law [176] prevents us using a larger number of cores than  $\sim 700$ . But this is due to "more" serial parts (IO, gauge update, etc.) of the remaining code, which have to improved for larger lattices as well. The matrix-vector multiplication could be parallelized with even a larger amount of cores without loosing

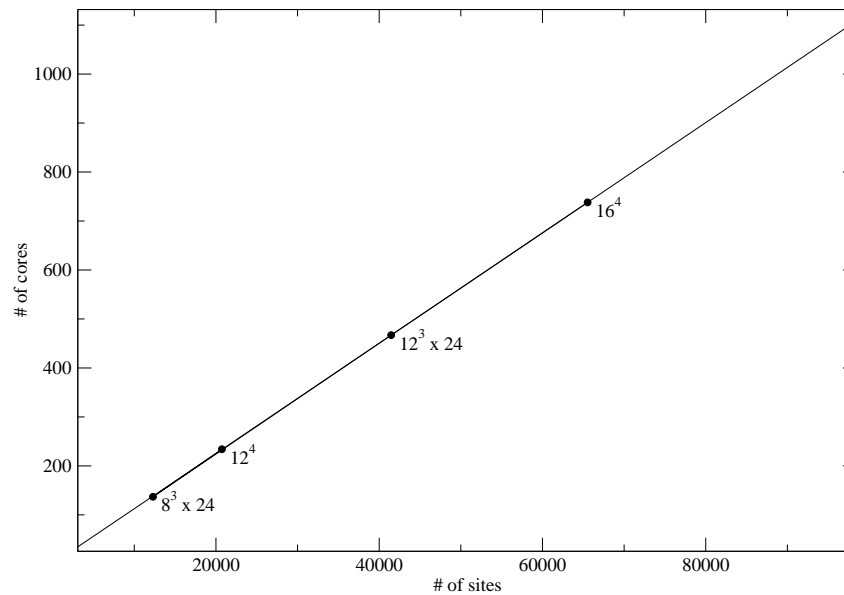


Figure 12.3: We plot here how the number of cores has to be increased in order to be able to use for the matrix-vector multiplication the L3 cache exclusively.

its efficiency. In fact, there is a high probability that the efficiency of the  $Dv$  would further increase with a larger number of cores (super linear speedup).

However, we also experienced that such large jobs stay a very long time in the queue, because we have to distribute the job over several partitions<sup>6</sup> of the system. Furthermore we have to use more than one partition, but in those partitions not all cores are finally used, not to get an unbalanced MPI job. Thus, it becomes very difficult to get those large jobs started quickly. Hence, we only do production runs on a single partition and we decide to use 288 cores as a tradeoff between efficiency and the time spent in the queue. Every time we calculate the Dirac operator times a vector we need the same number of floating-point operations as described in Eq. (12.49). In  $\sim 35\%$  of the time the code is running within the  $Dv$  subroutine (parallelization with 288 cores). Thus it is the most expensive part of the computation and improvements there have heavily effected the overall performance of the code.

Referring to the Table 12.1 we summarize that the matrix-vector multiplication is expected to work well even for larger lattices, i.e., using the  $\gamma_5$ -hermicity of the Dirac operator makes it possible to aim for larger lattices without losing efficiency of the most time consuming part of the algorithm.

### 12.7.3 Occurrence of matrix-vector multiplications in the algorithm

Independently of the way we parallelize the code, the number of  $Dv$  serves as a parameter how expensive a single part of the simulation is actually. We therefore give the averaged numbers of matrix-vector multiplications within the different parts of the code as far as they are measured in Table 12.2.

#### Arnoldi algorithm - PARPACK

The Arnoldi process is a technique for approximating a few eigenvalues and corresponding eigenvectors of a general  $n \times n$  matrix. It is most appropriate for large structured matrices  $A$ , where structure means that a matrix-vector product  $Av$  requires  $\mathcal{O}(n)$  rather than the usual  $\mathcal{O}(n^2)$  floating point operations.

In our case we make use of the parallelized version of ARPACK, the so-called PARPACK, which can be downloaded from the Web at <http://www.caam.rice.edu/software/ARPACK>. We compute with it the low-lying

<sup>6</sup>The SGI Altix 4700 in Garching exists out of 19 partitions a 512 cores.

lattice	# of processors	$N_4 \times N_3 \times N_2 \times N_1$	time in ms	efficiency in %
$8^3 \times 24$	12	$12 \times 1 \times 1 \times 1$	105.2	17.7
	24	$24 \times 1 \times 1 \times 1$	54.1	17.2
	48	$24 \times 2 \times 1 \times 1$	27.9	16.7
	96	$24 \times 4 \times 1 \times 1$	13.6	17.2
	192	$24 \times 8 \times 1 \times 1$	6.1	19.1
	384	$24 \times 8 \times 2 \times 1$	3.2	18.0
	768	$24 \times 8 \times 4 \times 1$	2.4	12.2
$12^4$	12	$12 \times 1 \times 1 \times 1$	188.4	16.7
	24	$12 \times 2 \times 1 \times 1$	92.5	17.0
	36	$12 \times 3 \times 1 \times 1$	62.0	16.9
	48	$12 \times 4 \times 1 \times 1$	46.0	17.1
	72	$12 \times 6 \times 1 \times 1$	31.9	16.5
	144	$12 \times 12 \times 1 \times 1$	16.3	16.1
	288	$12 \times 12 \times 2 \times 1$	7.0	18.7
	432	$12 \times 12 \times 3 \times 1$	4.6	19.1
	576	$12 \times 12 \times 4 \times 1$	2.9	22.6
	864	$12 \times 12 \times 6 \times 1$	2.9	15.1
$12^3 \times 24$	12	$12 \times 1 \times 1 \times 1$	375.3	16.8
	48	$24 \times 2 \times 1 \times 1$	90.4	17.4
	72	$24 \times 3 \times 1 \times 1$	61.8	17.0
	96	$24 \times 4 \times 1 \times 1$	45.4	17.3
	144	$24 \times 6 \times 1 \times 1$	30.7	17.1
	288	$24 \times 12 \times 1 \times 1$	19.1	13.7
	576	$24 \times 12 \times 2 \times 1$	7.1	18.4
	864	$24 \times 12 \times 3 \times 1$	4.5	19.4

Table 12.1: Here we present a scaling analysis for the  $8^3 \times 24$  lattice, the  $12^4$  lattice and the  $12^3 \times 24$  lattice. For all three lattices the efficiencies are quite the same. The efficiency is calculated by the ratio of the theoretical floating-point operations for one  $D^{(m)}v$  (12.49) and the peak performance of the Itanium2 cores in the SGI Altix 4700 in Garching (6.4 GFlop/s). For the timings we have averaged the time for 100  $Dv$  operations on a fully occupied vector  $v$ . We have used the Intel Fortran Compiler, Version 9.1.

eigenvalues and the corresponding eigenvectors of the Dirac operator. We need that to calculate the  $S_{\text{IR}}$  in the action of our simulation. Furthermore, we store the eigenvalues and -vectors to use them later in the analysis (cf. Sections 8.1.2 and 8.4). In [177] one finds a comparison of a Conjugate Gradient (CG) method and the public PARPACK which both have been tested for the parametrized FP Dirac operator.

### Inversion - Bi-CGSTAB( $\ell$ )

For a number of linear systems of equations using the Bi-CGSTAB algorithm of van der Vorst [178] is very attractive. We use a generalized Bi-CGSTAB algorithm, the so-called Bi-CGSTAB( $\ell$ ) algorithm of Sleijpen and Fokkema [179]. In some sense, the new algorithm combines GMRES( $\ell$ ) and Bi-CG and profits from both.

Without going into detail the GMRES( $\ell$ ) part is very cheap demanding only  $\frac{1}{2}(\ell^2 + 3\ell)$  dot products. The expensive part is the Bi-CG part of the algorithm, which requires  $2\ell$  matrix-vector multiplications and  $2\ell$  dot products.

In our code we need the inversion of the Dirac operator mainly in the stochastic estimator. There we have to calculate 138 inversions for the  $m_{ud}$  and 96 inversions for the  $m_s$  Dirac operator. The  $\ell$  parameter is then tuned dynamically, starting with a relative large  $\ell = \mathcal{O}(5 - 10)$  for the smaller masses in the ladder method and decreasing it successively for the heavier masses. If the residuum of the final step is a magnitude smaller than the exit condition would require, we set  $\ell = \ell - 1$ , if  $\ell \geq 2$ , for the next inversion we need in the ladder method.

	part of the code	$N_{Dv}$	$\overline{N}_{Dv}$
gauge configuration	Arnoldi (96 eigenvalues & -vectors)	$\approx 1445 - 1460$	1452
	Bi-CGSTAB( $\ell$ ) ( $m_{ud}$ )	$\approx 10 - 160$	67
	stoch. estimator for $m_{ud}$ (138 pseudo-fermions)	$\approx 12250 - 12300$	12261
	complex multi-mass Bi-CGSTAB ( $m_s$ )	$\approx 10 - 160$	72
	stoch. estimator for $m_s$ (96 pseudo-fermions)	$\approx 6800 - 7000$	6879
	one 3rd A/R step	$\approx 43900 - 44400$	44087
point-to-all propagator (point source)	Bi-CGSTAB( $\ell$ ) ( $m_{ud}$ )	$\approx 105 - 130$	114
	Bi-CGSTAB( $\ell$ ) ( $m_s$ )	$\approx 90 - 110$	100
point-to-all propagator ( $R^{-1}$ source)	Bi-CGSTAB( $\ell$ ) ( $m_{ud}$ )	$\approx 105 - 130$	115
	Bi-CGSTAB( $\ell$ ) ( $m_s$ )	$\approx 90 - 110$	100
point-to-all propagator (smeared source)	Bi-CGSTAB( $\ell$ ) ( $m_{ud}$ )	$\approx 120 - 145$	131
	Bi-CGSTAB( $\ell$ ) ( $m_s$ )	$\approx 110 - 125$	115
all-to-all propagator (point source)	Bi-CGSTAB( $\ell$ ) ( $m_{ud}$ )	$\approx 125 - 150$	136
	Bi-CGSTAB( $\ell$ ) ( $m_s$ )	$\approx 110 - 125$	119
meson correlator	Bi-CGSTAB( $\ell$ ) (low-high averaging)	$\approx 90 - 120$	100

Table 12.2: We give here the number of matrix-vector multiplications in the corresponding code blocks, which is proportional to the computational costs.  $N_{Dv}$  denotes the number of matrix-vector multiplications which are needed in the corresponding parts of the code. We list here the numbers for the  $12^4$  lattice.

Therefore in the beginning the residuum makes within one Bi-CGSTAB( $\ell$ ) step very large steps towards the exit condition, while at the end of the ladder we approach the residuum also very fast even using  $\ell = 1$ . To summarize we need less matrix-vector multiplications for the same parameters in the ladder method to get the same result.

In the analysis part, especially for generating propagators, we use  $\ell = 4$  for the inversion of the  $D^{(m_{ud})}$  and  $\ell = 2$  for the  $D^{(m_s)}$ . There we also combine the Bi-CGSTAB( $\ell$ ) with the Subtraction technique to lower the condition number of the inversion.

# Chapter 13

## Low Energy Constants

Spontaneous chiral symmetry breaking and the related existence of light Goldstone bosons is a basic feature of QCD. Chiral Perturbation Theory (ChPT) provides a systematic description of this physics in terms of a set of low energy constants (LECs) which encode the related non-perturbative features of QCD. The method of low energy effective Lagrangians simplifies the calculations significantly [89, 180, 181, 182] and over the years ChPT became a refined powerful technique. Gasser and Leutwyler recognized very early, decades before the numerical calculations could attack such problems, that these constants can also be fixed using finite size effects which, presumably, will never be measured in real experiments. They can be studied, however, in lattice QCD.

Both in the  $\delta$ - and  $\epsilon$ -regimes as discussed in Section 3.3 the finite size effects are dominated by the Goldstone bosons. In the  $\delta$ -regime the box is elongated in the Euclidean time direction which allows to study the low-lying spectrum. In the  $\epsilon$ -regime the box is essentially hypercubic, where different correlation functions can be measured. Due to the small time extension the spectrum can not be resolved, but the shape of the correlation functions can be determined. These numerical results are compared with the ChPT predictions which depend on the LECs and so these constants can be determined. The numerical difficulty lies in the fact that the quark masses should be light and the box should be sufficiently large. The Goldstone bosons should strongly feel the boundaries, while the non-Goldstone bosons excitations should have small finite size effects only.

We consider  $2 + 1$  light flavor QCD applying the parametrized fixed-point (FP) action [7]. The exact FP action has nice features, most importantly, it has exact chiral symmetry. The parametrized FP action is an approximation which already gave very promising results in the quenched approximation, in particular good scaling even at  $a = 0.15$  fm and the spectrum of the FP Dirac operator was close to that required by chiral symmetry. In our algorithm presented in Chapter 12 the contribution of the lowest lying modes is calculated exactly, the rest is treated stochastically. As a spinoff, for all the configurations in the Markov chain we have the low-lying eigenvectors which can also be used in the analysis.

In this Chapter we report on the results we obtained with the dynamical algorithm for the fixed-point action. We start to simulate gauge configurations on a  $8^3 \times 24$  lattice with  $a = 0.15$  fm. This shape corresponds to the  $\delta$ -regime, but the box size is probably too small to satisfy the conditions of it. However, we use this lattice to test whether the algorithm, which is presented in Chapter 12, and numerical techniques, as the low-mode averaging in Section 8.4, are working. Subsequently we use our algorithm to simulate a symmetric  $12^4$  lattice with  $a = 0.129$  fm. There we are definitely in the  $\epsilon$ -regime, where we can first of all make use of predictions from ChRMT to obtain  $\Sigma$ . Secondly we derive additional informations on LECs through fitting two-point correlators to ChPT predictions.

### 13.1 The $\delta$ -regime

For the  $\delta$ -regime we want to use the parametrized fixed-point Dirac operator which approximately satisfies the Ginsparg-Wilson relation (6.1) and is limited to a hypercube [183]. We tuned the coupling in our full QCD simulation to be close to  $a = 0.15$  fm [169], and the measurement of the Sommer parameter  $r_0$  gave a result in

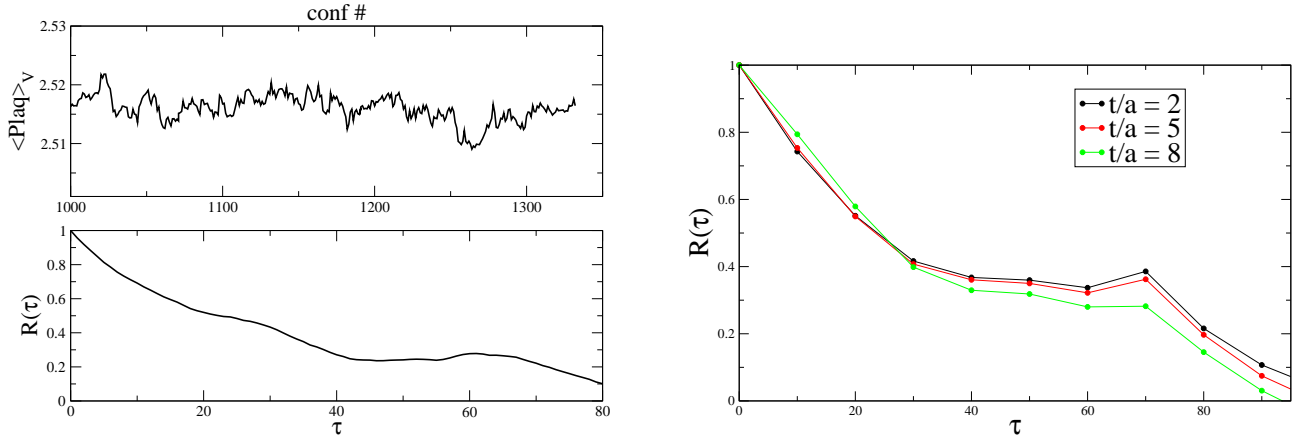


Figure 13.1: **Left:** We show the Monte Carlo history for the plaquette  $\langle \text{Plaq} \rangle_V$  calculated on smeared gauge configurations and the corresponding autocorrelation function  $R(\tau)$ . We find an autocorrelation time of  $\tau_0 \approx 40$ .

Figure 13.2: **Right:** We give the autocorrelation function for the  $\langle \hat{P}(t)P(0) \rangle$  correlator at different  $t$  values.

agreement with this value. The results presented here refer to a  $8^3 \times 24$  lattice, which should be seen as a test run for larger lattices. Due to the fact that the spatial volume of the  $8^3 \times 24$  is rather small we have to check our physical predictions on this lattice on larger lattices also.

### 13.1.1 Autocorrelation times

We estimated the autocorrelation time of plaquettes built from smeared links and that of the pseudoscalar-pseudoscalar correlator. We are using a global update [169], the configurations are separated by  $\approx 0.7$  standard Metropolis sweeps.

Fig. 13.2 shows an extraction of the Monte Carlo history for the plaquette obtained on smeared gauge configurations  $\langle \text{Plaq} \rangle_V$  (smeared plaquettes), the autocorrelation function extracted from it and the autocorrelation function for the zero-momentum  $\langle \hat{P}(t)P(0) \rangle$  correlator at different time separations  $t$ . We find an autocorrelation time of  $\tau_0 \approx 40$  for the smeared plaquettes and a somewhat higher autocorrelation for the correlation functions. Therefore we only store every 10th configuration in our Markov Chain. However, the analysis of the autocorrelation of our data shows that we are able to reach the thermalized region using our algorithm within a feasible amount of computer time.

### 13.1.2 Low-mode averaging

In Section 8.4.4 we have already compared the zero momentum correlator  $\hat{C}_{PP}(t) = \langle \hat{P}(t)P(0) \rangle$  at time separation  $t = 5$  for the different amounts of averaging. We show that while the low-low averaging is very effective, the low-high averaging barely shows further suppression of the fluctuations. Since the latter one is also much more expensive, one can safely ignore this option and average only the low-low part of the correlator. Replacing the low-low part by the averaged one works very well for the pseudoscalar channel, so that we could calculate  $\hat{C}_{PP}(t)$  even on few configurations quite precisely. For other channels this is not expected necessarily.

Based on the tests for low-mode averaging on the  $8^3 \times 24$  lattice we decide to use only those correlators where the low-low part is replaced by the averaged one. Applying this technique we are able to obtain effective mass plateaus in the time dependency of the correlators, which we employ to examine the AWI mass and the mass gap of the rotator spectrum in the  $\delta$ -regime. Without the application of the low-mode averaging technique this would be an impossible task.

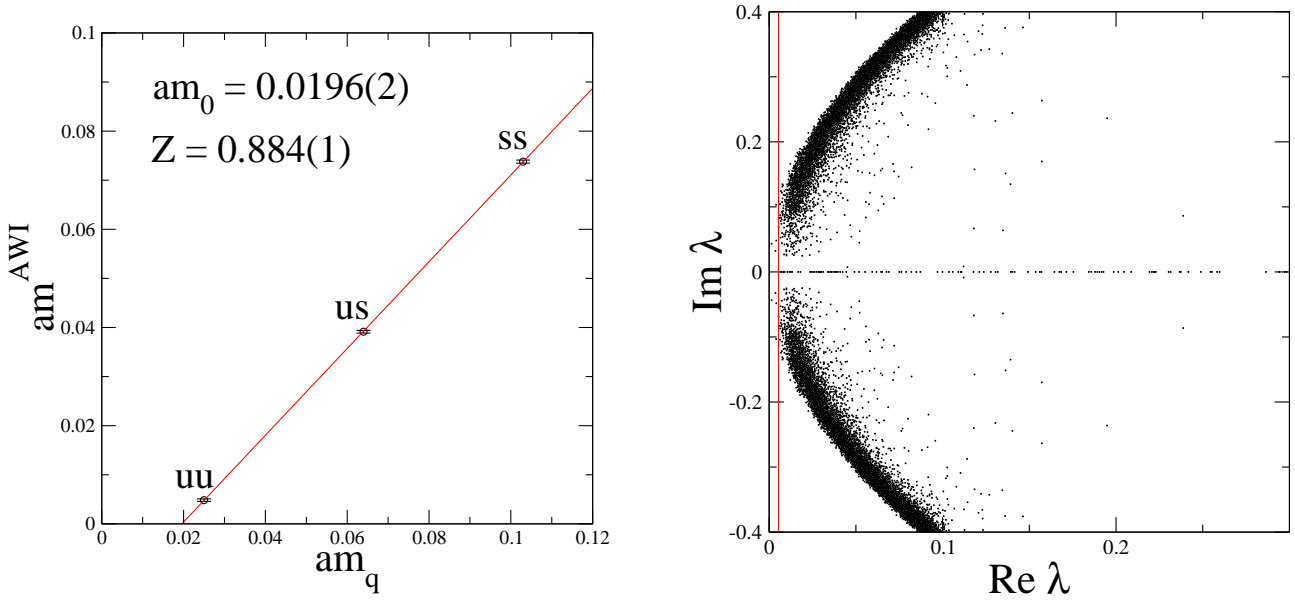


Figure 13.3: **Left:** The chiral extrapolation of  $m_{ff'}^{\text{AWI}}$  using the combinations  $ud$ ,  $us$ , and  $ss$  for the quark flavors. We find an additive mass renormalization of  $am_0 = 0.0196(2)$  and a slope of  $Z = 0.8837(7)$ .

Figure 13.4: **Right:** We show here the low-lying eigenvalues of the massive Dirac operator for  $am_u = 0.025$  on 50 configurations. The red line shows the quark mass with this mass shift subtracted,  $am_{\text{sub}} = am_q - am_0$ .

### 13.1.3 The AWI mass

Because we are using the parametrized fixed-point action which solves the Ginsparg-Wilson-equation only approximately we get a small additive mass renormalization for our AWI masses (cf. Section 9.2.2). The size of this mass shift is an indicator for the quality of our chiral approximation. From preliminary quenched runs [169] we estimate this additive mass renormalization to be around 0.02 in lattice units.

We run the present simulations with lattice quark masses  $am_{ud} = 0.025$ ,  $am_s = 0.103$ . To determine the additive mass renormalization for the dynamical simulation we again calculate ratios

$$\partial_t \langle \hat{A}_{ff'}(t) P_{ff'}(0) \rangle = 2m^{\text{AWI}} \langle \hat{P}_{ff'}(t) P_{ff'}(0) \rangle \quad (13.1)$$

where  $ff' = uu, us, ss$ ,  $\partial_t$  is the lattice derivative in time direction and  $A = \bar{\psi} \gamma_4 \gamma_5 \psi$ ,  $P = \bar{\psi} \gamma_5 \psi$  are the naive operators for the axialvector current and the pseudoscalar density. For both correlator functions in (13.1) we use low-mode averaging and find well-defined plateaus, typically beyond  $t \approx 5$ . These we denote by  $m_{ff'}^{\text{AWI}}$ . Plotting  $m_{ff'}^{\text{AWI}}$  against  $m_q \equiv (m_f + m_{f'})/2$  and extrapolating in  $m_q$  to  $m^{\text{AWI}} = 0$  we obtain the mass shift  $m_0$ .

Using naive interpolators, i.e., the non-conserved axialvector current in the numerator and the non-covariant pseudoscalar density in the denominator of Eq. (13.1), we also get a factor  $Z$ :

$$m^{\text{AWI}}(m_q) = Z(m_q - m_0), \quad m_q = \frac{1}{2}(m_f + m_{f'}). \quad (13.2)$$

As seen in Fig. 13.3 the actual values are described very well by this linear dependence. We can determine an additive mass renormalization of  $am_0 = 0.0196(2)$ , which we have expected from quenched results, and a factor  $Z = 0.8837(7)$ , which is relatively close to 1. Whereas  $am_0 \neq 0$  comes from the fact that we are using only approximate chiral fermions we get  $Z \neq 1$  due to the fact, that in addition to the approximate chiral fermions we apply naive interpolators (cf. Section 9.2.2).

We have stored the 48 lowest lying eigenvalues and their corresponding eigenvectors for all of our configurations with  $am_{ud} = 0.025$  on the  $8^3 \times 24$  lattice. In Fig. 13.4 we plot the stored low modes of 50 configurations.

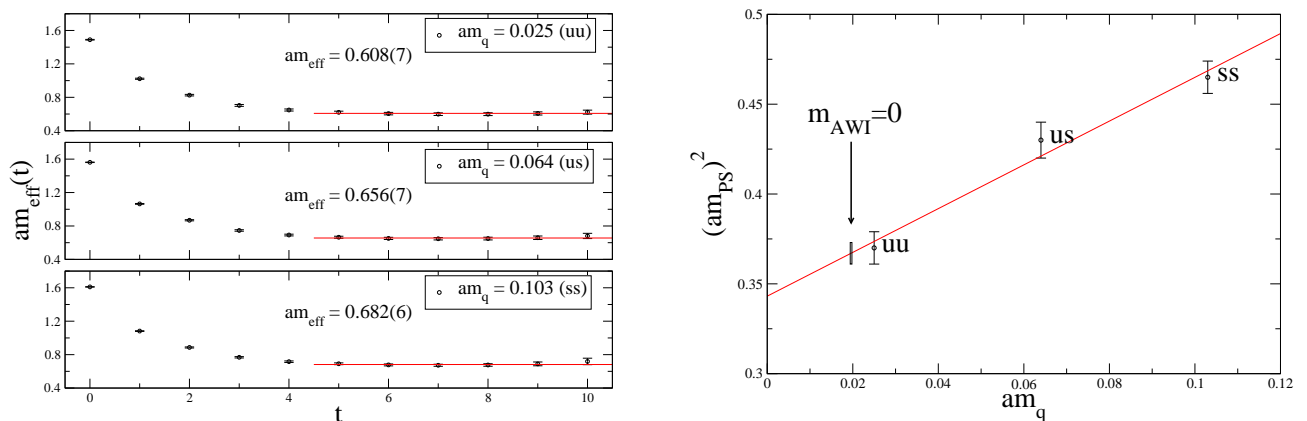


Figure 13.5: **Left:** Plateaus in the effective mass of the pseudoscalar-pseudoscalar correlator  $\langle \hat{P}_{ff'}(t) P_{ff'}(0) \rangle$  for  $ff' = ud, us, ss$ .

Figure 13.6: **Right:** The chiral extrapolations in the pseudoscalar channel. We extrapolate  $(am_{\text{gap}})^2$  linearly in  $am_q$  to the physical point, where the AWI mass  $m^{\text{AWI}}$  is vanishing per definition.

We find that they approximately lie on the Ginsparg-Wilson circle shifted by the subtracted mass  $am_{\text{sub}} = am_u - am_0 = 0.0054(2)$ , corresponding to a bare  $ud$ -quark mass of  $7.2(4)$  MeV, away from  $\text{Re } \lambda = 0$ . This confirms the calculation of the additive quark mass. The subtracted lattice quark mass for the strange quark is  $am_s - am_0 = 0.083$ , corresponding to a bare  $s$ -quark mass of  $\sim 110$  MeV.

### 13.1.4 Mass gap in the rotator spectrum

Although our  $8^3 \times 24$  lattice is too small to have controlled predictions, we nevertheless try to find the mass gap in the rotator spectrum. Therefore we have a closer look on the pseudoscalar channel.

For the point-like naive pseudoscalar density  $P = \bar{\psi} \gamma_5 \psi$  we calculate the zero-momentum  $\hat{C}_{PP}(t)$  correlator for three different quark flavor combinations ( $uu$ ,  $us$ ,  $ss$ ) using low-mode averaging and find very stable effective mass plateaus shown on the in Fig. 13.5. Here we can be rather sure, that we see the lowest lying excitations in the correlator. If we are in the  $\delta$ -regime this excitation corresponds to the mass gap in the rotator spectrum (cf. Section 9.3.4). A linear chiral extrapolation of  $m_{\text{gap}}^2$  in  $m_q$  to the chiral limit, shown in Fig. 13.6, gives:

$$(am_{\text{gap}})^2(m_0) = 0.367(6). \quad (13.3)$$

Using the finite volume mass gap in LO of chiral perturbation theory in the  $\delta$ -regime, shown in Eq. (9.62), this would lead to  $F = 92.7(4)$  MeV, where we only quote the statistical error coming from Eq. (13.3). However, this result is accidental, since the spatial extend of our small lattices is uncomfortably small, and sizeable corrections (80%) to the leading order result of Eq. (9.62) are calculated in [91]. There is an ongoing project at Bern university which will calculate the NNLO of the mass gap [184]. The corrections in NNLO are again assumed to be large.

## 13.2 The $\epsilon$ -regime

The  $\epsilon$ -regime [26, 27, 28, 32, 185] describes physics close to the chiral limit in a box whose size is larger than the typical non-Goldstone scale. On the other hand, the size of the box relative to the Goldstone boson correlation length must be small. Under these conditions the Goldstone bosons feel the effect of boundaries strongly. ChPT provides a powerful and systematic way to calculate the finite size corrections. It can also be an excellent tool to determine the low-energy constants of ChPT. We use in our calculation for the  $\epsilon$ -regime a symmetric  $12^4$  lattice with  $a = 0.129$  fm.

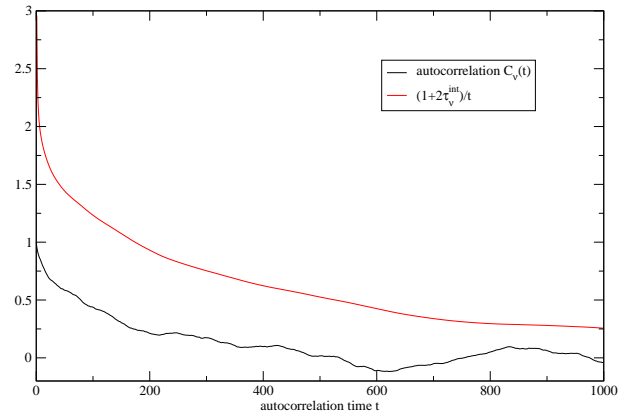
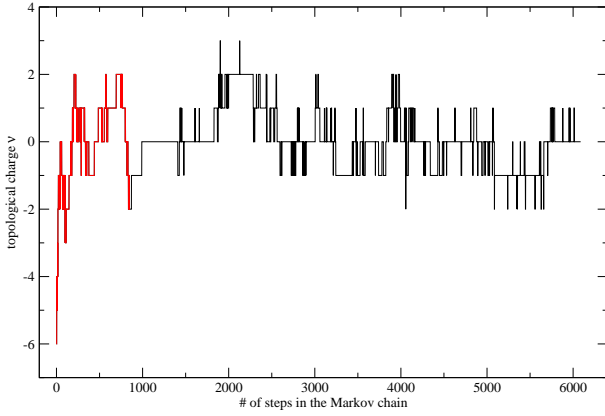


Figure 13.7: **Left:** We plot the topological charge  $Q_{\text{top}} = \nu$  for all configurations in the Markov chain for our  $12^4$  lattice. The red curve are the neglected configurations due to thermalizing the production run.

Figure 13.8: **Right:** We show here the correction factor to the variance for independent configurations according to Eq. (7.24).

A nice additional feature of the  $\epsilon$ -regime is that Random Matrix Theory (RMT) [34, 36, 41] makes precise predictions for microscopic observables. RMT relates in particular the distribution of low-lying eigenvalues of the Dirac operator in different topological sectors to the chiral condensate  $\Sigma$ .

The  $\epsilon$ -regime is defined by:

$$m_{\text{PS}}L_s \lesssim \mathcal{O}(1), \quad m_{\text{PS}}L_4 \lesssim \mathcal{O}(1), \quad (13.4)$$

where at the same time the box size should be large enough,  $4\pi F^2 L^2 \gg 1$ , for the validity of chiral perturbation theory. Here  $m_{\text{PS}}$  is the pseudoscalar mass in infinite volume. In order to reach this regime the simulation should be done with sufficiently small quark masses. This requires a Dirac operator with good chiral behavior at the actual lattice spacing. This became possible in full QCD only recently [7, 186, 187, 188].

### 13.2.1 Remarks on numerical implementation and the Markov chain

Aiming for a larger lattice we have to tune and improve some critical parameters and subroutines. The main changes can be summarized in five points:

- In the algorithm the trial configurations offered in the last stochastic accept/reject step differ by a full Metropolis sweep now (instead of 70% on the smaller  $8^3 \times 24$  lattice) and are still accepted with  $P_{\text{acc}} \approx 0.6$ .
- On distributed memory architectures it is very important to get into the cache of the single cores (cf. Section 12.7.1). Therefore we use  $\gamma_5$ -hermicity of the FP Dirac operator to minimize the size of the Dirac operator in the local cache.
- We have replaced the serial gauge update by a parallelized version [175].
- For the stochastic estimator of the  $s$ -quark determinant we use a rational approximation [174], instead of a Taylor expansion for the square root.
- The latency occurring in the communication of the parallelized matrix-vector multiplication  $Dv$  is avoided by using larger packages. Therefore the efficiency of the matrix-vector multiplication does not change for different parallelizations (cf. Section 12.7.2).

We have  $\sim 6000$  configurations in the Markov chain using the partially global update algorithm [169]. We neglect the first 500 accepted configurations (854 steps in the Markov chain) of the run in order to thermalize. We show in Fig. 13.7 the autocorrelation in the topological charge which usually is an observable with a

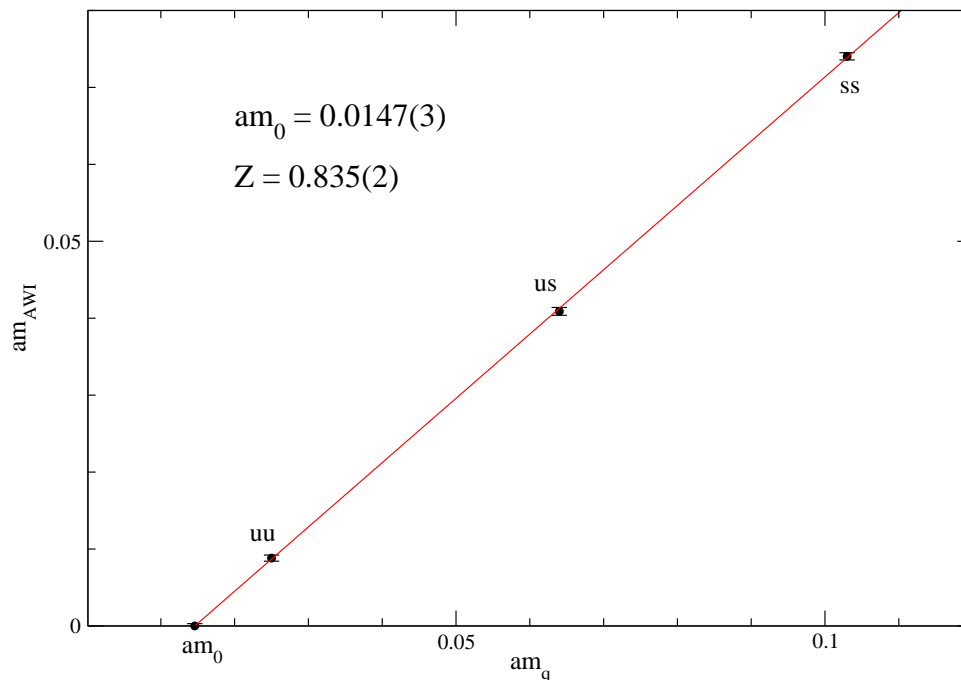


Figure 13.9: The AWI mass  $am^{AWI}$  vs. the average quark mass  $am_q = a(m_f + m_{f'})/2$ . We determine the additive mass renormalization  $m_0$ .

long autocorrelation time. We find a autocorrelation time of  $\tau_A \approx 170$  (cf. 13.8). In order to reduce the autocorrelation time (and the expenses of the analysis) we only store every 10th configuration in the Markov chain. In addition to that in the analysis we bin the data in blocksizes of 10-20 configurations to get reliable error bars. Therefore we can use  $\sim 500$  configurations for the statistical analysis.

### 13.2.2 Technicalities - $12^4$ lattice

Our lattice spacing is  $a = 0.129(5)$  fm determined from the Sommer parameter at  $r_0 = 0.49$  fm. Therefore our  $12^4$  lattice has a volume of  $V \approx (1.55 \text{ fm})^4$ . Beside the configurations we also store  $\sim 100$  of the lowest-lying eigenvalues and eigenvectors of the Dirac operator, which we can use in both, generating the configurations and analysis. Applying low-mode averaging we can calculate the additive mass shift of  $am_0 = 0.0147(3)$  through the axial Ward identity in Eq. (13.1). In Fig. 13.9 we plot the AWI mass  $m^{AWI}$  as a function of the averaged quark mass  $m_q = \frac{1}{2}(m_f + m_{f'})$ , together with a linear fit. The intercept with the horizontal axis again gives the additive mass renormalization of the quark masses. The points  $uu$ ,  $us$  and  $ss$  refer to the corresponding flavors in Eq. (13.1). Subtracting the mass shift  $m_0$  we get for the bare quark masses  $m_{ud}^{\text{bare}} = 16(1)$  MeV and  $m_s^{\text{bare}} \approx 137$  MeV. Here we also obtain a  $Z$ -factor of the same order as for the smaller  $8^3 \times 24$  lattice (cf. Fig 13.3).

After fixing the bare quark mass we have noticed that we were overcautious by choosing the  $ud$ -quark mass parameter  $am_{ud} = 0.025$ . Our Dirac operator would have allowed to even calculate with a quark mass of  $am_{ud} = 0.017$ . We will take this issue into account for future projects.

RMT predicts the probability distribution  $p_{\nu k}(\xi_{\nu k})$  for the  $k$ -th low-lying eigenvalue ( $k = 1, 2, \dots$ ) of the Dirac operator in the topological sector  $\nu$ , which we want to use in the following (cf. Section 9.3.3). Denoting the corresponding eigenvalues of the (continuum) Dirac operator by  $i\alpha_{\nu k}$ , the variable  $\xi_{\nu k}$  is related to the bare chiral condensate  $\Sigma$  as  $\xi_{\nu k} = \alpha_{\nu k} \Sigma V$ . Fig. 13.10 shows the prediction of RMT for the cumulative distributions

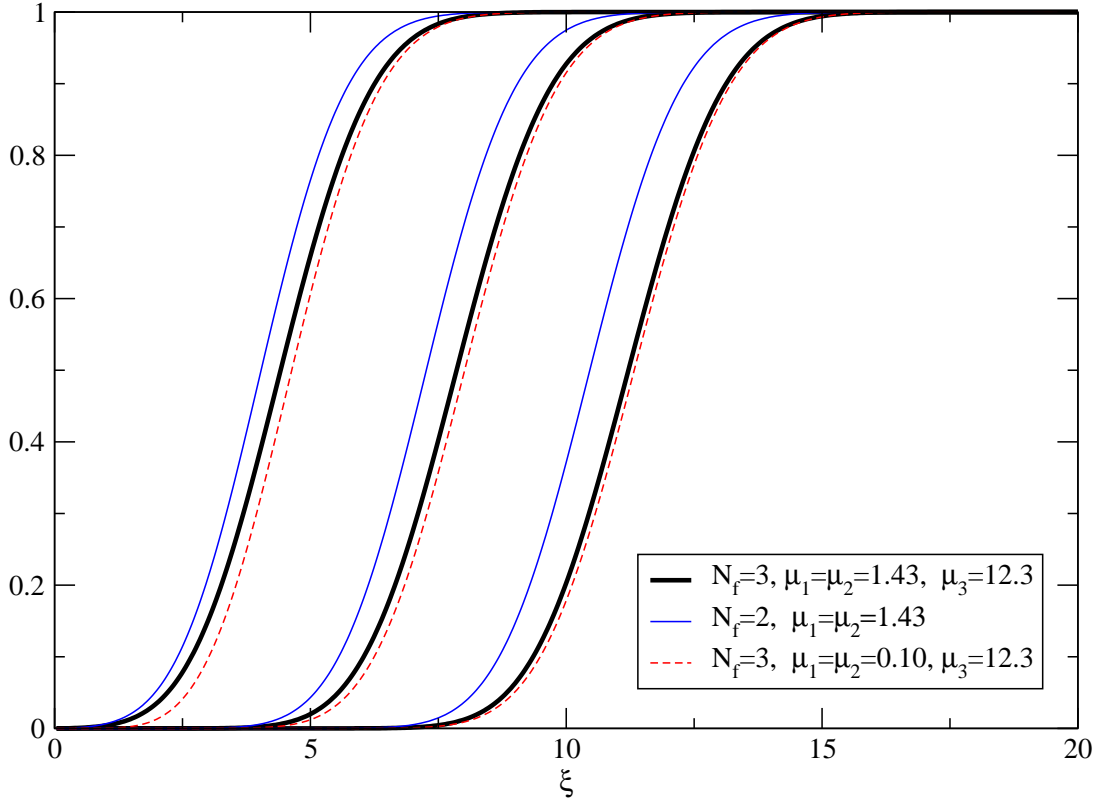


Figure 13.10: Random Matrix Theory prediction for the cumulative distribution of  $\xi = \xi_{\nu k} = \alpha_{\nu k} \Sigma V$ , where  $i\alpha_{\nu k}$  is the  $k$ -th eigenvalue of the continuum Dirac operator in a gauge background with topological charge  $\nu$ , and  $\mu_i = m_i \Sigma V$ . Here the  $\nu = 0$  results are shown, but the picture is similar for  $\nu = 1, 2$ .

$\int_0^{\xi_{\nu k}} d\xi p_{\nu k}(\xi)$  for  $\nu = 0$  and  $k = 1, 2, 3$ . The distributions depend on  $\mu_i = m_i \Sigma V$  where  $m_i$  are the quark masses. Decreasing the  $m_{ud}$  mass by more than a factor 10 (at fixed  $m_s$ ) the cumulative distributions practically remain unchanged. On the other hand sending the strange quark mass to infinity (at fixed  $m_{ud}$ ) we land on a  $N_f = 2$  flavor theory with a visibly different distribution. The strange quark has a (modest) effect on our observables and we have to use the RMT predictions for  $N_f = 3$ .

However, when we compare our data to ChPT predictions the situation is different, because the excitations containing the strange quark are coded in the LECs. As long as we have  $m_{ud} \ll m_s$  these effects become negligible for obtaining LECs and we are allowed to use the  $SU(N_f = 2)$  predictions.

### 13.3 Comparing results in the $\epsilon$ -regime with RMT predictions

As we have already discussed in Section 4.2, the partition function of chiral RMT and that of QCD in the  $\epsilon$ -regime can be matched. This fact can be used to match the low-lying eigenvalue spectrum of the QCD Dirac operator with that of ChRMT and to obtain LECs. In our case we are only interested in the bare chiral condensate  $\Sigma$  and use only RMT predictions without chemical potential.

#### 13.3.1 Eigenvalues of the Dirac operator

The FP Dirac operator follows Eq. (6.1). On low-lying eigenvectors the operator  $2R$  is close to 1 and we ignore it for simplicity first and correct the errors afterwards, i.e., we initially set  $2R = 1$ . Then the low-lying complex spectrum of  $D_{FP}$  lies on a circle to a good approximation, while some of the real eigenvalues are scattered away

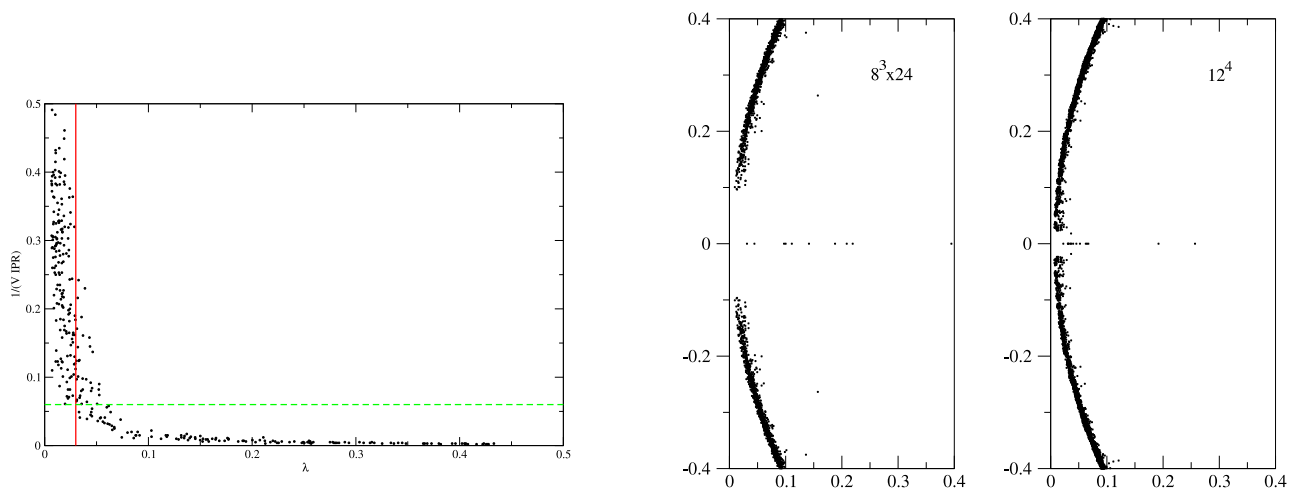


Figure 13.11: **Left:** The relative effective volume occupied by the wave function  $(V \times IPR)^{-1}$  (Participation Ratio) vs. the eigenvalue of  $D_{FP}$  for the real modes. The red line at  $\lambda = 0.03$  is used to distinguish between real modes which were counted for the topological charge and those which are not. The dashed green line is a more restrictive way to define the cut. All the wavefunctions of the real modes which lies above the green line occupy more than 6% of the whole lattice.

Figure 13.12: **Right:** We show the low-lying eigenvalues of the parametrized FP Dirac operator on 50 configurations at the volumes  $8^3 \times 24$  and  $12^4$ .

from the origin. It is expected that the size of a effective support of the wave function and the position of the real eigenvalue are strongly correlated. Thus we introduce the inverse participation ratio (IPR) by

$$IPR = \sum_x \|\psi^{(\lambda)}(x)\|^4, \quad \text{where} \quad \|\psi^{(\lambda)}(x)\|^2 = \sum_{i=1}^{12} |\psi_i^{(\lambda)}(x)|^2 \quad (13.5)$$

for a normalized eigenvector  $\psi^{(\lambda)}$ . In Fig. 13.11 we plot the participation ratio  $p = (V \times IPR)^{-1}$ , where we get  $p \rightarrow \mathcal{O}(1)$  for delocalized and  $p \rightarrow \mathcal{O}(1/V)$  for localized eigenvectors  $\psi^{(\lambda)}$ . Due to the fact that we use the parametrized FP Dirac operator the index theorem (cf. Section 2.4.2) is valid only approximately and the real modes are scattered along the real axis (cf. Fig. 13.12). We expect that the real modes which are far from  $\lambda = 0$  are artifacts with a small extension on the lattice (unlike the true topological object which are extended). The red line in Fig. 13.11 is where we have made the cut  $\lambda = 0.03$  to determine whether the wavefunctions of the real modes are either localized or delocalized. To determine the topological sector of the configurations we only use those real modes whose participation ratio lies on the left hand side of the red line. All the other real modes are neglected, because they probably are artifacts. With this cut we find 389, 98 and 35 configurations for the  $\nu = 0, 1, 2$  sectors, respectively. This cut is sufficiently smaller than the typical gap in the complex eigenvalues (cf. Fig. 13.12) and corresponds to a larger participation ratio ( $> 6\%$ ).

Note that this cut can also be made for a certain participation ratio, e.g.,  $p = 6\%$ . If the wavefunction of a real mode is extended over 6% of the lattice we accept it as a true topological object and ignore it otherwise. Different ways of defining the cut give practically the same results.

### 13.3.2 Matching RMT predictions

First we use the stereographic projection of the complex eigenvalues of the parametrized FP Dirac operators to the imaginary axis

$$i\alpha = \frac{\lambda}{1 - \lambda/2}, \quad (13.6)$$

and can afterwards match the obtained imaginary eigenvalue spectrum with that of the continuum Dirac operator.

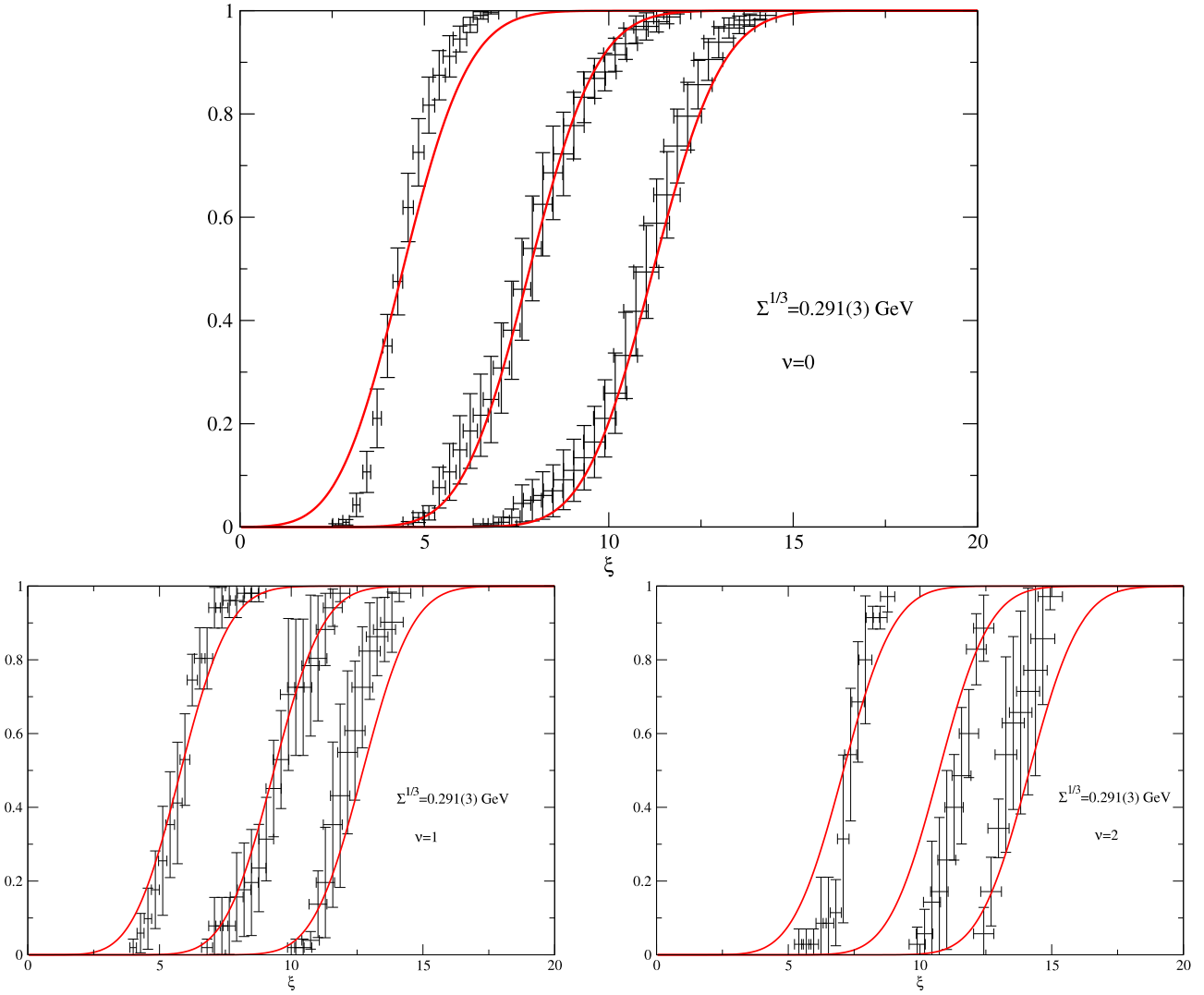


Figure 13.13: Cumulative distributions of  $\xi_{\nu k}$  in the topological sector  $\nu = 0, 1, 2$ . We show the  $k$ -th smallest eigenvalues for  $k = 1, 2, 3$ . We obtained the result for this bare quantity  $\Sigma^{1/3} = 0.291(3)(9)$  GeV, where the two errors come from the fit and setting the scale, respectively. Both errors are statistical.

We denote the  $k$ -th eigenvalue in the  $Q_{\text{top}} = \nu$  sector as  $\alpha_{\nu k}$ . Random Matrix Theory (RMT) predicts the distribution of the scaled eigenvalues  $\xi_{\nu k}(\mu_i) = \alpha_{\nu k} \Sigma V$  depending on  $\mu_i = m_i \Sigma V$ ,  $i = 1, \dots, N_f$ . The cumulative distributions of  $\xi_{\nu k}$  have only one matching parameter, which is the bare condensate  $\Sigma$ . Fitting the distribution of the 3 lowest lying eigenvalues in the  $\nu = 0, 1$  topological sector to the RMT predictions we get<sup>1</sup>  $\Sigma^{1/3} = 0.291(3)(9)$  GeV.

The result in Fig. 13.13 receives a small correction due to the fact that, for simplifying the presentation, we suppressed a technical complication. As mentioned before the exact fixed-point operator satisfies a Ginsparg-Wilson relation in Eq. (6.1) with a local operator  $2R$ . For this reason the quark mass enters in a simple additive way and effectively the operator  $2R$  behaves in the infrared like a constant close to 1. Its expectation value for the lowest  $\sim 100$  eigenvectors is 1.05 within 1%. Using the spectrum of  $\mathcal{D}$  the matching with RMT gives the slightly changed result<sup>1</sup>:

$$\Sigma^{1/3} = 0.286(3)(9) \text{ GeV} . \quad (13.7)$$

As Fig. 13.13 shows the distributions for different  $\nu, k$  values are consistent with each other. Note, however,

<sup>1</sup>The first error comes from the statistical errors of the measured distributions, the second one is due to the error in the lattice scale  $a$ .

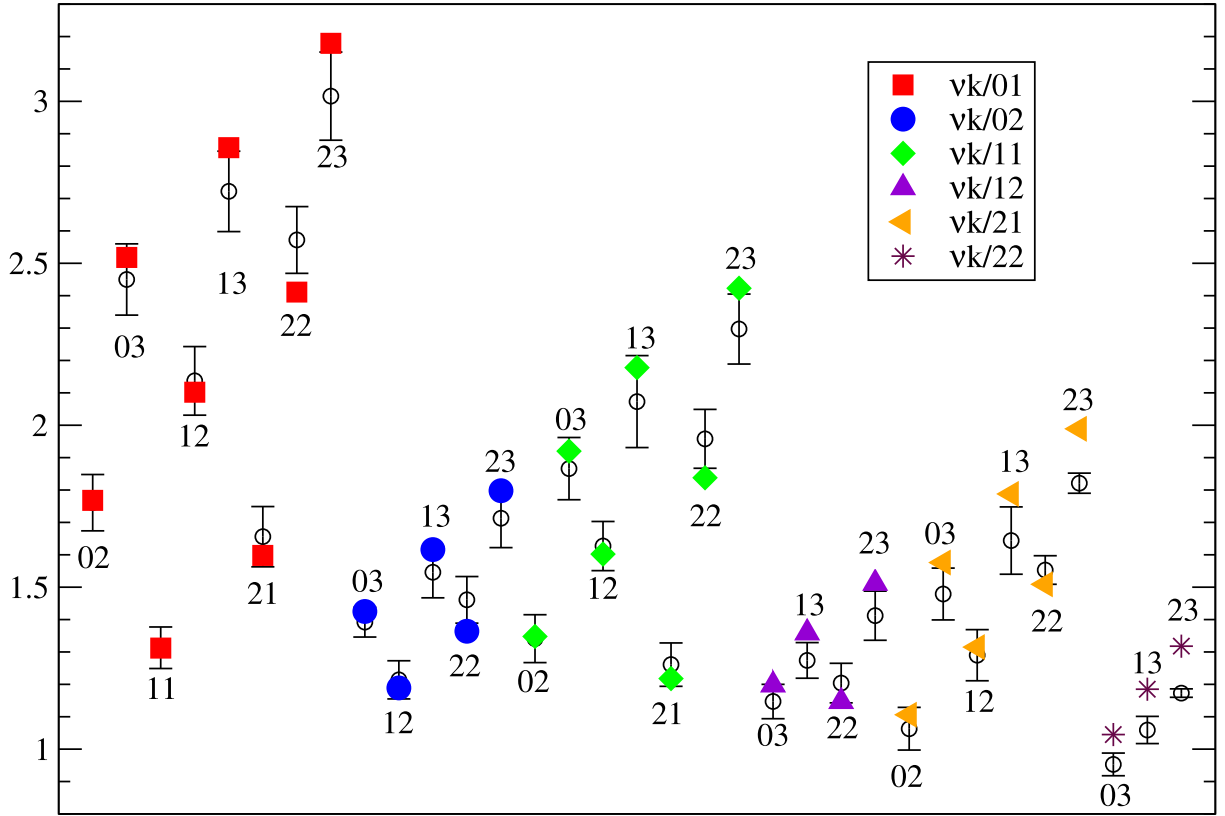


Figure 13.14: We calculate the ratios between different averaged eigenvalues  $\langle \xi_{\nu k} \rangle / \langle \xi_{\nu' k'} \rangle$  on the lattice. We distinguish the averages in the nominator by the numbers denoted below and the averages in the denominator by the colored symbols. The different symbols again denote the RMT predictions for our corresponding results.

that the shape of the  $\nu = 0$ ,  $k = 1$  distribution is different from that of the RMT. The deviation in the shape could be a finite-size effect (which shows up at smallest eigenvalue, i.e., for largest wavelength), but this needs further investigations on larger lattices. At the present situation we are not able to give another explanation of this effect.

We also compute the ratios  $\langle \xi_{\nu k} \rangle / \langle \xi_{\nu' k'} \rangle$  of the mean eigenvalues and compare them to the RMT predictions. Note, that those ratios are independent of the bare chiral condensate  $\Sigma$  and the volume  $V$ . Because of the latter, we expect a very good matching with RMT. We summarize our results in Fig. 13.14, where we find a generally good agreement even in higher topological sectors, e.g., in topological sector  $\nu = 2$ , where the statistical data is poor, the statistical errors are still small. Due to the fact that we only quote the statistical errors and those data points could have larger autocorrelations than in the lower topological sectors, we probably underestimate the errors there.

### 13.3.3 Finite Volume corrections of the bare quark condensate

The determined  $\Sigma$  in the previous Section 13.3.2 is the bare condensate of QCD in finite volume. Thus, we have to correct the finite size effects using chiral perturbation theory with  $N_f = 2$ , assuming that in this correction the  $s$ -quark contribution is negligible [32]

$$\Sigma = \rho_1 \Sigma_\infty = \Sigma_\infty \left( 1 + \frac{3}{2} \frac{\beta_1}{F^2 L^2} + \dots \right), \quad (13.8)$$

where  $\beta_1 = 0.14046$  is the shape coefficient for our lattice. After the finite size correction we get for the infinite-volume bare condensate

$$\Sigma_\infty^{1/3} = 0.255(3)(9) \text{ GeV}. \quad (13.9)$$

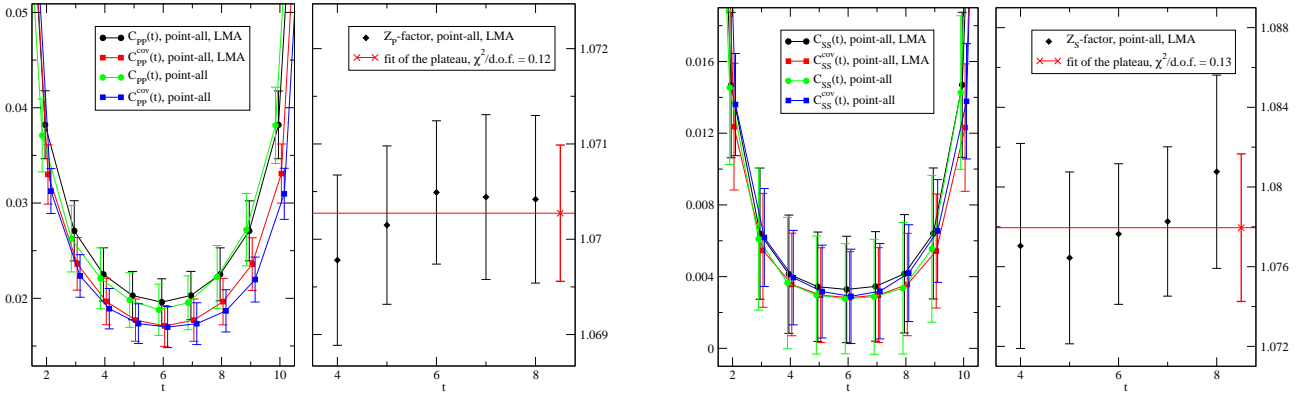


Figure 13.15: **Left:** We plot on the lhs. the naive pseudoscalar-pseudoscalar correlator  $\langle \hat{P}(t)P(0)^\dagger \rangle$  and covariant pseudoscalar-pseudoscalar correlator  $\langle \hat{P}(t)P(0)^\dagger \rangle_{\text{cov}}$  obtained with point-to-all propagators. We show the effect of low mode averaging, where the correlators without LMA have larger fluctuations. On the rhs. we plot the square root of the ratio of the naive correlator  $\langle \hat{P}(t)P(0)^\dagger \rangle$  and the covariant correlator  $\langle \hat{P}(t)P(0)^\dagger \rangle_{\text{cov}}$  using point-to-all propagators with LMA. We only plot the correlators and ratios for our smaller quark mass  $m_{ud}$ .

Figure 13.16: **Right:** We plot on the lhs. the scalar-scalar correlator  $\langle \hat{S}(t)S(0)^\dagger \rangle$  and  $\langle \hat{S}(t)S(0)^\dagger \rangle_{\text{cov}}$  obtained with point-to-all propagators. Here the effect of low mode averaging is less pronounced. On the rhs. we plot the square root of the ratio of the naive correlator  $\langle PP^\dagger \rangle$  with the covariant correlator  $\langle PP^\dagger \rangle_{\text{cov}}$  using point-to-all propagators with LMA. Also here we only plot the correlators and ratios for our smaller quark mass  $m_{ud}$ .

## 13.4 Comparing results in the $\epsilon$ -regime with ChPT predictions

Correlators in the  $\epsilon$ -regime are strongly influenced by finite size effects. As discussed at the beginning of this section just these effects contain information about the parameters of ChPT, the LECs. ChPT gives predictions on these correlators in terms of the LECs which can be constrained by the measured correlators.

### 13.4.1 The relation between naive and covariant quantities

For the LECs we have to determine the  $Z_P$ - and  $Z_A$ -factors. Although we will later simply use the covariant correlators to determine the LECs, we can also analyze the  $Z$ -factors beforehand, which we define as the square root of the ratio between the naive and the covariant correlators on each timeslice<sup>1</sup>:

$$Z_{\mathcal{O}} \equiv Z_{\mathcal{O}}(t) = \sqrt{\frac{\hat{C}_{\mathcal{O}\mathcal{O}}(t)}{\hat{C}_{\mathcal{O}\mathcal{O}}^{\text{cov}}(t)}}, \quad (13.10)$$

which should be constant in time<sup>2</sup>. Due to the fact that the pseudoscalar density has non-zero anomalous dimension we calculate the ratio between  $Z_P$  (pseudoscalar) and  $Z_S$  (scalar) which should be finite in the continuum. Furthermore, for covariant densities this ratio should be exact one and due to the fact using only approximately chiral Dirac operators, the discrepancy from one is, in our case, related to the chiral properties of the parametrized FP Dirac operator. The  $Z_A$ -factor can be determined through the ratio between the naive and the covariant conserved currents.

In Fig. 13.15 we show the ratio between the naive and the covariant pseudoscalar-pseudoscalar correlators obtained from point-to-all propagators with low mode averaging (LMA). We also include the naive and covariant correlators without low-mode averaging (LMA) into the left figure. Their values (green, blue) are significantly different from the correlators using LMA and show their sensitivity of the low-modes in the pseudoscalar channel. In Fig. 13.16 we plot the naive and covariant scalar-scalar correlators obtained from point-to-all propagators with

<sup>1</sup>In this section we do not consider the renormalization constants, but the ratio between the naive and the covariant correlators.

<sup>2</sup>Note that these ratios cannot replace the calculation of the renormalization constants as in Ref. [189].

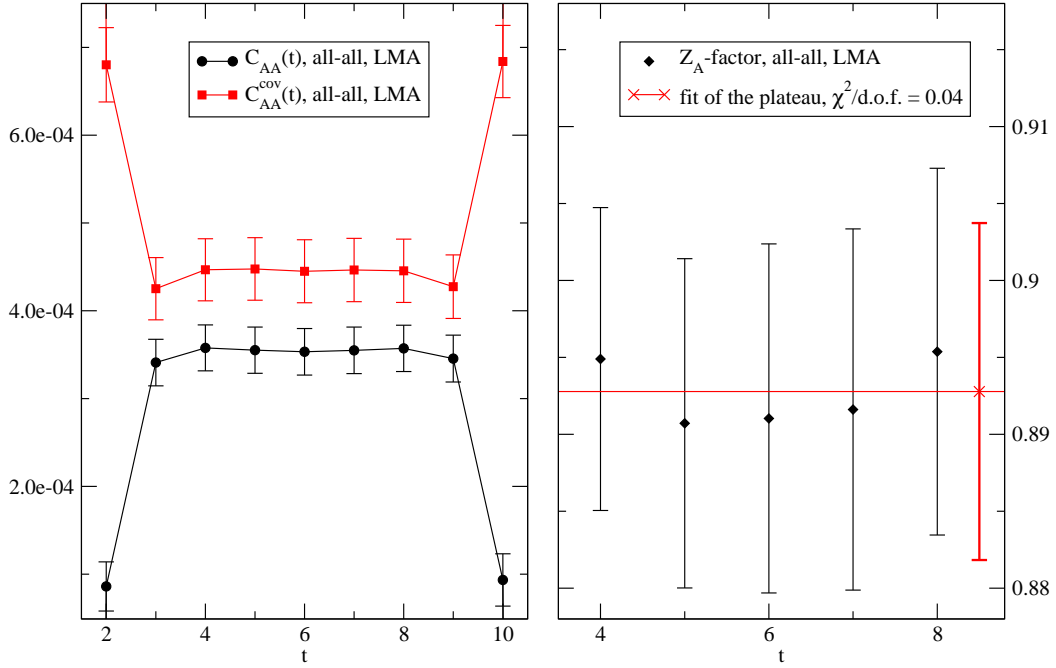


Figure 13.17: We plot on the lhs. the naive axialvector-axialvector correlators  $\langle A_4 A_4 \rangle$  obtained from all-to-all propagators and the covariant correlator  $\langle A_4 A_4 \rangle_{\text{cov}}$  obtained from all-to-all propagators. On the rhs. we plot the square root of the ratio between the naive correlators  $\langle A_4 A_4 \rangle$  and the covariant correlator  $\langle A_4 A_4 \rangle_{\text{cov}}$ . We plot the  $Z_A$ -factors only for the  $m_{ud}$  mass.

and without LMA. Here the differences between the correlators with and without LMA are far less pronounced as in the pseudoscalar channel. We obtain in both channels, the pseudoscalar and scalar ones, a plateau in the region  $t \in [4, \dots, 8]$ :

$$Z_P(m_{ud}) = 1.0703(8), \quad (13.11)$$

$$Z_S(m_{ud}) = 1.078(4). \quad (13.12)$$

In Fig. (13.17) we show the  $Z_A$ -factors of the naive correlators. They are calculated by the square root of the ratio between the naive (black) and the covariant (red) axialvector-axialvector correlator using all-to-all propagators. Here the statistical errors are bigger compared to Fig. 13.15, because we have a factor of 10 less statistics for the all-to-all propagator than for the point-to-all propagator. In the all-to-all propagators, as discussed in Section 8.1.2, we also use LMA explicitly. We quote as a result for the  $Z_A$ -factor:

$$Z_A(m_{ud}) = 0.89(1). \quad (13.13)$$

In Fig. 13.18 the ratios between  $Z_P$  and  $Z_S$  are plotted. We find a very small discrepancy to one, which indicates a good chiral behavior of the FP Dirac operator:

$$\frac{Z_P}{Z_S} = 0.993(3), \quad \frac{Z_S}{Z_P} = 1.007(3). \quad (13.14)$$

It also proves that we will be allowed to use our covariant densities as input for the ChPT predictions. The discrepancy is negligibly small compared to other sources of error.

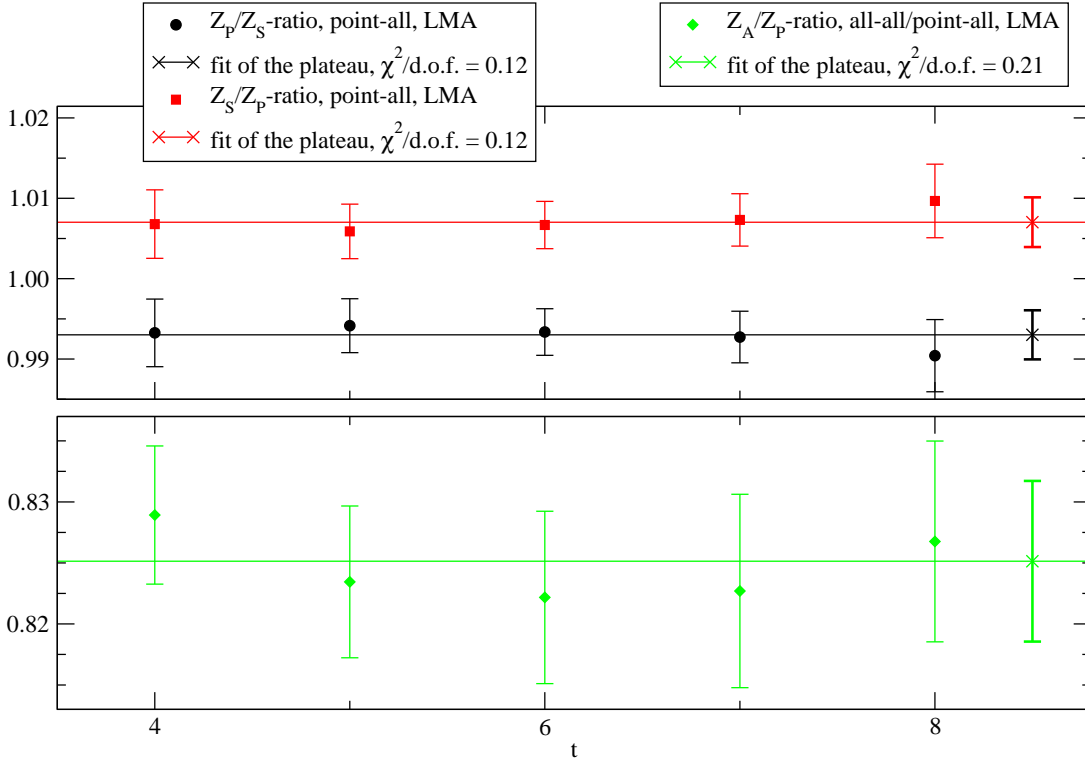


Figure 13.18: **Top:** These are the ratios between the  $Z_P$  and  $Z_S$  for our small mass  $m_{ud}$ . For covariant densities these ratios should be exactly one. The discrepancy comes from the fact that we are using an approximately chiral Dirac operator also to obtain the covariant scalar and pseudoscalar densities in Eq. (D.21). However, the error assuming we have exact covariant densities, is negligibly small.

Figure 13.19: **Bottom:** Here we show the ratio of  $Z_A$  and  $Z_P$ . The obtained result agrees with the slope of the chiral extrapolation in Fig. 13.9.

The results in Eqs. (13.11) and (13.13) can be cross-checked with the slope of the chiral fit in Fig. 13.9, which is the ratio between  $Z_A$  and  $Z_P$  in our case (cf. Section 9.2.2). We find in Fig. 13.19<sup>3</sup>:

$$\frac{Z_A(m_{ud})}{Z_P(m_{ud})} = 0.825(7). \quad (13.15)$$

This ratio is very closed to the slope of the chiral fit  $Z = 0.835(2)$ , where we quote in both results only the statistical error of the fit.

### 13.4.2 The bare $\Sigma$

Using Eq. (9.48) we apply a single parameter fit to find the bare quark condensate<sup>4</sup>. We use the scale-independent LECs  $\bar{l}_3$  and  $\bar{l}_4$ , which are defined as [89, 190, 191]

$$\bar{l}_3 \equiv \ln \frac{\Lambda_3^2}{M^2} \Big|_{M=139.6 \text{ MeV}} = 2.9(2.4), \quad (13.16)$$

$$\bar{l}_4 \equiv \ln \frac{\Lambda_4^2}{M^2} \Big|_{M=139.6 \text{ MeV}} = 4.4(2), \quad (13.17)$$

<sup>3</sup>In Section 9.2.2 we write the slope in terms of the renormalization constant  $Z_A$  which is defined in the continuum. Here we just compare the difference between the naive and the covariant correlators.

<sup>4</sup>In Eq. (9.48) the coefficients are given in terms of  $\Sigma$ ,  $F$ ,  $\Lambda_M \equiv \Lambda_3$  and  $\Lambda_F \equiv \Lambda_4$ .

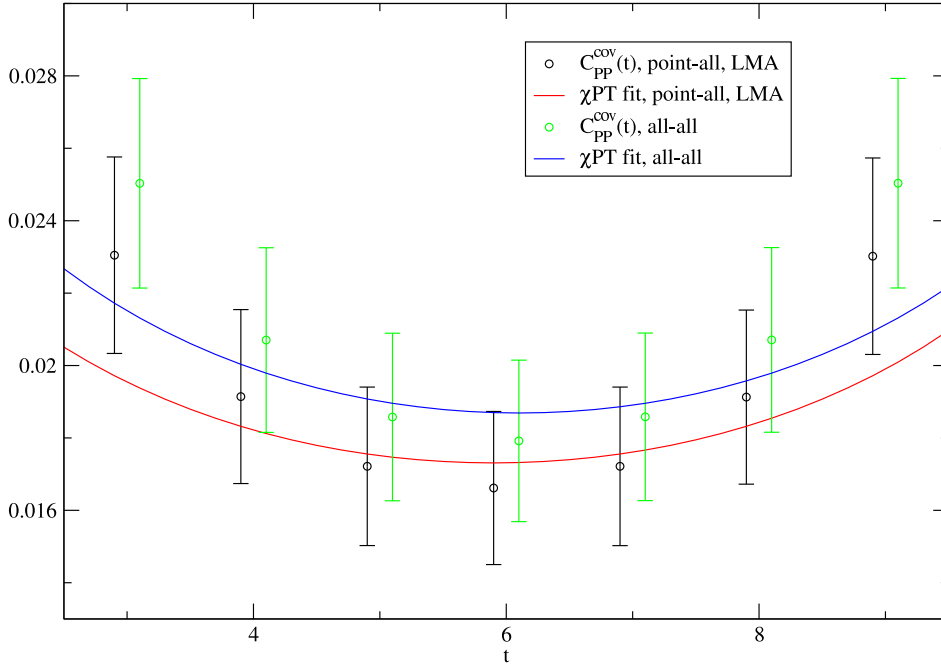


Figure 13.20: Here we show the covariant pseudoscalar-pseudoscalar density correlators obtained from the point-to-all propagators with low-mode averaging (black) and from all-to-all propagators (green). The errors are determined by a Jackknife analysis. We only fit in the region  $t \in [4, \dots, 8]$  to ChPT predictions in Eq. (9.48), where we insert experimental data for all parameters in higher orders, but the  $\Sigma$ . We recursively use a one-parameter fit to extract the bare  $\Sigma$  from LO ChPT.

Furthermore we insert for the pion decay constant in the chiral limit  $F = 86.2(5)$  MeV and use the obtained  $\Sigma$  in the fit recursively until the inserted  $\Sigma$  and the obtained one are the same. This recursion converges relatively fast. Due to the fact that we are only interested in the prefactor we have to be careful with the  $Z$ -factors of our correlators. In Section 8.5 we introduce covariant operators and use them to determine correlation functions without  $Z$ -factors<sup>5</sup>. In this way it is enough to obtain the prefactor in Eq. (9.48) which is proportional to  $\Sigma^2$ . On our relatively small  $12^4$  lattice we can apply Eq. (9.48) only for values of  $t \in [4, \dots, 8]$ . Therefore, differently to other groups [192, 193, 194] using larger lattices we cannot use this fit to obtain further LECs.

We show in Fig. 13.20 the fits of the covariant pseudoscalar-pseudoscalar correlators to the formula in Eq. (9.48). We obtain from the correlator using covariant point-to-all propagators with low-mode averaging:

$$\Sigma^{1/3} = 233(5) \text{ MeV} , \quad (13.18)$$

where the error is the statistical error of the fit. The analysis of the correlator using all-to-all propagators yields:

$$\Sigma^{1/3} = 237(5) \text{ MeV} , \quad (13.19)$$

Note that a renormalization factor  $Z^{\overline{MS}}$  has not been calculated yet and that we can only quote the bare results here. We can simply compare these bare values with the bare result (13.9) obtained from RMT predictions at the moment and find a  $2\sigma$  discrepancy. Because of the small volume of our lattice and the fact that we have problems in determining the topological sector, this might explain the higher result from the RMT predictions. But further investigations are still necessary. The renormalized  $\Sigma^{\overline{MS}}$  will be published in an upcoming paper [195].

<sup>5</sup>Because we only use approximately chiral fermions there is still a  $Z$ -factor in front of the correlators. However, using covariant operators works as a  $\mathcal{O}(a)$  improvement and pushes therefore  $Z$  towards 1.

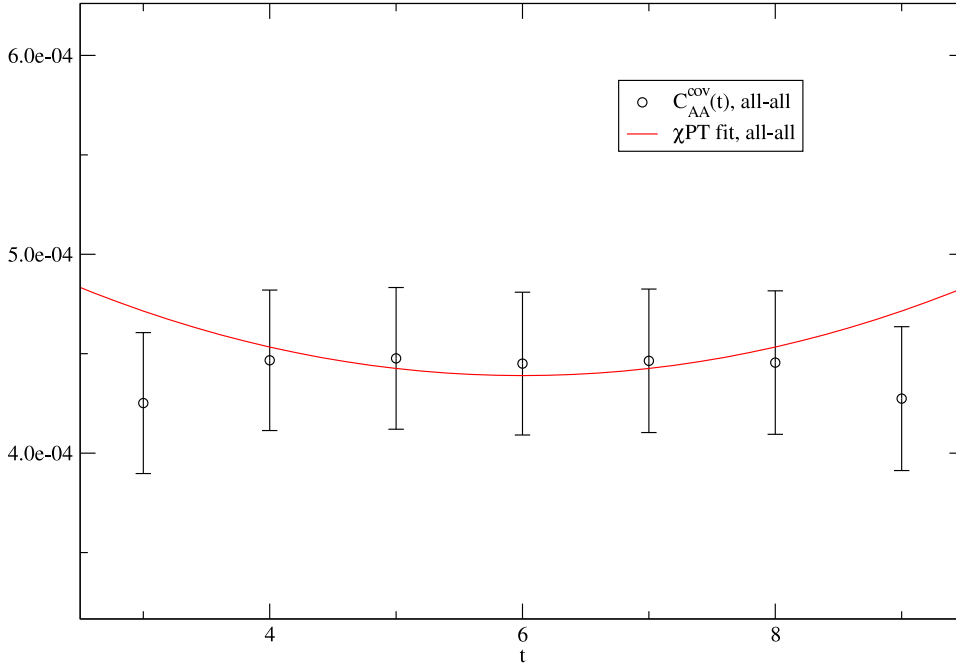


Figure 13.21: We show here the covariant axialvector-axialvector current correlators obtained from the all-to-all propagator. The errors are obtained from a Jackknife analysis. We only fit in the region  $t \in [4, \dots, 8]$  to chiral perturbation theory predictions in Eq. (9.49). We can apply a recursive one-parameter fit to obtain  $F_\pi$  from LO ChPT.

### 13.4.3 The pion decay constant $F$

Like for the pseudoscalar case there also exists a NLO prediction for the axialvector-axialvector correlator discussed in Section 9.3.2. Due to the fact that we are interested in the prefactor we apply covariant currents, which are realized by all-to-all propagators (cf. Eq. (8.132)). We set the fitting range to  $t \in [4, \dots, 8]$  and use the result (13.19), which is also obtained by using all-to-all propagators, for  $\Sigma$ . From Fig. 13.21 we can extract the pseudoscalar decay constant  $F_{PS}$  (cf. Eq. (9.49)) at a pseudoscalar mass of  $m_{PS} = 262(28)$  MeV ( $\Sigma^{1/3} = 237$  MeV) and get:

$$F_{PS} = 96.0(3.9) \text{ MeV} . \quad (13.20)$$

Solving Eq. (9.56) numerically provides us the pion decay constant in the chiral limit  $F$ :

$$F = 78.6(8.2) \text{ MeV} . \quad (13.21)$$

These results are in agreement with values obtained from phenomenological analysis. However, on a larger lattice we could increase the fitting range and can use the higher order terms of the fit to extract NLO LECs as well. This is an ongoing project.

## Part V

# Conclusion

# Summary

In the introduction we started to discuss the relation between QCD and the standard model and gave so the background for QCD on the lattice. We cited also the papers published already.

In Part I we went more into detail. We defined and introduced there symmetries of QCD in the continuum which we used later to model QCD on a finite lattice. Calculating LECs being the parameters of an effective theory is only useful if one knows the effective theory underneath. Therefore, we gave a brief introduction into chiral perturbation theory. We also tried to explain the different regimes in which it is possible to obtain LECs. For one of the regimes, the  $\epsilon$ -regime, we made use of RMT predictions to obtain  $\Sigma$ , one of the LECs in leading order. To give at least some justification for using RMT predictions we briefly introduced chiral Random Matrix Theory. We can use a quite different RMT approach to obtain the same physical relevant observables of our QCD calculations.

In Part II we focused on lattice QCD. Going through the chapters we followed the way from the start to the end of a typical lattice simulation. Putting a quantum field theory on a discrete space-time lattice one naturally obtains a regularization scheme via the lattice spacing  $a$ . In addition to the space-time we also need a discretized form of the gauge and the fermion action. There are several different possibilities which all have their justification to be used in a simulation. In this work we make use of approximately chiral Dirac operators, which are a compromise between exact chirality and the needed computer resources. Keeping all these different ways in mind we have to choose some gauge and fermion action and start a simulation<sup>6</sup>.

The most expensive part of a dynamical simulation is the generation of gauge configurations<sup>7</sup>. We are using Monte Carlo methods with importance sampling. We also discussed how a simulation is managed practically. After this production step we analyzed the gained data. As an intermediate step before obtaining physical quantities we had to calculate propagators which we then used to evaluate correlation functions. Because of  $\gamma_5$ -hermicity of both Dirac operators, the CI Dirac operator and the parametrized FP Dirac operator, we created point-to-all propagators and were able to use them in correlation functions. A more sophisticated way is the usage of all-to-all propagators, which were calculated for FP fermions for the first time.

The correlation functions are again subject to some improvements, which were used in our projects to increase the signal to noise ratio significantly. We adopted the low-mode averaging technique for the FP Dirac operator and extended the methods also to low-high averaging. Secondly, we calculate covariant densities using both, point-to-all and all-to-all propagators. Furthermore, we also computed conserved currents numerically. Both, the covariant densities and the conserved currents, were first applied for FP fermions in this work.

After briefly discussing the setting of the scale we started to show why and how two-point correlation functions are used and presented two examples: one for a meson correlator and another for a baryon correlator. For the baryon correlators we also showed a way to obtain only a single parity state from a baryon correlator using different boundary conditions in the temporal direction. Another important piece of information is the mass shift which can be obtained from the AWI mass. We also discussed several scenarios which were relevant for the mass shift and renormalization factors.

We discuss the data analysis for LECs. To do so, we apply  $\chi$ PT in a finite box in the so-called  $\epsilon$ -expansion. Results can be obtained either by comparing our eigenvalue distribution with that of RMT predictions or by fitting correlation functions to  $\chi$ PT predictions. We also started to use the  $\delta$ -expansion for obtaining LECs. Finally, the systematical and statistical errors of the data have to be estimated. In this work we used the

---

<sup>6</sup>In standard lattice calculations one uses hypercubic lattices as a natural choice. In principle one can also chose a different discretization of the lattice itself, e.g., a hexagonal lattice.

<sup>7</sup>For a quenched simulation the task of ensemble generation is in terms of computer resources very easy to do.

Jackknife or the Bootstrap methods to estimate the statistical errors. We also used binning to minimize the systematical errors due to autocorrelation in our Markov chains.

In Part III we presented results obtained from quenched configurations using the CI Dirac operator and Lüscher-Weisz gauge action.

In Chapter 10 we showed a quenched spectroscopy calculation of excited baryons using the variational method. We used interpolators with different Dirac structures. Furthermore each quark could either have a narrow or a wide source such that the states can have nodes in their spatial wave function.

For the positive parity baryons we found that the ground state masses were compatible with the experimental numbers, while for the excited states the masses were systematically 20% - 25% above the experimental numbers. We believe that the failure to reproduce the masses of the positive parity excited baryons is indeed mainly due to quenching which has the consequence that a significant part of chiral physics is missing. Large finite volume effects could not be excluded either.

For negative parity, we found that our masses were in reasonable agreement with the experimental numbers, although here our statistical errors were larger and a further lowering of our results for a lattice with a higher cutoff could not be excluded.

For four of the analyzed channels our data are convincing enough to quote the final results as a prediction: The first excited positive parity  $\Omega$  state, the negative parity  $\Omega$  ground state, and the ground and first excited negative parity  $\Xi$  states (Table 10.5). Those particles have not been found so far.

In Chapter 11 we presented the results of a pilot study for  $\Theta^+$  searches on the lattice using different types of operators. We found that for negative parity our results were in good agreement with a  $n$ - $K$  scattering state in the ground state and a quite noisy signal for the first excited state. For positive parity we found states which were typically more than 500 MeV heavier than the  $\Theta^+$  and thus not compatible with a  $\Theta^+$  mass of 1540 MeV. In our calculation we did not find any hints for a  $\Theta^+$  using in addition to standard ones the new interpolators (11.31)-(11.34). Due to a lack of computer resources we were not able to introduce  $p$ -waves in our calculation, which were claimed to be necessary for pentaquark interpolators by some theoretical predictions. The missing  $p$ -waves and the quenched approximation could be a reason why we do not see a pentaquark state in our results, if it existed. However, the latter seems very unlikely in the light of recent experimental results.

In Part IV we presented the starting phase of a huge project to determine LECs from lattice simulations. Starting with the presentation of the developed algorithm we could already show some results on relatively small lattices which were at least as good as those obtained by other groups which were using much more computer and men power than our group could afford. Simulating the parametrized FP action with a partially global update procedure we were able to reach sufficiently small quark masses to study both the  $\delta$ - and the  $\epsilon$ -regime in  $2 + 1$  flavor QCD.

In Chapter 12 we describe the algorithm for  $2 + 1$  dynamical FP fermions. We had to use a global update algorithm due to the fact that we apply also in the gauge action a RG smearing which can not be differentiated with respect to the gauge fields. Therefore, a state-of-the-art variant of a Hybrid Monte Carlo cannot be used. Walking through the configurations space in reasonable steps the acceptance rate would decrease very fast. To get non-vanishing acceptance rates and at the same time quite decorrelated configurations we needed to introduce some tricks:

- Reduction brings all UV modes very close together and minimizes therefore their fluctuation.
- Subtraction treats the low-lying eigenvalues and -vectors exactly and one can use, at least in the low-mode part of the propagator, the translational invariance of the lattice explicitly.
- Relative gauge fixing reduces the fluctuations in the determinants
- Determinant breakup divides the problem into smaller ones, which can be solved more stably.

To improve the achievable acceptance rates even more we repeated the cheaper parts of the global update more often than the more expensive ones and could so update a larger region in the configuration space within a single step.

The central operation in this algorithm is the matrix-vector multiplication of the FP Dirac operator with a vector, i.e., using profiling tools one finds that this operation takes most of the execution time. Improving the performance in this part promised therefore the largest savings of computer time and was the fastest way to

reach the most optimal code for this algorithm.

Whereas the code was already running on various architectures it was optimized for small partitions and showed both, a bad weak and hard scaling on the new SGI Altix system in Munich. With our improvements we can now use the matrix-vector multiplication nearly with arbitrary parallelizations in all four directions. Extrapolating to larger lattices we have still the same efficiency in the  $Dv$  operation (cf. Table 12.1). Furthermore we can exclusively use the L3 cache on the SGI Altix system even for larger lattices, which will become interesting for our future physics program (cf. Fig. 12.3).

In principle, the code is written to run on nearly every distributed memory machine using MPI. This statement also remains true for both, small PC clusters or massively parallel machines like the SGI Altix 4700 or a BlueGene/P system.

In Chapter 13 we presented the first results of the physics program which could be done in the  $\delta$ - and the  $\epsilon$ -regime. As a start we tried to proof that we can reach the  $\delta$ -regime using our algorithm for dynamical FP fermions. We reported on the autocorrelation time and determination of the AWI mass on the  $8^3 \times 24$  lattice. We found the predicted mass gap in the rotator spectrum and applied LO chiral perturbation theory to compute the pion decay constant. Unfortunately, the spatial box was too small to compare the result with the analytic predictions. The calculation of the NLO contributions to the  $\delta$ -regime is an ongoing project at Bern university. On our larger  $12^4$  lattice we are in the  $\epsilon$ -regime. To reach this regime we again needed very small quark masses and a Dirac operator with good chiral properties. Both requirements could be achieved by the parametrized FP action and its corresponding FP Dirac operator. In this study we were furthermore using dynamical configurations which also contributed to improve the parts of our calculation which were sensitive to the chiral properties. We reported on the numerical implementation and the autocorrelation in the Markov chain. In the measurement of the meson correlators the low-mode averaging was found to improve the signal significantly. Since the low-lying eigenmodes of the Dirac operator were available on each configuration from our updating, this did not require extensive computing resources. We determined the additive mass renormalization and verified that our light quark masses were near to the chiral limit. However, it would have been possible to further decrease the mass of the  $ud$ -quark in the algorithm on the  $12^4$  lattice. Unfortunately we were overcautious in this point. We found that the AWI mass depended nearly linearly on the average of the corresponding lattice quark masses and that the eigenvalues lied in good approximation on the shifted Ginsparg-Wilson circle.

We compared the eigenvalue distribution of the FP Dirac operator with RMT predictions. Due to the fact that FP fermions are only approximately chiral, the index theorem is also only approximately fulfilled. Therefore, we introduced the inverse participation ratio (IPR) to assign the gauge configurations to topological sectors. We have checked several methods for the identification of the topological charge which gave all nearly the same results.

We used the stereographic projection on the eigenvalues of the FP Dirac operator and compared the eigenvalue distribution with RMT predictions. The distributions for different  $\nu$  and  $k$  are consistent with each other, although the identification of the topological charge is somewhat ambiguous. From the RMT predictions we find  $\Sigma^{1/3} = 0.286(3)(9)$  GeV in finite volume, which can be corrected to a reasonable  $\Sigma_\infty^{1/3}(N_f = 3) = 0.255(3)(9)$  GeV in infinite volume. However, the shape of the  $\nu = 0, k = 1$  distribution differed from that of the RMT, which could be a finite-size effect. If we will be able to verify this finite-size effect on our larger lattice, many groups would profit from this result, as it would give an lower bound for applying RMT in the  $\epsilon$ -regime. We also gave the ratios of the mean eigenvalues and found even for higher topological sectors good agreement with RMT predictions. So it seemed that we are just in that region where RMT predictions become valid.

We also used  $\chi$ PT predictions to obtain LECs from correlation functions. This way of calculating LECs is quite new and promising. Although the fit formulas have been known for nearly 2 decades, only the recently available lattices and small quark masses allowed to apply them in lattice calculations. We calculate various ratios between the naive and the covariant correlators. After that we could fit the covariant correlators to the  $\chi$ PT predictions and get consistent results for the bare  $\Sigma^{1/3} = 237(5)$  MeV and the pion decay constant in the chiral limit  $F = 78.6(8.2)$  MeV.

# Outlook

The results in Chapter 10 are suffering from the quenched approximation. This project has already been continued on larger lattices with  $N_f = 2$  dynamical CI fermions. There will also be more correlators available which are not taken into account here. The predictions we gave at the end of the chapter are already comparable to QCD sum rules and are part of ongoing research.

In our quenched calculation in Chapter 11 we only use one lattice volume and one spatial boundary condition. If we had found a  $\Theta^+$  candidate, for the final distinction between a bound or a scattering state we would at least have to study the volume dependence. As it stands, there is no motivation to do so and due to the fact that more and more experimental results in favor of the  $\Theta^+$  cannot be reproduced by other experiments, it is very unlikely that there is a  $\Theta^+$  state at all, which has a very narrow width of  $< 25$  MeV. Therefore, even if there are dynamical configurations produced with chiral fermions available in the near future, the search for the  $\Theta^+$  will always have an exotic touch. However, if the current experimental situation will change in favor of a pentaquark with a narrow width of  $< 25$  MeV this project can immediately be continued with the existing code using dynamical fermions.

With the presented algorithm in Chapter 12 it is possible to simulate  $N_f = 2 + 1$  flavors of dynamical FP fermions. We present several tricks which allow us to use nested global update steps, to get reasonable acceptance rates and autocorrelation times. However, due to our RG smearing which is not differentiable we cannot use a Hybrid Monte Carlo at the moment. But there are some ongoing tests to change this in future. Furthermore, we have seen that for our  $12^4$  lattice we can even simulate at smaller masses than we have used in this work, without facing the problem of exceptional configurations. Hence, we will still be in the  $\epsilon$ -regime, even if we increase the lattice sizes. We have also shown that the efficiency of the matrix-vector multiplications ( $Dv$ ) does not depend on the number of used cores. Therefore, the code is ready to be used for larger lattices without changing the parallelization.

Simulating small quark masses on an asymmetric lattice,  $L^3 \times T$  with  $L < T$ , and using the FP action at the same time, will take us into the  $\delta$ -regime, which is a nearly "untouched" field and where we can obtain several LECs in different ways. The work presented in this thesis is the starting point for very interesting new physics. If we use our experiences with the  $8^3 \times 24$  lattice we think that we might be able to obtain LECs even on a  $12^3 \times 24$  lattice using  $\delta$ -regime predictions. Furthermore, the extension of the predictions in the  $\delta$ -regime to NLO is an ongoing project at Bern university and will further increase the accuracy of the results.

Although the  $\epsilon$ -expansion is known for nearly 2 decades lattice calculations have only recently reached the necessary conditions, e.g., small quark masses and good chiral behavior of the Dirac operator. We have compared our result found in this regime with RMT predictions and can find a matching with the distributions of our eigenvalues in several topological sections. However, the shape of our  $\nu = 0$ ,  $k = 1$  eigenvalue distribution cannot be reproduced by RMT predictions. This can be explained by a finite size effect of our relatively small  $(1.55 \text{ fm})^4$  lattice which is also small compared to those lattice sizes used by other groups. We will check this issue on larger symmetric lattices. We also compare our results in the  $\epsilon$ -regime with ChPT predictions. On our current lattice we can only use the ChPT prediction in a very small region. Using a larger lattice we plan to verify our results on the smaller lattice and to find further NLO LECs from the higher contributions of the ChPT predictions.

# Acknowledgements

I would like to thank my advisor Andreas Schäfer for giving me the opportunity to work at his chair, sharing his experience and knowledge with me, and for the guidance into the world of physics. Andreas, you allowed me great latitude but nevertheless you pushed me to the right direction when it was necessary. Thank you very much.

I am indebted to Peter Hasenfratz for many enlightening discussions and ideas. It was a great experience to collaborate with someone who has pushed our field by that amount. I also want to thank Ferenc Niedermayer who lent a hand for any numerical or theoretical problem. Especially when I was finishing and the pressure became stronger and stronger, you helped me a lot. As well, I thank both of you for your hospitality whenever I was visiting Bern.

Gunnar Bali, Jacques Bloch, Tommy Burch, Christian Ehmann, Christof Gattringer, Meinulf Göckeler and Christian Hagen, thank you for discussing innumerable questions on Lattice QCD.

In this context also many thanks to the BGR collaboration, especially to Christoph Weiermann, Manuel Weingart, Vidushi Maillart, Christian Lang and Markus Limmer for fruitful discussions.

I want to appreciate the proof-readers of this work: Jacques Bloch, Meinulf Göckeler, Christian Hagen, Peter Hasenfratz, Alexander Manashov, Ferenc Niedermayer and Nikolaus Warkentin. I thank you so much.

Special thanks to Tommy Burch, Christian Hagen, Michael Hartung, Thilo Mauerer, Stefan Solbrig and Nikolaus Warkentin for the coffee breaks and the discussions about all the world and his brother.

I also wish to thank Monika Maschek and Heidi Decock for helping me through all the bureaucracy and the administrative stuff.

I want to thank Heribert Weigert, Carmen Frammelsberger, Nigel Cundy and Christian Ehmann for their patience while sharing an office with me. I also appreciate the discussions a lot.

Also being a computer administrator at the chair several years I know how much efforts it is to keep the system running. Christian Hagen, Michael Hartung, Christian Ehmann, Michael Wimmer and Martin Hetzenegger keep on doing your best and let the others also know what you have to fight with every day.

I also want to include all the other members of the chairs Schäfer and Braun for the always cooperative and friendly atmosphere.

I would like to thank the Leibniz Rechenzentrum for the computer time and support on the Hitachi SR8000 and the SGI Altix 4700 systems. Furthermore part III would have not been possible without support and computer time at the Forschungszentrum Jülich and their JUMP cluster. I was also allowed to use gauge configurations produced at CSCS in Manno and on the ITP Cluster in Bern. Finally I do not want to forget the people at RZ Regensburg for their support of the local RZ cluster, old but important for part III. I also thank my admin colleagues for the work they have also invested in the cluster of the theoretical physics department together with its storage.

I thank the BMBF and GSI for financial support while working on the project "QCD-Rechnungen", 06RYZ58.

Schließlich möchte ich mich bei meinen Eltern Veronika und Rudolf, meiner Schwester Marion und meiner Freundin Carina bedanken. Vielen Dank für Euerer Unterstützung in jeder erdenklichen Art und Weise während der letzten Jahre. Ohne Euch wäre ich wahrscheinlich nicht so weit gekommen.

# Appendix

# Appendix A

## Definitions

### A.1 Gamma matrices

The Euclidean gamma matrices  $\gamma_\mu$ ,  $\mu = 1, 2, 3, 4$  can be expressed through the Minkowski gamma matrices  $\gamma_\mu^M$ ,  $\mu = 0, 1, 2, 3$  via

$$\gamma_1 = -i\gamma_1^M, \quad \gamma_2 = -i\gamma_2^M, \quad \gamma_3 = -i\gamma_3^M, \quad \gamma_4 = \gamma_0^M. \quad (\text{A.1})$$

They satisfy the Euclidean anti-commutation relation:

$$\{\gamma_\mu, \gamma_\nu\} = 2\delta_{\mu\nu}\mathbb{1}_{4\times 4}. \quad (\text{A.2})$$

We also define the  $\gamma_5$  matrix as

$$\gamma_5 = \gamma_1\gamma_2\gamma_3\gamma_4 = i\gamma_0^M\gamma_1^M\gamma_2^M\gamma_3^M = \gamma_5^M, \quad (\text{A.3})$$

which obeys  $\gamma_5^2 = \mathbb{1}_{4\times 4}$  and anti-commutes with all other gamma matrices

$$\{\gamma_5, \gamma_\nu\} = 0. \quad (\text{A.4})$$

The Euclidean matrices read in the chiral representation:

$$\begin{aligned} \gamma_1 &= \begin{pmatrix} 0 & 0 & 0 & -i \\ 0 & 0 & -i & 0 \\ 0 & i & 0 & 0 \\ i & 0 & 0 & 0 \end{pmatrix}, & \gamma_2 &= \begin{pmatrix} 0 & 0 & 0 & -1 \\ 0 & 0 & 1 & 0 \\ 0 & 1 & 0 & 0 \\ -1 & 0 & 0 & 0 \end{pmatrix}, & \gamma_3 &= \begin{pmatrix} 0 & 0 & -i & 0 \\ 0 & 0 & 0 & i \\ i & 0 & 0 & 0 \\ 0 & -i & 0 & 0 \end{pmatrix} \\ \\ \gamma_4 &= \begin{pmatrix} 0 & 0 & 1 & 0 \\ 0 & 0 & 0 & 1 \\ 1 & 0 & 0 & 0 \\ 0 & 1 & 0 & 0 \end{pmatrix}, & \gamma_5 &= \begin{pmatrix} 1 & 0 & 0 & 0 \\ 0 & 1 & 0 & 0 \\ 0 & 0 & -1 & 0 \\ 0 & 0 & 0 & -1 \end{pmatrix} \end{aligned} \quad (\text{A.5})$$

In addition to the anti-commutation relation the gamma matrices satisfy:

$$\gamma_\mu = \gamma_\mu^\dagger = \gamma_\mu^{-1} \quad \text{for } \mu = 1, 2, 3, 4, \quad \gamma_5 = \gamma_5^\dagger = \gamma_5^{-1}. \quad (\text{A.6})$$

We can write all possible complex  $4 \times 4$ -matrices in a basis of: (S)calar ( $\mathbb{1}$ ), (P)seudoscalar ( $\gamma_5$ ), (V)ector ( $\gamma_\mu$ ), (A)xial ( $\gamma_\mu\gamma_5$ ) and (T)ensor ( $\sigma_{\mu\nu}$ ) Lorentz combinations of the gamma matrices  $\Gamma_{(S)}$ ,  $\Gamma_{(P)}$ ,  $\Gamma_{(V)}$ ,  $\Gamma_{(A)}$ ,  $\Gamma_{(T)}$ , respectively, where  $\sigma_{\mu\nu} = \frac{1}{2}[\gamma_\mu, \gamma_\nu]$ .

In Minkowski space it is:

$$\gamma_0^M \left(\Gamma_{(i)}^M\right)^\dagger \gamma_0^M = \Gamma_{(i)}^M \quad \text{for } i = S, V, A, T \quad (\text{A.7})$$

$$\gamma_0^M \left(\Gamma_{(i)}^M\right)^\dagger \gamma_0^M = -\Gamma_{(i)}^M \quad \text{for } i = P. \quad (\text{A.8})$$

## A.2 Gell-Mann matrices

$abc$	$f^{abc}$ (antisymmetric)	$abc$	$d^{abc}$ (symmetric)
123	1	118	$1/\sqrt{3}$
147	$1/2$	146	$1/2$
156	$-1/2$	157	$1/2$
246	$1/2$	228	$1/\sqrt{3}$
257	$1/2$	247	$-1/2$
345	$1/2$	256	$1/2$
367	$-1/2$	338	$1/\sqrt{3}$
458	$\sqrt{3}/2$	344	$1/2$
678	$\sqrt{3}/2$	355	$1/2$
		366	$-1/2$
		377	$-1/2$
		448	$-1/(2\sqrt{3})$
		558	$-1/(2\sqrt{3})$
		668	$-1/(2\sqrt{3})$
		778	$-1/(2\sqrt{3})$
		888	$-1/\sqrt{3}$

Table A.1: Antisymmetric and symmetric structure constants of the Gell-Mann matrices (cf. Ref. [196]).

The generator of the  $su(n)$  algebra are denoted by  $t^a$ . They are hermitian  $n \times n$  matrices with

$$\text{tr} [t^a] = 0 \quad \text{and} \quad (t^a)^\dagger = t^a . \quad (\text{A.9})$$

They are normalized via

$$\text{tr} [t^a t^b] = \frac{1}{2} \delta^{ab} . \quad (\text{A.10})$$

and satisfy the following (anti-)commutator relations:

$$[t^a, t^b] = i f^{abc} t^c \quad \text{and} \quad \{t^a, t^b\} = \frac{1}{3} \delta^{ab} \mathbb{1} + d^{abc} t^c , \quad (\text{A.11})$$

where  $f^{abc}$  is the antisymmetric structure constant and  $d^{abc}$  is the symmetric one. In Tab. A.1 one can find the values of the structure functions for  $n = 3$ .

The generators of the  $su(3)$  algebra are usually proportional to the the Gell-Mann matrices:

$$t^a = \frac{\lambda^a}{2} . \quad (\text{A.12})$$

The usual representation of the 8 Gell-Mann matrices is:

$$\begin{aligned}
\lambda_1 &= \begin{pmatrix} 0 & 1 & 0 \\ 1 & 0 & 0 \\ 0 & 0 & 0 \end{pmatrix} & \lambda_2 &= \begin{pmatrix} 0 & -i & 0 \\ i & 0 & 0 \\ 0 & 0 & 0 \end{pmatrix} & \lambda_3 &= \begin{pmatrix} 1 & 0 & 0 \\ 0 & -1 & 0 \\ 0 & 0 & 0 \end{pmatrix} \\
\lambda_4 &= \begin{pmatrix} 0 & 0 & 1 \\ 0 & 0 & 0 \\ 1 & 0 & 0 \end{pmatrix} & \lambda_5 &= \begin{pmatrix} 0 & 0 & -i \\ 0 & 0 & 0 \\ i & 0 & 0 \end{pmatrix} & \lambda_6 &= \begin{pmatrix} 0 & 0 & 0 \\ 0 & 0 & 1 \\ 0 & 1 & 0 \end{pmatrix} \\
\lambda_7 &= \begin{pmatrix} 0 & 0 & 0 \\ 0 & 0 & -i \\ 0 & i & 0 \end{pmatrix} & \lambda_8 &= \begin{pmatrix} \frac{1}{\sqrt{3}} & 0 & 0 \\ 0 & \frac{1}{\sqrt{3}} & 0 \\ 0 & 0 & -\frac{2}{\sqrt{3}} \end{pmatrix}
\end{aligned} \tag{A.13}$$

### A.3 Grassmann Numbers

A generator of the Grassmann algebra  $\Theta_i$  anti-commutes with every other generator of the Grassmann algebra  $\Theta_j$ :

$$\Theta_i \Theta_j = -\Theta_j \Theta_i . \tag{A.14}$$

It follows directly from (A.14) that the generators of the Grassmann algebra are nilpotent:

$$\Theta_i^2 = 0 . \tag{A.15}$$

This makes the Grassmann algebra very easy, because due to (A.15) one can write every Grassmann number  $A$  as:

$$\begin{aligned}
A &= a + \sum_i a_i \Theta_i + \frac{1}{2!} \sum_{i,j} a_{ij} \Theta_i \Theta_j + \dots + \frac{1}{N!} \sum_{i_1, \dots, i_N} a_{i_1 \dots i_N} \Theta_{i_1} \dots \Theta_{i_N} , \\
a_{i_1 \dots i_n} &\in \mathbb{C}, \quad i_1 \dots i_n \text{ are totally antisymmetric} ,
\end{aligned} \tag{A.16}$$

where the polynoms in  $A$  form a  $N$ -dimensional Grassmann algebra.

The derivative with respect to Grassmann variables is defined as:

$$\frac{\partial}{\partial \Theta_i} 1 = 0 , \tag{A.17}$$

$$\frac{\partial}{\partial \Theta_i} \Theta_i = 1 , \tag{A.18}$$

$$\frac{\partial^2}{\partial \Theta_i^2} A = 0 , \tag{A.19}$$

$$\frac{\partial^2}{\partial \Theta_i \partial \Theta_j} A = -\frac{\partial^2}{\partial \Theta_j \partial \Theta_i} A . \tag{A.20}$$

The integration over Grassmann variables has to obey the following constraints:

1. The integral has to be a complex and linear functional:

$$\int d^N \Theta A \in \mathbb{C} , \tag{A.21}$$

$$\int d^N \Theta (\lambda_1 A_1 + \lambda_2 A_2) = \lambda_1 \int d^N \Theta A_1 + \lambda_2 \int d^N \Theta A_2 \tag{A.22}$$

$$\text{with } d^N \Theta = d\Theta_N d\Theta_{N-1} \dots d\Theta_1 . \tag{A.23}$$

2. It has to be integrable:

$$\int d^N \Theta \frac{\partial}{\partial \Theta_i} A = 0. \quad (\text{A.24})$$

3. And finally it is supposed to be normalized:

$$\int d^N \Theta \Theta_1 \Theta_2 \dots \Theta_N = 1. \quad (\text{A.25})$$

These rules include the following:

$$\int d^N \Theta A = a_{12\dots N}, \quad (\text{A.26})$$

$$\{d\Theta_i, d\Theta_j\} = \{d\Theta_i, \Theta_j\} = 0, \quad (\text{A.27})$$

$$\int d\Theta 1 = 0, \quad (\text{A.28})$$

$$\int d\Theta \Theta = 1 \quad \text{and} \quad (\text{A.29})$$

$$\int d\Theta_i A = \frac{\partial}{\partial \Theta_i} A. \quad (\text{A.30})$$

Because of (A.15) an analytic function  $f$  depending on a Grassmann number  $A$  can be defined as:

$$f(A) = f(0) + f'(0)\Theta + \frac{1}{2}f''(0)\Theta^2 + \dots = f(0) + f'(0)\Theta, \quad (\text{A.31})$$

After a transformation of variables  $\Theta'_i = a_{ij}\Theta_j$  one gets:

$$d^N \Theta = \det A d^N \Theta'. \quad (\text{A.32})$$

Let  $D_{ij}$  be a complex  $N \times N$  matrix and  $\Theta_1, \dots, \Theta_N, \bar{\Theta}_1, \dots, \bar{\Theta}_N$  generators of a  $2N$ -dimensional Grassmann algebra, then the Gaussian integral over Grassmann variables reads:

$$\begin{aligned} \prod_{k=1}^N \int d\Theta_k d\bar{\Theta}_k e^{-\sum_{i,j} \bar{\Theta}_i D_{ij} \Theta_j} &= \det D \prod_{k=1}^N \int d\Theta'_k d\bar{\Theta}_k e^{-\sum_i \bar{\Theta}_i \Theta'_i} \\ &= \det D \prod_{k=1}^N \int d\Theta'_k d\bar{\Theta}_k (1 - \bar{\Theta}_k \Theta'_k) = (-1)^N \det D. \end{aligned} \quad (\text{A.33})$$

## A.4 Discrete symmetries

In addition to continuous symmetries discussed in Chapter 2, one often finds a variety of discrete transformations as well. To preserve the symmetries of the continuum space-time also on the lattice, we have to take them into account in the discretization of the space-time. Furthermore constructing interpolators for hadron spectroscopy the discrete symmetries identify the parity and charge conjugation quantum numbers.

### A.4.1 Parity $\mathcal{P}$

The parity transformation is defined by:

$$\mathcal{P} : x_\mu = (x_1, x_2, x_3, x_4) \mapsto (-x_1, -x_2, -x_3, x_4). \quad (\text{A.34})$$

To show that QCD is invariant under parity is the same as to prove that the QCD action (2.1) is invariant. The fields transform like:

$$\psi(x) \rightarrow \gamma^4 \psi(\mathcal{P}x), \quad (\text{A.35})$$

$$\bar{\psi}(x) \rightarrow \bar{\psi}(\mathcal{P}x) \gamma^4, \quad (\text{A.36})$$

$$A^\mu(x) \rightarrow A^\mu(\mathcal{P}x). \quad (\text{A.37})$$

The parity operator is unitary.

### A.4.2 Time reversal $\mathcal{T}$

The time reversal transformation is defined by:

$$\mathcal{T} : x_\mu = (x_1, x_2, x_3, x_4) \mapsto (x_1, x_2, x_3, -x_4). \quad (\text{A.38})$$

The fields transform like:

$$\psi(x) \rightarrow -\gamma^4 \gamma^1 \gamma^3 \bar{\psi}^T(\mathcal{T}x), \quad (\text{A.39})$$

$$\bar{\psi}(x) \rightarrow -\psi^T(\mathcal{T}x) \gamma^1 \gamma^3 \gamma^4, \quad (\text{A.40})$$

$$A^\mu(x) \rightarrow A^\mu(\mathcal{T}x), \quad (\text{A.41})$$

The time reversal operator is anti-unitary.

### A.4.3 Charge conjugation $\mathcal{C}$

An additional operation typically considered in conjunction with parity and time reversal is that of charge conjugation, the mapping of matter into antimatter. The charge conjugation transformation is defined by:

$$\psi(x) \rightarrow \gamma^2 \gamma^4 \bar{\psi}^T(x), \quad (\text{A.42})$$

$$\bar{\psi}(x) \rightarrow \psi^T(x) \gamma^2 \gamma^4, \quad (\text{A.43})$$

$$A^\mu(x) \mapsto -A^\mu(x). \quad (\text{A.44})$$

## Appendix B

# Path integral formalism on the lattice

### B.1 The generating functional for fermions

The generating functional is defined as:

$$Z[\eta, \bar{\eta}] = \prod_{k=1}^N \int d\Theta_k d\bar{\Theta}_k, e^{-\sum_{i,j} (\bar{\Theta}_i D_{ij} \Theta_j) + \sum_i (\bar{\Theta}_i \eta_i - \bar{\eta}_i \Theta_i)}. \quad (\text{B.1})$$

The Grassmann variables  $\eta_i, \bar{\eta}_i$ ,  $i = 1, \dots, N$  generate together with the generators  $\Theta_i, \bar{\Theta}_i$ ,  $i = 1, \dots, N$  a  $2N$ -dimensional algebra. For the exponent one can write:

$$-\sum_{i,j} (\bar{\Theta}_i D_{ij} \Theta_j) + \sum_i (\bar{\Theta}_i \eta_i - \bar{\eta}_i \Theta_i) = \sum_{i,j} [- (\bar{\Theta}_i + \bar{\eta}_j D_{ji}^{-1}) D_{ij} (\Theta_j - D_{ji}^{-1} \eta_i) - \bar{\eta}_i D_{ij}^{-1} \eta_j]. \quad (\text{B.2})$$

After a transformation of variables we find for (B.1):

$$Z[\eta, \bar{\eta}] = e^{-\sum_{i,j} \bar{\eta}_i D_{ij}^{-1} \eta_j} \prod_{k=1}^N \int d\Theta'_k d\bar{\Theta}'_k e^{-\sum_{i,j} \bar{\Theta}'_i D_{ij} \Theta'_j}, \quad (\text{B.3})$$

$$\begin{aligned} &= (-1)^{2N} \det D e^{-\sum_{i,j} \bar{\eta}_i D_{ij}^{-1} \eta_j}, \\ &= \det D e^{-\sum_{i,j} \bar{\eta}_i D_{ij}^{-1} \eta_j}. \end{aligned} \quad (\text{B.4})$$

The generating functional in (B.4) can be used to determine vacuum expectation values of fermionic observables<sup>1</sup>:

$$\begin{aligned} &\langle \Theta_{i_1} \bar{\Theta}_{j_1} \Theta_{i_2} \bar{\Theta}_{j_2} \dots \Theta_{i_n} \bar{\Theta}_{j_n} \rangle = \\ &= \frac{1}{Z[0,0]} \prod_{k=1}^n \int (d\Theta_k d\bar{\Theta}_k) \Theta_{i_1} \bar{\Theta}_{j_1} \Theta_{i_2} \bar{\Theta}_{j_2} \dots \Theta_{i_n} \bar{\Theta}_{j_n} e^{-\sum_{i,j} (\bar{\Theta}_i D_{ij} \Theta_j)}, \\ &= \frac{1}{Z[0,0]} \prod_{k=1}^n \left( \frac{\partial}{\partial \bar{\eta}_{i_k}} \frac{\partial}{\partial \eta_{j_k}} \right) Z[\eta, \bar{\eta}] \Big|_{\substack{\eta=0 \\ \bar{\eta}=0}} = \prod_{k=1}^n \left( \frac{\partial}{\partial \bar{\eta}_{i_k}} \frac{\partial}{\partial \eta_{j_k}} \right) e^{-\sum_{i,j} \bar{\eta}_i D_{ij}^{-1} \eta_j} \Big|_{\substack{\eta=0 \\ \bar{\eta}=0}}, \\ &= \sum_{\substack{\text{permutations} \\ p \in \{1, \dots, n\}}} \epsilon(p) (D^{-1})_{i_{p_1} j_1} (D^{-1})_{i_{p_2} j_2} \dots (D^{-1})_{i_{p_n} j_n}, \end{aligned} \quad (\text{B.5})$$

where  $\epsilon(p)$  is the sign function of the permutation  $p \in 1, \dots, n$ . Every fermionic operator can be written as a sum over the permutations of Dirac propagator products. The propagators again can be calculated on lattice configurations.

<sup>1</sup>In principle one has also to cover the gauge variables, but this is beyond the content of this work.

## B.2 Expectation values of fermionic operators

Using (B.5) it is possible to integrate out the fermionic fields from the path integral (2.10)<sup>2</sup>:

$$\langle \mathcal{O}[\psi, \bar{\psi}, U] \rangle = \frac{\int [dU][d\psi][d\bar{\psi}] e^{-S_{\text{ferm}}[\psi, \bar{\psi}, U]} e^{-S_{\text{gauge}}[U]} \mathcal{O}[\psi, \bar{\psi}, U]}{\int [dU][d\psi][d\bar{\psi}] e^{-S_{\text{ferm}}[\psi, \bar{\psi}, U]} e^{-S_{\text{gauge}}[U]}}, \quad (\text{B.6})$$

$$= \frac{\int [dU] e^{-S_{\text{gauge}}[U]} \int [d\psi][d\bar{\psi}] e^{-S_{\text{ferm}}[\psi, \bar{\psi}, U]} \mathcal{O}[\psi, \bar{\psi}, U]}{\int [dU] e^{-S_{\text{gauge}}[U]} \int [d\psi][d\bar{\psi}] e^{-S_{\text{ferm}}[\psi, \bar{\psi}, U]}}, \quad (\text{B.7})$$

$$= \frac{\int [dU] e^{-S_{\text{gauge}}[U]} \det D[U] \mathcal{O}[D^{-1}, U]}{\int [dU] e^{-S_{\text{gauge}}[U]} \det D[U]} = \langle \mathcal{O}[D^{-1}, U] \rangle. \quad (\text{B.8})$$

The step from (B.7) to (B.8) has to be explained in more detail and we write the flavor index explicitly:

$$\prod_{f=1}^{N_f} \int [d\psi_f][d\bar{\psi}_f] e^{-S_{\text{ferm}}[\psi_f, \bar{\psi}_f, U]} \mathcal{O}[\psi_f, \bar{\psi}_f, U] = \prod_{f=1}^{N_f} \mathcal{O}\left[\frac{\partial}{\partial \bar{\eta}_f}, \frac{\partial}{\partial \eta_f}, U\right] Z[\eta_f, \bar{\eta}_f] \Big|_{\substack{\eta_f=0 \\ \bar{\eta}_f=0}}, \quad (\text{B.9})$$

$$= \prod_{f=1}^{N_f} \det D_f[U] \mathcal{O}[D_f^{-1}, U], \quad (\text{B.10})$$

where the generating functional for fermions is defined as:

$$Z[\eta, \bar{\eta}] = \prod_{k=1}^{N_f} \int (d\psi_k d\bar{\psi}_k) e^{-\sum_{i,j} (\bar{\psi}_i D_{ij} \psi_j) + \sum_i (\bar{\psi}_i \eta_i - \bar{\eta}_i \psi_i)}. \quad (\text{B.11})$$

Now we can work with the Operator  $\mathcal{O}[D^{-1}, U]$  which is more feasible than  $\mathcal{O}[\psi, \bar{\psi}, U]$ . Furthermore we do not have to be worried about the determinants in the denominator. These determinants are canceled within the Monte Carlo calculation of expectation values, but the determinants in the nominator have to be taken into account in the generation of new gauge configurations.

<sup>2</sup>On the lattice we are using the elements  $U$  of the group  $SU(3)$  instead of the elements  $A$  of the algebra  $su(3)$ .

# Appendix C

## Chiral transformations (extended)

In the present work we heavily use approximate chiral fermions. But why is it so interesting to put also chirality on the lattice? We try to explain this with the enormous complexity which comes into play when putting continuum theories on a discretized space-time. In this chapter we mainly follow the considerations in [58].

### C.1 Left- and right handed projectors

We use in the following the  $t^a = \frac{1}{2}\lambda^a$  matrices which are the generators of the  $su(3)$  algebra for  $a = 1, \dots, 8$  and  $t^0 = \mathbb{1}_{3 \times 3}$  as they are defined in Appendix A.2. If we have a Dirac operator satisfying the Ginsparg-Wilson relation (6.4) exactly, then we can introduce the left- and right-handed projectors as in (2.23) and (6.12), respectively. First we write the chiral transformations in (6.15) using these projectors:

$$\delta^a \psi = i\epsilon t^a (\hat{P}_L - \hat{P}_R)\psi, \quad \delta^a \bar{\psi} = i\bar{\psi}(P_L - P_R)t^a \epsilon. \quad (\text{C.1})$$

We obtain for the variation of the lattice fermion action (5.32):

$$\delta^a S_{\text{ferm}} = (\delta^a \bar{\psi})D\psi + \bar{\psi}D(\delta^a \psi), \quad (\text{C.2})$$

$$= i\bar{\psi}(P_L - P_R)t^a \epsilon D\psi + i\bar{\psi}D\epsilon t^a (\hat{P}_L - \hat{P}_R)\psi, \quad (\text{C.3})$$

$$= i\epsilon \bar{\psi} t^a \left( (P_L - P_R)D + D(\hat{P}_L - \hat{P}_R) \right) \psi = 0, \quad (\text{C.4})$$

where we have used:

$$P_R D \hat{P}_L = P_R D = D \hat{P}_L = 2P_R \hat{P}_L, \quad (\text{C.5})$$

$$P_L D \hat{P}_R = P_L D = D \hat{P}_R = 2P_L \hat{P}_R. \quad (\text{C.6})$$

We can also define the right- and left-handed transformation:

$$\delta_L^a \psi = i\epsilon t^a \hat{P}_L \psi \quad \delta_L^a \bar{\psi} = -i\bar{\psi} P_R t^a \epsilon, \quad (\text{C.7})$$

$$\delta_R^a \psi = i\epsilon t^a \hat{P}_R \psi \quad \delta_R^a \bar{\psi} = -i\bar{\psi} P_L t^a \epsilon, \quad (\text{C.8})$$

$$\delta_A^a = \delta_L^a - \delta_R^a \quad \delta_V^a = \delta_L^a + \delta_R^a, \quad (\text{C.9})$$

and get the global axial and vector transformations<sup>1</sup>:

$$\delta_A^a \psi = i\epsilon t^a (\hat{P}_L - \hat{P}_R)\psi \quad \delta_A^a \bar{\psi} = i\bar{\psi}(P_L - P_R)t^a \epsilon, \quad (\text{C.10})$$

$$\delta_V^a \psi = i\epsilon t^a (\hat{P}_L + \hat{P}_R)\psi \quad \delta_V^a \bar{\psi} = -i\bar{\psi}(P_L + P_R)t^a \epsilon. \quad (\text{C.11})$$

<sup>1</sup>We have already introduced the axial transformation in (C.1), but did not show why this correspond to an axial transformation, which is defined in terms of left- and right-handed transformations originally.

To address also local transformations we define the local left- and right-handed transformations as follows:

$$\delta_L^a \psi = it^a \hat{P}_L \epsilon \hat{P}_L \psi \quad \delta_L^a \bar{\psi} = -i \bar{\psi} P_R \epsilon P_R t^a, \quad (\text{C.12})$$

$$\delta_R^a \psi = it^a \hat{P}_R \epsilon \hat{P}_R \psi \quad \delta_R^a \bar{\psi} = -i \bar{\psi} P_L \epsilon P_L t^a, \quad (\text{C.13})$$

where  $\epsilon$  is now  $x$ -dependent:

$$\epsilon_{xy} = \epsilon(x) \delta_{xy}. \quad (\text{C.14})$$

This form of the local transformations is motivated by the fact that  $\epsilon \hat{P}_L \psi$  and  $\epsilon \hat{P}_R \psi$  are neither left-handed or right-handed fields if  $\epsilon$  is depending on  $x$ . Hence, the local axial and vector transformations look like:

$$\delta_A^a \psi = it^a (\hat{P}_L \epsilon \hat{P}_L - \hat{P}_R \epsilon \hat{P}_R) \psi \quad \delta_A^a \bar{\psi} = i \bar{\psi} (P_L \epsilon P_L - P_R \epsilon P_R) t^a, \quad (\text{C.15})$$

$$\delta_V^a \psi = it^a (\hat{P}_L \epsilon \hat{P}_L + \hat{P}_R \epsilon \hat{P}_R) \psi \quad \delta_V^a \bar{\psi} = -i \bar{\psi} (P_L \epsilon P_L + P_R \epsilon P_R) t^a. \quad (\text{C.16})$$

## C.2 Global covariant densities and conserved currents

In Eq. (6.21) we define a covariant scalar and a covariant pseudoscalar density. If we use those densities we can obtain:

$$\frac{i}{\epsilon} \delta_A^a S^b = -\bar{\psi} (P_L - P_R) \left( \mathbb{1} - \frac{a}{2} D \right) t^a t^b \psi - \bar{\psi} \left( \mathbb{1} - \frac{a}{2} D \right) (\hat{P}_L - \hat{P}_R) t^b t^a \psi, \quad (\text{C.17})$$

$$= -\bar{\psi} (P_L - P_R) \left( \mathbb{1} - \frac{a}{2} D \right) t^a t^b \psi - \bar{\psi} (P_L - P_R) \left( \mathbb{1} - \frac{a}{2} D \right) t^b t^a \psi, \quad (\text{C.18})$$

$$= -\bar{\psi} \gamma_5 \left( \mathbb{1} - \frac{a}{2} D \right) \{t^a, t^b\} \psi, \quad (\text{C.19})$$

where one heavily makes use of

$$P_{L,R} \left( \mathbb{1} - \frac{a}{2} D \right) = \left( \mathbb{1} - \frac{a}{2} D \right) \hat{P}_{L,R}. \quad (\text{C.20})$$

Analogously we obtain:

$$\frac{i}{\epsilon} \delta_A^a S^b = -\frac{1}{3} \delta_{ab} P - d_{abc} P^c, \quad \frac{i}{\epsilon} \delta_V^a S^b = i f_{abc} S^c, \quad (\text{C.21})$$

$$\frac{i}{\epsilon} \delta_A^a P^b = -\frac{1}{3} \delta_{ab} S - d_{abc} S^c, \quad \frac{i}{\epsilon} \delta_V^a P^b = i f_{abc} P^c, \quad (\text{C.22})$$

$$\frac{i}{\epsilon} \delta_A^a S = -2P^a, \quad \frac{i}{\epsilon} \delta_A^a P = -2S^a, \quad (\text{C.23})$$

which is the same as in the continuum. (We use  $S = S^0$  and  $P = P^0$  for the flavor singlet quantities.)

One can also show that the axialvector and vector currents defined in (6.22) satisfy the continuum relations:

$$\frac{i}{\epsilon} \delta_A^a V_\mu^b(x) = i f_{abc} A_\mu^c(x), \quad \frac{i}{\epsilon} \delta_V^a V_\mu^b(x) = i f_{abc} V_\mu^c(x), \quad (\text{C.24})$$

$$\frac{i}{\epsilon} \delta_A^a A_\mu^b(x) = i f_{abc} V_\mu^c(x), \quad \frac{i}{\epsilon} \delta_V^a A_\mu^b(x) = i f_{abc} A_\mu^c(x). \quad (\text{C.25})$$

## C.3 Local covariant densities and conserved currents

For the local axial and vector transformations we use the covariant densities in Eqs. (6.21) and (6.23) and find:

$$\begin{aligned} i \frac{\delta_A^a S^b}{\delta \epsilon(x)} &= -\frac{1}{3} \delta_{ab} P(x) - d_{abc} P^c(x), & i \frac{\delta_V^a S^b}{\delta \epsilon(x)} &= i f_{abc} S^c(x), \\ i \frac{\delta_A^a P^b}{\delta \epsilon(x)} &= -\frac{1}{3} \delta_{ab} S(x) - d_{abc} S^c(x), & i \frac{\delta_V^a P^b}{\delta \epsilon(x)} &= i f_{abc} P^c(x), \\ i \frac{\delta_A^a S}{\delta \epsilon(x)} &= -2P^a(x), & i \frac{\delta_A^a P}{\delta \epsilon(x)} &= -2S^a(x), \end{aligned} \quad (\text{C.26})$$

where

$$\sum_x S^a(x) = S^a, \quad \sum_x P^a(x) = P^a. \quad (\text{C.27})$$

To find the corresponding covariant axial and vector currents which are related to the densities in (C.26) is a more complicated task. We again consider a global transformation  $\psi \rightarrow \psi + \delta\psi$ ,  $\bar{\psi} \rightarrow \bar{\psi} + \delta\bar{\psi}$  and assume that the massless action

$$\mathcal{A}_0 = \bar{\psi} D(U) \psi \quad (\text{C.28})$$

is invariant under this transformation,  $\delta\mathcal{A}_0 = 0$ . Under the corresponding local transformation the current  $J_\mu(x)$  is defined by:

$$\delta\mathcal{A}_0 = i \sum_x \partial_\mu \epsilon(x) J_\mu(x) = -i \sum_x \epsilon(x) \partial_\mu^* J_\mu(x), \quad (\text{C.29})$$

where  $\partial_\mu$  and  $\partial_\mu^*$  are the forward and backward lattice derivatives, respectively. Applying the axial transformation (C.15) on the massless action we obtain:

$$\delta_A^a \mathcal{A}_0 = i \bar{\psi} \left( P_R[D(U), \epsilon] \hat{P}_L - P_L[D(U), \epsilon] \hat{P}_R \right) t^a \psi, \quad (\text{C.30})$$

$$\delta_V^a \mathcal{A}_0 = i \bar{\psi} \left( P_R[D(U), \epsilon] \hat{P}_L + P_L[D(U), \epsilon] \hat{P}_R \right) t^a \psi, \quad (\text{C.31})$$

For an infinitesimal  $U(1)$  gauge transformation the change of  $D(U)$  is given by

$$\delta_g D(U) = -i[D(U), \epsilon] = -i \sum_x \partial_\mu \epsilon(x) K_\mu(x), \quad (\text{C.32})$$

where the kernel  $K_\mu(x)$  can be used to get the conserved current  $J_\mu(x)$ .

Eq. (C.32) can also be applied to determine the kernel  $K_\mu(x)$  numerically. To linear order we have:

$$\delta_g D(U) = D(U^{(\alpha)}) - D(U) = - \sum_x \partial_\mu \epsilon(x) \left. \frac{\delta D(U_\mu^{(\alpha)})}{\delta \alpha_\mu(x)} \right|_{\alpha=0}, \quad (\text{C.33})$$

where we introduce a infinitesimal  $U(1)$  transformation

$$U_\mu(x) \rightarrow U_\mu^{(\alpha)}(x) = e^{i\alpha_\mu(x)} U_\mu(x) \quad (\text{C.34})$$

on each link and taking the values of  $\alpha_\mu(x)$  to be

$$\alpha_\mu(x) = -\partial_\mu \epsilon(x). \quad (\text{C.35})$$

Combing Eqs. (C.32) and (C.33) we obtain:

$$K_\mu(x) = -i \left. \frac{\delta D(U_\mu^{(\alpha)})}{\delta \alpha_\mu(x)} \right|_{\alpha=0}. \quad (\text{C.36})$$

From (C.30), (C.31) and (C.36) we get the conserved axial and analogously the conserved vector current defined in (6.22).

Note that we obtain:

$$i \frac{\delta_A^a \mathcal{A}_0}{\delta \epsilon(x)} = \partial_\mu^* A_\mu^a(x), \quad (\text{C.37})$$

$$i \frac{\delta_V^a \mathcal{A}_0}{\delta \epsilon(x)} = \partial_\mu^* V_\mu^a(x). \quad (\text{C.38})$$

If the massless action  $\mathcal{A}_0$  is also invariant under these local transformations, we obtain conserved currents which also appear in the axial and vector Ward identities.

## C.4 Neglecting contact terms in the densities

In Section 8.5 we calculate correlators using covariant operators. At least for the correlation functions which combine covariant densities we can derive the  $Z_P$  and  $Z_S$  factors for the densities in Eqs. (6.21) and simplify the complicated local operators in Eqs. (6.23).

For the next steps we commemorate Eq. (6.20) for  $\bar{m}$  and introduce the following for  $\tilde{m}$ :

$$\bar{m} = 1 - \frac{am}{2}, \quad \tilde{m} = 1 + \frac{am}{2}. \quad (\text{C.39})$$

We begin to write (6.19) in the other way around:

$$D^{(0)} = \bar{m}^{-1} \left( D^{(m)} - m\mathbb{1} \right). \quad (\text{C.40})$$

If we replace in Eqs. (6.21) all massless Dirac operators  $D^{(0)}$  by Eq. (C.40), we get:

$$S^a = \bar{\psi} \left( \frac{1}{\bar{m}} \mathbb{1} - \frac{a}{2\bar{m}} D^{(m)} \right) t^a \psi, \quad P^a = \bar{\psi} \gamma_5 \left( \frac{1}{\bar{m}} \mathbb{1} - \frac{a}{2\bar{m}} D^{(m)} \right) t^a \psi. \quad (\text{C.41})$$

Interested in the correlation functions  $\langle SS^\dagger \rangle_{\text{cov}}$  and  $\langle PP^\dagger \rangle_{\text{cov}}$  we can integrate out all fermion fields using the Wick theorem (B.5). All term proportional to a  $D^{(m)}$ -factor are in this way multiplied by a propagator  $G^{(m)}$ . These products only give contact terms:

$$\sum_y D^{(m)}(x, y) G^{(m)}(y, z) = \sum_y G^{(m)}(x, y) D^{(m)}(y, z) = \mathbb{1} \delta_{x, z}. \quad (\text{C.42})$$

Contact terms only contributes in the correlator for timeslice  $t = 0$ , which is not relevant for our purposes. Hence we neglect these contact terms completely and find:

$$S^a \approx \frac{1}{\bar{m}} \bar{\psi} t^a \psi, \quad P^a \approx \frac{1}{\bar{m}} \bar{\psi} \gamma_5 t^a \psi, \quad (\text{C.43})$$

where the  $\approx$  sign indicates the neglect of the contact terms. This gives for the scalar and pseudoscalar densities the following  $Z$ -factors using Dirac operators obeying Eq. (6.4):

$$Z_S = Z_P \approx \bar{m}^{-1}. \quad (\text{C.44})$$

Using (C.40) in Eqs. (6.23) we get for the local covariant densities first of all:

$$\begin{aligned} S^a(x) &\approx \bar{\psi}_1 \left[ \frac{1}{2\bar{m}_2} E(x) + \frac{1}{4\bar{m}_1} (E(x) + \hat{\gamma}_5 E(x) \hat{\gamma}_5) \right] t^a \psi_2, \\ P^a(x) &\approx \bar{\psi}_1 \left[ \frac{1}{2\bar{m}_2} E(x) \gamma_5 + \frac{1}{4\bar{m}_1} (\hat{\gamma}_5 E(x) + E(x) \hat{\gamma}_5) \right] t^a \psi_2, \end{aligned} \quad (\text{C.45})$$

where we have introduced  $m_1$  and  $m_2$  which are the corresponding masses to the fields  $\psi_1$  and  $\psi_2$ , respectively.

If we write  $\hat{\gamma}_5$  and  $\gamma_5 D^{(m)}$  in such a form that we can act with propagators on the corresponding Dirac operators coming either from the right or the left hand side, we find further contact terms through:

$$\hat{\gamma}_5 = \gamma_5 \frac{\tilde{m}}{\bar{m}} \mathbb{1} - \gamma_5 \frac{a}{\bar{m}} D^{(m)}, \quad (\text{C.46})$$

$$\gamma_5 D^{(m)} = \frac{2m}{\tilde{m}} \gamma_5 \mathbb{1} - \frac{\tilde{m}}{\bar{m}} D^{(m)} \hat{\gamma}_5, \quad (\text{C.47})$$

where we have used the Ginsparg-Wilson Eq. (6.4) together with Eq. (C.40). Finally we get:

$$\begin{aligned} S^a(x) &\approx \bar{\psi}_1 \left[ \frac{1}{2\bar{m}_2} E(x) \mathbb{1} + \frac{1}{4\bar{m}_1} \left( E(x) \mathbb{1} + \left( \frac{\tilde{m}_1}{\bar{m}_1} \gamma_5 \mathbb{1} - \frac{a}{\bar{m}_1} \gamma_5 D^{(m_1)} \right) E(x) \gamma_5 \frac{\tilde{m}_2}{\bar{m}_2} \right) \right] t^a \psi_2, \\ &\approx \left[ \frac{1}{2\bar{m}_2} + \frac{1}{4\bar{m}_1} + \frac{\tilde{m}_2}{4\bar{m}_2 \tilde{m}_1} \right] \bar{\psi}_1 E(x) t^a \psi_2, \end{aligned} \quad (\text{C.48})$$

$$\begin{aligned} P^a(x) &\approx \bar{\psi}_1 \left[ \frac{1}{2\bar{m}_2} E(x) \gamma_5 \mathbb{1} + \frac{1}{4\bar{m}_1} \left( \left( \frac{\tilde{m}_1}{\bar{m}_1} \gamma_5 \mathbb{1} - \frac{a}{\bar{m}_1} \gamma_5 D^{(m_1)} \right) E(x) + \frac{\tilde{m}_2}{\bar{m}_2} E(x) \gamma_5 \mathbb{1} \right) \right] t^a \psi_2, \\ &\approx \left[ \frac{1}{2\bar{m}_2} + \frac{1}{4\tilde{m}_1} + \frac{\tilde{m}_2}{4\bar{m}_1 \bar{m}_2} \right] \bar{\psi}_1 E(x) \gamma_5 t^a \psi_2, \end{aligned} \quad (\text{C.49})$$

where we obtain for  $m_1 = m_2 = m$  the result in [58]:

$$\begin{aligned} S^a(x) &\approx \frac{1}{\tilde{m}} \bar{\psi} E(x) t^a \psi, \\ P^a(x) &\approx \frac{1}{\tilde{m}^2} \bar{\psi} E(x) \gamma_5 t^a \psi, \end{aligned} \quad (\text{C.50})$$

## C.5 The AWI mass in $N_f = 2 + 1$

$D$  is in the following a massless Dirac operator satisfying (6.4). Consider the massive fermion action  $S_{\text{ferm}} \equiv \mathcal{A}_M$  with a flavor variant mass term matrix  $M_{ff'}$ :

$$\mathcal{A}_M = \bar{\psi} D \psi + \bar{\psi}_L M \psi_R + \bar{\psi}_R M \psi_L = \mathcal{A}_0 + M_{ff'} S_{ff'}^0, \quad (\text{C.51})$$

where  $M$  is diagonal in flavor space and the flavor singlet scalar density  $S = S^0$  is defined in Eq. (6.21). We introduce  $m = m_u = m_d$ ,

$$M_{ff'} = \begin{pmatrix} m & 0 & 0 \\ 0 & m & 0 \\ 0 & 0 & m_s \end{pmatrix}_{ff'} = \frac{1}{3} (2m + m_s) t_{ff'}^0 + \frac{2}{\sqrt{3}} (m - m_s) t_{ff'}^8. \quad (\text{C.52})$$

and we get:

$$\mathcal{A}_M = \mathcal{A}_0 + \frac{1}{3} (2m + m_s) S^0 + \frac{2}{\sqrt{3}} (m - m_s) S^8. \quad (\text{C.53})$$

The local axial transformations of the covariant scalar density can be found in Eqs. (C.26). Using  $a = 1, 2$  gives for the local axial transformation of the action<sup>2</sup>:

$$i \frac{\delta_A^{1,2} \mathcal{A}_M}{\delta \epsilon(x)} = \partial_\mu^* A_\mu^{1,2}(x) - \left( \frac{2}{3} (2m + m_s) + \frac{1}{\sqrt{3}} \frac{2}{\sqrt{3}} (m - m_s) \right) P^{1,2}(x) = \partial_\mu^* A_\mu^{1,2}(x) - 2m P^{1,2}(x), \quad (\text{C.54})$$

and using  $a = 6, 7$  gives<sup>3</sup>:

$$i \frac{\delta_A^{6,7} \mathcal{A}_M}{\delta \epsilon(x)} = \partial_\mu^* A_\mu^{6,7}(x) - \left( \frac{2}{3} (2m + m_s) - \frac{1}{2\sqrt{3}} \frac{2}{\sqrt{3}} (m - m_s) \right) P^{6,7}(x) = \partial_\mu^* A_\mu^{6,7}(x) - (m + m_s) P^{6,7}(x). \quad (\text{C.55})$$

If we have a chiral invariant action  $\mathcal{A}_M$ , then we get the operator identities:

$$\partial_\mu^* A_\mu^{1,2}(x) = 2m P^{1,2}(x) \quad \text{and} \quad \partial_\mu^* A_\mu^{6,7}(x) = (m + m_s) P^{6,7}(x), \quad (\text{C.56})$$

where  $A_\mu^a(x)$  and  $P^a(x)$  are conserved currents (6.22) and covariant densities (6.23), which covariantly transform under a local axial rotation, respectively.  $m = m_u = m_d$  and  $m_s$  are the bare masses of the  $u$ ,  $d$  and  $s$  quarks in the action.

<sup>2</sup>We are mainly interested in the case  $a = 1, 2$  because we want to compute  $\bar{u} \gamma_5 (\mathbb{1} - \frac{1}{2} D) d = P^1 + iP^2$ .

<sup>3</sup>To determine the AWI mass for  $m_s$  we have to compute  $\bar{d} \gamma_5 (\mathbb{1} - \frac{1}{2} D) s = P^6 + iP^7$ .

# Appendix D

## Chiral transformations with $2R \neq 1$

Using the FP Dirac operator which obeys Eq. (6.1) we get some changes in the formulas compared to those in the previous Appendix C. Because of  $2R \neq 1$  we have to consider the influence on the correlators.

### D.1 The general chiral transformations on the lattice

Applying Eq. (6.3) to Eq. (6.15) we derive the more general form of chiral transformations on the lattice:

$$\delta^a \Psi_f = i\epsilon t_{ff'}^a \hat{\Gamma}_5 \Psi_{f'} , \quad \delta^a \bar{\Psi}_f = i\bar{\Psi}_{f'} \gamma_5 t_{f'f}^a \epsilon , \quad (\text{D.1})$$

where

$$\hat{\Gamma}_5 = \sqrt{2R} \hat{\gamma}_5 \frac{1}{\sqrt{2R}} = \gamma_5 (1 - a 2R \mathcal{D}) . \quad (\text{D.2})$$

One easily finds:

$$\gamma_5 \mathcal{D} + \mathcal{D} \gamma_5 - a \mathcal{D} \gamma_5 2R \mathcal{D} = \gamma_5 \mathcal{D} + \mathcal{D} \hat{\Gamma}_5 = 0 . \quad (\text{D.3})$$

Due to these relations we can simply derive the  $2R \neq 1$  case via replacing  $\hat{\gamma}_5$  by  $\hat{\Gamma}_5$ :

$$\hat{\mathcal{P}}_L = \frac{\mathbb{1} + \hat{\Gamma}_5}{2} , \quad \hat{\mathcal{P}}_R = \frac{\mathbb{1} - \hat{\Gamma}_5}{2} . \quad (\text{D.4})$$

We can again decompose the massless fermion action into left- and right-handed fermion fields:

$$\bar{\Psi} \mathcal{D} \Psi = \bar{\Psi}_L \mathcal{D} \Psi_L + \bar{\Psi}_R \mathcal{D} \Psi_R = \bar{\Psi} \left( P_R \mathcal{D} \hat{\mathcal{P}}_L + P_L \mathcal{D} \hat{\mathcal{P}}_R \right) \Psi , \quad (\text{D.5})$$

where

$$\begin{aligned} \bar{\psi}_L = \bar{\psi} P_R = \bar{\Psi} \frac{1}{\sqrt{2R}} P_R = \bar{\Psi} P_R \frac{1}{\sqrt{2R}} = \bar{\Psi}_L \frac{1}{\sqrt{2R}} , & \quad \psi_L = \hat{P}_L \psi = \hat{P}_L \frac{1}{\sqrt{2R}} \Psi = \frac{1}{\sqrt{2R}} \hat{P}_L \Psi = \frac{1}{\sqrt{2R}} \Psi_L , \\ \bar{\psi}_R = \bar{\psi} P_L = \bar{\Psi} \frac{1}{\sqrt{2R}} P_L = \bar{\Psi} P_L \frac{1}{\sqrt{2R}} = \bar{\Psi}_R \frac{1}{\sqrt{2R}} , & \quad \psi_R = \hat{P}_R \psi = \hat{P}_R \frac{1}{\sqrt{2R}} \Psi = \frac{1}{\sqrt{2R}} \hat{P}_R \Psi = \frac{1}{\sqrt{2R}} \Psi_R , \end{aligned} \quad (\text{D.6})$$

and

$$\begin{aligned} P_R \mathcal{D} \hat{\mathcal{P}}_L &= P_R \mathcal{D} = \mathcal{D} \hat{\mathcal{P}}_L = \frac{1}{2R} 2P_R \hat{\mathcal{P}}_L , \\ P_L \mathcal{D} \hat{\mathcal{P}}_R &= P_L \mathcal{D} = \mathcal{D} \hat{\mathcal{P}}_R = \frac{1}{2R} 2P_L \hat{\mathcal{P}}_R . \end{aligned} \quad (\text{D.7})$$

The massive Ginsparg-Wilson Dirac operator with  $2R \neq 1$  is defined by:

$$S_{\text{ferm}}^{\text{lat}}[\psi, \bar{\psi}, U] = \bar{\psi} D^{(m)} \psi = \bar{\psi} \left( \bar{m} D^{(0)} + m \mathbb{1} \right) \psi = \bar{\Psi} \mathcal{D}^{(m)} \Psi = S_{\text{ferm}}^{\text{lat}}[\Psi, \bar{\Psi}, U], \quad (\text{D.8})$$

where

$$\mathcal{D}^{(m)} = \bar{m} \mathcal{D}^{(0)} + \frac{m}{2} R^{-1}. \quad (\text{D.9})$$

This is also consistent with a scalar density which can be introduced in the language of Eq. (D.5):

$$\bar{\Psi}_L \Psi_R + \bar{\Psi}_R \Psi_L = \bar{\Psi} \frac{1}{2R} (P_R \hat{\mathcal{P}}_R + P_L \hat{\mathcal{P}}_L) \Psi = \bar{\Psi} \left( \frac{1}{2R} - \frac{a}{2} \mathcal{D} \right) \Psi, \quad (\text{D.10})$$

and we obtain the same massive Dirac operator as in Eq. (D.9)

$$\mathcal{D}^{(m)} = \mathcal{D}^{(0)} + m \left( \frac{1}{2R} - \frac{a}{2} \mathcal{D}^{(0)} \right). \quad (\text{D.11})$$

In addition to replacing all  $\hat{\gamma}_5$  by  $\hat{\Gamma}_5$  we derive the  $2R \neq 1$  case from the  $2R = 1$  case via replacing

$$\left( \mathbb{1} - \frac{a}{2} \mathcal{D}^{(0)} \right) \quad \text{by} \quad \left( \frac{1}{2R} - \frac{a}{2} \mathcal{D}^{(0)} \right). \quad (\text{D.12})$$

For instance one finds according to Eq. (C.20):

$$P_{L,R} \left( \frac{1}{2R} - \frac{a}{2} \mathcal{D}^{(0)} \right) = \left( \frac{1}{2R} - \frac{a}{2} \mathcal{D}^{(0)} \right) \hat{\mathcal{P}}_{L,R}. \quad (\text{D.13})$$

## D.2 Neglecting the contact terms in the densities

Using Eq. (D.9) we get:

$$\mathcal{D}^{(0)} = \frac{1}{\bar{m}} \left( \mathcal{D}^{(m)} - \frac{m}{2R} \right). \quad (\text{D.14})$$

The Eqs. (6.21) changes for  $2R \neq 1$  into:

$$S^a = \bar{\Psi} \left( \frac{1}{2R} - \frac{a}{2} \mathcal{D}^{(0)} \right) t^a \Psi, \quad P^a = \bar{\Psi} \gamma_5 \left( \frac{1}{2R} - \frac{a}{2} \mathcal{D}^{(0)} \right) t^a \Psi. \quad (\text{D.15})$$

Again, we neglect the contact terms and find:

$$S^a = \frac{1}{\bar{m}} \bar{\Psi} \frac{1}{2R} t^a \Psi, \quad P^a = \frac{1}{\bar{m}} \bar{\Psi} \gamma_5 \frac{1}{2R} t^a \Psi. \quad (\text{D.16})$$

The local conserved currents in Eqs. (6.23) transform for  $2R \neq 1$  into:

$$\begin{aligned} S^a(x) &= \bar{\Psi} \left[ \frac{1}{2} E(x) \left( \frac{1}{2R} - \frac{a}{2} \mathcal{D}^{(0)} \right) + \frac{1}{4} \left( \frac{1}{2R} - \frac{a}{2} \mathcal{D}^{(0)} \right) \left( E(x) + \hat{\Gamma}_5 E(x) \hat{\Gamma}_5 \right) \right] t^a \Psi, \\ P^a(x) &= \bar{\Psi} \left[ \frac{1}{2} E(x) \gamma_5 \left( \frac{1}{2R} - \frac{a}{2} \mathcal{D}^{(0)} \right) + \frac{1}{4} \left( \frac{1}{2R} - \frac{a}{2} \mathcal{D}^{(0)} \right) \left( \hat{\Gamma}_5 E(x) + E(x) \hat{\Gamma}_5 \right) \right] t^a \Psi. \end{aligned} \quad (\text{D.17})$$

Using (D.14) we get:

$$\begin{aligned} S^a(x) &\approx \bar{\Psi}_1 \left[ \frac{1}{2\bar{m}_2} E(x) \frac{1}{2R} + \frac{1}{4\bar{m}_1} \frac{1}{2R} \left( E(x) + \hat{\Gamma}_5 E(x) \hat{\Gamma}_5 \right) \right] t^a \Psi_2, \\ P^a(x) &\approx \bar{\Psi}_1 \left[ \frac{1}{2\bar{m}_2} E(x) \frac{1}{2R} \gamma_5 + \frac{1}{4\bar{m}_1} \frac{1}{2R} \left( \hat{\Gamma}_5 E(x) + E(x) \hat{\Gamma}_5 \right) \right] t^a \Psi_2. \end{aligned} \quad (\text{D.18})$$

Again we rewrite  $\hat{\gamma}_5$  and  $\gamma_5 \mathcal{D}^{(m)}$  in a suitable form, so that we can use them to find further contact terms:

$$\hat{\Gamma}_5 = \gamma_5 \left( \frac{\tilde{m}}{\bar{m}} \mathbb{1} - \frac{a}{\bar{m}} 2R \mathcal{D}^{(m)} \right), \quad (\text{D.19})$$

$$\gamma_5 \mathcal{D}^{(m)} = \left( \frac{2m}{\tilde{m}} \frac{1}{2R} \gamma_5 - \frac{\bar{m}}{\tilde{m}} \mathcal{D}^{(m)} \hat{\Gamma}_5 \right). \quad (\text{D.20})$$

We obtain:

$$\begin{aligned} S^a(x) &\approx \bar{\Psi}_1 \left[ \frac{1}{2\tilde{m}_2} E(x) \frac{1}{2R} + \frac{1}{4\tilde{m}_1} \frac{1}{2R} E(x) + \frac{\tilde{m}_2 \tilde{m}_1}{4\tilde{m}_1^2 \tilde{m}_2} \frac{1}{2R} E(x) - \frac{a\tilde{m}_2}{4\tilde{m}_1^2 \tilde{m}_2} \gamma_5 \mathcal{D}^{(m_1)} \gamma_5 E(x) \right] t^a \Psi_2, \\ &\approx \bar{\Psi}_1 \left[ \frac{1}{2\tilde{m}_2} E(x) \frac{1}{2R} + \left( \frac{1}{4\tilde{m}_1} + \frac{\tilde{m}_2}{4\tilde{m}_1 \tilde{m}_2} \right) \frac{1}{2R} E(x) \right] t^a \Psi_2, \\ &\approx \frac{1}{2\tilde{m}_2} \bar{\Psi}_1 \left[ E(x) \frac{1}{2R} + \left( \frac{\tilde{m}_2}{2\tilde{m}_1} + \frac{\tilde{m}_2}{2\tilde{m}_1} \right) \frac{1}{2R} E(x) \right] t^a \Psi_2, \\ P^a(x) &\approx \bar{\Psi}_1 \left[ \frac{1}{2\tilde{m}_2} E(x) \frac{1}{2R} \gamma_5 + \frac{\tilde{m}_1}{4\tilde{m}_1^2} \frac{1}{2R} E(x) \gamma_5 + \frac{\tilde{m}_2}{4\tilde{m}_1 \tilde{m}_2} \frac{1}{2R} E(x) \gamma_5 - \frac{a}{4\tilde{m}_1^2} \gamma_5 \mathcal{D}^{(m_1)} E(x) \right] t^a \Psi_2, \\ &\approx \bar{\Psi}_1 \left[ \frac{1}{2\tilde{m}_2} E(x) \frac{1}{2R} + \left( \frac{1}{4\tilde{m}_1} + \frac{\tilde{m}_2}{4\tilde{m}_1 \tilde{m}_2} \right) \frac{1}{2R} E(x) \right] \gamma_5 t^a \Psi_2, \\ &\approx \frac{1}{2\tilde{m}_2} \bar{\Psi}_1 \left[ E(x) \frac{1}{2R} + \left( \frac{\tilde{m}_2}{2\tilde{m}_1} + \frac{\tilde{m}_2}{2\tilde{m}_1} \right) \frac{1}{2R} E(x) \right] \gamma_5 t^a \Psi_2. \end{aligned} \quad (\text{D.21})$$

where we again find for  $m_1 = m_2 = m$  the result in [58]:

$$\begin{aligned} S^a(x) &\approx \frac{1}{2\tilde{m}} \bar{\Psi} \left[ E(x) \frac{1}{2R} + \frac{1}{2R} E(x) \right] t^a \Psi, \\ P^a(x) &\approx \frac{1}{2\tilde{m}} \bar{\Psi} \left[ E(x) \frac{1}{2R} + \frac{\bar{m}^2 + \tilde{m}^2}{2\tilde{m}\bar{m}} \frac{1}{2R} E(x) \right] \gamma_5 t^a \Psi. \end{aligned} \quad (\text{D.22})$$

### D.3 Covariant conserved currents with $2R \neq 1$

We redefine Eqs. (6.22) and (C.36) through:

$$V_\mu^a(x) = \bar{\Psi} \left( P_R \mathcal{K}_\mu(x) \hat{\mathcal{P}}_L + P_L \mathcal{K}_\mu(x) \hat{\mathcal{P}}_R \right) t^a \Psi, \quad A_\mu^a(x) = \bar{\Psi} \left( P_R \mathcal{K}_\mu(x) \hat{\mathcal{P}}_L - P_L \mathcal{K}_\mu(x) \hat{\mathcal{P}}_R \right) t^a \Psi, \quad (\text{D.23})$$

where  $\mathcal{K}_\mu(x)$  is defined as:

$$\mathcal{K}_\mu(x) = -i \left. \frac{\delta \mathcal{D}(U_\mu^{(\alpha)})}{\delta \alpha_\mu(x)} \right|_{\alpha=0}. \quad (\text{D.24})$$

# Appendix E

## Group Theory

### E.1 Young tableaux

Taking, for instance, the direct product of a triplet with itself any number of times, we immediately obtain representations of higher dimensions  $3 \otimes 3$ ,  $3 \otimes 3 \otimes 3$ , etc. These representations are reducible. To decompose representations into reducible ones, we compose the corresponding product space into invariant irreducible subspaces<sup>1</sup>. Then, the representations induced by the fundamental representation in these subspaces are irreducible representations. We are using for these purposes Young tableaux.

#### E.1.1 How to construct Young tableaux

Let  $x_{i_1 \dots i_n}$  be a tensor that transforms like the product  $x_{i_1} \dots x_{i_n}$ . It can be decomposed into tensors of different symmetry classes with respect to a permutation of the indices  $i_1, \dots, i_n$ . By definition, a tensor belonging to a definite symmetry class is obtained from  $x_{i_1 \dots i_n}$  through the following construction:

1. First, pick  $n_1$  of the indices, and symmetries among them. Display this operation symbolically in the picture below:

$$\begin{array}{c}
 \boxed{\phantom{x}} \boxed{\phantom{x}} \boxed{\phantom{x}} \dots \boxed{\phantom{x}} \\
 \underbrace{\hspace{10em}} \\
 n_1 \text{ boxes}
 \end{array} \tag{E.1}$$

2. Next, pick  $n_2 \leq n_1$  of the remaining indices, and symmetrize among them:

$$\begin{array}{c}
 \boxed{\phantom{x}} \boxed{\phantom{x}} \boxed{\phantom{x}} \dots \boxed{\phantom{x}} \\
 \underbrace{\hspace{10em}} \\
 n_2 \text{ boxes}
 \end{array} \tag{E.2}$$

3. Repeat the procedure until all indices have been used. Stack up the rows to form the following tableau, called a Young tableau, e.g.:

$$\begin{array}{cccccc}
 \square & \square & \square & \square & \square & \square \\
 \square & \square & \square & \square & & \\
 \square & \square & \square & & & \\
 \square & \square & & & & \\
 \square & & & & & \\
 \square & & & & & 
 \end{array} \tag{E.3}$$

4. Finally, anti-symmetrize the indices in each column of the tableau separately and independently.

The geometrical form of the Young tableau characterizes a symmetry class.

<sup>1</sup>Invariant means the space goes into itself under the group transformations. Irreducible means it does not contain a smaller invariant subspace.

## E.2 $SU(2)$ symmetry group

In elementary particle physics the  $SU(2)$  symmetry occurs in terms like the spin or the isospin.

### E.2.1 Symmetry classes in $SU(2)$

To construct the different representations we always add one extra particle from step to step:

- Particle and antiparticle: Both are in the same symmetry class in  $SU(2)$ :

$$\square = \text{particle in } SU(2), \quad (\text{E.4})$$

$$\square = \text{antiparticle in } SU(2). \quad (\text{E.5})$$

- 2 particles:

$$\begin{aligned} \square \otimes \square &= \square \oplus \begin{array}{|c|} \hline \square \\ \hline \square \\ \hline \end{array}, \\ 2 \otimes 2 &= 3 \oplus 1. \end{aligned} \quad (\text{E.6})$$

- 3 particles:

$$\begin{aligned} \square \otimes \square &= \square \oplus \begin{array}{|c|c|} \hline \square & \square \\ \hline \square & \square \\ \hline \end{array}, \\ 3 \otimes 2 &= 4 \oplus 2, \end{aligned} \quad (\text{E.7})$$

$$\begin{aligned} \begin{array}{|c|} \hline \square \\ \hline \square \\ \hline \end{array} \otimes \square &= \begin{array}{|c|c|} \hline \square & \square \\ \hline \square & \square \\ \hline \end{array}, \\ 1 \otimes 2 &= 2. \end{aligned} \quad (\text{E.8})$$

- 4 particles:

$$\begin{aligned} \square \otimes \square &= \square \oplus \begin{array}{|c|c|c|} \hline \square & \square & \square \\ \hline \square & \square & \square \\ \hline \end{array}, \\ 4 \otimes 2 &= 5 \oplus 3, \end{aligned} \quad (\text{E.9})$$

$$\begin{aligned} 2 \times \begin{array}{|c|c|} \hline \square & \square \\ \hline \square & \square \\ \hline \end{array} \otimes \square &= 2 \times \begin{array}{|c|c|c|} \hline \square & \square & \square \\ \hline \square & \square & \square \\ \hline \end{array} \oplus 2 \times \begin{array}{|c|c|} \hline \square & \square \\ \hline \square & \square \\ \hline \end{array}, \\ 2_2 \otimes 2 &= 3_2 \oplus 1_2. \end{aligned} \quad (\text{E.10})$$

- 4 particles and 1 antiparticle:

$$\begin{aligned} \square \otimes \square &= \square \oplus \begin{array}{|c|c|c|} \hline \square & \square & \square \\ \hline \square & \square & \square \\ \hline \end{array}, \\ 5 \otimes \bar{2} &= 6 \oplus 4, \end{aligned} \quad (\text{E.11})$$

$$\begin{aligned} 3 \times \begin{array}{|c|c|c|} \hline \square & \square & \square \\ \hline \square & \square & \square \\ \hline \end{array} \otimes \square &= 3 \times \begin{array}{|c|c|c|c|} \hline \square & \square & \square & \square \\ \hline \square & \square & \square & \square \\ \hline \end{array} \oplus 3 \times \begin{array}{|c|c|} \hline \square & \square \\ \hline \square & \square \\ \hline \end{array}, \\ 3_3 \otimes \bar{2} &= 4_3 \oplus 2_3, \end{aligned} \quad (\text{E.12})$$

$$\begin{aligned} 2 \times \begin{array}{|c|c|} \hline \square & \square \\ \hline \square & \square \\ \hline \end{array} \otimes \square &= 2 \times \begin{array}{|c|c|c|} \hline \square & \square & \square \\ \hline \square & \square & \square \\ \hline \end{array}, \\ 1_2 \otimes \bar{2} &= 2_2. \end{aligned} \quad (\text{E.13})$$

## E.2.2 Physical particles

**Meson:** A meson consists out of two particles: 1 quark and 1 anti-quark. We get in the  $SU(2)$  symmetry group 2 symmetry classes, a triplet and a singlet:

$$\begin{aligned} \square \otimes \square &= \square\square \oplus \begin{array}{c} \square \\ \square \end{array}, \\ 2 \otimes \bar{2} &= 3 \oplus 1. \end{aligned} \quad (\text{E.14})$$

**Baryon:** A baryon is built up by three quarks. In  $SU(2)$  this leads us to 2 symmetry classes:

$$\begin{aligned} \square \otimes \square \otimes \square &= \square\square\square \oplus 2 \times \begin{array}{cc} \square & \square \\ \square & \end{array}, \\ 2 \otimes 2 \otimes 2 &= 4 \oplus 2_2. \end{aligned} \quad (\text{E.15})$$

**Pentaquark:** In the pentaquark one finds 4 quarks and 1 anti-quark. Here we show both, the symmetry classes of the 4 quarks

$$\begin{aligned} \square \otimes \square \otimes \square \otimes \square &= \square\square\square\square \oplus 3 \times \begin{array}{ccc} \square & \square & \square \\ \square & & \end{array} \oplus 2 \times \begin{array}{cc} \square & \square \\ \square & \square \end{array}, \\ 2 \otimes 2 \otimes 2 \otimes 2 &= 5 \oplus 3_3 \oplus 1_2, \end{aligned} \quad (\text{E.16})$$

and the symmetry classes of the whole pentaquark

$$\begin{aligned} \square \otimes \square \otimes \square \otimes \square \otimes \square &= \square\square\square\square\square \oplus 4 \times \begin{array}{cccc} \square & \square & \square & \square \\ \square & & & \end{array} \oplus 5 \times \begin{array}{ccc} \square & \square & \square \\ \square & \square & \end{array}, \\ 2 \otimes 2 \otimes 2 \otimes 2 \otimes \bar{2} &= 6 \oplus 4_4 \oplus 2_5. \end{aligned} \quad (\text{E.17})$$

## E.3 $SU(3)$ symmetry group

### E.3.1 Symmetry classes in $SU(3)$

- Particle and antiparticle: In  $SU(3)$  the fundamental and the its conjugate representations are different from each other:

$$\square = \text{particle in } SU(3), \quad (\text{E.18})$$

$$\begin{array}{c} \square \\ \square \end{array} = \text{antiparticle in } SU(3). \quad (\text{E.19})$$

- 2 particles:

$$\begin{aligned} \square \otimes \square &= \square\square \oplus \begin{array}{c} \square \\ \square \end{array}, \\ 3 \otimes 3 &= 6 \oplus \bar{3}. \end{aligned} \quad (\text{E.20})$$

- 3 particles:

$$\begin{aligned} \square\square \otimes \square &= \square\square\square \oplus \begin{array}{cc} \square & \square \\ \square & \end{array}, \\ 6 \otimes 3 &= 10 \oplus 8, \end{aligned} \quad (\text{E.21})$$

$$\begin{aligned} \begin{array}{c} \square \\ \square \end{array} \otimes \square &= \begin{array}{cc} \square & \square \\ \square & \end{array} \oplus \begin{array}{c} \square \\ \square \\ \square \end{array}, \\ \bar{3} \otimes 3 &= 8 \oplus 1. \end{aligned} \quad (\text{E.22})$$

- 4 particles:

$$\begin{array}{c}
 \begin{array}{|c|c|c|} \hline \square \\ \hline \end{array} \otimes \begin{array}{|c|} \hline \square \\ \hline \end{array} = \begin{array}{|c|c|c|c|} \hline \square \\ \hline \end{array} \oplus \begin{array}{|c|c|c|} \hline \square \\ \hline \end{array}, \\
 10 \otimes 3 = 15 \oplus 15',
 \end{array} \tag{E.23}$$

$$\begin{array}{c}
 2 \times \begin{array}{|c|c|} \hline \square \\ \hline \end{array} \otimes \begin{array}{|c|} \hline \square \\ \hline \end{array} = 2 \times \begin{array}{|c|c|c|} \hline \square \\ \hline \end{array} \oplus 2 \times \begin{array}{|c|c|} \hline \square \\ \hline \end{array} \oplus 2 \times \begin{array}{|c|} \hline \square \\ \hline \end{array}, \\
 8_2 \otimes 3 = 15'_2 \oplus \bar{6}_2 \oplus 3_2,
 \end{array} \tag{E.24}$$

$$\begin{array}{c}
 \begin{array}{|c|} \hline \square \\ \hline \end{array} \otimes \begin{array}{|c|} \hline \square \\ \hline \end{array} = \begin{array}{|c|c|} \hline \square \\ \hline \end{array}, \\
 1 \otimes 3 = 3.
 \end{array} \tag{E.25}$$

- 4 particles and 1 antiparticle:

$$\begin{array}{c}
 \begin{array}{|c|c|c|c|} \hline \square \\ \hline \end{array} \otimes \begin{array}{|c|} \hline \square \\ \hline \end{array} = \begin{array}{|c|c|c|c|c|} \hline \square \\ \hline \end{array} \oplus \begin{array}{|c|c|c|} \hline \square \\ \hline \end{array}, \\
 15 \otimes \bar{3} = 35 \oplus 10,
 \end{array} \tag{E.26}$$

$$\begin{array}{c}
 3 \times \begin{array}{|c|c|c|} \hline \square \\ \hline \end{array} \otimes \begin{array}{|c|} \hline \square \\ \hline \end{array} = 3 \times \begin{array}{|c|c|c|c|} \hline \square \\ \hline \end{array} \oplus 3 \times \begin{array}{|c|c|c|c|} \hline \square \\ \hline \end{array} \oplus 3 \times \begin{array}{|c|c|c|} \hline \square \\ \hline \end{array}, \\
 15'_3 \otimes \bar{3} = 27_3 \oplus 10_3 \oplus 8_3,
 \end{array} \tag{E.27}$$

$$\begin{array}{c}
 2 \times \begin{array}{|c|c|} \hline \square \\ \hline \end{array} \otimes \begin{array}{|c|} \hline \square \\ \hline \end{array} = 2 \times \begin{array}{|c|c|c|} \hline \square \\ \hline \end{array} \oplus 2 \times \begin{array}{|c|c|} \hline \square \\ \hline \end{array}, \\
 \bar{6}_2 \otimes \bar{3} = \bar{10}_2 \oplus 8_2,
 \end{array} \tag{E.28}$$

$$\begin{array}{c}
 3 \times \begin{array}{|c|c|} \hline \square \\ \hline \end{array} \otimes \begin{array}{|c|} \hline \square \\ \hline \end{array} = 3 \times \begin{array}{|c|c|c|} \hline \square \\ \hline \end{array} \oplus 3 \times \begin{array}{|c|c|} \hline \square \\ \hline \end{array}, \\
 3_3 \otimes \bar{3} = 8_3 \oplus 1_3.
 \end{array} \tag{E.29}$$

### E.3.2 Physical particles

**Meson:** A meson consists out of two particles: 1 quark and 1 anti-quark. We get in the  $SU(3)$  symmetry group 2 symmetry classes, an octet and a singlet:

$$\begin{array}{c}
 \begin{array}{|c|} \hline \square \\ \hline \end{array} \otimes \begin{array}{|c|} \hline \square \\ \hline \end{array} = \begin{array}{|c|c|} \hline \square \\ \hline \end{array} \oplus \begin{array}{|c|} \hline \square \\ \hline \end{array}, \\
 3 \otimes \bar{3} = 8 \oplus 1.
 \end{array} \tag{E.30}$$

**Baryon:** A baryon is built up by three quarks. In  $SU(3)$  this leads us to 3 symmetry classes:

$$\begin{array}{c}
 \begin{array}{|c|} \hline \square \\ \hline \end{array} \otimes \begin{array}{|c|} \hline \square \\ \hline \end{array} \otimes \begin{array}{|c|} \hline \square \\ \hline \end{array} = \begin{array}{|c|c|c|} \hline \square \\ \hline \end{array} \oplus 2 \times \begin{array}{|c|c|} \hline \square \\ \hline \end{array} \oplus \begin{array}{|c|} \hline \square \\ \hline \end{array}, \\
 3 \otimes 3 \otimes 3 = 10 \oplus 8_2 \oplus 1.
 \end{array} \tag{E.31}$$

**Pentaquark:** For a pentaquark consisting of 4 particles and 1 antiparticle it is accordingly more complicated to decompose it into its symmetry classes:

$$\square \otimes \square \otimes \square \otimes \square \otimes \begin{array}{|c|} \hline \square \\ \hline \square \\ \hline \end{array} = \begin{array}{|c|c|c|c|c|} \hline \square & \square & \square & \square & \square \\ \hline \square & & & & \\ \hline \end{array} \oplus 3 \times \begin{array}{|c|c|c|c|} \hline \square & \square & \square & \square \\ \hline \square & & & \\ \hline \end{array} \oplus 4 \times \begin{array}{|c|c|c|c|} \hline \square & \square & \square & \square \\ \hline \square & & & \\ \hline \end{array} \oplus 2 \times \begin{array}{|c|c|c|} \hline \square & \square & \square \\ \hline \square & & \\ \hline \end{array} \quad (\text{E.32})$$

$$\oplus 8 \times \begin{array}{|c|c|c|} \hline \square & \square & \square \\ \hline \square & & \\ \hline \end{array} \oplus 3 \times \begin{array}{|c|c|} \hline \square & \square \\ \hline \square & \\ \hline \end{array}, \quad (\text{E.33})$$

$$3 \otimes 3 \otimes 3 \otimes 3 \otimes \bar{3} = 35 \oplus 27_3 \oplus 10_4 \oplus \bar{10}_2 \oplus 8_8 \oplus 1_3 .$$

## E.4 $SU(6)$ symmetry group

### E.4.1 Symmetry classes in $SU(6)$

- Particle and antiparticle: In  $SU(6)$  the fundamental and the its conjugate representations are different from each other:

$$\square = \text{particle in } SU(6), \quad (\text{E.34})$$

$$\begin{array}{|c|} \hline \square \\ \hline \square \\ \hline \square \\ \hline \square \\ \hline \square \\ \hline \end{array} = \text{antiparticle in } SU(6). \quad (\text{E.35})$$

- 2 particles:

$$\begin{array}{|c|} \hline \square \\ \hline \square \\ \hline \end{array} \otimes \begin{array}{|c|} \hline \square \\ \hline \square \\ \hline \end{array} = \begin{array}{|c|c|} \hline \square & \square \\ \hline \square & \square \\ \hline \end{array} \oplus \begin{array}{|c|} \hline \square \\ \hline \square \\ \hline \square \\ \hline \end{array}, \quad (\text{E.36})$$

$$6 \otimes 6 = 21 \oplus \bar{15} .$$

- 3 particles:

$$\begin{array}{|c|c|} \hline \square & \square \\ \hline \square & \square \\ \hline \end{array} \otimes \begin{array}{|c|} \hline \square \\ \hline \square \\ \hline \end{array} = \begin{array}{|c|c|c|} \hline \square & \square & \square \\ \hline \square & \square & \square \\ \hline \end{array} \oplus \begin{array}{|c|c|} \hline \square & \square \\ \hline \square & \square \\ \hline \end{array}, \quad (\text{E.37})$$

$$21 \otimes 6 = 56 \oplus 70 ,$$

$$\begin{array}{|c|} \hline \square \\ \hline \square \\ \hline \end{array} \otimes \begin{array}{|c|} \hline \square \\ \hline \square \\ \hline \end{array} = \begin{array}{|c|c|} \hline \square & \square \\ \hline \square & \square \\ \hline \end{array} \oplus \begin{array}{|c|} \hline \square \\ \hline \square \\ \hline \square \\ \hline \end{array} \quad (\text{E.38})$$

$$\bar{15} \otimes 6 = 70 \oplus 20 .$$

- 4 particles:

$$\begin{aligned}
 \begin{array}{|c|c|c|} \hline \square & \square & \square \\ \hline \end{array} \otimes \begin{array}{|c|} \hline \square \\ \hline \end{array} &= \begin{array}{|c|c|c|c|} \hline \square & \square & \square & \square \\ \hline \end{array} \oplus \begin{array}{|c|c|c|} \hline \square & \square & \square \\ \hline \end{array}, \\
 56 \otimes 6 &= 126 \oplus 210,
 \end{aligned} \tag{E.39}$$

$$\begin{aligned}
 2 \times \begin{array}{|c|c|} \hline \square & \square \\ \hline \end{array} \otimes \begin{array}{|c|} \hline \square \\ \hline \end{array} &= 2 \times \begin{array}{|c|c|c|} \hline \square & \square & \square \\ \hline \end{array} \oplus 2 \times \begin{array}{|c|c|} \hline \square & \square \\ \hline \end{array} \oplus 2 \times \begin{array}{|c|} \hline \square \\ \hline \end{array}, \\
 70_2 \otimes 6 &= 210_2 \oplus 105'_2 \oplus 105_2,
 \end{aligned} \tag{E.40}$$

$$\begin{aligned}
 \begin{array}{|c|} \hline \square \\ \hline \end{array} \otimes \begin{array}{|c|} \hline \square \\ \hline \end{array} &= \begin{array}{|c|c|} \hline \square & \square \\ \hline \end{array} \otimes \begin{array}{|c|} \hline \square \\ \hline \end{array}, \\
 20 \otimes 6 &= 105 \oplus \overline{15}'.
 \end{aligned} \tag{E.41}$$

- 4 particles and 1 antiparticle:

$$\begin{aligned}
 \begin{array}{|c|c|c|c|} \hline \square & \square & \square & \square \\ \hline \end{array} \otimes \begin{array}{|c|} \hline \square \\ \hline \end{array} &= \begin{array}{|c|c|c|c|} \hline \square & \square & \square & \square \\ \hline \end{array} \oplus \begin{array}{|c|c|c|} \hline \square & \square & \square \\ \hline \end{array}, \\
 126 \otimes \overline{6} &= 700 \oplus 56',
 \end{aligned} \tag{E.42}$$

$$\begin{aligned}
 3 \times \begin{array}{|c|c|} \hline \square & \square \\ \hline \end{array} \otimes \begin{array}{|c|} \hline \square \\ \hline \end{array} &= 3 \times \begin{array}{|c|c|c|} \hline \square & \square & \square \\ \hline \end{array} \oplus 3 \times \begin{array}{|c|c|} \hline \square & \square \\ \hline \end{array} \oplus 3 \times \begin{array}{|c|} \hline \square \\ \hline \end{array}, \\
 210_3 \otimes \overline{6} &= 1134_3 \oplus 56'_3 \oplus 70'_3,
 \end{aligned} \tag{E.43}$$

$$\begin{aligned}
 2 \times \begin{array}{|c|c|} \hline \square & \square \\ \hline \end{array} \otimes \begin{array}{|c|} \hline \square \\ \hline \end{array} &= 2 \times \begin{array}{|c|c|c|} \hline \square & \square & \square \\ \hline \end{array} \oplus 2 \times \begin{array}{|c|} \hline \square \\ \hline \end{array}, \\
 105'_2 \otimes \overline{6} &= 560_2 \oplus 70'_2,
 \end{aligned} \tag{E.44}$$

$$\begin{aligned}
 3 \times \begin{array}{|c|c|} \hline \square & \square \\ \hline \end{array} \otimes \begin{array}{|c|} \hline \square \\ \hline \end{array} &= 3 \times \begin{array}{|c|c|c|} \hline \square & \square & \square \\ \hline \end{array} \oplus 3 \times \begin{array}{|c|c|} \hline \square & \square \\ \hline \end{array} \oplus 3 \times \begin{array}{|c|} \hline \square \\ \hline \end{array}, \\
 105_3 \otimes \overline{6} &= 540_3 \oplus 70'_3 \oplus 20'_3,
 \end{aligned} \tag{E.45}$$

$$\begin{aligned}
 \begin{array}{|c|} \hline \square \\ \hline \end{array} \otimes \begin{array}{|c|} \hline \square \\ \hline \end{array} &= \begin{array}{|c|c|} \hline \square & \square \\ \hline \end{array} \oplus \begin{array}{|c|} \hline \square \\ \hline \end{array}, \\
 \overline{15}' \otimes \overline{6} &= 70'' \oplus 20'.
 \end{aligned} \tag{E.46}$$

### E.4.2 Physical particles

**Meson:** A meson consists out of two particles: 1 quark and 1 anti-quark. We get in the  $SU(6)$  symmetry group 2 symmetry classes, a **35**-plet and a singlet:

$$\begin{array}{c}
 \square \otimes \begin{array}{|c|} \hline \square \\ \hline \square \\ \hline \square \\ \hline \square \\ \hline \end{array} = \begin{array}{|c|c|} \hline \square & \square \\ \hline \square & \square \\ \hline \square & \square \\ \hline \square & \square \\ \hline \end{array} \oplus \begin{array}{|c|} \hline \square \\ \hline \square \\ \hline \square \\ \hline \square \\ \hline \end{array}, \\
 6 \otimes \bar{6} = 35 \oplus 1.
 \end{array} \tag{E.47}$$

**Baryon:** A baryon is built up by three quarks. In  $SU(6)$  this leads us to 3 symmetry classes:

$$\begin{array}{c}
 \square \otimes \square \otimes \square = \begin{array}{|c|c|c|} \hline \square & \square & \square \\ \hline \end{array} \oplus 2 \times \begin{array}{|c|c|} \hline \square & \square \\ \hline \end{array} \oplus \begin{array}{|c|} \hline \square \\ \hline \square \\ \hline \end{array}, \\
 6 \otimes 6 \otimes 6 = 56 \oplus 70_2 \oplus 20.
 \end{array} \tag{E.48}$$

**Pentaquark:** For a pentaquark consisting of 4 particles and 1 antiparticle it is accordingly more complicated to decompose it into its symmetry classes:

$$\begin{array}{c}
 \square \otimes \square \otimes \square \otimes \square \otimes \begin{array}{|c|} \hline \square \\ \hline \square \\ \hline \square \\ \hline \square \\ \hline \end{array} = 3 \times \begin{array}{|c|c|c|} \hline \square & \square & \square \\ \hline \square & \square & \square \\ \hline \square & \square & \square \\ \hline \end{array} \oplus \begin{array}{|c|c|c|c|} \hline \square & \square & \square & \square \\ \hline \square & \square & \square & \square \\ \hline \square & \square & \square & \square \\ \hline \square & \square & \square & \square \\ \hline \end{array} \oplus 2 \times \begin{array}{|c|c|c|} \hline \square & \square & \square \\ \hline \square & \square & \square \\ \hline \square & \square & \square \\ \hline \end{array} \oplus 3 \times \begin{array}{|c|c|c|} \hline \square & \square & \square \\ \hline \square & \square & \square \\ \hline \square & \square & \square \\ \hline \end{array} \\
 \oplus 8 \times \begin{array}{|c|c|c|} \hline \square & \square & \square \\ \hline \square & \square & \square \\ \hline \square & \square & \square \\ \hline \end{array} \oplus \begin{array}{|c|c|} \hline \square & \square \\ \hline \square & \square \\ \hline \square & \square \\ \hline \end{array} \oplus 4 \times \begin{array}{|c|c|c|} \hline \square & \square & \square \\ \hline \square & \square & \square \\ \hline \square & \square & \square \\ \hline \end{array} \oplus 4 \times \begin{array}{|c|c|} \hline \square & \square \\ \hline \square & \square \\ \hline \square & \square \\ \hline \end{array}, \\
 6 \otimes 6 \otimes 6 \otimes 6 \otimes \bar{6} = 1134_3 \oplus 700 \oplus 560_2 \oplus 540_3 \oplus 70'_8 \oplus 70'' \oplus 56'_4 \oplus 20'_4.
 \end{array} \tag{E.49}$$

$$\begin{array}{c}
 \oplus 8 \times \begin{array}{|c|c|c|} \hline \square & \square & \square \\ \hline \square & \square & \square \\ \hline \square & \square & \square \\ \hline \end{array} \oplus \begin{array}{|c|c|} \hline \square & \square \\ \hline \square & \square \\ \hline \square & \square \\ \hline \end{array} \oplus 4 \times \begin{array}{|c|c|c|} \hline \square & \square & \square \\ \hline \square & \square & \square \\ \hline \square & \square & \square \\ \hline \end{array} \oplus 4 \times \begin{array}{|c|c|} \hline \square & \square \\ \hline \square & \square \\ \hline \square & \square \\ \hline \end{array}, \\
 6 \otimes 6 \otimes 6 \otimes 6 \otimes \bar{6} = 1134_3 \oplus 700 \oplus 560_2 \oplus 540_3 \oplus 70'_8 \oplus 70'' \oplus 56'_4 \oplus 20'_4.
 \end{array} \tag{E.50}$$

# Appendix F

## Quark models

### F.1 The spin-0 and spin-1 meson nonets

Mesons have baryon number  $\mathcal{B} = 0$ . In the quark model they are  $q\bar{q}'$  bound states of quarks  $q$  and anti-quarks  $\bar{q}'$  (the flavors of  $q$  and  $q'$  may be different). If the orbital angular momentum of the  $q\bar{q}'$  state is  $l$ , then the parity  $P$  is  $(-1)^{l+1}$ . The meson spin  $J$  is given by the usual relation  $|l - s| < J < |l + s|$  where  $s = 0$  (antiparallel quark spins) or  $s = 1$  (parallel quark spins). The charge conjugation  $C = (-1)^{l+s}$  is defined only for the  $q\bar{q}$  states made of quarks and their own anti-quarks.

The mesons are classified in  $J^{PC}$  multiplets (cf. Tab. F.1). The  $l = 0$  states are the pseudoscalars ( $0^{-+}$ ) and the vectors ( $1^{--}$ ). The orbital excitations  $l = 1$  are the scalars ( $0^{++}$ ) and the axialvectors ( $1^{++}$ ) and ( $1^{+-}$ ).

Following  $SU(3)_F$  the nine possible  $q\bar{q}'$  combinations containing the light  $u$ ,  $d$  and  $s$  quarks are grouped into an octet and a singlet of light quark mesons in flavor space (cf. Eq. (E.30)):

$$3 \otimes \bar{3} = 8 \oplus 1.$$

For these mesons, flavor and spin may be combined in an approximate flavor-spin  $SU(6)$  in which the six basic states are  $u \uparrow$ ,  $u \downarrow$ ,  $d \uparrow$ ,  $d \downarrow$ ,  $s \uparrow$ ,  $s \downarrow$  ( $\uparrow, \downarrow =$  spin up, down). Then the baryons belong to the multiplets on the right side of Eq. (E.47)

$$6 \otimes 6 = 35 \oplus 1.$$

These  $SU(6)_{FS}$  multiplets decompose into flavor  $SU(3)_F$  multiplets as follows:

$$35 = {}^3 8 \oplus {}^1 8 \oplus {}^3 1, \tag{F.1}$$

$$1 = {}^1 1. \tag{F.2}$$

In Fig. F.1 we depict the spin-0 ( ${}^1 8 \oplus {}^1 1$ ) and the spin-1 ( ${}^3 8 \oplus {}^3 1$ ) meson nonets.

state	$J^{PC}$	$\Gamma$	particles
scalar	$0^{++}$	$\mathbf{1}$	$f_0, a_0$
pseudoscalar	$0^{-+}$	$\gamma_5, \gamma_4 \gamma_5$	$\pi, \eta, \eta', K$
vector	$1^{--}$	$\gamma_i, \gamma_4 \gamma_i$	$\rho, \omega, K^*, \phi$
axialvector	$1^{++}$	$\gamma_i \gamma_5$	$a_1, f_1$
axialvector	$1^{+-}$	$\gamma_i \gamma_j$	$h_1, b_1$

Table F.1: Quantum numbers of the interpolators (8.31) for different choices of  $\Gamma$ . We remark that the classification with respect to  $C$  is for flavor degenerate interpolators only. Mesons with a higher spin than 1 can only be constructed via covariant derivatives, which are not discussed in this work.

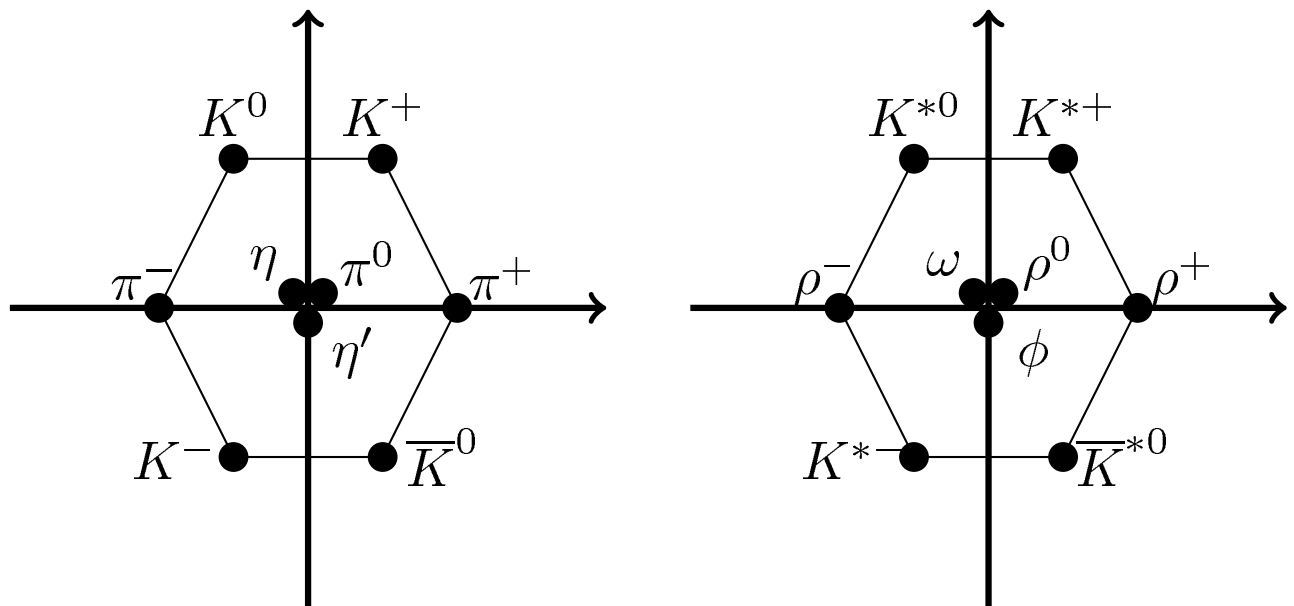


Figure F.1: These are the meson nonets with spin-0 on the left and with spin-1 on the right hand side.

## F.2 The baryon octet and decuplet

All the established baryons are apparently 3-quark ( $qqq$ ) states, and each such state is an  $SU(3)$  color singlet, a completely antisymmetric state of the three possible colors. Since the quarks are fermions, the state function for any baryon must be antisymmetric under interchange of any two equal-mass quarks (up and down quarks in the limit of isospin symmetry). Thus the state function may be written as

$$\langle qqq \rangle = |\text{color}\rangle_A |\text{orbital, spin, flavor}\rangle_S, \quad (\text{F.3})$$

where the subscripts S and A indicate symmetry or antisymmetry under interchange of any two of the equal-mass quarks.

The 3-quark baryons are made up of  $u$ ,  $d$ , and  $s$  quarks. The three flavors imply an approximate flavor  $SU(3)_F$ , which requires that baryons made of these quarks belong to the multiplets on the right side of Eq. (E.31)

$$3 \otimes 3 \otimes 3 = 10 \oplus 8_2 \oplus 1.$$

For these baryons, flavor and spin may be combined in an approximate flavor-spin  $SU(6)$ . Then the baryons belong to the multiplets on the right side of Eq. (E.48)

$$6 \otimes 6 \otimes 6 = 56 \oplus 70_2 \oplus 20.$$

These  $SU(6)_{FS}$  multiplets decompose into flavor  $SU(3)_F$  and spin  $SU(2)_S$  multiplets as follows:

$$56 = {}^4 10 \oplus {}^2 8, \quad (\text{F.4})$$

$$70 = {}^2 10 \oplus {}^4 8 \oplus {}^2 8 \oplus {}^2 1, \quad (\text{F.5})$$

$$20 = {}^2 8 \oplus {}^4 1. \quad (\text{F.6})$$

In (F.4) we find that the spin-3/2 decuplet and the spin-1/2 octet baryons form the symmetric  $56_{FS}$ -plet in flavor-spin space (cf. Fig. F.2). From (F.3) follows that those particles have to have a symmetric state function also in orbital space. In the  $56$ -plet we thus find the ground-states of 3-quark baryons.

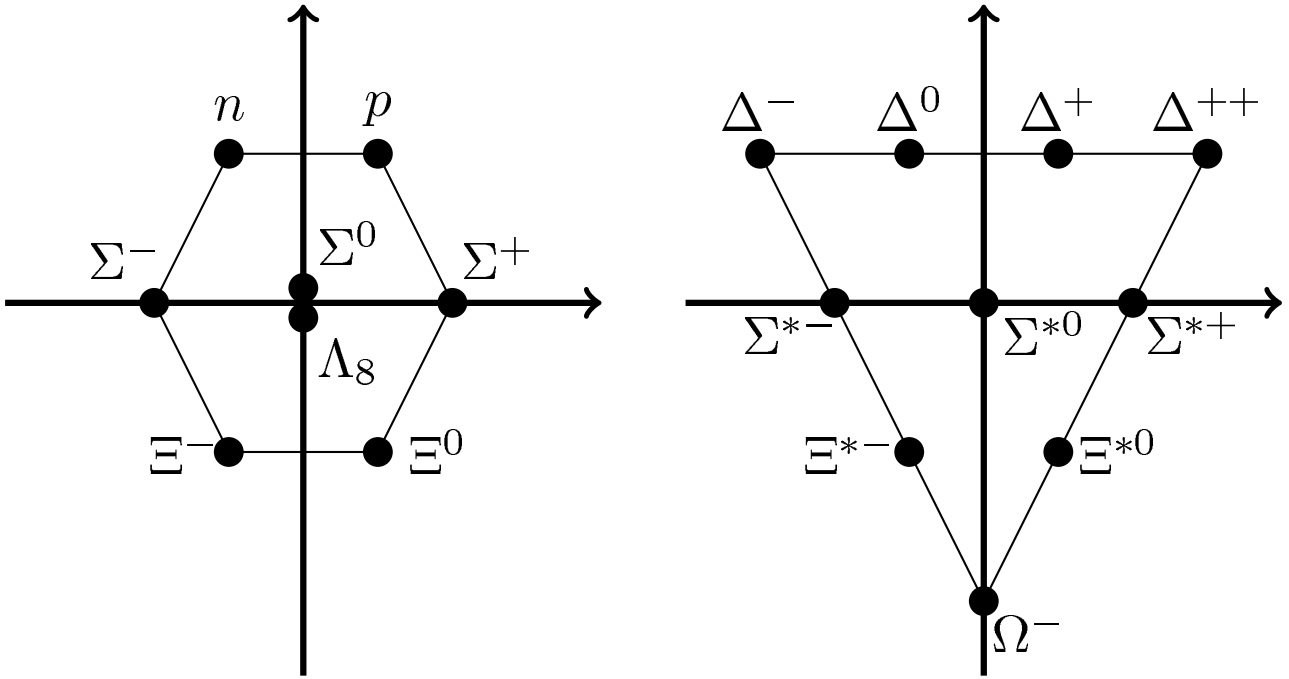


Figure F.2: The ground-state 3-quark baryons are located in the  $56_{F8}$ -plet. On the left hand side there are the ground-state baryons with spin-1/2. On the right hand side we find the heavier spin-3/2 ground-state baryons.

### F.3 Diquarks and triquarks

In some quark models we need diquarks which consists out of 2 quarks. According to those quark models they form a bound state within a hadron according to those quark models. The color-orbit or color-spin quantum numbers in the  $SU(6)$  symmetry group are decomposed as follows:

$$\begin{aligned}
 6 \otimes 6 &= \bar{15} \oplus 21, & \text{where} \\
 15 &= {}^1_6 \oplus {}^3\bar{3}, \\
 21 &= {}^3_6 \oplus {}^1\bar{3}.
 \end{aligned}$$

In the context of pentaquarks some models predict also a triquark within the pentaquark consisting out of two quarks and one anti-quark. In  $SU(6)$  we get:

$$\begin{aligned}
 6 \otimes 6 \otimes \bar{6} &= 120 \oplus 84 \oplus 6_2, & \text{where} \\
 120 &= {}^4_15 \oplus {}^2_15 \oplus {}^2\bar{6} \oplus {}^4_3 \oplus {}^2_3, \\
 84 &= {}^4_6 \oplus {}^2_15 \oplus {}^2\bar{6} \oplus {}^4_3 \oplus {}^2_3, \\
 6 &= {}^2_3.
 \end{aligned}$$

# Appendix G

## Parameters for CI fermions

### G.1 Parameters of the simulation

size	$\beta$	confs.	$a$ [fm]	$a^{-1}$ [MeV]	$N(n, w)$	$\kappa(n, w)$
$20^3 \times 32$	8.15	100	0.119	1658	22, 62	0.21, 0.1865
$16^3 \times 32$	7.90	100	0.148	1333	18, 41	0.21, 0.1910
$12^3 \times 24$	7.90	100	0.148	1333	18, -	0.21, -

Table G.1: Parameters of our simulation. We list the lattice size, the inverse coupling  $\beta$ , the number of configurations, the lattice spacing  $a$ , the cutoff  $a^{-1}$  and the smearing parameters  $N$  and  $\kappa$  for the narrow and wide sources. The  $16^3 \times 32$  and  $20^3 \times 32$  lattices are used for the excited baryon project, while we compute the pentaquark project on the smaller  $12^3 \times 24$  lattice.

We work with quenched gauge configurations generated with the Lüscher-Weisz action [197, 198]. We use for the baryon spectroscopy two sets of lattices,  $20^3 \times 32$  and  $16^3 \times 32$ , at couplings  $\beta = 8.15$  and  $\beta = 7.90$  corresponding to lattice spacings of  $a = 0.119$  fm and  $a = 0.148$  fm, determined from the Sommer parameter in [199]. Thus for both lattices we have a spatial extent of  $L \sim 2.4$  fm. The two different values of the lattice constant  $a$  allow us to assess the cutoff dependence  $a \rightarrow 0$ .

For the pentaquark project the gauge fields are generated on a  $12^3 \times 24$  lattice again with the Lüscher-Weisz gauge action at  $\beta = 7.90$ . The corresponding value of the lattice spacing is  $a = 0.148$  fm as determined from the Sommer parameter. For the quark sources we use a Gaussian-type distribution generated with Jacobi smearing [74, 75]. The error bars are computed using the jackknife method. The  $s$ -quark mass  $am_s = 0.0888(17)$  is determined from the Kaon mass. The parameters of the gauge configurations are collected in Table G.1.

Our quark propagators are computed using the Chirally Improved (CI) Dirac operator [63, 64]. We work with several quark masses in the range  $am = 0.02, \dots, 0.2$ , leading to pion masses down to 350 MeV. For setting the strange quark mass we use the  $K$ -meson with the light quark mass extrapolated to the chiral limit.

Our quark sources are placed at  $t = 0$  and the generalized eigenvalue problem (8.79) for the variational method is normalized at  $t_0 = a$ . The final results for the baryon masses were obtained from a fully correlated fit to the eigenvalues. The errors are statistical errors determined with single elimination jackknife.

### G.2 Dirac structure and quark sources

We are using 3-quark operators (8.43) with narrow and wide smeared sources. The interpolating fields for the different particles are summarized in Table G.2. Our interpolators for the  $\Delta$  and the  $\Omega$  still have overlap with

particle	interpolating fields	operator content
Nucleon	$N^{(i)}, i = 1, 2, 3$	$\mathcal{O}_{(i)}^{uud} - \mathcal{O}_{(i)}^{udu}$
$\Sigma$	$\Sigma^{(i)}, i = 1, 2, 3$	$\mathcal{O}_{(i)}^{uus} - \mathcal{O}_{(i)}^{usu}$
$\Xi$	$\Xi^{(i)}, i = 1, 2, 3$	$\mathcal{O}_{(i)}^{ssu} - \mathcal{O}_{(i)}^{sus}$
$\Lambda$ -octet	$\Lambda_8^{(i)}, i = 1, 2, 3$	$\mathcal{O}_{(i)}^{sud} - \mathcal{O}_{(i)}^{sdu} + \mathcal{O}_{(i)}^{usd} - \mathcal{O}_{(i)}^{dsu}$
$\Lambda$ -singlet	$\Lambda_1$	$\mathcal{O}_{(1)}^{uds} - \mathcal{O}_{(1)}^{usd} + \mathcal{O}_{(1)}^{dsu} - \mathcal{O}_{(1)}^{sdu} + \mathcal{O}_{(1)}^{sud} - \mathcal{O}_{(1)}^{dsu}$
$\Delta$ -decuplet	$\Delta_\mu$	$P_{\mu\nu}^{3/2} \mathcal{O}_{(4),\nu}^{uuu}$
$\Omega$ -decuplet	$\Omega_\mu$	$P_{\mu\nu}^{3/2} \mathcal{O}_{(4),\nu}^{sss}$

Table G.2: We summarize here all interpolating fields we used in our calculations in Chapter 10. Note that we have to project  $\Delta_\mu$  and  $\Omega_\mu$  to definite spin-3/2 via (8.53). Note that for the spin-3/2 projection only the spatial components of  $P_{\mu\nu}^{3/2}$  are non-zero.

both spin-1/2 and spin-3/2. Thus, we need a projection to definite angular momentum. We use the continuum formulation of a spin-3/2 projection for a Rarita-Schwinger field  $P^{3/2}$  in (8.53) projected to zero momentum. The different possible choices for  $\Gamma_1^{(i)}$  and  $\Gamma_2^{(i)}$  are listed in Table G.3.

	$\Gamma_1^{(i)}$	$\Gamma_2^{(i)}$
$i = 1$	$\mathbb{1}$	$C\gamma_5$
$i = 2$	$\gamma_5$	$C$
$i = 3$	$i\mathbb{1}$	$C\gamma_4\gamma_5$
$i = 4$	$\mathbb{1}$	$C\gamma_\nu$

Table G.3: Dirac structures used for the baryons in Chapter 10.

In addition to the different Dirac structures, we construct the interpolators listed in Table G.2 from quarks with sources created by different amount of smearing. In particular, we use Jacobi smearing [74, 75] with two different sets of parameters (number of smearing steps  $N$ , amplitude of hopping term  $\kappa$ , cf. Section 8.3.1) to create narrow and wide sources. The shapes of these sources are approximately Gaussian with  $\sigma \sim 0.27$  fm for the narrow source and  $\sigma \sim 0.41$  fm for the wide source. Details of the source preparation and plots of the source shapes can be found in [1, 2, 9, 110, 112, 117].

Each quark in our baryon interpolators can either be narrowly ( $n$ ) or widely ( $w$ ) smeared giving rise to the following eight combinations for the sources:

$$n(nn), \quad n(nw), \quad n(wn), \quad w(nn), \quad w(nw), \quad w(nw), \quad w(wn), \quad w(ww). \quad (\text{G.1})$$

In this notation the order of the quark fields is understood as in Eqs. (10.1) – (10.7) and the parentheses indicate which quarks are combined in the diquark combination. Since the smearing used here is a purely scalar operation, the assignment of quantum numbers, as given in the last Section, remains unchanged.

Taking into account the different Dirac structures discussed in the last Section, we can work with 24 different interpolators for nucleon,  $\Sigma$ ,  $\Xi$  and  $\Lambda_8$ . For the  $\Lambda_1$  and the  $\Delta$  we have only one Dirac structure and consequently a total of 8 different interpolators. We remark that in the final analysis not all interpolators are used. We prune the maximal correlation matrix and remove some of the correlators that couple only weakly to the physical states or add no new information, thus enhancing the numerical noise. The criterion for the selection of the interpolators is the optimization of the quality of the plateaus in the effective mass plots.

# Appendix H

## Parameters for FP fermions

### H.1 Parameters in the algorithm

#### H.1.1 Parallelization

It is possible to parallelize the work in all four directions. Due to the fact that we have chosen the indexing of our lattice as described in Eq. (12.57), we have to parallelize the fourth direction first, then the third and so on. In this way the communication between the processors is minimized and thus more favorable. For the  $12^4$  lattice we use:

direction $i$	extention $L_i$	parallelization $N_i$
4	12	12
3	12	12
2	12	2
1	12	1

Table H.1: Parallelization for the  $12^4$  lattice.

In some parts of the algorithm we have to satisfy special constraints. In the gauge update we are using a parallelized version of the original code<sup>1</sup> which divides the processors into several groups which work on different parts of the lattice independently. But there are some constraints on the used parallelization there:

$$\frac{L_4}{5} \geq N_{\text{groups}} , \quad (\text{H.1})$$

$$2^{N_{\text{groups}}} - 1 \leq \prod_i N_i , \quad (\text{H.2})$$

$$N_{\text{groups}} \prod_i N_i^{\text{smear}} \leq \prod_i N_i . \quad (\text{H.3})$$

In the production run for the  $12^4$  lattice we can only use  $N_{\text{groups}} = 2$  smearing groups which is mainly because of constraint (H.1): In contrast to the global parallelization in the gauge update part a small surface of the local volume is more favorable.

At some point we have to build up the Dirac operator  $D$ . This is done in a own subroutine which also has some constraints:

$$\frac{L_4}{3} \geq L_4^D , \quad (\text{H.4})$$

$$\text{mod} (L_4, L_4^D) = 0 . \quad (\text{H.5})$$

<sup>1</sup>This part was written by Christoph Weiermann [175].

direction $i$	parallelization $N_i^{\text{smear}}$
4	3
3	4
2	4
1	3

Table H.2: Parallelization for the  $12^4$  lattice in the gauge update written by Christoph Weiermann [175].

## H.1.2 Characteristics in the nested A/R steps

### Subtraction

In the Subtraction we use for the lattices different numbers of eigenvalues and -vectors. We find that at a certain point a larger number of eigenvectors does not improve both the calculation of the determinants and the condition number of the inversion of the Dirac operator compared to the numerical effort in the Arnoldi. Therefore we try to balance the numerical costs and the improvement by the Subtraction.

size	# of eigenvalues and -vectors
$8^3 \times 24$	48
$12^3 \times 24$	96
$12^4$	96

Table H.3: For the small  $8^3 \times 24$  lattice 48 eigenvalues and -vectors are enough to get a good balance between the numerical costs and the improvement. For the larger lattices 48 eigenvalues and -vectors are no longer sufficient and we therefore have to increase the numerical efforts more than twice because they do not grow linearly with the number of eigenvalues and the corresponding eigenvectors.

### Determinant breakup

First we have used the ladder method for both the  $ud$ - and the  $s$ -quark determinant breakup, where we have to choose the number of intervals such that all intervals contributes approximately the same. Later Manuel Weingart in [174] replaced the ladder method for the  $s$ -quark determinant by the  $N$ th-root method because of performance reasons. Furthermore the Taylor expansion of the  $s$ -quark determinant was replaced by a rational approximation which shows a 30% improvement of the algorithm in this part. We have summarized the breakups in Table H.4

quark mass	# of intervals/products	method
$m_{ud}$	138	ladder
$m_s$	96	ladder
$m_s$	96	$N$ th-root

Table H.4: To satisfy the condition that every interval or product should contribute nearly the same to the whole determinant we use the given amount of determinant breakup.

part of the code	number of iterations	averaged acceptance rate
gauge update	$n_p = 576$	
1st accept/reject step	$N^{1\text{st}} = 20$	$acc^{1\text{st}} \approx 56\%$
2nd accept/reject step	$N^{2\text{nd}} = 3$	$acc^{2\text{nd}} \approx 76\%$
3rd accept/reject step	$N^{3\text{rd}} \approx 10$	$acc^{3\text{rd}} \approx 64\%$

Table H.5: In the gauge update we use a Metropolis updating algorithm. In the 1st and 2nd A/R steps we tune the parameters  $N^{1\text{st}}$  and  $N^{2\text{nd}}$  in such way that we obtain the given acceptance rates. Especially  $N^{3\text{rd}}$  is very sensitive to these acceptance rates. In contrast to  $N^{1\text{st}}$  and  $N^{2\text{nd}}$ ,  $N^{3\text{rd}}$  cannot be set as a starting parameter, but it is generated dynamically.  $N^{3\text{rd}}$  is the number of 3rd accept/reject steps which are needed for a single independent configuration, i.e., it is the autocorrelation time of the run. The averaged numbers which are given in the table are obtained from simulations of a  $12^4$  lattice.

size	confs.	$\beta$	$a$ [fm]	$a^{-1}$ [MeV]	$L$ [fm]	$am_{ud}, am_s$	$m_{ud}^{\text{bare}}, m_s^{\text{bare}}$ [MeV]
$8^3 \times 24$	445	2.925	0.148	1333	1.18	0.025, 0.103	7.2(4), $\sim 110$
$12^3 \times 24$	?	2.925	$\sim 0.15$	$\sim 1333$	$\sim 1.8$	0.025, 0.103	?, ?
$12^4$	522	2.925	0.129(5)	1530(60)	1.55	0.025, 0.103	16(1), $\sim 137$

Table H.6: Parameters of our simulations. We list the lattice size, the inverse coupling  $\beta$ , the number of configurations, the lattice spacing  $a$ , the cutoff  $a^{-1}$ , the sea quark masses  $m_{ud}$ ,  $m_{ud}$  in lattice units, the bare quark masses  $m_{ud}^{\text{bare}}, m_s^{\text{bare}}$  and the number of stored eigenvectors in the Arnoldi. We find that the  $8^3 \times 24$  and  $12^3 \times 24$  lattices are in the  $\delta$ -regime, while the  $12^4$  lattice is in the  $\epsilon$ -regime. For the  $12^3 \times 24$  lattice we have not decided yet how much configurations we will produce. Furthermore at the present stage we cannot determine the exact lattice spacing or the bare quark masses for this lattice due to a lack of statistics.

### H.1.3 Acceptance rates

We are using nested accept/reject steps to improve the acceptance rate of our algorithm. In Table H.5 we give the parameters which are used in the production runs for the  $12^4$  lattice. These parameters have a very large impact in the resulting acceptance rate for each steps and may not be changed running a Markov chain. So it is very important to smartly choose the parameters already at the beginning of the runs. At least after equilibration they have to be fixed.

## H.2 Parameters of the simulations

Within this project we have aimed at quite small volumes on which we want to compute very small quark masses. We have three different lattices. The  $8^3 \times 24$  lattice is the lattice on which we have tested several algorithmic details. This lattice has a too small spatial volume to be for sure in the  $\delta$ -regime. On the  $12^4$  lattice we want to explore the  $\epsilon$ -regime. Therefore we use a symmetric lattice, which is not elongated in the temporal direction. The next lattice is the  $12^3 \times 24$  lattice which should have a large enough spatial volume to target the  $\delta$ -regime. There we will try to find the rotator spectrum which readily holds some low energy constants. The production runs of this lattice have not yet started due to lack of computing power, but the code is already available and the parameters for the simulations are already tuned. In this work we do not present results obtained from this lattice. In Table H.6 we give an overview of the different lattices.



# Bibliography

- [1] T. Burch *et al.*, “Masses of excited baryons from chirally improved quenched lattice QCD,” *Nucl. Phys.* **A755** (2005) 481–484, [arXiv:nucl-th/0501025](#).
- [2] T. Burch *et al.*, “Baryon spectroscopy with spatially improved quark sources,” *PoS LAT2005* (2006) 075, [arXiv:hep-lat/0509051](#).
- [3] T. Burch *et al.*, “Excited hadrons on the lattice: Baryons,” *Phys. Rev.* **D74** (2006) 014504, [arXiv:hep-lat/0604019](#).
- [4] D. Hierl, C. Hagen, and A. Schäfer, “The exotic baryon  $\Theta^+(1540)$  on the lattice,” *PoS LAT2005* (2006) 026, [arXiv:hep-lat/0509109](#).
- [5] C. Hagen, D. Hierl, and A. Schäfer, “Search for the  $\Theta^+(1540)$  in lattice QCD,” *Eur. Phys. J.* **A29** (2006) 221, [arXiv:hep-lat/0606006](#).
- [6] A. Hasenfratz, P. Hasenfratz, F. Niedermayer, D. Hierl, and A. Schäfer, “First results in QCD with 2 + 1 light flavors using the fixed-point action,” *PoS LAT2006* (2006) 178, [arXiv:hep-lat/0610096](#).
- [7] P. Hasenfratz *et al.*, “2 + 1 Flavor QCD simulated in the  $\epsilon$ -regime in different topological sectors,” [arXiv:0707.0071 \[hep-lat\]](#).
- [8] P. Hasenfratz *et al.*, “2 + 1 flavor QCD with the fixed-point action in the  $\epsilon$ -regime,” *PoS LAT2007* (2007) 077, [arXiv:0710.0551 \[hep-lat\]](#).
- [9] T. Burch *et al.*, “Excited meson spectroscopy with chirally improved fermions,” *PoS LAT2005* (2006) 097, [arXiv:hep-lat/0509086](#).
- [10] F. Belletti *et al.*, “QCD on the Cell Broadband Engine,” *PoS LATTICE2007* (2007) 039, [arXiv:0710.2442 \[hep-lat\]](#).
- [11] D. J. Gross and F. Wilczek, “Ultraviolet behavior of non-abelian gauge theories,” *Phys. Rev. Lett.* **30** (1973) 1343–1346.
- [12] H. D. Politzer, “Reliable perturbative results for strong interactions?,” *Phys. Rev. Lett.* **30** (1973) 1346–1349.
- [13] D. J. Gross and F. Wilczek, “Asymptotically free gauge theories. 1,” *Phys. Rev.* **D8** (1973) 3633–3652.
- [14] H. D. Politzer, “Asymptotic Freedom: An approach to strong interactions,” *Phys. Rept.* **14** (1974) 129–180.
- [15] Z. Prkacin *et al.*, “Anatomy of string breaking in QCD,” *PoS LAT2005* (2006) 308, [arXiv:hep-lat/0510051](#).
- [16] S. Hands, “The phase diagram of QCD,” *Contemporary Physics* **42** (2001) 209, <http://www.citebase.org/abstract?id=oai:arXiv.org:physics/0105022>.

- [17] W.-M. Yao, C. Amsler, D. Asner, R. Barnett, J. Beringer, P. Burchat, C. Carone, C. Caso, O. Dahl, G. D'Ambrosio, A. DeGouvea, M. Doser, S. Eidelman, J. Feng, T. Gherghetta, M. Goodman, C. Grab, D. Groom, A. Gurtu, K. Hagiwara, K. Hayes, J. Hernández-Rey, K. Hikasa, H. Jawahery, C. Kolda, K. Y., M. Mangano, A. Manohar, A. Masoni, R. Miquel, K. Mönig, H. Murayama, K. Nakamura, S. Navas, K. Olive, L. Pape, C. Patrignani, A. Piepke, G. Punzi, G. Raffelt, J. Smith, M. Tanabashi, J. Terning, N. Törnqvist, T. Trippe, P. Vogel, T. Watari, C. Wohl, R. Workman, P. Zyla, B. Armstrong, G. Harper, V. Lugovsky, P. Schaffner, M. Artuso, K. Babu, H. Band, E. Barberio, M. Battaglia, H. Bichsel, O. Biebel, P. Bloch, E. Blucher, R. Cahn, D. Casper, A. Cattai, A. Ceccucci, D. Chakraborty, R. Chivukula, G. Cowan, T. Damour, T. DeGrand, K. Desler, M. Dobbs, M. Drees, A. Edwards, D. Edwards, V. Elvira, J. Erler, V. Ezhela, W. Fetscher, B. Fields, B. Foster, D. Froidevaux, T. Gaisser, L. Garren, H.-J. Gerber, G. Gerbier, L. Gibbons, F. Gilman, G. Giudice, A. Gribsan, M. Grünewald, H. Haber, C. Hagmann, I. Hinchliffe, A. Höcker, P. Igo-Kemenes, J. Jackson, K. Johnson, D. Karlen, B. Kayser, D. Kirkby, S. Klein, K. Kleinknecht, I. Knowles, R. Kowalewski, P. Kreitz, B. Krusche, Y. Kuyanov, O. Lahav, P. Langacker, A. Liddle, Z. Ligeti, T. Liss, L. Littenberg, L. Liu, K. Lugovsky, S. Lugovsky, T. Mannel, D. Manley, W. Marciano, A. Martin, D. Milstead, M. Narain, P. Nason, Y. Nir, J. Peacock, S. Prell, A. Quadt, S. Raby, B. Ratcliff, E. Razuvaev, B. Renk, P. Richardson, S. Roesler, G. Rolandi, M. Ronan, L. Rosenberg, C. Sachrajda, S. Sarkar, M. Schmitt, O. Schneider, D. Scott, T. Sjöstrand, G. Smoot, P. Sokolsky, S. Spanier, H. Spieler, A. Stahl, T. Stanev, R. Streitmatter, T. Sumiyoshi, N. Tkachenko, G. Trilling, G. Valencia, K. van Bibber, M. Vincet, D. Ward, B. Webber, J. Wells, M. Whalley, L. Wolfenstein, J. Womersley, C. Woody, A. Yamamoto, O. Zenin, J. Zhang, and R.-Y. Zhu, "Review of Particle Physics," *Journal of Physics G* **33** (2006) 1+. <http://pdg.lbl.gov>.
- [18] M. E. Peskin and D. V. Schroeder, *An introduction to Quantum Field Theory*. Westview Press, 1995.
- [19] R. A. Bertlmann, *Anomalies in quantum field theory*. The international series of monographs on physics, 91. Oxford University Press, 1996.
- [20] J. F. Donoghue, E. Golowich, and B. R. Holstein, *Dynamics of the Standard Model*, vol. 2 of *Cambridge Monographs on Particle Physics, Nuclear Physics and Cosmology*. Cambridge University Press, 1996.
- [21] G. 't Hooft, "Computation of the quantum effects due to a four-dimensional pseudoparticle," *Phys. Rev.* **D14** (1976) 3432–3450.
- [22] G. 't Hooft, "Symmetry breaking through Bell-Jackiw anomalies," *Phys. Rev. Lett.* **37** (1976) 8–11.
- [23] M. Gell-Mann, R. J. Oakes, and B. Renner, "Behavior of current divergences under  $SU(3) \times SU(3)$ ," *Phys. Rev.* **175** (1968) 2195–2199.
- [24] B. R. Holstein, "A brief introduction to chiral perturbation theory," *Czech. J. Phys.* **50S4** (2000) 9–23, [arXiv:hep-ph/9911449](https://arxiv.org/abs/hep-ph/9911449).
- [25] G. Colangelo, S. Dürr, and C. Haefeli, "Finite volume effects for meson masses and decay constants," *Nucl. Phys.* **B721** (2005) 136–174, [arXiv:hep-lat/0503014](https://arxiv.org/abs/hep-lat/0503014).
- [26] J. Gasser and H. Leutwyler, "Light quarks at low temperatures," *Phys. Lett.* **B184** (1987) 83.
- [27] J. Gasser and H. Leutwyler, "Thermodynamics of chiral symmetry," *Phys. Lett.* **B188** (1987) 477.
- [28] J. Gasser and H. Leutwyler, "Spontaneously broken symmetries: Effective Lagrangians at finite volume," *Nucl. Phys.* **B307** (1988) 763.
- [29] H. Leutwyler and A. Smilga, "Spectrum of Dirac operator and role of winding number in QCD," *Phys. Rev.* **D46** (1992) 5607–5632.
- [30] H. Neuberger, "Soft pions in large boxes," *Nucl. Phys.* **B300** (1988) 180.
- [31] H. Neuberger, "A better way to measure  $f_\pi$  in the linear sigma model," *Phys. Rev. Lett.* **60** (1988) 889.
- [32] P. Hasenfratz and H. Leutwyler, "Goldstone boson related finite size effects in field theory and critical phenomena with  $O(N)$  symmetry," *Nucl. Phys.* **B343** (1990) 241–284.

- [33] H. Leutwyler, “Energy levels of light quarks confined to a box,” *Phys. Lett.* **B189** (1987) 197.
- [34] J. J. M. Verbaarschot and T. Wettig, “Random Matrix Theory and chiral symmetry in QCD,” *Ann. Rev. Nucl. Part. Sci.* **50** (2000) 343–410, [arXiv:hep-ph/0003017](#).
- [35] T. Banks and A. Casher, “Chiral symmetry breaking in confining theories,” *Nucl. Phys.* **B169** (1980) 103.
- [36] E. V. Shuryak and J. J. M. Verbaarschot, “Random Matrix Theory and spectral sum rules for the Dirac operator in QCD,” *Nucl. Phys.* **A560** (1993) 306–320, [arXiv:hep-th/9212088](#).
- [37] F. Basile and G. Akemann, “Equivalence of QCD in the  $\epsilon$ -regime and chiral Random Matrix Theory with or without chemical potential,” [arXiv:0710.0376 \[hep-th\]](#).
- [38] J. J. M. Verbaarschot and I. Zahed, “Spectral density of the QCD Dirac operator near zero virtuality,” *Phys. Rev. Lett.* **70** (1993) 3852–3855, [arXiv:hep-th/9303012](#).
- [39] J. J. M. Verbaarschot, “The spectrum of the QCD Dirac operator and chiral Random Matrix Theory: The Threefold way,” *Phys. Rev. Lett.* **72** (1994) 2531–2533, [arXiv:hep-th/9401059](#).
- [40] T. Wilke, T. Guhr, and T. Wettig, “The microscopic spectrum of the QCD Dirac operator with finite quark masses,” *Phys. Rev.* **D57** (1998) 6486–6495, [arXiv:hep-th/9711057](#).
- [41] P. H. Damgaard and S. M. Nishigaki, “Distribution of the  $k$ -th smallest Dirac operator eigenvalue,” *Phys. Rev.* **D63** (2001) 045012, [arXiv:hep-th/0006111](#).
- [42] K. G. Wilson, “Confinement of quarks,” *Phys. Rev.* **D10** (1974) 2445–2459.
- [43] G. P. Lepage and P. B. Mackenzie, “On the viability of lattice perturbation theory,” *Phys. Rev.* **D48** (1993) 2250–2264, [arXiv:hep-lat/9209022](#).
- [44] P. Hasenfratz, “The theoretical background and properties of perfect actions,” [arXiv:hep-lat/9803027](#).
- [45] M. Blatter and F. Niedermayer, “New fixed-point action for  $SU(3)$  lattice gauge theory,” *Nucl. Phys.* **B482** (1996) 286–304, [arXiv:hep-lat/9605017](#).
- [46] H. B. Nielsen and M. Ninomiya, “Absence of neutrinos on a lattice. 1. Proof by homotopy theory,” *Nucl. Phys.* **B185** (1981) 20.
- [47] H. B. Nielsen and M. Ninomiya, “Absence of neutrinos on a lattice. 2. Intuitive topological proof,” *Nucl. Phys.* **B193** (1981) 173.
- [48] M. Bochicchio, L. Maiani, G. Martinelli, G. C. Rossi, and M. Testa, “Chiral symmetry on the lattice with Wilson fermions,” *Nucl. Phys.* **B262** (1985) 331.
- [49] P. H. Ginsparg and K. G. Wilson, “A remnant of chiral symmetry on the lattice,” *Phys. Rev.* **D25** (1982) 2649.
- [50] P. Hasenfratz, V. Laliena, and F. Niedermayer, “The index theorem in QCD with a finite cut-off,” *Phys. Lett.* **B427** (1998) 125–131, [arXiv:hep-lat/9801021](#).
- [51] H. Neuberger, “Exactly massless quarks on the lattice,” *Phys. Lett.* **B417** (1998) 141–144, [arXiv:hep-lat/9707022](#).
- [52] H. Neuberger, “More about exactly massless quarks on the lattice,” *Phys. Lett.* **B427** (1998) 353–355, [arXiv:hep-lat/9801031](#).
- [53] I. Horváth, “Ginsparg-Wilson relation and ultralocality,” *Phys. Rev. Lett.* **81** (1998) 4063–4066, [arXiv:hep-lat/9808002](#).
- [54] P. Hernández, K. Jansen, and M. Lüscher, “Locality properties of Neuberger’s lattice Dirac operator,” *Nucl. Phys.* **B552** (1999) 363–378, [arXiv:hep-lat/9808010](#).

- [55] M. Lüscher, “Exact chiral symmetry on the lattice and the Ginsparg-Wilson relation,” *Phys. Lett.* **B428** (1998) 342–345, [arXiv:hep-lat/9802011](#).
- [56] Y. Kikukawa and A. Yamada, “A note on the exact lattice chiral symmetry in the overlap formalism,” [arXiv:hep-lat/9810024](#).
- [57] Y. Kikukawa and A. Yamada, “Axialvector current of exact chiral symmetry on the lattice,” *Nucl. Phys.* **B547** (1999) 413–423, [arXiv:hep-lat/9808026](#).
- [58] P. Hasenfratz, S. Hauswirth, T. Jörg, F. Niedermayer, and K. Holland, “Testing the fixed-point QCD action and the construction of chiral currents,” *Nucl. Phys.* **B643** (2002) 280–320, [arXiv:hep-lat/0205010](#).
- [59] K. Fujikawa, “A continuum limit of the chiral Jacobian in lattice gauge theory,” *Nucl. Phys.* **B546** (1999) 480–494, [arXiv:hep-th/9811235](#).
- [60] H. Suzuki, “Simple evaluation of chiral Jacobian with the overlap Dirac operator,” *Prog. Theor. Phys.* **102** (1999) 141–147, [arXiv:hep-th/9812019](#).
- [61] K. Fujikawa, “Generalized Ginsparg-Wilson algebra and index theorem on the lattice,” *Int. J. Mod. Phys.* **B16** (2002) 1931–1942, [arXiv:hep-lat/0205024](#).
- [62] D. H. Adams, “Axial anomaly and topological charge in lattice gauge theory with overlap Dirac operator,” *Annals Phys.* **296** (2002) 131–151, [arXiv:hep-lat/9812003](#).
- [63] C. Gattringer, “A new approach to Ginsparg-Wilson fermions,” *Phys. Rev.* **D63** (2001) 114501, [arXiv:hep-lat/0003005](#).
- [64] C. Gattringer, I. Hip, and C. B. Lang, “Approximate Ginsparg-Wilson fermions: A first test,” *Nucl. Phys.* **B597** (2001) 451–474, [arXiv:hep-lat/0007042](#).
- [65] C. Morningstar, “The Monte Carlo method in quantum field theory,” [arXiv:hep-lat/0702020](#).
- [66] N. Metropolis, A. W. Rosenbluth, M. N. Rosenbluth, A. H. Teller, and E. Teller, “Equation of state calculations by fast computing machines,” *J. Chem. Phys.* **21** (1953) 1087–1092.
- [67] A. D. Kennedy, “Algorithms for dynamical fermions,” [arXiv:hep-lat/0607038](#).
- [68] **APE** Collaboration, M. Albanese *et al.*, “Glueball masses and string tension in lattice QCD,” *Phys. Lett.* **B192** (1987) 163.
- [69] T. A. DeGrand, A. Hasenfratz, and T. G. Kovacs, “Revealing topological structure in the  $SU(2)$  vacuum,” *Nucl. Phys.* **B520** (1998) 301–322, [arXiv:hep-lat/9711032](#).
- [70] T. Jörg, “Chiral measurements in quenched lattice QCD with fixed-point fermions,” [arXiv:hep-lat/0206025](#).
- [71] A. Hasenfratz and F. Knechtli, “Flavor symmetry and the static potential with hypercubic blocking,” *Phys. Rev.* **D64** (2001) 034504, [arXiv:hep-lat/0103029](#).
- [72] J. Foley *et al.*, “Practical all-to-all propagators for lattice QCD,” *Comput. Phys. Commun.* **172** (2005) 145–162, [arXiv:hep-lat/0505023](#).
- [73] D. B. Leinweber, W. Melnitchouk, D. G. Richards, A. G. Williams, and J. M. Zanotti, “Baryon spectroscopy in lattice QCD,” *Lect. Notes Phys.* **663** (2005) 71–112, [arXiv:nucl-th/0406032](#).
- [74] S. Gusken *et al.*, “Non-singlet axial vector couplings of the baryon octet in lattice QCD,” *Phys. Lett.* **B227** (1989) 266.
- [75] C. Best *et al.*, “Pion and rho structure functions from lattice QCD,” *Phys. Rev.* **D56** (1997) 2743–2754, [arXiv:hep-lat/9703014](#).
- [76] C. Michael, “Adjoint sources in Lattice Gauge Theory,” *Nucl. Phys.* **B259** (1985) 58.

- [77] M. Lüscher and U. Wolff, “How to calculate the elastic scattering matrix in two-dimensional quantum field theories by numerical simulation,” *Nucl. Phys.* **B339** (1990) 222–252.
- [78] R. G. Edwards, “Topology and low-lying fermion modes,” *Nucl. Phys. Proc. Suppl.* **106** (2002) 38–46, [arXiv:hep-lat/0111009](#).
- [79] T. A. DeGrand and S. Schaefer, “Improving meson two-point functions in lattice QCD,” *Comput. Phys. Commun.* **159** (2004) 185–191, [arXiv:hep-lat/0401011](#).
- [80] L. Giusti, P. Hernández, M. Laine, P. Weisz, and H. Wittig, “Low-energy couplings of QCD from current correlators near the chiral limit,” *JHEP* **04** (2004) 013, [arXiv:hep-lat/0402002](#).
- [81] H. Fukaya, S. Hashimoto, and K. Ogawa, “Low-lying mode contribution to the quenched meson correlators in the  $\epsilon$ -regime,” *Prog. Theor. Phys.* **114** (2005) 451–476, [arXiv:hep-lat/0504018](#).
- [82] R. Sommer, “A New way to set the energy scale in lattice gauge theories and its applications to the static force and  $\alpha_s$  in  $SU(2)$  Yang-Mills theory,” *Nucl. Phys.* **B411** (1994) 839–854, [arXiv:hep-lat/9310022](#).
- [83] E. Eichten, K. Gottfried, T. Kinoshita, K. D. Lane, and T.-M. Yan, “Charmonium: Comparison with experiment,” *Phys. Rev.* **D21** (1980) 203.
- [84] J. L. Richardson, “The heavy quark potential and the  $\Upsilon$ ,  $J/\psi$  systems,” *Phys. Lett.* **B82** (1979) 272.
- [85] S. Sasaki, T. Blum, and S. Ohta, “A lattice study of the nucleon excited states with domain wall fermions,” *Phys. Rev.* **D65** (2002) 074503, [arXiv:hep-lat/0102010](#).
- [86] G. Martinelli, S. Petrarca, C. T. Sachrajda, and A. Vladikas, “Non-perturbative renormalization of two-quark operators with an improved lattice fermion action,” *Phys. Lett.* **B311** (1993) 241–248.
- [87] S. Necco, “Determining QCD low-energy couplings from lattice simulations,” *PoS LATTICE2007* (2006) 021, [arXiv:0710.2444 \[hep-lat\]](#).
- [88] F. C. Hansen and H. Leutwyler, “Charge correlations and topological susceptibility in QCD,” *Nucl. Phys.* **B350** (1991) 201–227.
- [89] J. Gasser and H. Leutwyler, “Chiral perturbation theory to one loop,” *Ann. Phys.* **158** (1984) 142.
- [90] S. M. Nishigaki, P. H. Damgaard, and T. Wettig, “Smallest Dirac eigenvalue distribution from Random Matrix Theory,” *Phys. Rev.* **D58** (1998) 087704, [arXiv:hep-th/9803007](#).
- [91] P. Hasenfratz and F. Niedermayer, “Finite size and temperature effects in the AF Heisenberg model,” [arXiv:hep-lat/9212022](#).
- [92] M. Lüscher, “Volume dependence of the energy spectrum in massive quantum field theories. 1. Stable particle states,” *Commun. Math. Phys.* **104** (1986) 177.
- [93] S. R. Sharpe and N. Shoreh, “Physical results from unphysical simulations,” *Phys. Rev.* **D62** (2000) 094503, [arXiv:hep-lat/0006017](#).
- [94] S. R. Sharpe, “Applications of chiral perturbation theory to lattice QCD,” [arXiv:hep-lat/0607016](#).
- [95] L. Lyons, *A practical guide to data analysis for physical science students*. Cambridge University Press, 1991.
- [96] I. Montvay and G. Münster, *Quantum fields on a lattice*. Cambridge, UK: Univ. Pr., 1994.
- [97] F. X. Lee and D. B. Leinweber, “Negative-parity baryon spectroscopy,” *Nucl. Phys. Proc. Suppl.* **73** (1999) 258–260, [arXiv:hep-lat/9809095](#).
- [98] **CP-PACS** Collaboration, T. Yamazaki *et al.*, “Spectral function and excited states in lattice QCD with maximum entropy method,” *Phys. Rev.* **D65** (2002) 014501, [arXiv:hep-lat/0105030](#).
- [99] F. X. Lee, D. B. Leinweber, L. Zhou, J. M. Zanotti, and S. Choe, “ $N^*$  masses from an anisotropic lattice QCD action,” *Nucl. Phys. Proc. Suppl.* **106** (2002) 248–250, [arXiv:hep-lat/0110164](#).

- [100] W. Melnitchouk *et al.*, “Baryon resonances from a novel fat-link fermion action,” *Nucl. Phys. Proc. Suppl.* **109A** (2002) 96–100, [arXiv:hep-lat/0201005](#).
- [101] W. Melnitchouk *et al.*, “Excited baryons in lattice QCD,” *Phys. Rev.* **D67** (2003) 114506, [arXiv:hep-lat/0202022](#).
- [102] F. X. Lee *et al.*, “Excited baryons from Bayesian priors and overlap fermions,” *Nucl. Phys. Proc. Suppl.* **119** (2003) 296–298, [arXiv:hep-lat/0208070](#).
- [103] S. Sasaki, K. Sasaki, T. Hatsuda, and M. Asakawa, “Bayesian approach to the first excited nucleon state in lattice QCD,” *Nucl. Phys. Proc. Suppl.* **119** (2003) 302–304, [arXiv:hep-lat/0209059](#).
- [104] **CSSM Lattice** Collaboration, J. M. Zanotti *et al.*, “Spin-3/2 nucleon and Delta baryons in lattice QCD,” *Phys. Rev.* **D68** (2003) 054506, [arXiv:hep-lat/0304001](#).
- [105] **BGR (Bern-Graz-Regensburg)** Collaboration, D. Brömmel *et al.*, “Excited nucleons with chirally improved fermions,” *Phys. Rev.* **D69** (2004) 094513, [arXiv:hep-ph/0307073](#).
- [106] K. Sasaki, S. Sasaki, T. Hatsuda, and M. Asakawa, “Excited nucleon spectrum from lattice QCD with maximum entropy method,” *Nucl. Phys. Proc. Suppl.* **129** (2004) 212–214, [arXiv:hep-lat/0309177](#).
- [107] S. Sasaki, “Latest results from lattice QCD for the Roper resonance,” *Prog. Theor. Phys. Suppl.* **151** (2003) 143–148, [arXiv:nucl-th/0305014](#).
- [108] **BGR (Bern-Graz-Regensburg)** Collaboration, D. Brömmel *et al.*, “Low lying nucleons from chirally improved fermions,” *Nucl. Phys. Proc. Suppl.* **129** (2004) 251–253, [arXiv:hep-lat/0309036](#).
- [109] N. Mathur *et al.*, “Roper resonance and  $S_{11}(1535)$  from lattice QCD,” *Phys. Lett.* **B605** (2005) 137–143, [arXiv:hep-ph/0306199](#).
- [110] **BGR (Bern-Graz-Regensburg)** Collaboration, T. Burch *et al.*, “Spatially improved operators for excited hadrons on the lattice,” *Phys. Rev.* **D70** (2004) 054502, [arXiv:hep-lat/0405006](#).
- [111] D. Guadagnoli, M. Papinutto, and S. Simula, “Extracting excited states from lattice QCD: The Roper resonance,” *Phys. Lett.* **B604** (2004) 74–81, [arXiv:hep-lat/0409011](#).
- [112] **BGR (Bern-Graz-Regensburg)** Collaboration, T. Burch *et al.*, “Excited hadrons from improved interpolating fields,” *Nucl. Phys. Proc. Suppl.* **140** (2005) 284–286, [arXiv:hep-lat/0409014](#).
- [113] K. Sasaki, S. Sasaki, and T. Hatsuda, “Spectral analysis of excited nucleons in lattice QCD with maximum entropy method,” *Phys. Lett.* **B623** (2005) 208–217, [arXiv:hep-lat/0504020](#).
- [114] **Lattice Hadron Physics (LHPC)** Collaboration, S. Basak *et al.*, “Clebsch-Gordan construction of lattice interpolating fields for excited baryons,” *Phys. Rev.* **D72** (2005) 074501, [arXiv:hep-lat/0508018](#).
- [115] K. Sasaki and S. Sasaki, “Excited baryon spectroscopy from lattice QCD: Finite size effect and hyperfine mass splitting,” *Phys. Rev.* **D72** (2005) 034502, [arXiv:hep-lat/0503026](#).
- [116] K. Sasaki and S. Sasaki, “Finite size effect in excited baryon spectroscopy,” *PoS LAT2005* (2006) 060, [arXiv:hep-lat/0508026](#).
- [117] T. Burch *et al.*, “Excited hadrons on the lattice: Mesons,” *Phys. Rev.* **D73** (2006) 094505, [arXiv:hep-lat/0601026](#).
- [118] S. Basak *et al.*, “Lattice QCD determination of patterns of excited baryon states,” *Phys. Rev.* **D76** (2007) 074504, [arXiv:0709.0008 \[hep-lat\]](#).
- [119] M. Asakawa, T. Hatsuda, and Y. Nakahara, “Maximum entropy analysis of the spectral functions in lattice QCD,” *Prog. Part. Nucl. Phys.* **46** (2001) 459–508, [arXiv:hep-lat/0011040](#).
- [120] G. P. Lepage *et al.*, “Constrained curve fitting,” *Nucl. Phys. Proc. Suppl.* **106** (2002) 12–20, [arXiv:hep-lat/0110175](#).

- [121] D. Diakonov, V. Petrov, and M. V. Polyakov, “Exotic anti-decuplet of baryons: Prediction from chiral solitons,” *Z. Phys.* **A359** (1997) 305–314, [arXiv:hep-ph/9703373](#).
- [122] L. Y. Glozman and D. O. Riska, “The spectrum of the nucleons and the strange hyperons and chiral dynamics,” *Phys. Rept.* **268** (1996) 263–303, [arXiv:hep-ph/9505422](#).
- [123] L. Y. Glozman, W. Plessas, K. Varga, and R. F. Wagenbrunn, “Unified description of light- and strange-baryon spectra,” *Phys. Rev.* **D58** (1998) 094030, [arXiv:hep-ph/9706507](#).
- [124] L. Y. Glozman, “Origins of the baryon spectrum,” *Nucl. Phys.* **A663** (2000) 103–112, [arXiv:hep-ph/9908423](#).
- [125] R. H. Dalitz, J. McGinley, C. Belyea, and S. Anthony, “Theory of low-energy kaon-nucleon scattering,” Invited paper given at Int. Conf. on Hypernuclear and Kaon Physics, Heidelberg, West Germany, Jun 20-25, 1982.
- [126] J. N. Labrenz and S. R. Sharpe, “Quenched chiral perturbation theory for baryons,” *Phys. Rev.* **D54** (1996) 4595–4608, [arXiv:hep-lat/9605034](#).
- [127] **CLAS** Collaboration, S. Stepanyan *et al.*, “Observation of an exotic  $S = +1$  baryon in exclusive photoproduction from the deuteron,” *Phys. Rev. Lett.* **91** (2003) 252001, [arXiv:hep-ex/0307018](#).
- [128] **LEPS** Collaboration, T. Nakano *et al.*, “Observation of  $S = +1$  baryon resonance in photo-production from neutron,” *Phys. Rev. Lett.* **91** (2003) 012002, [arXiv:hep-ex/0301020](#).
- [129] **SAPHIR** Collaboration, J. Barth *et al.*, “Observation of the positive-strangeness pentaquark  $\Theta^+$  in photoproduction with the SAPHIR detector at ELSA,” *Phys. Lett.* **B572** (2003) 127–132, [arXiv:hep-ex/0307083](#).
- [130] **DIANA** Collaboration, V. V. Barmin *et al.*, “Observation of a baryon resonance with positive strangeness in  $K^+$  collisions with  $Xe$  nuclei,” *Phys. Atom. Nucl.* **66** (2003) 1715–1718, [arXiv:hep-ex/0304040](#).
- [131] A. E. Asratyan, A. G. Dolgolenko, and M. A. Kubantsev, “Evidence for formation of a narrow  $K_S^0 p$  resonance with mass near 1533 MeV in neutrino interactions,” *Phys. Atom. Nucl.* **67** (2004) 682–687, [arXiv:hep-ex/0309042](#).
- [132] **CLAS** Collaboration, V. Kubarovsky *et al.*, “Observation of an exotic baryon with  $S = +1$  in photoproduction from the proton,” *Phys. Rev. Lett.* **92** (2004) 032001, [arXiv:hep-ex/0311046](#).
- [133] **HERMES** Collaboration, A. Airapetian *et al.*, “Evidence for a narrow  $|S| = 1$  baryon state at a mass of 1528 MeV in quasi-real photoproduction,” *Phys. Lett.* **B585** (2004) 213, [arXiv:hep-ex/0312044](#).
- [134] **ZEUS** Collaboration, S. Chekanov *et al.*, “Evidence for a narrow baryonic state decaying to  $K_S^0 p$  and  $K_S^0$  anti- $p$  in deep inelastic scattering at HERA,” *Phys. Lett.* **B591** (2004) 7–22, [arXiv:hep-ex/0403051](#).
- [135] **SVD** Collaboration, A. Aleev *et al.*, “Observation of narrow baryon resonance decaying into  $p K_S^0$  in  $p A$  interactions at 70 GeV/c with SVD-2 setup,” *Phys. Atom. Nucl.* **68** (2005) 974–981, [arXiv:hep-ex/0401024](#).
- [136] **COSY-TOF** Collaboration, M. Abdel-Bary *et al.*, “Evidence for a narrow resonance at 1530 MeV in the  $K^0 p$  system of the reaction  $p p \rightarrow \Sigma^+ K^0 p$  from the COSY-TOF experiment,” *Phys. Lett.* **B595** (2004) 127–134, [arXiv:hep-ex/0403011](#).
- [137] P. Z. Aslanyan, V. N. Emelyanenko, and G. G. Rikhkvitzkaya, “Observation of  $S = +1$  narrow resonances in the system  $K_S^0 p$  from  $p + C_3H_8$  collision at 10 GeV/c,” *Nucl. Phys.* **A755** (2005) 375–378, [arXiv:hep-ex/0403044](#).
- [138] **BES** Collaboration, J. Z. Bai *et al.*, “Search for the pentaquark state in  $\psi(2S)$  and  $J/\psi$  decays to  $K_S^0 p K^-$  anti- $n$  and  $K_S^0$  anti- $p K^+ n$ ,” *Phys. Rev.* **D70** (2004) 012004, [arXiv:hep-ex/0402012](#).

- [139] **HERA-B** Collaboration, K. T. Knopfle, M. Zavertyaev, and T. Zivko, “Search for  $\Theta^+$  and  $\Xi(3/2) -$  pentaquarks in HERA-B,” *J. Phys.* **G30** (2004) S1363–S1366, [arXiv:hep-ex/0403020](#).
- [140] A. C. Kraan, “Interactions of heavy stable hadronizing particles,” *Eur. Phys. J.* **C37** (2004) 91–104, [arXiv:hep-ex/0404001](#).
- [141] **HyperCP** Collaboration, M. J. Longo *et al.*, “High statistics search for the  $\Theta^+(1540)$  pentaquark,” *Phys. Rev.* **D70** (2004) 111101, [arXiv:hep-ex/0410027](#).
- [142] **BaBar** Collaboration, T. Berger-Hryn’ova, “A study of  $B^+ \rightarrow p$  anti- $p$   $K^+$  and a search for a  $\Theta^{++}$  pentaquark candidate in  $B$  decay,” *Int. J. Mod. Phys.* **A20** (2005) 3749–3752, [arXiv:hep-ex/0411017](#).
- [143] **Belle** Collaboration, K. Abe *et al.*, “Search for pentaquarks at Belle,” [arXiv:hep-ex/0411005](#).
- [144] **CDF** Collaboration, D. O. Litvintsev, “Pentaquark searches at CDF,” *Nucl. Phys. Proc. Suppl.* **142** (2005) 374–377, [arXiv:hep-ex/0410024](#).
- [145] S. R. Armstrong, “Pentaquark searches in electron positron annihilations and two-photon collisions at LEP,” *Nucl. Phys. Proc. Suppl.* **142** (2005) 364–369, [arXiv:hep-ex/0410080](#).
- [146] S. Ricciardi, “Pentaquarks and new hadron spectroscopy at BaBar,” [arXiv:hep-ex/0507027](#).
- [147] **Belle** Collaboration, K. Abe *et al.*, “Search for the  $\Theta^+(1540)$  pentaquark using kaon secondary interactions at Belle,” *Phys. Lett.* **B632** (2006) 173–180, [arXiv:hep-ex/0507014](#).
- [148] Y. Azimov, K. Goetze, and I. Strakovsky, “A possible explanation why the  $\Theta^+$  is seen in some experiments and not in others,” [arXiv:0704.3045 \[hep-ph\]](#).
- [149] F. Csikor, Z. Fodor, S. D. Katz, and T. G. Kovacs, “Pentaquark hadrons from lattice QCD,” *JHEP* **11** (2003) 070, [arXiv:hep-lat/0309090](#).
- [150] S. Sasaki, “Lattice study of exotic  $S = +1$  baryon,” *Phys. Rev. Lett.* **93** (2004) 152001, [arXiv:hep-lat/0310014](#).
- [151] T.-W. Chiu and T.-H. Hsieh, “A study of  $\Theta^+$  ( $udud$  anti- $s$ ) in lattice QCD with exact chiral symmetry,” *Phys. Rev.* **D72** (2005) 034505, [arXiv:hep-ph/0403020](#).
- [152] N. Ishii *et al.*, “Pentaquark in anisotropic lattice QCD,” *Nucl. Phys.* **A755** (2005) 467–470, [arXiv:hep-lat/0501022](#).
- [153] T. T. Takahashi, T. Umeda, T. Onogi, and T. Kunihiro, “Search for the possible  $S = +1$  pentaquark states in quenched lattice QCD,” *Phys. Rev.* **D71** (2005) 114509, [arXiv:hep-lat/0503019](#).
- [154] C. Alexandrou and A. Tsapalis, “A lattice study of the pentaquark state,” *Phys. Rev.* **D73** (2006) 014507, [arXiv:hep-lat/0503013](#).
- [155] F. Csikor, Z. Fodor, S. D. Katz, T. G. Kovacs, and B. C. Toth, “A comprehensive search for the  $\Theta^+$  pentaquark on the lattice,” *Phys. Rev.* **D73** (2006) 034506, [arXiv:hep-lat/0503012](#).
- [156] N. Mathur *et al.*, “A study of pentaquarks on the lattice with overlap fermions,” *Phys. Rev.* **D70** (2004) 074508, [arXiv:hep-ph/0406196](#).
- [157] B. G. Lasscock *et al.*, “Search for the pentaquark resonance signature in lattice QCD,” *Phys. Rev.* **D72** (2005) 014502, [arXiv:hep-lat/0503008](#).
- [158] **BGR (Bern-Graz-Regensburg)** Collaboration, K. Holland and K. J. Juge, “Absence of evidence for pentaquarks on the lattice,” *Phys. Rev.* **D73** (2006) 074505, [arXiv:hep-lat/0504007](#).
- [159] R. L. Jaffe and F. Wilczek, “Diquarks and exotic spectroscopy,” *Phys. Rev. Lett.* **91** (2003) 232003, [arXiv:hep-ph/0307341](#).
- [160] L. Y. Glozman, “ $\Theta^+$  in a chiral constituent quark model and its interpolating fields,” *Phys. Lett.* **B575** (2003) 18–24, [arXiv:hep-ph/0308232](#).

- [161] J. K. Perring and T. H. R. Skyrme, “A model unified field equation,” *Nucl. Phys.* **31** (1962) 550–555.
- [162] T. H. R. Skyrme, “A unified field theory of mesons and baryons,” *Nucl. Phys.* **31** (1962) 556–569.
- [163] E. Witten, “Current algebra, baryons, and quark confinement,” *Nucl. Phys.* **B223** (1983) 433–444.
- [164] E. Guadagnini, “Baryons as solitons and mass formulas,” *Nucl. Phys.* **B236** (1984) 35.
- [165] M. Karliner and H. J. Lipkin, “A diquark-triquark model for the  $KN$  pentaquark,” *Phys. Lett.* **B575** (2003) 249–255, [arXiv:hep-ph/0402260](#).
- [166] C. Michael, “Hadronic decays,” *PoS LAT2005* (2006) 008, [arXiv:hep-lat/0509023](#).
- [167] M. Lüscher, “Signatures of unstable particles in finite volume,” *Nucl. Phys.* **B364** (1991) 237–254.
- [168] N. Ishii *et al.*, “Pentaquark baryon in anisotropic lattice QCD,” *Phys. Rev.* **D71** (2005) 034001, [arXiv:hep-lat/0408030](#).
- [169] A. Hasenfratz, P. Hasenfratz, and F. Niedermayer, “Simulating full QCD with the fixed-point action,” *Phys. Rev.* **D72** (2005) 114508, [arXiv:hep-lat/0506024](#).
- [170] G. I. Egri, Z. Fodor, S. D. Katz, and K. K. Szabó, “Topology with dynamical overlap fermions,” *JHEP* **01** (2006) 049, [arXiv:hep-lat/0510117](#).
- [171] H. Fukaya, “Lattice QCD with fixed topology,” [arXiv:hep-lat/0603008](#).
- [172] F. Knechtli and U. Wolff, “Dynamical fermions by global acceptance steps,” *Nucl. Phys. Proc. Suppl.* **129** (2004) 823–825, [arXiv:hep-lat/0308026](#).
- [173] **Alpha** Collaboration, F. Knechtli and U. Wolff, “Dynamical fermions as a global correction,” *Nucl. Phys.* **B663** (2003) 3–32, [arXiv:hep-lat/0303001](#).
- [174] M. Weingart, “Stochastic estimator of the  $s$ -quark determinant in full QCD simulation,” diploma thesis, University of Bern, Switzerland, 2007.
- [175] C. Weiermann. PhD thesis, University of Bern, Switzerland, 2009. in progress.
- [176] G. M. Amdahl, “Validity of the single-processor approach to achieving large scale computing capabilities,” in *AFIPS Conference Proceedings*, 30, pp. 483–485. 1967.
- [177] V. Maillart, “First results in  $2 + 1$  flavor QCD with the fixed-point action,” diploma thesis, University of Bern, Switzerland, 2007.
- [178] H. A. van der Vorst, “Bi-CGSTAB: A fast and smoothly converging variant of Bi-CG for the solution of nonsymmetric linear systems,” *SIAM J. Sci. Stat. Comput.* **13** (1992) no. 2, 631–644.
- [179] G. L. G. Sleijpen and D. R. Fokkema, “Bi-CGSTAB( $\ell$ ) for linear equations involving unsymmetric matrices with complex spectrum,” *Electron. Trans. Numer. Anal.* **1** (1993) no. Sept., 11–32 (electronic only).
- [180] S. Weinberg, “Phenomenological Lagrangians,” *Physica* **A96** (1979) 327.
- [181] J. Gasser and H. Leutwyler, “On the low-energy structure of QCD,” *Phys. Lett.* **B125** (1983) 321.
- [182] J. Gasser and H. Leutwyler, “Chiral perturbation theory: Expansions in the mass of the strange quark,” *Nucl. Phys.* **B250** (1985) 465.
- [183] P. Hasenfratz, “Prospects for perfect actions,” *Nucl. Phys. Proc. Suppl.* **63** (1998) 53–58, [arXiv:hep-lat/9709110](#).
- [184] P. Hasenfratz in preparation, 2008.
- [185] F. C. Hansen, “Finite size effects in spontaneously broken  $SU(N) \times SU(N)$  theories,” *Nucl. Phys.* **B345** (1990) 685–708.

- [186] T. DeGrand, Z. Liu, and S. Schaefer, “Quark condensate in two-flavor QCD,” *Phys. Rev.* **D74** (2006) 094504, [arXiv:hep-lat/0608019](#).
- [187] T. DeGrand and S. Schaefer, “The complete lowest order chiral Lagrangian from a little box,” *PoS LATTICE2007* (2006) 069, [arXiv:0709.2889 \[hep-lat\]](#).
- [188] H. Fukaya *et al.*, “Two-flavor lattice QCD in the  $\epsilon$ -regime and chiral Random Matrix Theory,” *Phys. Rev.* **D76** (2007) 054503, [arXiv:0705.3322 \[hep-lat\]](#).
- [189] G. Martinelli, C. Pittori, C. T. Sachrajda, M. Testa, and A. Vladikas, “A general method for non-perturbative renormalization of lattice operators,” *Nucl. Phys.* **B445** (1995) 81–108, [arXiv:hep-lat/9411010](#).
- [190] G. Colangelo, J. Gasser, and H. Leutwyler, “ $\pi$ - $\pi$  scattering,” *Nucl. Phys.* **B603** (2001) 125–179, [arXiv:hep-ph/0103088](#).
- [191] J. Bijnens, “Quark Mass dependence at Two Loops for Meson Properties,” *PoS LATTICE2007* (2006) 004, [arXiv:0708.1377 \[hep-lat\]](#).
- [192] K. Jansen, A. Nube, A. Shindler, C. Urbach, and U. Wenger, “Exploring the  $\epsilon$ -regime with twisted mass fermions,” *PoS LATTICE2007* (2006) 084, [arXiv:0711.1871 \[hep-lat\]](#).
- [193] **JLQCD** Collaboration, H. Fukaya *et al.*, “Lattice study of meson correlators in the  $\epsilon$ -regime of two-flavor QCD,” [arXiv:0711.4965 \[hep-lat\]](#).
- [194] A. Hasenfratz, R. Hoffmann, and S. Schaefer, “Reweighting towards the chiral limit,” [arXiv:0805.2369 \[hep-lat\]](#).
- [195] P. Hasenfratz *et al.* 2008.
- [196] K. Huang, *Quarks, Leptons and Gauge Fields*. World Scientific, 1st ed., 1982.
- [197] G. Curci, P. Menotti, and G. Paffuti, “Symanzik’s improved Lagrangian for lattice gauge theory,” *Phys. Lett.* **B130** (1983) 205.
- [198] M. Lüscher and P. Weisz, “On-shell improved lattice gauge theories,” *Commun. Math. Phys.* **97** (1985) 59.
- [199] C. Gattringer, R. Hoffmann, and S. Schaefer, “Setting the scale for the Lüscher-Weisz action,” *Phys. Rev.* **D65** (2002) 094503, [arXiv:hep-lat/0112024](#).